Consortium for Small-Scale Modelling

A Description of the

Nonhydrostatic Regional COSMO Model

Part II :

Physical Parameterization

G. Doms, J. Förstner, E. Heise, H.-J. Herzog, D. Mironov, M. Raschendorfer,
T. Reinhardt, B. Ritter, R. Schrodin, J.-P. Schulz and G. Vogel

LM_F90 4.20 **September 2011**

www.cosmo-model.org

Printed at Deutscher Wetterdienst, P.O. Box 100465, 63004 Offenbach, Germany

A Description of the Nonhydrostatic Regional COSMO Model

Part II: Physical Parameterization

Table of Contents

Acknowledgements

The devolopment, coding and documentation of a complex numerical weather prediction model is a joint and continuous effort of many people. We would like to thank all of you who have contributed to the present version of the LM. The model development has especially benefited from various collaborations and discussions with numerous scientists from inside and outside the COSMO community, which we want to appreciate. We are also grateful for all the comments concerning errors and discrepancies in the former version of the model documentation, which helped to improve the present manuscript.

Concerning the model dynamics and numerics, our special thanks go to Louis Wicker for providing the Runge-Kutta based 2-timelevel integration scheme, to Peter Lynch for implementing the digital filtering initialization scheme, to Steve Thomas for the development and coding of the 3-d semi-implicit model version, to Daniel Leuenberger for implementing the SLEVE vertical coordinate, to Hendrik Elbern and Jürgen Rissmann for providing a prototype version of the 2-way interactive nesting, and to Almut Gassmann for a number of developments and extensions related to the filtering of topography, the 3-d transport of precipitation and to the 2-timelevel integration scheme.

Section 1

Overview on the Model System

1.1 General Remarks

The *COSMO-Model* is a nonhydrostatic limited-area atmospheric prediction model. It has been designed for both operational numerical weather prediction (NWP) and various scientific applications on the meso-β and meso-γ scale. The COSMO-Model is based on the primitive thermo-hydrodynamical equations describing compressible flow in a moist atmosphere. The model equations are formulated in rotated geographical coordinates and a generalized terrain following height coordinate. A variety of physical processes are taken into account by parameterization schemes.

Besides the forecast model itself, a number of additional components such as data assimilation, interpolation of boundary conditions from a driving host model, and postprocessing utilities are required to run the model in NWP-mode, climate mode or for case studies. The purpose of the *Description of the Nonhydrostatic Regional COSMO-Model* is to provide a comprehensive documentation of all components of the system and to inform the user about code access and how to install, compile, configure and run the model.

The basic version of the COSMO-Model (formerly known as *Lokal Modell (LM)*) has been developed at the *Deutscher Wetterdienst* (DWD). The COSMO-Model and the triangular mesh global gridpoint model GME form – together with the corresponding data assimilation schemes – the NWP-system at DWD, which is run operationally since end of 1999. The subsequent developments related to the model have been organized within COSMO, the *Consortium for Small-Scale Modelling*. COSMO aims at the improvement, maintenance and operational application of a non-hydrostatic limited-area modelling system, which is now consequently called the COSMO-Model. The meteorological services participating to COSMO at present are listed in Table 1.1.

For more information about COSMO, we refer to the web-site *www.cosmo-model.org*.

The COSMO-Model is available free of charge for scientific and educational purposes, especially for cooperational projects with COSMO members. However, all users are required to sign an agreement with a COSMO national meteorological service and to respect certain conditions and restrictions on code usage. For questions concerning the request and the agreement, please contact the chairman of the COSMO Steering Committee. In the case of a planned operational or commercial use of the COSMO-Model package, special regulations

Table 1.1: COSMO: Participating Meteorological Services

DWD	Deutscher Wetterdienst, Offenbach, Germany
MeteoSwiss	Meteo-Schweiz, Zürich, Switzerland
USAM	Ufficio Generale Spazio Aero e Meteorologia, Roma, Italy
HNMS	Hellenic National Meteorological Service, Athens, Greece
IMGW	Institute of Meteorology and Water Management, Warsaw, Poland
ARPA-SIMC	Agenzia Regionale per la Protezione Ambientale dell Emilia-Romagna Servizio Idro Meteo Clima Bologna, Italy
ARPA-Piemonte	Agenzia Regionale per la Protezione Ambientale, Piemonte, Italy
CIRA	Centro Italiano Ricerche Aerospaziali, Italy
AGeoBW	Amt für Geoinformationswesen der Bundeswehr, Euskirchen, Germany
NMA	National Meteorological Administration, Bukarest, Romania
RosHydroMet	Hydrometeorological Centre of Russia, Moscow, Russia

will apply.

The further development of the modelling system within COSMO is organized in Working Groups which cover the main research and development activities: data assimilation, numerical aspects, physical aspects, interpretation and applications, verification and case studies, reference version and implementation. In 2005, the COSMO Steering Committee decided to define *Priority Projects* with the goal to focus the scientific activities of the COSMO community on some few key issues and support the permanent improvement of the model. For contacting the Work Package Coordinators or members of the Working Groups or Priority Projects, please refer to the COSMO web-site.

At present, the COSMO meteorological services are not equipped to provide extensive support to external users of the model. If problems occur in certain aspects, we would kindly ask you to contact the corresponding Work Package Coordinators or the current Scientific Project Manager. We try to assist you as well as possible.

The authors of this document recognize that typographical and other errors as well as discrepancies in the code and deficiencies regarding the completeness may be present, and your assistance in correcting them is appreciated. All comments and suggestions for improvement or corrections of the documentation and the model code are welcome and may be directed to the authors.

1.2 Basic Model Design and Features

The nonhydrostatic fully compressible COSMO-Model has been developed to meet high-resolution regional forecast requirements of weather services and to provide a flexible tool for various scientific applications on a broad range of spatial scales. Many NWP-models operate on hydrostatic scales of motion with grid spacings down to about 10 km and thus lack the spatial resolution required to explicitly capture small-scale severe weather events. The COSMO-Model has been designed for meso-β and meso-γ scales where nonhydrostatic effects begin to play an essential role in the evolution of atmospheric flows.

By employing 1 to 3 km grid spacing for operational forecasts over a large domain, it is expected that deep moist convection and the associated feedback mechanisms to the larger scales of motion can be explicitly resolved. Meso-γ scale NWP-models thus have the principle potential to overcome the shortcomings resulting from the application of parameterized convection in current coarse-grid hydrostatic models. In addition, the impact of topography on the organization of penetrative convection by, e.g. channeling effects, is represented much more realistically in high resolution nonhydrostatic forecast models.

The present operational application of the model within COSMO is mainly on the meso-β scale using a grid spacing of 7 km. The key issue is an accurate numerical prediction of near-surface weather conditions, focusing on clouds, fog, frontal precipitation, and orographically and thermally forced local wind systems. Since April 2007, a meso-γ scale version is running operationally at DWD by employing a grid spacing of 2.8 km. We expect that this will allow for a direct simulation of severe weather events triggered by deep moist convection, such as supercell thunderstorms, intense mesoscale convective complexes, prefrontal squall-line storms and heavy snowfall from wintertime mesocyclones.

The requirements for the data assimilation system for the operational COSMO-Model are

mainly determined by the very high resolution of the model and by the task to employ it also for nowcasting purposes in the future. Hence, detailed high-resolution analyses have to be able to be produced frequently and quickly, and this requires a thorough use of asynoptic and high-frequency observations such as aircraft data and remote sensing data. Since both 3-dimensional and 4-dimensional variational methods tend to be less appropriate for this purpose, a scheme based on the observation nudging technique has been chosen for data assimilation.

Besides the operational application, the COSMO-Model provides a nonhydrostatic modelling framework for various scientific and technical purposes. Examples are applications of the model to large-eddy simulations, cloud resolving simulations, studies on orographic flow systems and storm dynamics, development and validation of large-scale parameterization schemes by fine-scale modelling, and tests of computational strategies and numerical techniques. For these types of studies, the model should be applicable to both real data cases and artificial cases using idealized initial data.

Such a wide range of applications imposes a number of requirements for the physical, numerical and technical design of the model. The main design requirements are:

(i) use of nonhydrostatic, compressible dynamical equations to avoid restrictions on the spatial scales and the domain size, and application of an efficient numerical method of solution;

(ii) provision of a comprehensive physics package to cover adequately the spatial scales of application, and provision of high-resolution data sets for all external parameters required by the parameterization schemes;

(iii) flexible choice of initial and boundary conditions to accommodate both real data cases and idealized initial states, and use of a mesh-refinement technique to focus on regions of interest and to handle multi-scale phenomena;

(iv) use of a high-resolution analysis method capable of assimilating high-frequency asynoptic data and remote sensing data;

(v) use of pure Fortran constructs to render the code portable among a variety of computer systems, and application of the standard MPI-software for message passing on distributed memory machines to accommodate broad classes of parallel computers.

The development of the COSMO-Model was organized along these basic guidelines. However, not all of the requirements are fully implemented, and development work and further improvement is an ongoing task. The main features and characteristics of the present release are summarized below.

Dynamics

- **Model Equations** – Nonhydrostatic, full compressible hydro-thermodynamical equations in advection form. Subtraction of a hydrostatic base state at rest.
- **Prognostic Variables** – Horizontal and vertical Cartesian wind components, pressure perturbation, temperature, specific humidity, cloud water content. Optionally: cloud ice content, turbulent kinetic energy, specific water content of rain, snow and graupel.
- **Diagnostic Variables** – Total air density, precipitation fluxes of rain and snow.

- **Coordinate System** – Generalized terrain-following height coordinate with rotated geographical coordinates and user defined grid stretching in the vertical. Options for (i) base-state pressure based height coordinate, (ii) Gal-Chen height coordinate and (iii) exponential height coordinate (SLEVE) according to Schär et al. (2002).

Numerics

- **Grid Structure** – Arakawa C-grid, Lorenz vertical grid staggering.
- **Spatial Discretization** – Second-order finite differences. For the two time-level scheme also 1st and 3rd to 6th order horizontal advection (default: 5th order). Option for explicit higher order vertical advection.
- **Time Integration** – Second-order leapfrog HE-VI (horizontally explicit, vertically implicit) time-split integration scheme by default, including extensions proposed by Skamarock and Klemp (1992). Option for a three time-level 3-d semi-implicit scheme (Thomas et al., 2000). Several Options for two time-level 2nd and 3rd order Runge-Kutta split-explicit scheme after Wicker and Skamarock (2002) and a TVD-variant (Total Variation Diminishing) of a 3rd order Runge-Kutta split-explicit scheme.
- **Numerical Smoothing** – 4th-order linear horizontal diffusion with option for a monotonic version including an orographic limiter. Rayleigh damping in upper layers. 2-d divergence damping and off-centering in the vertical in split time steps.

Initial and Boundary Conditions

- **Initial Conditions** – Interpolated initial data from various coarse-grid driving models (GME, ECMWF, COSMO-Model) or from the continuous data assimilation stream (see below). Option for user-specified idealized initial fields.
- **Lateral Boundary Conditions** – 1-way nesting by Davies-type lateral boundary formulation. Data from several coarse-grid models can be processed (GME, IFS, COSMO-Model). Option for periodic boundary conditions.
- **Top Boundary Conditions** – Options for rigid lid condition and Rayleigh damping layer.
- **Initialization** – Digital-filter initialization of unbalanced initial states (Lynch et al., 1997) with options for adiabatic and diabatic initialization.

Physical Parameterizations

- **Subgrid-Scale Turbulence** – Prognostic turbulent kinetic energy closure at level 2.5 including effects from subgrid-scale condensation and from thermal circulations. Option for a diagnostic second order K-closure of hierarchy level 2 for vertical turbulent fluxes. Preliminary option for calculation of horizontal turbulent diffusion in terrain following coordinates (3D Turbulence).
- **Surface Layer Parameterization** – A Surface layer scheme (based on turbulent kinetic energy) including a laminar-turbulent roughness layer. Option for a stability-dependent drag-law formulation of momentum, heat and moisture fluxes according to similarity theory (Louis, 1979).
- **Grid-Scale Clouds and Precipitation** – Cloud water condensation and evaporation by saturation adjustment. Precipitation formation by a bulk microphysics parameterization including water vapour, cloud water, cloud ice, rain and snow with 3D transport for the precipitating phases. Option for a new bulk scheme including graupel. Option for a simpler column equilibrium scheme.
- **Subgrid-Scale Clouds** – Subgrid-scale cloudiness is interpreted by an empirical function depending on relative humidity and height. A corresponding cloud water content is also interpreted. Option for a statistical subgrid-scale cloud diagnostic for turbulence.

- **Moist Convection** – Tiedtke (1989) mass-flux convection scheme with equilibrium closure based on moisture convergence. Option for the Kain-Fritsch (1992) convection scheme with non-equilibrium CAPE-type closure.
- **Shallow Convection** – Reduced Tiedtke scheme for shallow convection only.
- **Radiation** – δ two-stream radiation scheme after Ritter and Geleyn (1992) for short and longwave fluxes (employing eight spectral intervals); full cloud-radiation feedback.
- **Soil Model** – Multi-layer version of the former two-layer soil model after Jacobsen and Heise (1982) based on the direct numerical solution of the heat conduction equation. Snow and interception storage are included. Option for the (old) two-layer soil model employing the extended force-restore method still included.
- **Terrain and Surface Data** – All external parameters of the model are available at various resolutions for a pre-defined region covering Europe. For other regions or grid-spacings, the external parameter file can be generated by a preprocessor program using high-resolution global data sets.

Data Assimilation

- **Basic Method** – Continuous four-dimensional data assimilation based on observation nudging, with lateral spreading of upper-air observation increments along horizontal surfaces. Explicit balancing by a hydrostatic temperature correction for surface pressure updates, a geostrophic wind correction, and a hydrostatic upper-air pressure correction.
- **Assimilated Atmospheric Observations** – Radiosonde (wind, temperature, humidity), aircraft (wind, temperature), wind profiler (wind), and surface-level data (SYNOP, SHIP, BUOY: pressure, wind, humidity). Optionally RASS (temperature), and ground-based GPS (integrated water vapour) data. Surface-level temperature is used for the soil moisture analysis only.
- **Radar derived rain rates** – Assimilation of near surface rain rates based on latent heat nudging. It locally adjusts the three-dimensional thermodynamical field of the model in such a way that the modelled precipitation rates should resemble the observed ones.
- **Surface and Soil Fields** – Additional two-dimensional intermittent analysis:
  - **Soil Moisture Analysis** – Daily adjustment of soil moisture by a variational method (Hess, 2001) in order to improve 2-m temperature forecasts; use of a Kalman-Filter-like background weighting.
  - **Sea Surface Temperature Analysis** – Daily Cressman-type correction, and blending with global analysis. Use of external sea ice cover analysis.
  - **Snow Depth Analysis** – 6-hourly analysis by weighted averaging of snow depth observations, and use of snowfall data and predicted snow depth.

Code and Parallelization

- **Code Structure** – Modular code structure using standard Fortran constructs.
- **Parallelization** – The parallelization is done by horizontal domain decomposition using a soft-coded gridline halo (2 lines for Leapfrog, 3 for the Runge-Kutta scheme). The *Message Passing Interface* software (MPI) is used for message passing on distributed memory machines.
- **Compilation of the Code** – The compilation of all programs is performed by a Unix shell script invoking the Unix *make* command. All dependencies of the routines are automatically taken into account by the script.
- **Portability** – The model can be easily ported to various platforms; current applications are on conventional scalar machines (UNIX workstations, LINUX and Windows-NT PCs), on vector computers (NEC SX series) and MPP machines (CRAY-XT3, IBM-SP series, SGI ALTIX series).
- **Model Geometry** – 3-d, 2-d and 1-d model configurations. Metrical terms can be adjusted to represent tangential Cartesian geometry with constant or zero Coriolis parameter.

Table 1.2: COSMO Documentation: A Description of the Nonhydrostatic Regional COSMO-Model

Part I:	Dynamics and Numerics
Part II:	Physical Parameterization
Part III:	Data Assimilation
Part IV:	Implementation Documentation
Part V:	Preprocessing: Initial and Boundary Data for the COSMO-Model
Part VI:	Postprocessing
Part VII:	User's Guide

1.3 Organization of the Documentation

For the documentation of the model we follow closely the *European Standards for Writing and Documenting Exchangeable Fortran 90-Code*. These standards provide a framework for the use of Fortran-90 in European meteorological organizations and weather services and thereby facilitate the exchange of code between these centres. According to these standards, the model documentation is split into two categories: external documentation (outside the code) and internal documentation (inside the code). The model provides extensive documentation within the codes of the subroutines. This is in form of procedure headers, section comments and other comments. The external documentation is split into seven parts, which are listed in Table 1.2.

Parts I - III form the scientific documentation, which provides information about the theoretical and numerical formulation of the model, the parameterization of physical processes and the four-dimensional data assimilation. The scientific documentation is independent of (i.e. does not refer to) the code itself. Part IV will describe the particular implementation of the methods and algorithms as presented in Parts I - III, including information on the basic code design and on the strategy for parallelization using the MPI library for message passing on distributed memory machines (not available yet). The generation of initial and boundary conditions from coarse grid driving models is described in Part V. This part is a description of the interpolation procedures and algorithms used (not yet complete) as well as a User's Guide for the interpolation program INT2LM. Available postprocessing utilities will be described (in the future) in Part VI. Finally, the User's Guide of the COSMO-Model provides information on code access and how to install, compile, configure and run the model. The User's Guide contains also a detailed description of various control parameters in the model input file (in NAMELIST format) which allow for a flexible model set-up for various applications. All parts of the documentation are available at the COSMO web-site (*www.cosmo-model.org*).

Section 2

Introduction

Processes in the atmosphere span horizontal scales from molecular to planetary, and they span time scales from less than seconds to longer than annual scales. Because of the limited space and time resolutions of atmospheric models, some important part of these physical processes is not accounted for by the explicit solution in the model grid of the basic equations. This concerns on the one hand all molecular processes as radiation, cloud microphysics and laminar transport in the immediate vicinity of solid boundaries. On the other hand there are processes as turbulence and convection. So-called cloud resolving models are able to explicitly simulate at least part of the convective processes, but in present day numerical weather prediction models both turbulence and convection are not resolved. All processes not explicitly simulated by the model which are considered to be important for the model results have to be dealt with in a special manner which is called parameterization.

Parameterization can be said to be the formulation of the ensemble effect of subgrid-scale processes on the resolved variables. This is a basic assumption for all parameterizations. The formulation is again done in terms of the resolved variables. Parameterization methods rely on a simple modeling of the process under consideration, where at some point a closure condition is required to link the parameterization to the explicitly resolved processes (see, e. g., the chapter on convection, where the closure condition plays an especially important role). For parameterizations to be well posed problems a gap in the space and time scales between explicitly resolved and parameterized processes is required. If there is no scale gap, a mixture of resolved and parameterized parts of a process will be present simultaneously in the simulation. The separation between explicitly resolved and parameterized parts is likely to depend on the actual atmospheric state. Under such circumstances the formulation of a parameterization is extremely difficult. A typical example of this problem is convection. The larger structures of convection (e. g. mesoscale convective complexes) can be resolved by the grids of present day limited area models, but single updrafts and downdrafts of an active cell are not resolved. But in contrast to the horizontal scales, the typical time-scale of penetrating convection is very well resolved by the time-step of numerical models of the atmosphere. Therefore, the assumption of a formulation of the ensemble effect of a subgrid-scale process is not fulfilled in the case of convection.

In contrast to global models, the set of LM-parameterizations does not include a subgrid-scale orography scheme to account for the form drag and the wave drag exerted by the subgrid-scale part of the mountains. The drag effect is partly accounted for by the formulation of the influence of subgrid-scale orography on the roughness length (see the section on external

parameters). The influence of the wave drag on upper tropospheric flow is left to explicitly resolved motions.

Part II of the LM documentation is organized as follows. In Section 3 the implemented schemes for the parameterization of subgrid-scale turbulence are described and Section 4 explains the parameterization of the surface fluxes. Section 5 presents the schemes for describing grid-scale clouds and precipitation and the moist convection is documented in Section 6. The documentation of the parameterization of subgrid-scale cloudiness (Section 7) is not included yet. The radiation scheme is documented in Section 8. The soil and vegetation model, which is described in Section 10 (for the old 2-layer version) or Section 11 (for the multi-layer version), resp., deals with the (explicit) prediction of temperature, water and ice content in the soil. Additionally, the evapotranspiration from the surface of the earth is parameterized. The derivation of data-sets of external parameters as required by the model (orography, land-sea-mask, soiltype, roughness length, plant cover, leaf area index) from basic data-sets (orography, soil texture, land cover) is explained in Section 14.

Section 3

Subgrid Scale Turbulence Closure

The parameterization of small-scale turbulence links the resolvable scales and the nonresolvable fluctuating scales of motion. Turbulent fluxes provide an exchange of momentum, heat and humidity between the earth's surface and the free atmosphere and are thus of crucial importance for a successful numerical simulation of atmospheric flows.

This Chapter first describes the basic formulation of the turbulent mixing terms in the model equations for the general case of threedimensional turbulent fluxes. Then, the special case of one-dimensional, i.e. exclusively vertical turbulent fluxes is discussed, which is based on the assumption of horizontal homogeneity. The corresponding diagnostic closure scheme of LM is described. An option for a full threedimensional treatment of turbulence, which may be used for small-scale simulations, has been implemented lately and is under testing. Finally, the parameterization of the surface fluxes in the Prandtl layer, which constitute the lower boundary conditions of the atmospheric part of the model, is discussed.

3.1 Turbulent mixing formulation

The feedback of subgrid scale turbulent diffusion on the grid-scale variables is represented by the source terms M_ψ^{TD} in the model equations (cf. Part I, (3-143) - (3-150)). First, these terms have to be transformed to the terrain-following ζ-coordinate system. From their definition (cf. PartI, (3-69)), the mixing terms are calculated in terms of the Reynolds stress tensor $\underline{\mathbf{T}}$, the turbulent flux $\mathbf{H}$ of sensible heat and the moisture fluxes $\mathbf{F}^x$ according to

$$M_u^{TD} \equiv -\frac{1}{\rho}(\nabla \cdot \underline{\mathbf{T}}) \cdot \mathbf{e}_\lambda \,, \quad M_v^{TD} \equiv -\frac{1}{\rho}(\nabla \cdot \underline{\mathbf{T}}) \cdot \mathbf{e}_\varphi \,, \quad M_w^{TD} \equiv -\frac{1}{\rho}(\nabla \cdot \underline{\mathbf{T}}) \cdot \mathbf{e}_z$$

for the momentum equations and according to

$$M_T^{TD} \equiv -\frac{1}{\rho c_{pd}} \nabla \cdot \mathbf{H} \,, \qquad M_{q^x}^{TD} \equiv -\frac{1}{\rho} \nabla \cdot \mathbf{F}^x$$

for the heat equation and the equations for the water substances. In order to compute these terms in the ζ-system, the turbulent fluxes will be expressed with physical vector and tensor

components respective the unit base vectors of the orthogonal (λ, φ, z)-system:

$$\begin{aligned}
\underline{\mathbf{T}} &= \tau^{11}\mathbf{e}_\lambda\mathbf{e}_\lambda + \tau^{12}\mathbf{e}_\lambda\mathbf{e}_\varphi + \tau^{13}\mathbf{e}_\lambda\mathbf{e}_z + \\
&\quad \tau^{21}\mathbf{e}_\varphi\mathbf{e}_\lambda + \tau^{22}\mathbf{e}_\varphi\mathbf{e}_\varphi + \tau^{23}\mathbf{e}_\varphi\mathbf{e}_z + \\
&\quad \tau^{31}\mathbf{e}_z\,\mathbf{e}_\lambda + \tau^{32}\mathbf{e}_z\,\mathbf{e}_\varphi + \tau^{33}\mathbf{e}_z\,\mathbf{e}_z \\
\mathbf{H} &= H^1\mathbf{e}_\lambda + H^2\mathbf{e}_\varphi + H^3\mathbf{e}_z \\
\mathbf{F}^x &= F_x^1\,\mathbf{e}_\lambda + F_x^2\,\mathbf{e}_\varphi + F_x^3\,\mathbf{e}_z\,.
\end{aligned} \tag{3.1}$$

Since the Reynolds stress tensor $\underline{\mathbf{T}}$ is symmetric by definition, its components τ^{ij} obey the relation $\tau^{ij} = \tau^{ji}$. The divergence of these fluxes may be calculated in the terrain-following system by applying the conservative formulation (cf. Part I, (3-120)). This yields the mixing terms in the momentum equations as

$$\begin{aligned}
M_u^{TD} &= -\frac{1}{\rho\sqrt{G}}\frac{1}{a\cos\varphi}\left\{\frac{\partial}{\partial\lambda}\left(\sqrt{G}\tau^{11}\right) + \frac{\partial}{\partial\varphi}\left(\sqrt{G}\tau^{12}\cos\varphi\right)\right\} \\
&\quad -\frac{1}{\rho\sqrt{G}}\frac{\partial}{\partial\zeta}\left(\frac{J_\lambda}{a\cos\varphi}\,\tau^{11} + \frac{J_\varphi}{a}\,\tau^{12} - \tau^{13}\right) \\
M_v^{TD} &= -\frac{1}{\rho\sqrt{G}}\frac{1}{a\cos\varphi}\left\{\frac{\partial}{\partial\lambda}\left(\sqrt{G}\tau^{12}\right) + \frac{\partial}{\partial\varphi}\left(\sqrt{G}\tau^{22}\cos\varphi\right)\right\} \\
&\quad -\frac{1}{\rho\sqrt{G}}\frac{\partial}{\partial\zeta}\left(\frac{J_\lambda}{a\cos\varphi}\,\tau^{12} + \frac{J_\varphi}{a}\,\tau^{22} - \tau^{23}\right) \\
M_w^{TD} &= -\frac{1}{\rho\sqrt{G}}\frac{1}{a\cos\varphi}\left\{\frac{\partial}{\partial\lambda}\left(\sqrt{G}\tau^{13}\right) + \frac{\partial}{\partial\varphi}\left(\sqrt{G}\tau^{23}\cos\varphi\right)\right\} \\
&\quad -\frac{1}{\rho\sqrt{G}}\frac{\partial}{\partial\zeta}\left(\frac{J_\lambda}{a\cos\varphi}\,\tau^{13} + \frac{J_\varphi}{a}\,\tau^{23} - \tau^{33}\right).
\end{aligned} \tag{3.2}$$

The turbulent mixing term in the heat equation can be written as

$$\begin{aligned}
M_T^{TD} &= -\frac{1}{\rho c_{pd}\sqrt{G}}\frac{1}{a\cos\varphi}\left\{\frac{\partial}{\partial\lambda}\left(\sqrt{G}H^1\right) + \frac{\partial}{\partial\varphi}\left(\sqrt{G}H^2\cos\varphi\right)\right\} \\
&\quad -\frac{1}{\rho c_{pd}\sqrt{G}}\frac{\partial}{\partial\zeta}\left(\frac{J_\lambda}{a\cos\varphi}\,H^1 + \frac{J_\varphi}{a}\,H^2 - H^3\right),
\end{aligned} \tag{3.3}$$

and the impact of turbulent fluxes on the water substances is formulated as

$$\begin{aligned}
M_{q^x}^{TD} &= -\frac{1}{\rho\sqrt{G}}\frac{1}{a\cos\varphi}\left\{\frac{\partial}{\partial\lambda}\left(\sqrt{G}F_x^1\right) + \frac{\partial}{\partial\varphi}\left(\sqrt{G}F_x^2\cos\varphi\right)\right\} \\
&\quad -\frac{1}{\rho\sqrt{G}}\frac{\partial}{\partial\zeta}\left(\frac{J_\lambda}{a\cos\varphi}\,F_x^1 + \frac{J_\varphi}{a}\,F_x^2 - F_x^3\right).
\end{aligned} \tag{3.4}$$

The parameterization of the turbulent flux $\mathbf{F}_\psi$ of a scalar quantity ψ is based on K-theory, which relates the subgrid scale flux to the gradient of ψ and a diffusion coefficient K for transport. The general constitutive equation for the fluxes is of the form

$$\mathbf{F}_\psi = -\,\underline{\mathbf{K}}_\psi \cdot \nabla\psi, \tag{3.5}$$

where $\underline{\mathbf{K}}_\psi$ is a dyadic coefficient for diffusion and $-\nabla\psi$ takes the role of a thermodynamic forcing function for the flux. We make use of a very simple structure of the tensor $\underline{\mathbf{K}}_\psi$ by assuming a diagonal form in the z-system and distinguishing a coefficient K_ψ^h for horizontal transports and a coefficient K_ψ^v for vertical transports:

$$\underline{\mathbf{K}}_\psi = K_\psi^h \, \mathbf{e}_\lambda \mathbf{e}_\lambda + K_\psi^h \, \mathbf{e}_\varphi \mathbf{e}_\varphi + K_\psi^v \, \mathbf{e}_z \mathbf{e}_z \, . \tag{3.6}$$

Furthermore, the mixing coefficients are taken to be the same for all scalar quantities, i.e. for heat, water vapour, liquid water and ice. Denoting these coefficients by K_h^h and K_h^v and using Eq. (3-116, Part I) for the calculation of $\nabla\psi$ in the terrain-following coordinate system, the constitutive relation (3.5) yields

$$\begin{aligned} H^1 &= -\rho c_{pd}\pi K_h^h \frac{1}{a\cos\varphi}\left(\frac{\partial\theta}{\partial\lambda} + \frac{J_\lambda}{\sqrt{G}}\frac{\partial\theta}{\partial\zeta}\right) \\ H^2 &= -\rho c_{pd}\pi K_h^h \frac{1}{a}\left(\frac{\partial\theta}{\partial\varphi} + \frac{J_\lambda}{\sqrt{G}}\frac{\partial\theta}{\partial\zeta}\right) \\ H^3 &= +\rho c_{pd}\pi K_h^v \frac{1}{\sqrt{G}}\frac{\partial\theta}{\partial\zeta} \end{aligned} \tag{3.7}$$

for the physical components of the sensible heat flux $\mathbf{H}$, where π is the Exner-scaled pressure and θ is potential temperature (see Section 2.2). Correspondingly, the turbulent fluxes of the moisture variables q^x read

$$\begin{aligned} F_x^1 &= -\rho K_h^h \frac{1}{a\cos\varphi}\left(\frac{\partial q^x}{\partial\lambda} + \frac{J_\lambda}{\sqrt{G}}\frac{\partial q^x}{\partial\zeta}\right) \\ F_x^2 &= -\rho K_h^h \frac{1}{a}\left(\frac{\partial q^x}{\partial\varphi} + \frac{J_\lambda}{\sqrt{G}}\frac{\partial q^x}{\partial\zeta}\right) \\ F_x^3 &= +\rho K_h^v \frac{1}{\sqrt{G}}\frac{\partial q^x}{\partial\zeta} \, . \end{aligned} \tag{3.8}$$

In a similar way, a provision is made to consider anisotropic turbulence for momentum transports by distinguishing the value of the diffusion coefficient for horizontal momentum transport, K_m^h, from the value for vertical momentum exchange, K_m^v. The parameterization of the Reynolds stress tensor is done in terms of a dyadic forcing function $\tilde{\underline{\mathbf{D}}}$, which is taken to be the anisotropic symmetric part of the dyadic tensor $\nabla\mathbf{v}$:

$$\tilde{\underline{\mathbf{D}}} = \nabla\mathbf{v} + (\nabla\mathbf{v})^c - \frac{2}{3}\nabla\cdot\mathbf{v}\,\underline{\mathbf{E}} = \underline{\mathbf{D}} - \frac{2}{3}\nabla\cdot\mathbf{v}\,\underline{\mathbf{E}} \, .$$

Here, $(\nabla\mathbf{v})^c$ is the conjugate of $\nabla\mathbf{v}$, $\underline{\mathbf{D}} = \nabla\mathbf{v} + (\nabla\mathbf{v})^c$ is the deformation tensor and $\underline{\mathbf{E}}$ is the unit tensor. The constitutive equations for the elements τ^{ij} of the Reynolds stress tensor read

$$\begin{aligned} \tau^{11} &= -\rho K_m^h \, (D_{11} - 2D/3) \\ \tau^{22} &= -\rho K_m^h \, (D_{22} - 2D/3) \\ \tau^{33} &= -\rho K_m^v \, (D_{33} - 2D/3) \\ \\ \tau^{12} &= \tau^{21} = -\rho K_m^h D_{12} \\ \tau^{13} &= \tau^{31} = -\rho K_m^v D_{13} \\ \tau^{23} &= \tau^{32} = -\rho K_m^v D_{23} \, . \end{aligned} \tag{3.9}$$

D_{ij} are the physical components of the deformation tensor with respect to the orthogonal base vectors $\mathbf{e}_i$ of the original z-system and D is the wind divergence from Eq. (3-122, Part I). Since $\underline{\mathbf{D}}$ is symmetric, $D_{ij} = D_{ji}$. In the terrain-following ζ-coordinate system, the components D_{ij} can be calculated from

$$\begin{aligned}
D_{11} &= \frac{2}{a\cos\varphi}\left(\frac{\partial u}{\partial\lambda} + \frac{J_\lambda}{\sqrt{G}}\frac{\partial u}{\partial\zeta} - v\sin\varphi\right) \\
D_{22} &= \frac{2}{a}\left(\frac{\partial v}{\partial\varphi} + \frac{J_\varphi}{\sqrt{G}}\frac{\partial v}{\partial\zeta}\right) \\
D_{33} &= -\frac{2}{\sqrt{G}}\frac{\partial w}{\partial\zeta} \\
D_{12} &= \frac{1}{a\cos\varphi}\left(\frac{\partial v}{\partial\lambda} + \frac{J_\lambda}{\sqrt{G}}\frac{\partial v}{\partial\zeta} + u\sin\varphi + \cos\varphi\frac{\partial u}{\partial\varphi} + \cos\varphi\frac{J_\varphi}{\sqrt{G}}\frac{\partial u}{\partial\zeta}\right) \\
D_{13} &= \frac{1}{a\cos\varphi}\left(\frac{\partial w}{\partial\lambda} + \frac{J_\lambda}{\sqrt{G}}\frac{\partial w}{\partial\zeta}\right) - \frac{1}{\sqrt{G}}\frac{\partial u}{\partial\zeta} \\
D_{23} &= \frac{1}{a}\left(\frac{\partial w}{\partial\varphi} + \frac{J_\varphi}{\sqrt{G}}\frac{\partial w}{\partial\zeta}\right) - \frac{1}{\sqrt{G}}\frac{\partial v}{\partial\zeta}\,.
\end{aligned} \tag{3.10}$$

The mixing terms M_ψ^{TD} can now be calculated from (3.2) - (3.4) using the turbulent fluxes according to (3.7) - (3.9), provided that the turbulent diffusion coefficients K_h^h, K_h^v, K_m^h and K_m^v are known. Thus, the key to a turbulence closure scheme is the determination of these mixing coefficients in terms of the grid scale variables.

As can be inferred from the equations above, the evaluation of the mixing terms M_ψ^{TD} is complex and computationally very expensive for the full threedimensional case. This general case is not yet implemented in the model. At present, only a simplified one-dimensional closure scheme is available. It makes use of the so-called boundary layer approximation by neglecting all horizontal turbulent fluxes. This scheme is described in the next section.

3.2 1-D Diagnostic Closure

The diagnostic closure scheme described in this section has been adapted from the operational hydrostatic model EM and DM of DWD. It makes use of the so-called boundary layer approximation by imposing horizontal homogeneity of variables and fluxes resulting in a neglection of all horizontal turbulent fluxes. This approximation is applicable when the horizontal scales of motion are much larger than the vertical scale, since in this case the contributions from horizontal turbulent fluxes become negligible when compared to the dominating vertical transports. The boundary layer approximation is usually justified for model applications to meso-β scale flow systems.

Using this approximation, the mixing terms $M\psi^{TD}$ take a much simpler form. With $H^1 = H^2 = 0$ and $F_x^1 = F_x^2 = 0$, the source terms due to turbulent vertical mixing in the heat equation and in the equations for the water substances read

$$M_T^{TD} = \frac{1}{\rho\sqrt{G}}\frac{\partial}{\partial\zeta}\left(\frac{\rho\pi K_h^v}{\sqrt{G}}\frac{\partial\theta}{\partial\zeta}\right), \tag{3.11}$$

$$M_{q^x}^{TD} = \frac{1}{\rho\sqrt{G}}\frac{\partial}{\partial\zeta}\left(\frac{\rho K_h^v}{\sqrt{G}}\frac{\partial q^x}{\partial\zeta}\right). \tag{3.12}$$

The assumption of horizontal homogeneity also implies that the vertical velocity vanishes. Thus, we set $w = 0$ with respect to the constitutive relations (3.9) for the stress tensor and neglect the horizontal stresses by $\tau^{11} = \tau^{22} = \tau^{12} = 0$. This yields the following form of the mixing terms in the momentum equations:

$$M_u^{TD} = \frac{1}{\rho\sqrt{G}} \frac{\partial}{\partial\zeta} \left(\frac{\rho K_m^v}{\sqrt{G}} \frac{\partial u}{\partial\zeta} \right) , \tag{3.13}$$

$$M_v^{TD} = \frac{1}{\rho\sqrt{G}} \frac{\partial}{\partial\zeta} \left(\frac{\rho K_m^v}{\sqrt{G}} \frac{\partial v}{\partial\zeta} \right) , \tag{3.14}$$

$$M_w^{TD} = 0 . \tag{3.15}$$

The calculation of the vertical diffusion coefficients for momentum and heat is based on the hierarchy level 2 approximation of the equations for the second order moments (see, e.g. Stull (1988)) which are also formulated with the boundary layer approximation. In the level 2 scheme, the coefficients K_m^v and K_h^v can be derived from a diagnostic form of the equation for turbulent kinetic energy. This diagnostic form reveals an equilibrium between the dissipation of turbulent kinetic energy and its production due to mechanical forcing by vertical shear and thermal forcing by buoyancy.

A detailed theoretical formulation of the scheme is given by Müller (1981). The coefficients K_m^v and K_h^v for vertical turbulent transport of momentum and heat are defined as

$$K_m^v = l^2 S_m^{3/2} \sqrt{M^2 - \alpha_n S_h N^2} , \tag{3.16}$$

$$K_h^v = \alpha_n S_h K_m^v . \tag{3.17}$$

The characteristic length scale l for vertical mixing is calculated according to a proposal by Blackadar (1962),

$$l = \frac{\kappa z}{1 + (\kappa z)/l_\infty} , \tag{3.18}$$

where κ is the von-Karman constant and l_∞ is an asymptotic mixing length. The constant parameter α_n denotes the ratio of the diffusion coefficients for heat and momentum at neutral thermal stratification, N^2 is the squared Brunt-Väisälä frequency

$$N^2 = \frac{g}{\theta_v} \frac{\partial \theta_v}{\partial z} , \tag{3.19}$$

where $\theta_v = T_v/\pi$ is virtual potential temperature, and M^2 denotes the square of the vertical wind shear:

$$M^2 = \left(\frac{\partial u}{\partial z} \right)^2 + \left(\frac{\partial v}{\partial z} \right)^2 . \tag{3.20}$$

S_m and S_h are stability functions which depend according to

$$\begin{aligned} S_m &= 1 - \frac{\alpha_0 \Gamma}{S_h} \\ S_h &= \frac{1 - b_1 \Gamma}{1 - b_2 \Gamma} \end{aligned} \tag{3.21}$$

on the stability parameter Γ, defined as

$$\Gamma \;=\; \frac{R_f}{1-R_f}\,. \tag{3.22}$$

R_f in (3.22) denotes the flux-Richardson number, i.e the ratio of the vertical heat flux and the vertical flux of momentum. R_f can be calculated from the quadratic equation

$$R_f \;=\; c_1 \left(Ri + c_2 - \sqrt{Ri^2 - c_3 Ri + c_2^2} \right) , \tag{3.23}$$

where Ri denotes the gradient-Richardson number:

$$Ri \;=\; \frac{N^2}{M^2} = \frac{g}{\theta_v}\frac{\partial \theta_v}{\partial z} \left\{ \left(\frac{\partial u}{\partial z}\right)^2 + \left(\frac{\partial v}{\partial z}\right)^2 \right\}^{-1} . \tag{3.24}$$

The constant parameters α_0, b_1 and b_2 in the definition (3.21) of the stability functions and c_1, c_2 and c_3 in the relation (3.23) for the flux-Richardson number are determined from some universal constants of turbulence theory and from matching conditions to surface layer scaling. They take different values for stable conditions ($Ri > 0$) and for unstable conditions including the neutral case ($Ri \leq 0$). We use the following values of these constants:

		stable	unstable
α_0	=	3.7000 ,	4.025
b_1	=	2.5648 ,	3.337
b_2	=	1.1388 ,	0.688
c_1	=	0.8333 ,	1.285
c_2	=	0.2805 ,	0.2305
c_3	=	0.1122 ,	−0.1023 .

Eq. (3.23) reveals that the scheme does not give a physical meaningful solution for highly stable stratification when the Richardson number exceeds a critical value. In this case it is assumed that the diffusion coefficients for momentum and heat are proportional to their values at neutral stability:

$$\text{if } Ri > Ri_c : \qquad K_m^v \;=\; k_{m0} l^2 M^2 \qquad K_h^v \;=\; \alpha_n k_{h0} l^2 M^2 \,. \tag{3.25}$$

The parameters in (3.25) and those from the mixing length formulation (3.18) have the following values:

$$\begin{aligned} Ri_c &= 0.38\,, \\ k_{m0} &= 0.010\,, \\ k_{h0} &= 0.007\,, \\ \alpha_n &= 1.0\,, \\ \kappa &= 0.4\,, \\ l_\infty &= 500\,m\,. \end{aligned}$$

3.3 1-D TKE-Based Diagnostic Closure

The LM standard scheme for vertical turbulent transport is based on a second-order closure at hierarchy level 2.0 (Mellor and Yamada (1974)), resulting in a traditional diagnostic K-closure as described above. For the Prandtl-layer, a stability and roughness-length dependent surface flux formulation according to Louis (1979) is applied (see Section 4.1). Results from verification and model diagnostics, however, reveal a number of drawbacks:

- There is often insufficient vertical mixing in case of stable stratification during nighttime. This results in too cold and too shallow inversion layers, with a tendency for a decoupling of the surface and the lower atmosphere.
- Also, at the top of the boundary layer there is insufficient mixing in many cases. Here, stratiform PBL (planetary boundary layer) clouds tend to disperse too slowly.
- The scheme gives no solution for large Richardson numbers exceeding a critical value. Thus, there is almost no physical mixing above the boundary layer, which contributes to a too weak PBL entrainment.
- No distinction is made between the values of variables at the surface and in the roughness height z_0. This results in a too small diurnal cycle of surface temperature and too strong evaporation from bare soils.

Instead of searching for remedies within the diagnostic K-closure, a new scheme based on prognostic turbulent kinetic energy (TKE) has been developed. Specific features of the scheme are:

(i) formulation in terms of liquid water potential temperature and total water content,

(ii) inclusion of subgrid thermal inhomogeneities and

(iii) application of a generalized averaging operator to include the interaction of the flow with solid obstacles (roughness elements such as trees or buildings) within a grid box.

The latter option, however, is not applied operationally. The parameterization of surface-layer fluxes has also been completely reformulated in the framework of the TKE-scheme (see Section 4.2). Some details on the new turbulence formulation are described in the following subsections.

3.3.1 General Concept

The vertical diffusion scheme is based on the second order moments of the basic equations. In deriving these equations, however, a more general averaging operator is used which takes solid roughness elements within a control volume (the grid box volume) into account. This method has first been introduced by Raupach and Shaw (1981) for canopy-layer flow. Let V_0 be the volume of a rectangular control box, and $r_V = V/V_0$ the volume fraction which is filled with air (the remaining portion is filled with solid obstacles). Averaging is then done by a running volume mean (denoted by an overbar in the following) only for the part V of V_0. For the generic budget equation for a mass-specific quantity ψ,

$$\frac{\partial \rho\psi}{\partial t} + \nabla \cdot (\rho \mathbf{v}\psi - a^{\psi}\nabla\psi) = Q_{\psi}\,, \tag{3.26}$$

where a^{ψ} is the molecular diffusion constant and Q_{ψ} is the source function, the following form of filtered budget equations results:

$$\frac{\partial \overline{\rho}\widehat{\psi}}{\partial t} + \nabla \cdot (\overline{\rho}\widehat{\mathbf{v}}\widehat{\psi} + \mathbf{F}^{\psi} - a^{\psi}\nabla\overline{\psi}) + (R^{\psi}_{vol} + R^{\psi}_{mol}) = \overline{Q}_{\psi}\,. \tag{3.27}$$

Here, the mass-weighted mean $\widehat{\psi} = \overline{\rho\psi}/\overline{\rho}$ with the corresponding turbulent fluctuation $\psi'' = \psi - \widehat{\psi}$ is used for mass-specific variables. $\mathbf{F}^{\psi} = \overline{\rho\mathbf{v}''\psi''}$ denotes the mean turbulent flux. Two additional terms appear in (3.27) which are related to body-air interactions: A volume term R^{ψ}_{vol} describing the impact of spatial variations of the air-fraction r_V, and a surface term R^{ψ}_{mol} which takes molecular fluxes to the solid body surfaces into account. They are defined by

$$R^{\psi}_{vol} = (\overline{\rho}\widehat{\mathbf{v}}\widehat{\psi} + \mathbf{F}^{\psi} - a^{\psi}\nabla\overline{\psi}) \cdot \nabla(\ln r_V)\,, \tag{3.28}$$

$$R^{\psi}_{mol} = \frac{1}{V}\int_S (a^{\psi}\nabla\psi)\cdot\mathbf{n}\,dS\,, \tag{3.29}$$

where the integration in (3.29) is along the solid body surface S and $\mathbf{n}$ is the unit vector perpendicular to the surface. Using (3.26) and (3.27), the derivation of the second order moments, i.e. the budget equations for the turbulent fluxes, is straightforward. The resulting equations, however, will contain additional volume and surface terms corresponding to (3.28) and (3.29). A special example of a 2-nd order equation is the budget of turbulent kinetic energy (TKE) $e_t = \mathbf{v}''\cdot\mathbf{v}''/2$:

$$\frac{\partial \overline{\rho}\widehat{e_t}}{\partial t} + \nabla \cdot (\overline{\rho}\widehat{\mathbf{v}}\widehat{e_t} + \mathbf{F}^{e_t} - \mu\overline{\mathbf{v}''\cdot\nabla\mathbf{v}}) + (R^{e_t}_{vol} + R^{e_t}_{mol}) = -\overline{\mathbf{v}''\cdot\nabla p} - \overline{\rho\mathbf{v}''\mathbf{v}''}\cdot\cdot\nabla\widehat{\mathbf{v}} - \varepsilon\,. \tag{3.30}$$

The volume and surface term are given in a similar way as in (3.28) and (3.29), and the dissipation rate is denoted by $\varepsilon = \mu\overline{\nabla\mathbf{v}''\cdot\cdot\nabla\mathbf{v}}$, where μ is the dynamic viscosity. In the TKE-equation (3.30), the pressure correlation term may be expanded into

$$-\overline{\mathbf{v}''\cdot\nabla p} \simeq -\frac{1}{\overline{\rho}\overline{\theta}_v}\mathbf{F}^{\theta_v}\cdot\nabla\overline{p} + \widehat{\mathbf{v}}\cdot\overline{\nabla p'} \tag{3.31}$$

θ_v is virtual potential temperature and $\mathbf{F}^{\theta_v} = \mathbf{F}^{\theta} + \{1 + (R_v/R_a - 1\}\mathbf{F}^{q_v} - \mathbf{F}^{q_c}$ denotes the buoyant heat flux, which is comprised of the turbulent heat flux $\mathbf{F}^{\theta}$, the flux of specific humidity $\mathbf{F}^{q_v}$ and the flux of specific cloud water content $\mathbf{F}^{q_c}$. The second term in the pressure work function (3.31) represents the formation of TKE due to wake production from obstacles within the flow. Note that the generalized averaging operator does not commute with respect to partial spatial differentiation (i.e. $\overline{\nabla p'} \neq \nabla\overline{p'} = 0$). For $\overline{\nabla p'}$, the well know isotropic form-drag parameterization is applied.

For the derivation of the second order budgets, it is sufficient to use a somewhat simplified set of basic model equations: Coriolis forces, radiation and precipitation are not considered since the direct impact of these processes on turbulent fluxes is negligible. In order to avoid source term correlations, it is also convenient to apply a thermodynamically filtered set of equations where the phase transition rate due to cloud condensation/evaporation does not occur explicitly. This is achieved by transforming from (θ, q_v, q_c) to liquid water potential temperature $\theta_l = \theta - (L_V/c_{pd})q_c$ and total water $q_w = q_v + q_c$ as dependent variables. Both θ_l and q_w are conserved during moist adiabatic vertical displacements. The resulting second order moments will provide relations for the turbulent fluxes of θ_l and q_w. In order to recover the turbulent fluxes $\mathbf{F}^{\theta}$, $\mathbf{F}^{q_v}$ and $\mathbf{F}^{q_c}$ – which are required by the original model equations – from the fluxes $\mathbf{F}^{\theta_l}$ and $\mathbf{F}^{q_w}$ of the second order scheme, a closure condition for phase transitions is required to relate the variables (θ, q_v, q_c) in a unique way to (θ_l, q_w). We use a variant of the statistical cloud scheme of Sommeria and Deardorff (1977) for this purpose. By this scheme, fluctuations in the thermodynamic variables are no longer independent, but become coupled through instantaneous condensation or evaporation of cloud water. This results in an equivalent coupling of the corresponding fluxes. For instance, the buoyant heat flux in (3.31) is given by a linear relation between $\mathbf{F}^{\theta_l}$ and $A_q\mathbf{F}^{q_w}$,

$$\mathbf{F}^{\theta_v} = A_\theta \mathbf{F}^{\theta_l} + A_q \mathbf{F}^{q_w}\,, \tag{3.32}$$

where the factors A_θ and A_q depend on the saturation fraction r_c of a grid volume. r_c may be interpreted as the fractional cloud cover and is also diagnosed by the scheme. Similar linear relations hold for the calculation of $\mathbf{F}^{\theta}$, $\mathbf{F}^{q_v}$ and $\mathbf{F}^{q_c}$ in terms of $\mathbf{F}^{\theta_l}$ and $\mathbf{F}^{q_w}$. The major advantage of this approach is a consistent inclusion of the effects from sub-grid scale condensation on the turbulent fluxes of heat and moisture.

3.3.2 An Extended level 2.5 Scheme for Vertical Diffusion

For the 5 model variables u, v, w, θ_l, and q_w, the budgets for the corresponding second order moments build a set of 15 prognostic equations. To arrive at a tractable version, a closure on level 2.5 (in the notation of Mellor and Yamada (1982)) is applied. That is, local equilibrium is assumed for all moments except for TKE, where advection and turbulent transport is retained. Furthermore, Rotta-type relaxation approximations (return-to-isotropy) for the pressure covariance terms and Kolmogorov-Heisenberg closure conditions for the dissipation terms are utilized (see e.g. Stull (1988)). The boundary layer hypothesis of horizontal homogeneity is applied as usual, since effects from 3-D turbulence can be neglected for the present meso-β application of the model (these will be incorporated lateron). This leaves only vertical fluxes in the system of equations, where – with the help of the Boussinesq approximation – the difference between the mass-weighted and the Reynolds averages becomes obsolete: $\overline{\rho w''\psi''} \simeq \overline{\rho}\,\overline{w'\psi'}$. We arrive at a set of second order equations with a flux-gradient representation for the turbulent fluxes in the form

$$\overline{w'\psi'} = -K^H \frac{\partial \overline{\psi}}{\partial z}\,, \quad K^H = q\lambda S^H\,, \quad \text{for } \psi = \theta_l, q_l \tag{3.33}$$

$$\overline{w'\psi'} = -K^M \frac{\partial \overline{\psi}}{\partial z}, \quad K^M = q\lambda S^M, \quad \text{for } \psi = u, v \tag{3.34}$$

where the turbulent diffusion coefficients for heat (K^H) and momentum (K^M) are computed in terms of corresponding stability functions for scalars (S^H) and for momentum (S^M), of the turbulent length scale λ and of the turbulent velocity scale $q = \sqrt{2\overline{e_t}}$. The stability functions are determined by a set of two linear equations. For λ, the Blackadar mixing length is assumed and q is predicted using the TKE-equation in the form

$$\frac{\partial q^2}{\partial t} + \overline{\mathbf{v}} \cdot \nabla q^2 - \frac{1}{\overline{\rho}} \frac{\partial}{\partial z} \left(\alpha_T \overline{\rho} \lambda q \frac{\partial q^2}{\partial z} \right) = 2K_M \left\{ \left(\frac{\partial \overline{u}}{\partial z} \right)^2 + \left(\frac{\partial \overline{v}}{\partial z} \right)^2 \right\} + \frac{2g}{\overline{\theta}_v} \overline{w'\theta'_v} - \frac{q^3}{\alpha_M \lambda} \,. \quad (3.35)$$

Here, α_M and α_T are model constants related to the parameterization of the dissipation term and the flux-gradient representation of the turbulent TKE-transport, respectively. According to (3.32) and (3.33), the buoyant heat flux in (3.35) is given by

$$\overline{w'\theta'_v} = -K_H \Gamma_v \,, \quad \text{with} \quad \Gamma_v := A_\theta \frac{\partial \overline{\theta}_l}{\partial z} + A_q \frac{\partial \overline{q}_w}{\partial z} \,. \quad (3.36)$$

Γ_v denotes the effective gradient of virtual potential temperature. For dry conditions (cloud fraction $r_c = 0$), Γ_v is given by the gradient of potential temperature, whereas for moist saturated conditions (cloud fraction $r_c = 1$) Γ_v is given by the gradient of equivalent potential temperature. Thus, with increasing cloud fraction r_c, the state of neutral thermal stability is gradually shifted from dry adiabatic to moist adiabatic stratification. Thereby, higher in-cloud values of turbulent kinetic energy and the corresponding increased vertical mixing in case of a stratocumulus topped boundary layer are taken into account. Also, cloud-top entrainment will be simulated directly without a need for further parameterizations.

Besides the inclusion of sub-grid scale condensation, there are two major extensions compared to traditional level 2.5 schemes. The first is a consistent representation of interactions of the flow with solid obstacles within a grid volume, both in the grid-scale equations and in the second order equations. This concept is useful for various research purposes and allows for instance to resolve canopy layer flows explicitly (flow through porous media). In the current operational application of the model, however, this option is not used and it will not be described further. The second extension concerns the inclusion of subgrid thermal circulations. Inhomogeneities at the rigid surface will always give rise to differential heating and cooling resulting in direct thermal circulation patterns of a length scale being smaller than the grid scale but larger than that of small-scale turbulence. In such a situation, there will be a conversion of kinetic energy related to the circulation patterns (CKE) into TKE with a positive definite source term. This process will especially prevent the solution of the TKE-equation to tend to zero in case of very stable thermal stratification and the well known but unrealistic decoupling of the atmosphere and the surface can be avoided.

The key to get a formulation of this additional source term is the separation of the total sub-grid scale spectrum of motion into a small-scale turbulent part and a large-scale part associated with the thermal circulations. The covariance of two variables may then be decomposed

$$\overline{\phi'\psi'} = (\overline{\phi'\psi'})_L + (\overline{\phi'\psi'})_S \quad (3.37)$$

into a corresponding large-scale part $(\ldots)_L$ and a small-scale turbulent part $(\ldots)_S$. Using

this decomposition, it is possible to derive 2nd-order budgets for both parts separately. Formally, those band pass budgets differ from the total budgets only by conversion terms describing scale interactions of the circulation and the turbulent scales of motion. With a number of approximations and simplifications, it can be shown that the additional source term in the TKE equation is mainly formed by the large scale part of the buoyant heat flux. The simplified equations provide the relation

$$(\overline{w'\theta'_v})_L \propto \tau_L \frac{g}{\overline{\theta}_v} \overline{\theta'^2_v} \propto -\tau_L^2 \frac{g}{\overline{\theta}_v} \frac{\partial(\overline{\rho}\overline{w'\theta'^2_v})_L}{\overline{\rho}\partial z}\,, \tag{3.38}$$

where τ_L is the circulation time scale. This relation is obtained by considering the 2nd order large-scale budget of temperature variance only. Due to thermal inhomogeneities at the rigid surface, temperature variance will always be generated near the surface and then be transported into the atmosphere. According to (3.38), the large-scale heat flux is positive definite. Even in a stable boundary layer it is always directed upwards, but it will be over-compensated by the downward small-scale turbulent fluxes near the surface. The vertical integral of the total heat flux, however, will remain (slightly) positive, which gives the desired impact in the TKE equation. In the present version of the scheme, we use the following parameterization for the large-scale heat flux:

$$(\overline{w'\theta'_v})_L = -L_{pat} \left(\frac{\lambda}{q}\right)^2 \frac{g}{\overline{\theta}_v} \frac{\partial(\overline{\rho} K_H \Gamma_v^2)}{\overline{\rho}\partial z}\,. \tag{3.39}$$

L_{pat} is a pattern length scale representing the dominant scale of thermal inhomogeneities at the surface. Currently, L_{pat} is given a fixed value of 500 m for the model grid spacing of 7 km. Lateron, this value will be replaced by a location dependent external parameter field. The large-scale heat-flux parameterized by Eq. (3.39) is added to the small-scale one in (3.36) to give the total subgrid-scale heat flux used in the TKE equation (3.35).

3.4 3-D TKE-Based Prognostic Closure

3.4.1 Introduction

The parameterization of subgrid-scale turbulent processes, also called a subgrid-scale (SGS) model, is of particular meaning for highly resolved LES-like model simulations. Compared with the grid resolution of the current operational application of LM (7 km), the more refined grid resolution of about 2.8 km of the application LMK (LM-Kürzestfrist), which is under development at DWD, should have also consequences to choose a more adequate turbulence parameterization scheme. Such a scheme is expected to avoid the common boundary layer approximation. It should take into account a three-dimensional SGS model as a natural extension from a horizontally homogeneous scheme. Whether the three-dimensionality of the scheme is already imparative for the present LMK grid resolution is still open to be answered, but in any case this generalization is a good starting point for future grid refinement. In order to come to a reasonable, first result with not too much effort, we take advantage of an existing SGS model available from the LLM (96.5 m), which is a LES-like model closely related to the LM (Herzog et al. (2002) and Herzog et al. (2002)). For the sake of working economy, this three-dimensional scheme is essentially adopted and implemented in the LM

code. Although proceeding in a straightforward manner, we have to take into account the fact that no universal parameterization exists, but we meet always a specific dependence on the given grid resolution. Apart from first adaptations to the LMK grid resolution further work is open to be done in this line. It is important to note that this scheme is at the present stage a dry scheme not yet considering cloud water. The following description documents this first approach and gives the necessary technical explanation of the implementation background.

3.4.2 Physical conception of the SGS model

We start from the LM equation set, which is rewritten here, emphasising now the turbulent flux terms in their three-dimensional form:

$$\left(\frac{\partial \overline{u}_i}{\partial t}\right) = \ldots - \frac{1}{\rho}\frac{\partial \tau_{ij}}{\partial x_j} \tag{3.40}$$

$$\left(\frac{\partial \overline{T}}{\partial t}\right) = \ldots - \frac{1}{c_{pd}\rho}\frac{\partial h_j}{\partial x_j} \tag{3.41}$$

$$\left(\frac{\partial \overline{q}^k}{\partial t}\right) = \ldots - \frac{1}{\rho}\frac{\partial f_j^{q^k}}{\partial x_j} \tag{3.42}$$

In the following the three-dimensionality of these terms is completely retained. τ_{ij} $(i,j = 1,2,3)$ are the six independent components of the turbulent momentum flux tensor, and h_j and ${f_j}^{q^k}$ are the vector flux components of heat and water, respectively. The fluxes are specified by use of a first-order closure assumption, i.e. the fluxes are set proportional to the local gradient multiplied by a local diffusion coefficient. From a formal point of view it is possible to assume for the momentum flux tensor the following specification:

$$\tau_{ij} = -\rho K_m^{ij}\left(\frac{\partial \overline{u}_i}{\partial x_j} + \frac{\partial \overline{u}_j}{\partial x_i}\right) \tag{3.43}$$

where, in accordance with Hinze (1975), who also gives a critical discussion about, the diffusion coefficient is assumed to be a second-order tensor either. It is important to note that the upper indices ij at the diffusion coefficient in (3.43) are not meant to be involved in the common summation convention. In contrast to the SGS model formulation in the LLM, where the diffusion coefficients are assumed isotropic, we want to take into account here anisotropic properties. In that way we will at least distinguish between coefficients in horizontal and vertical direction. Therefore, the momentum coefficients are set

$$K_m^H := K_m^{11} = K_m^{12} = K_m^{22} \qquad 'horizontal\ momentum'; \tag{3.44}$$

$$K_m^V := K_m^{13} = K_m^{23} = K_m^{33} \qquad 'vertical\ momentum'. \tag{3.45}$$

For the scalar fluxes we stipulate as usual

$$h_j = -c_{pd}\rho\pi K_h^j \frac{\partial\overline{\Theta}}{\partial x_j}, \quad f_j^{q^k} = -\rho K_h^j \frac{\partial\overline{q}^k}{\partial x_j}. \tag{3.46}$$

π is the Exner function. Further notation of variables makes use of the usual meteorological symbols. For both the fluxes in (3.46) the scalar or thermal diffusion coefficients have three components each. We assume for them

$$K_h^H := K_h^1 = K_h^2 \qquad 'horizontal\ heat'; \tag{3.47}$$
$$K_h^V := K_h^3 \qquad 'vertical\ heat'. \tag{3.48}$$

In the present scheme we stipulate the following relation between horizontal and vertical diffusion coefficients in accordance with Schlünzen (1988) and Dunst (1980). The horizontal coefficients are determined from the vertical coefficients by use of an anisotropy factor considering the aspect ratio between horizontal and vertical mesh with:

$$K_{m,h}^H := r\frac{\sqrt{(a\cos\varphi\Delta\lambda)^2 + (a\Delta\varphi)^2}}{\Delta z} K_{m,h}^V \approx r\frac{\sqrt{2}\Delta}{\Delta z} K_{m,h}^V. \tag{3.49}$$

Tentatively, we assume $r = 0.1$, and $\Delta \approx 2.8$km. In particular, we have assumed the ratio between horizontal and vertical coefficients to be independent of stability. To determine the horizontal from the vertical coefficients from this relation the vertical coefficient is specified after Prandtl and Kolmogorov as follows:

$$\begin{aligned} K_m^V &= \phi_m\, l\, (\overline{e})^{\frac{1}{2}} \\ K_h^V &= \phi_h\, l\, (\overline{e})^{\frac{1}{2}} \end{aligned} \tag{3.50}$$

Here, the length scale l is adopted from Blackadar (1962) as a height-dependent scale of turbulence

$$l = \frac{\kappa z}{\left(1 + \frac{\kappa z}{l_\infty}\right)}. \tag{3.51}$$

Apart from the still undetermined factors ϕ_m and ϕ_h, which are thought to be stability-dependent, we need the determination of TKE

$$\overline{e} = \frac{1}{2}\left(\overline{u_i' u_i'}\right), \tag{3.52}$$

in order to close the given system. For that purpose we invoke the prognostic TKE-equation quoting Stull (1988), (p.152), which is written

$$\frac{\partial \overline{e}}{\partial t} + \overline{u}_j \frac{\partial \overline{e}}{\partial x_j} = \delta_{j3} \frac{g}{\overline{\Theta}_v} \overline{\left(u'_j \Theta'_v\right)} - \overline{(u'_i u'_j)} \frac{\partial \overline{u}_i}{\partial x_j} - \frac{\partial \overline{\left(u'_j e\right)}}{\partial x_j} - \frac{1}{\rho} \frac{\partial \overline{\left(u'_j p'\right)}}{\partial x_j} - \epsilon, \tag{3.53}$$

where the usual summation convention is valid. To come to a useful prognostic equation from (3.53), some parameterization of it is necessary to be done next. Using the flux-gradient specification and the distinction between horizontal and vertical diffusion coefficients according to (ref3dtke-5), (ref3dtke-6) and (ref3dtke-8), (ref3dtke-9), we arrive at

$$\begin{aligned} \frac{\partial \overline{e}}{\partial t} + \overline{u}_j \frac{\partial \overline{e}}{\partial x_j} &= -K_h^V N^2 + K_m^H S_H^2 + K_m^V S_V^2 + \\ +2 \left(\frac{\partial}{\partial x_1} \left(K_m^H \frac{\partial \overline{e}}{\partial x_1} \right) + \frac{\partial}{\partial x_2} \left(K_m^H \frac{\partial \overline{e}}{\partial x_2} \right) \right) &+ 2 \frac{\partial}{\partial x_3} \left(K_m^V \frac{\partial \overline{e}}{\partial x_3} \right) - c_\epsilon \frac{\overline{e}^{\frac{3}{2}}}{l}. \end{aligned} \tag{3.54}$$

Obviously, the dissipation term ϵ of equation (3.53) has been specified in a form corresponding to the last term on the right-hand side of (3.54), where c_ϵ is a tuning parameter still open to be determined finally. Further, we have introduced the Brunt-Väisälä frequency squared, $N^2 = \frac{g}{\overline{\Theta}_v} \frac{\partial \overline{\Theta}_v}{\partial z}$, in the buoyant production term. Due to the distinction between a horizontal and a vertical diffusion coefficient the shear production term has been split up as follows. From the general definition of the strain tensor

$$S_{ij} = \frac{1}{2} \left(\frac{\partial \overline{u}_i}{\partial x_j} + \frac{\partial \overline{u}_j}{\partial x_i} \right) \tag{3.55}$$

we define horizontal and vertical components from the deformation squared

$$S^2 = 2 S_{ij} S_{ij} \tag{3.56}$$

as follows

$$S_H^2 = 2(S_{11}^2 + S_{22}^2) + 4 S_{12}^2, \qquad S_V^2 = 2 S_{33}^2 + 4(S_{13}^2 + S_{23}^2). \tag{3.57}$$

to obtain then

$$S^2 = S_H^2 + S_V^2.$$

where this splitting-up is a logical association to the corresponding one of the diffusion coefficients. Finally, both the turbulent TKE transport term, which is a triple-correlation term, and the pressure correlation term in (3.53) are collected to form turbulent diffusion

terms as seen above in (3.54). Instead of an explicit new turbulent diffusion coefficient for TKE, it is crudely parameterized by twice the momentum coefficient (Stevens et al. (2000)). Solving this TKE-equation as an additional slow mode prognostic equation of the entire model system, the TKE involved in the Prandtl-Kolmogorov specification (3.50) is found. In order to complete the determination of the vertical coefficients $K^V_{m,h}$ from (3.50), we need the knowledge of the parameters ϕ_m and ϕ_h. They are to be determined as functions of stability to obtain a stability-dependent Prandtl number:

$$Pr = \frac{K^V_m}{K^V_h} = \frac{\phi_m}{\phi_h}. \tag{3.58}$$

In order to come to a reasonable solution, we start as an interlude from an updated version of a SGS-model primarily introduced by Mellor and Yamada (1974) and provided for the earlier operational DWD model EM and DM in a more appropriate form by Müller (1981). In our context with the prognostic TKE equation above this approach is characterised to fulfil an equilibrium limit case:

$$K^V_m S^2_V - K^V_h N^2 - c_\epsilon \frac{\overline{e}^{\frac{3}{2}}}{l} = 0. \tag{3.59}$$

In this model the diffusion coefficients read

$$\begin{aligned} K^V_m &= l^2 \sigma_m^{3/2} \left(S^2_V - \alpha_n \sigma_h N^2 \right)^{1/2}, \\ K^V_h &= \alpha_n l^2 \sigma_h \sigma_m^{3/2} \left(S^2_V - \alpha_n \sigma_h N^2 \right)^{1/2}. \end{aligned} \tag{3.60}$$

The stability dependence is given here in terms of the σ_m and σ_h having

$$\sigma_m = \frac{(1 - \alpha_0 \Gamma)}{\sigma_h}, \quad \sigma_h = \frac{(1 - b_1 \Gamma)}{(1 - b_2 \Gamma)}. \tag{3.61}$$

with

$$\Gamma = \frac{R_f}{(1 - R_f)}, \quad R_f = c_1 \left(Ri_V + c_2 - \sqrt{Ri_V^2 - c_3 Ri_V + c_2^2} \right). \tag{3.62}$$

For the constants see Section 3.2. The local Richardson number is given by

$$Ri_V = \frac{N^2}{S^2_V}, \tag{3.63}$$

and the turbulence length scale is taken from (3.51). Because of (3.60) the Prandtl number reads here

$$Pr = \frac{1}{\alpha_n \sigma_h}. \tag{3.64}$$

Due to the assumption of an equilibrium limit TKE equation for the given Mellor-Yamada model the associated TKE is directly found from (3.59) as

$$\overline{e} = c_\epsilon^{-2/3} \sigma_m^{3/2} l^2 S_V^2 \left(1 - Pr^{-1} Ri_V\right). \tag{3.65}$$

This value is used as an initial condition to start the integration of the prognostic TKE equation from. Reminding the purpose of this SGS model once again, we now stipulate its reasonable approximate connection with the more general TKE equation in such a way that for the equilibrium limit case the Prandtl-Kolmogorov specification for the diffusion coefficients (3.50) should coincide with the a-priori equilibrium specification (3.60), which gives

$$\phi_m \, l \, (\overline{e})^{\frac{1}{2}} = l^2 \, \sigma_m^{2/3} \, (S_V^2 - \alpha_n \sigma_h N^2)^{1/2}, \tag{3.66}$$

and with (3.65)

$$\phi_m = {c_\epsilon}^{1/3} \sigma_m. \tag{3.67}$$

Since the Prandtl number is given by (3.64), the associated expression for ϕ_h is as follows

$$\phi_h = \alpha_n c_\epsilon^{1/3} \sigma_m \sigma_h. \tag{3.68}$$

This result is now used to be valid as a reasonable parameterization of ϕ_m and ϕ_h for the general case solving the prognostic TKE equation with a stability-dependent Prandtl number for (3.50).

3.4.3 Numerical approximation

Before the LM-specific numerical approximation of the SGS-model can be given, some explanation about the following formulation is necessary. In Section 3.4.2, where the physical conception is emphasized, important properties concerning spherical coordinates in the horizontal as well as the special terrain-following vertical coordinate were deliberately ignored

for the sake of clearness. Here, these aspects have to be taken into account, although their consideration is made approximately. The metric terms both from the horizontal spherical and the generalized vertical coordinate have been dropped. While this simplification may be surely justified concerning the horizontal aspect, the vertical metric terms might be significant at least in case of steeper mountain slopes. Nevertheless, we ignore the latter, too, for the sake of convenience, because the difference approximation of these terms brings about a lot of difficulties, which we want to evade in the first place. A more thorough treatment considering metric terms neatly is still open and should be persued in line with more general formulations of the LM documentation. For the following difference formulae we have strictly adopted all the rules and definitions of differencing and averaging operators applied in the LM numerics as documented in the first part of this documentation (*Part I: Dynamics and Numerics*; see Doms and Schättler (2002)). This documentation is also obligatory upon the definition of all model variables, symbols, general indexing etc. we have used and not explained expressively here. Additionally, the placement of new variables and entities concerning the SGS-model on the horizontal C-grid and the vertical Lorenz-grid is documented in Herzog et al. (2002), but is self-evident with the governing rules of differencing and averaging. The main issue of the scheme is seen to be a consistent implementation in the given dynamics and numerics of the new dynamical core. This rests on two types of two-timelevel Runge-Kutta-schemes (normal 3rd-order or TVD-variant of 3rd-order) combined with forward-backward-scheme for the fast-mode equation part Förstner and Doms (2004) and Doms and Förstner (2004)).

For the relevant prognostic equations we have to incorporate here terms expressing the three-dimensional divergence of a turbulent flux for all three space directions. For the momentum equations they read in the appropriate difference form

$$\left(\frac{\partial \overline{u}}{\partial t}\right)^{(n)} = \ldots - \frac{1}{\overline{\rho^{(n)}}^{\lambda}}\left[\frac{1}{a\cos\varphi}\left(\delta_\lambda \tau_{11} + \cos\varphi\,\delta_\varphi \tau_{12}\right)^{(n)} - \frac{1}{\overline{\sqrt{G}}^{\lambda}}\left(\delta_\zeta \tau_{13}\right)^{(n,n+1)}\right] \quad (3.69)$$

$$\left(\frac{\partial \overline{v}}{\partial t}\right)^{(n)} = \ldots - \frac{1}{\overline{\rho^{(n)}}^{\varphi}}\left[\frac{1}{a\cos\varphi}\left(\delta_\lambda \tau_{12} + \cos\varphi\,\delta_\varphi \tau_{22}\right)^{(n)} - \frac{1}{\overline{\sqrt{G}}^{\varphi}}\left(\delta_\zeta \tau_{23}\right)^{(n,n+1)}\right] \quad (3.70)$$

$$\left(\frac{\partial \overline{w}}{\partial t}\right)^{(n)} = \ldots - \frac{1}{\overline{\rho^{(n)}}^{\zeta}}\left[\frac{1}{a\cos\varphi}\left(\delta_\lambda \tau_{13} + \cos\varphi\,\delta_\varphi \tau_{23}\right)^{(n)} - \frac{1}{\overline{\sqrt{G}}^{\zeta}}\left(\delta_\zeta \tau_{33}\right)^{(n,n+1)}\right] \quad (3.71)$$

For the six turbulent stress components follows

$$\tau_{11}^{(n)} = -\frac{\rho^{(n)}\overline{K_m^{H(n)}}^{\zeta}}{a\cos\varphi}2\delta_\lambda\overline{u}^{(n)} \tag{3.72}$$

$$\tau_{12}^{(n)} = -\frac{\overline{\rho^{(n)}\overline{K_m^{H(n)}}^{\zeta}}^{\lambda,\varphi}}{a\cos\varphi}\left(\delta_\lambda\overline{v}^{(n)} + \cos\varphi\,\delta_\varphi\overline{u}^{(n)}\right) \tag{3.73}$$

$$\tau_{13}^{(n,n+1)} = -\frac{\overline{\overline{\rho^{(n)}}^{\zeta}K_m^{V(n)}}^{\lambda}}{a\cos\varphi}\delta_\lambda\overline{w}^{(n)} + \overline{\left(\overline{\left(\frac{\rho^{(n)}}{\sqrt{G}}\right)}^{\zeta}K_m^{V(n)}\right)}^{\lambda}\left(\beta_d^+\delta_\zeta\overline{u}^{(n+1)} + \beta_d^-\delta_\zeta\overline{u}^{(n)}\right) \tag{3.74}$$

$$\tau_{13}^{(n)} = -\frac{\overline{\overline{\rho^{(n)}}^{\zeta}K_m^{V(n)}}^{\lambda}}{a\cos\varphi}\delta_\lambda\overline{w}^{(n)} + \overline{\left(\overline{\left(\frac{\rho^{(n)}}{\sqrt{G}}\right)}^{\zeta}K_m^{V(n)}\right)}^{\lambda}\delta_\zeta\overline{u}^{(n)}, \tag{3.75}$$

$$\tau_{22}^{(n)} = -\frac{\rho^{(n)}\overline{K_m^{H(n)}}^{\zeta}}{a}2\delta_\varphi\overline{v}^{(n)} \tag{3.76}$$

$$\tau_{23}^{(n,n+1)} = -\frac{\overline{\overline{\rho^{(n)}}^{\zeta}K_m^{V(n)}}^{\varphi}}{a}\delta_\varphi\overline{w}^{(n)} + \overline{\left(\overline{\left(\frac{\rho^{(n)}}{\sqrt{G}}\right)}^{\zeta}K_m^{V(n)}\right)}^{\varphi}\left(\beta_d^+\delta_\zeta\overline{v}^{(n+1)} + \beta_d^-\delta_\zeta\overline{v}^{(n)}\right) \tag{3.77}$$

$$\tau_{23}^{(n)} = -\frac{\overline{\overline{\rho^{(n)}}^{\zeta}K_m^{V(n)}}^{\varphi}}{a}\delta_\varphi\overline{w}^{(n)} + \overline{\left(\overline{\left(\frac{\rho^{(n)}}{\sqrt{G}}\right)}^{\zeta}K_m^{V(n)}\right)}^{\varphi}\delta_\zeta\overline{v}^{(n)} \tag{3.78}$$

$$\tau_{33}^{(n,n+1)} = \overline{\left(\overline{\left(\frac{\rho^{(n)}}{\sqrt{G}}\right)}^{\zeta}K_m^{V(n)}\right)}^{\zeta}2\left(\beta_d^+\delta_\zeta\overline{w}^{(n+1)} + \beta_d^-\delta_\zeta\overline{w}^{(n)}\right). \tag{3.79}$$

In a similar way the turbulent fluxes of sensible heat and moisture are considered

$$\left(\frac{\partial\overline{T}}{\partial t}\right)^{(n)} = \ldots - \frac{1}{\rho^{(n)}}\left[\frac{1}{a\cos\varphi}\left(\delta_\lambda h_1 + \cos\varphi\,\delta_\varphi h_2\right)^{(n)} - \frac{1}{\sqrt{G}}\left(\delta_\zeta h_3\right)^{(n,n+1)}\right] \tag{3.80}$$

$$h_1^{(n)} = -\frac{\overline{\pi^{(n)}\rho^{(n)}\overline{K_h^{H(n)}}^{\zeta}}^{\lambda}}{a\cos\varphi}\delta_\lambda\left(\frac{\overline{T}^{(n)}}{\pi^{(n)}}\right) \tag{3.81}$$

$$h_2^{(n)} = -\frac{\overline{\pi^{(n)}\rho^{(n)}\overline{K_h^{H(n)}}^{\zeta}}^{\varphi}}{a}\delta_\varphi\left(\frac{\overline{T}^{(n)}}{\pi^{(n)}}\right) \tag{3.82}$$

$$h_3^{(n,n+1)} = \overline{\left(\frac{\pi^{(n)}\rho^{(n)}}{\sqrt{G}}\right)}^{\zeta}K_h^{V(n)}\left(\beta_d^+\delta_\zeta\left(\frac{\overline{T}^{(n+1)}}{\pi^{(n+1)}}\right) + \beta_d^-\delta_\zeta\left(\frac{\overline{T}^{(n)}}{\pi^{(n)}}\right)\right) \tag{3.83}$$

$$\left(\frac{\partial\overline{q}^k}{\partial t}\right)^{(n)} = \ldots - \frac{1}{\rho^{(n)}}\left[\frac{1}{a\cos\varphi}\left(\delta_\lambda f_1^{q^k} + \cos\varphi\,\delta_\varphi f_2^{q^k}\right)^{(n)} - \frac{1}{\sqrt{G}}\left(\delta_\zeta f_3^{q^k}\right)^{(n,n+1)}\right] \tag{3.84}$$

$$f_1^{q^{k(n)}} = -\frac{\overline{\overline{\rho^{(n)}}^{\zeta}\overline{K_h^{H(n)}}^{\zeta}}^{\lambda}}{a\cos\varphi}\delta_\lambda \overline{q}^{k(n)}, \tag{3.85}$$

$$f_2^{q^{k(n)}} = -\frac{\overline{\overline{\rho^{(n)}}^{\zeta}\overline{K_h^{H(n)}}^{\zeta}}^{\varphi}}{a}\delta_\varphi \overline{q}^{k(n)}, \tag{3.86}$$

$$f_3^{q^{k(n,n+1)}} = \overline{\left(\frac{\rho^{(n)}}{\sqrt{G}}\right)}^{\zeta} K_h^{V(n)}\left(\beta_d^+\delta_\zeta \overline{q}^{k(n+1)} + \beta_d^-\delta_\zeta \overline{q}^{k(n)}\right). \tag{3.87}$$

As can be seen, all horizontal turbulent diffusion terms are treated by forward-in-time differences, and so those terms of vertical momentum fluxes arising from the consideration of horizontal inhomogeneities. The rest of vertical diffusion terms is treated implicitly by a Crank-Nicholson scheme. This leads together with the vertical advection terms to a tridiagonal vertical structure equation to be solved by a Gaussian elimination procedure.

In the following we add the numerics concerning the SGS-TKE model, starting from the TKE-equation (3.58), but here in spherical coordinates and using the LM-specific vertical coordinate. Due to a strict adaptation to the given LM numerics the spatial differencing is straightforward. Concerning the time differencing, a "mixed" scheme is applied: horizontal advection is approximated by a positive-definite advection scheme proposed from Lin and Rood (1996), for vertical advection and vertical diffusion a partially implicit Crank-Nicholson scheme is applied, and horizontal diffusion as well as source/sink-terms like shear production, buoyant production/consumption, dissipation are treated by a time-forward scheme.

For the following analysis we start from the analytic formulation of the TKE-equation in spherical coordinates

$$\begin{aligned}\frac{\partial \overline{e}}{\partial t} = &-\left[\frac{1}{a\cos\varphi}\left(\overline{u}\frac{\partial \overline{e}}{\partial \lambda} + \overline{v}\cos\varphi\frac{\partial \overline{e}}{\partial \varphi}\right)\right] - \dot{\zeta}\frac{\partial \overline{e}}{\partial \zeta} \\ &+ \frac{1}{a\cos\varphi}\frac{\partial}{\partial\lambda}\left(2K_m\frac{\partial \overline{e}}{a\cos\varphi\partial\lambda}\right) + \frac{1}{a}\frac{\partial}{\partial\varphi}\left(2K_m\frac{\partial \overline{e}}{a\partial\varphi}\right) \\ &+ \frac{1}{\sqrt{G}}\frac{\partial}{\partial\zeta}\left(\frac{1}{\sqrt{G}}2K_m\frac{\partial \overline{e}}{\partial\zeta}\right) \\ &+ K_m^H S_H^2 + K_m^V S_V^2 - K_h^V N^2 - c_\epsilon\frac{\overline{e}^{\frac{3}{2}}}{l}\end{aligned} \tag{3.88}$$

with

$$S_H^2 = 2\left[\left(\frac{\partial \overline{u}}{a\cos\varphi\partial\lambda}\right)^2 + \left(\frac{\partial \overline{v}}{a\partial\varphi}\right)^2\right] + \left(\frac{\partial \overline{u}}{a\partial\varphi} + \frac{\partial \overline{v}}{a\cos\varphi\partial\lambda}\right)^2 \tag{3.89}$$

$$S_V^2 = 2\left(\frac{1}{\sqrt{G}}\frac{\partial \overline{w}}{\partial\zeta}\right)^2 + \left(\frac{\partial \overline{w}}{a\cos\varphi\partial\lambda} - \frac{1}{\sqrt{G}}\frac{\partial \overline{u}}{\partial\zeta}\right)^2 + \left(\frac{\partial \overline{w}}{a\partial\varphi} - \frac{1}{\sqrt{G}}\frac{\partial \overline{v}}{\partial\zeta}\right)^2. \tag{3.90}$$

The TKE-equation in difference form reads

$$\begin{aligned}\left(\frac{\partial \overline{e}}{\partial t}\right)^{(n)} &= ADV_H^{PD(n)} + ADV_V^{PD(n)} + TDIF_H{}^{(n)} \\ &+ \frac{1}{\overline{\sqrt{G}}^{\zeta}}\delta_\zeta\left[2\overline{\left(\frac{1}{\overline{\sqrt{G}}^{\zeta}}K_m^{V(n)}\right)}^{\zeta}\left(\beta_d^+\delta_\zeta\overline{e}^{(n+1)} + \beta_d^-\delta_\zeta\overline{e}^{(n)}\right)\right] \\ &+ QS_k^{(n)}.\end{aligned} \tag{3.91}$$

$ADV_H^{PD(n)}$ and $ADV_V^{PD(n)}$ are symbols of the horizontal and vertical advection terms formulated by a positive definite advection scheme of Lin and Rood (1996).

The abbreviations above are defined as follows:

$$TDIF_H{}^{(n)} = \frac{\delta_\lambda}{a\cos\varphi}\left(2\overline{K_m^{H(n)}}^{\lambda}\frac{\delta_\lambda\overline{e}^{(n)}}{a\cos\varphi}\right) + \frac{\delta_\varphi}{a}\left(2\overline{K_m^{H(n)}}^{\varphi}\frac{\delta_\varphi\overline{e}^{(n)}}{a}\right) \tag{3.92}$$

$$QS^{(n)} = K_m^{H(n)}S_H^{2\,(n)} + K_m^{V(n)}S_V^{2\,(n)} - K_h^{V(n)}S^{2(n)}Ri^{(n)} - c_\epsilon\frac{\overline{e}^{(n)\,\frac{3}{2}}}{l} \tag{3.93}$$

$$S_H^2 = 2\left[\left(\frac{\overline{\delta_\lambda\overline{u}^{(n)}}^{\zeta}}{a\cos\varphi}\right)^2 + \left(\frac{\overline{\delta_\varphi\overline{v}^{(n)}}^{\zeta}}{a}\right)^2\right] + \left(\frac{\delta_\varphi\overline{\overline{u}^{(n)}}^{\lambda,\varphi^{\zeta}}}{a} + \frac{\delta_\lambda\overline{\overline{v}^{(n)}}^{\lambda,\varphi^{\zeta}}}{a\cos\varphi}\right)^2 \tag{3.94}$$

$$S_V^2 = 2\left(\frac{\delta_{2\zeta}\overline{w}^{(n)}}{\overline{\sqrt{G}}^{\zeta}}\right)^2 + \left(\frac{\delta_\lambda\overline{\overline{w}^{(n)}}^{\lambda}}{a\cos\varphi} - \frac{\delta_\zeta\overline{\overline{u}^{(n)}}^{\lambda}}{\overline{\sqrt{G}}^{\zeta}}\right)^2 + \left(\frac{\delta_\varphi\overline{\overline{w}^{(n)}}^{\varphi}}{a} - \frac{\delta_\zeta\overline{\overline{v}^{(n)}}^{\varphi}}{\overline{\sqrt{G}}^{\zeta}}\right)^2 \tag{3.95}$$

The local Richardson number reads

$$Ri = \frac{g\left(\overline{\Theta}_{v,k} - \overline{\Theta}_{v,k-1}\right)}{S^2\left(\overline{\Theta}_{v,k} + \overline{\Theta}_{v,k-1}\right)\left(z_{k+1} - z_{k-1}\right)}, \tag{3.96}$$

provided $S^2 = S_H^2 + S_V^2 \geq S_{min}^2 > 0$.

Some terms of equation (3.91) are summarized to

$$\Sigma^{(n)} = ADV_H^{PD(n)} + ADV_V^{PD(n)} + TDIF_H{}^{(n)} + QS^{(n)}. \tag{3.97}$$

For the vertical diffusion we use an implicit Crank-Nicolson scheme

$$\frac{\overline{e}_k^{(n+1)} - \overline{e}_k^{(n)}}{\Delta t} = \Sigma_k^{(n)} + \frac{2}{\overline{\sqrt{G}_k}^{\zeta}} \left[\overline{\left(\frac{K_m^{(n)}}{\overline{\sqrt{G}}^{\zeta}} \right)_k}^{\zeta} \left(\beta_d^+ \left(\overline{e}_{k+1}^{(n+1)} - \overline{e}_k^{(n+1)} \right) + \beta_d^- \left(\overline{e}_{k+1}^{(n)} - \overline{e}_k^{(n)} \right) \right) - \overline{\left(\frac{K_m^{(n)}}{\overline{\sqrt{G}}^{\zeta}} \right)_{k-1}}^{\zeta} \left(\beta_d^+ \left(\overline{e}_k^{(n+1)} - \overline{e}_{k-1}^{(n+1)} \right) + \beta_d^- \left(\overline{e}_k^{(n)} - \overline{e}_{k-1}^{(n)} \right) \right) \right]. \tag{3.98}$$

With the further definition of coefficients A_k, B_k, C_k and D_k of the tridiagonal matrix

$$A_k = \beta_d^+ A_k^d \tag{3.99}$$

$$B_k = \frac{1}{\Delta t} - A_k - C_k \tag{3.100}$$

$$C_k = \beta_d^+ C_k^d \tag{3.101}$$

$$D_k = \frac{1}{\Delta t} \overline{e}_k^{(n)} + \Sigma_k^{(n)} + \beta_d^- A_k^d \left(\overline{e}_k^{(n)} - \overline{e}_{k-1}^{(n)} \right) - \beta_d^- C_k^d \left(\overline{e}_{k+1}^{(n)} - \overline{e}_k^{(n)} \right) \tag{3.102}$$

and

$$A_k^d = -\frac{2}{\overline{\sqrt{G}_k}^{\zeta}} \overline{\left(\frac{K_m^{(n)}}{\overline{\sqrt{G}}^{\zeta}} \right)_{k-1}}^{\zeta}, \; C_k^d = -\frac{2}{\overline{\sqrt{G}_k}^{\zeta}} \overline{\left(\frac{K_m^{(n)}}{\overline{\sqrt{G}}^{\zeta}} \right)_k}^{\zeta} \tag{3.103}$$

we are able to write down a closed set of discretized TKE-equations forming a tri-diagonal vertical structural equation set for determining $\overline{e}_k^{(n+1)}$, which is the TKE at each vertical half-level k (in accordance with program code indexing) and at the prognostic time level $n+1$, where in the present version the upper and lower boundary condition $\overline{e}_1 = \overline{e}_{ke1} = 0$ is involved:

$$B_2 \overline{e}_2^{(n+1)} + C_2 \overline{e}_3^{(n+1)} = D_2^{(n)}, \tag{3.104}$$

$$A_k \overline{e}_{k-1}^{(n+1)} + B_k \overline{e}_k^{(n+1)} + C_k \overline{e}_{k+1}^{(n+1)} = D_k^{(n)} \quad \text{for } k \in [3, ke-1], \tag{3.105}$$

$$A_{ke} \overline{e}_{ke-1}^{(n+1)} + B_{ke} \overline{e}_{ke}^{(n+1)} = D_{ke}^{(n)}. \tag{3.106}$$

To solve this system, a Gaussian elimination procedure is used. For this, the functions A_k, B_k, C_k and D_k are known, because they are defined at time levels n and $n+1$, respectively. The equilibrium case (3.70) is used to determine the initial values of $\overline{e}_k$. These values have been kept constant in time during the integration course over the two grid point rows nearest to the lateral boundary.

Section 4

Parameterization of the Surface Fluxes

Mesoscale numerical modelling is often very sensitive to surface fluxes of momentum, heat and moisture. These fluxes provide a coupling between the atmospheric part of the model and the soil model. LM uses a stability and roughness-length dependent surface flux formulation which is based on modified Businger relations (Businger et al. (1971)). Instead of the commonly used iteration method, an analytic procedure according to Louis (1979) is applied in the flux calculation for a much improved computational efficiency. This formulation was further modified to achieve more realistic results for both highly stable and highly unstable thermal stratification.

4.1 The Standard Bulk-Transfer Scheme

This Section describes a stability and roughness-length dependent surface flux formulation based on Louis (1979). It is recommended to apply this scheme when using the 1-d diagnostic turbulence scheme described in Section 3.2.

4.1.1 Formulation of the Surface Fluxes

The surface fluxes enter the atmospheric part of the model as the lower boundary conditions for the turbulent momentum stresses τ^{13} and τ^{23} in the mixing terms M_u^{TD} and M_v^{TD} of the equations for horizontal momentum [Eq.(3.2)], for the sensible heat flux H^3 in the mixing term M_T^{TD} of the heat equation [Eq.(3.3)] and for the turbulent flux of water vapour, the moisture flux $F_{q^v}^3$ in the mixing term $M_{q^v}^{TD}$ of the prognostic equation for q^v [Eq.(3.4)] at the ground surface. The turbulent surface fluxes of the liquid and solid water substances are set to zero.

The momentum fluxes at the earth's surface are parameterized by a drag-law formulation:

$$\begin{aligned} \tau^{13}_{sfc} &= -\rho\, C^d_m |\mathbf{v}_h|\, u \\ \tau^{23}_{sfc} &= -\rho\, C^d_m |\mathbf{v}_h|\, v \end{aligned} \tag{4.1}$$

Here, u and v are the horizontal velocity components at the lowest grid level above the surface and $|\mathbf{v}_h| \equiv (u^2 + v^2)^{1/2}$ is the absolute wind speed at the same level. C^d_m is the drag coefficient for momentum exchange at the ground.

The surface flux of sensible heat is defined accordingly,

$$H^3_{sfc} = -\rho\, C^d_h\, |\mathbf{v}_h|\, (\theta \pi_{sfc} - T_{sfc})\,, \tag{4.2}$$

where C^d_h is the bulk-areodynamical transfer coefficient for turbulent heat exchange at the surface. θ and π_{sfc} are, respectively, the potential temperature at the lowest grid level above the earth's surface and the scaled pressure at the ground. T_{sfc} is the ground temperature which is either predicted by the soil model or can be specified by an external boundary field.

The parametric relation for surface flux of water vapour reads

$$(F^3_{q^v})_{sfc} = -\rho\, C^d_q\, |\mathbf{v}_h|\, (q^v - q^v_{sfc})\,, \tag{4.3}$$

where C^d_q is the bulk-aerodynamical coefficient for turbulent moisture transfer at the surface. q^v is the specific humidity at the lowest grid level above the ground and q^v_{sfc} is the ground level specific humidity. q^v_{sfc} is either predicted by the soil model or can be specified as an external boundary field.

The transfer coefficients C^d_m and C^d_h are calculated diagnostically as described below. In the present version of the model $C^d_q = C^d_h$ is assumed.

4.1.2 Transfer Coefficients Over Land

Formally, the Monin-Obukhov similarity theory for the constant-flux or surface layer can be used to derive the bulk transfer coefficients C^d_m and C^d_h. Let u_* be the frictional velocity, θ_* the surface-layer temperature scale, L the Monin-Obukhov length scale and ξ the L-scaled height defined by

$$\begin{aligned} u_* &\equiv \left\{ \left(\tau^{13}_{sfc}/\rho\right)^2 + \left(\tau^{23}_{sfc}/\rho\right)^2 \right\}^{1/4} \\ \theta_* &\equiv -\frac{1}{\rho c_{pd} \pi_{sfc}} \frac{H^3_{sfc}}{u_*} \\ L &\equiv \frac{\theta u_*^2}{\kappa g \theta_*}\,. \\ \xi &\equiv \frac{z}{L} \end{aligned} \tag{4.4}$$

According to similarity theory, the vertical variation of wind speed and potential temperature within the surface layer is related to the stresses and the heat flux by flux-profile relationships in the form

$$\frac{d|\mathbf{v}_h|}{dz} = \frac{u_*}{\kappa z}\Phi_m(\xi) \tag{4.5}$$

$$\frac{d\theta}{dz} = \frac{\theta_*}{\kappa z}\Phi_h(\xi) \tag{4.6}$$

where the profile functions Φ_m and Φ_h depend on the dimensionless height parameter ξ only.

Based on field experiment data, Businger et al. (1971) and Dyer (1974) independently estimated the functional form of the profile functions to be

$$\Phi_m(\xi) = \begin{cases} 1 + 4.7\xi & \text{if } \xi > 0 \text{ (stable)} \\ 1 & \text{if } \xi = 0 \text{ (neutral)} \\ (1 - 15\xi)^{-1/4} & \text{if } \xi < 0 \text{ (unstable)} \end{cases} \tag{4.7}$$

$$\Phi_h(\xi) = \begin{cases} \alpha_n(1 + 6.4\xi) & \text{if } \xi > 0 \text{ (stable)} \\ \alpha_n & \text{if } \xi = 0 \text{ (neutral)} \\ \alpha_n(1 - 9\xi)^{-1/2} & \text{if } \xi < 0 \text{ (unstable)} \end{cases} \tag{4.8}$$

As in Section 3.2, α_n denotes the ratio of the transport coefficients for heat and momentum at statically neutral stratification. Businger et al. (1971) derived the value $\alpha_n = 0.74$ from the experimental data. An improved re-evaluation of these data by Högström resulted in a value of 0.95 for α_n. For the parameterization of the surface fluxes in LM we set $\alpha_n = 1$ for simplicity.

Using the analytical form (4.7) and (4.8) for the profile functions, the flux-profile relationships (4.5) and (4.6) may be integrated with height from $z = z_0$ to $z = h$. z_0 denotes the aerodynamical roughness length and h is any height within the constant-flux layer. Usually, the top height of the surface layer is in the range of $10\,m$ to $30\,m$. In order to apply the similarity theory to parameterize the surface fluxes, the lowest terrain-following grid level of the model must be placed within the constant-flux layer. We then can identify h with the difference between the height of the lowest model level and the terrain height. The integration of the momentum flux relation yields

$$\frac{|\mathbf{v}_h|}{u_*} = \frac{1}{\kappa}\left\{\ln\left(\frac{h}{z_0}\right) + \Psi_m\left(\frac{h}{L}, \frac{z_0}{L}\right)\right\} \tag{4.9}$$

for the wind speed $|\mathbf{v}_h|$ at height h, i.e. at the lowest grid level of the model. Ψ_m is an integrated form of the profile function Φ_m. For the Dyer-Businger profile (4.7) Ψ_m has the analytic form

$$\Psi_m\left(\frac{h}{L},\frac{z_0}{L}\right) = \begin{cases} 4.7\,(h/L - z_0/L)\,, & \text{if } L > 0 \text{ (stable)} \\ 1.0\,, & \text{if } L = 0 \text{ (neutral)} \\ -2\,\ln\{(1+x)/(1+x_0)\} & \\ -\ln\left\{(1+x^2)/(1+x_0^2)\right\} & \\ +2\,\arctan x - 2\,\arctan x_0\,, & \text{if } L < 0 \text{ (unstable)} \end{cases}$$

with $x = (1 - 15h/L)^{1/4}$ and $x_0 = (1 - 15z_0/L)^{1/4}$.

From (4.9) and the parametric relation (3.24) for the surface stresses, the following equation for the drag coefficient C_m^d may be derived:

$$C_m^d \;=\; \frac{u_*^2}{|\mathbf{v}_h|^2} \;=\; \kappa^2 \left\{\ln\left(\frac{h}{z_0}\right) + \Psi_m\left(\frac{h}{L},\frac{z_0}{L}\right)\right\}^{-2}\,. \tag{4.10}$$

A corresponding equation for C_h^d results in a similar way from the integration of the heat flux relation (4.6). Thus, on the condition that the stability, the heat flux and the stresses are known in terms of L, θ_* and u_*, the transfer coefficients can be calculated from any specified set of profile functions Φ_m and Φ_h.

In practice, however, these equations have to be used in reverse: The heat flux and the stresses have to be estimated from the wind and the temperature profile before (4.10) can be applied. This is much more difficult because u_* and θ_* appear, hidden in L, on the right hand side of (4.10). This equation in turn is required to calculate u_* and θ_*. The resulting coupled set of equations has no analytic solution and involves a computationally expensive iterative approach.

One way around this problem is to simplify the flux-profile relationships and to use the gradient Richardson number Ri as a stability parameter instead of L. Since Ri is based on vertical gradients of potential temperature and wind speed, it is easily calculated directly from the model variables (or experimental data).

For the parameterization of the surface fluxes in LM we apply a method that has been proposed by Louis (1979). In this approach, the iterative solutions are approximated by simple analytical functions which relate the transfer coefficients to the roughness length, the height h within the surface layer and the bulk Richardson number Ri_B as a practical stability parameter. Ri_B is a discrete analogue of Ri. For the lowest grid level of the model with height h above the terrain height, it has the form

$$Ri_B \;=\; \frac{g}{\theta_{sfc}}\,\frac{(\theta - \theta_{sfc})(h - z_0)}{(u^2 + v^2)}\,. \tag{4.11}$$

The Louis method states the following equations for the transfer coefficients which resemble the basic functional form (4.10) from similarity theory:

$$\begin{aligned} C_m^d &= C_{m,n}^d\, f_m(Ri_B,\, h/z_0)\,, \\ C_h^d &= C_{h,n}^d\, f_h(Ri_B,\, h/z_0, h/z_h)\,. \end{aligned} \tag{4.12}$$

Here, the suggestion of Segami et al. (1989) is included as an extension of the original version of the scheme by considering a roughness length z_h for heat exchange in addition to z_0. $C^d_{m,n}$ and $C^d_{h,n}$ are the transfer coefficients at neutral stratification, and f_m and f_h are stability functions which approximate the iterative solutions for non-neutral conditions in the constant flux layer. The transfer coefficients for the neutral case are given by

$$\begin{aligned} C^d_{m,n} &= \kappa^2 \left\{\ln(h/z_0)\right\}^{-2} , \\ C^d_{h,n} &= \kappa^2 \left\{\ln(h/z_0)\right\}^{-1} \left\{\ln(h/z_h)\right\}^{-1} . \end{aligned} \tag{4.13}$$

The roughness length for heat exchange is, in a simple approach, set to the minimum of z_0 and a limiting value $z_{h,max}$ in order to avoid excessive heat exchange over rough terrain:

$$z_h = \min\left(z_0,\, z_{h,max}\right) . \tag{4.14}$$

The functional form of f_m and f_h may be chosen to include the limiting cases of laminar flow in a highly stable surface layer and of free convection at statically very unstable stratifications. For these cases, the commonly used iterative method breaks down and the Monin-Obukhov similarity theory does not hold either.

Especially, as was pointed out by Louis (1979), the laminar flow case may cause problems in numerical models. The iterative solution based on the Dyer-Businger flux-profile relations results in a critical Richardson number with the value $Ri_c \simeq 0.2$. Turbulent flows with Ri beyond this value are expected to become laminar, i.e. the transfer coefficients will vanish. However, this would completely decouple the atmosphere from the surface in a numerical model, resulting in a detrimental impact on the low-level flow structure. Therefore, the stability functions are chosen such that a critical Richardson number is not involved and the transfer coefficients asymptotically approach zero with increasing static stability. This is in accordance with recent theoretical and laboratory research which suggests that laminar flows become turbulent at $Ri \approx 0.25$ but that the termination of turbulence takes place at much higher static stability with $Ri \approx 1$; intermittent turbulence may occur at even higher stabilities.

The analytical form of the stability functions f_m and f_h in LM follows the formulation in the ECMWF-model (ECMWF (1991). In case of a statically stable surface layer these functions are defined by ($Ri_B \geq 0$)

$$\begin{aligned} f_m &= \frac{1}{1 + 2\,b\,Ri_B\,\left(1 + d\,Ri_B\right)^{-1/2}} \\ f_h &= \frac{1}{1 + 3\,b\,Ri_B\,\left(1 + d\,Ri_B\right)^{1/2}} \end{aligned} \tag{4.15}$$

and in case of unstable stratification f_m and f_h are given by ($Ri_B < 0$)

$$\begin{aligned} f_m &= 1 + \frac{2\,b\,|Ri_B|}{1 + 3\,b\,c\,C^d_{m,n}\left\{\,(h/z_0)^{1/3} - 1\right\}^{3/2}\sqrt{|Ri_B|}} \\ f_h &= 1 + \frac{3\,b\,|Ri_B|}{1 + 3\,b\,c\,C^d_{h,n}\left\{\,(h/z_h)^{1/3} - 1\right\}^{3/2}\sqrt{|Ri_B|}}\,. \end{aligned} \tag{4.16}$$

The limiting case of free convection with $|\mathbf{v}_h| \to 0$ and $Ri_B \to -\infty$ is included in this formulation: Using (4.16) the product $C^d_h|\mathbf{v}_h|$ in the parametric equation (4.2) for the surface heat flux may be rewritten as

$$C^d_h\,|\mathbf{v}_h| \;=\; C^d_{h,n}\left[|\mathbf{v}_h| + \frac{3\,b\,|\mathbf{v}_h|^2\,|Ri_B|}{|\mathbf{v}_h| + 3\,b\,c\,C^d_{h,n}\left\{\,(h/z_h)^{1/3} - 1\right\}^{3/2}\sqrt{|\mathbf{v}_h|^2|Ri_B|}}\right].$$

With (4.11) for the bulk Richardson number, this equation reveals the limiting value

$$\lim_{|\mathbf{v}_h|\to 0} C^d_h\,|\mathbf{v}_h| \;=\; \frac{\{(g/\theta_{sfc})|\theta - \theta_{sfc}|(h - z_h)\}^{1/2}}{c\left\{\,(h/z_h)^{1/3} - 1\right\}^{3/2}} \tag{4.17}$$

and thus a nonzero heat flux for the case of free convection. A corresponding value can be derived for the factor $C^d_m|\mathbf{v}_h|$ in the equations (4.1) for the stresses. However, as this factor is multiplied by the horizontal wind components, the resulting surface flux of horizontal momentum becomes zero.

The following values are used for the free parameters of the scheme:

$$\begin{aligned} \kappa &= 0.4\,, \\ b &= c \;=\; d \;=\; 5.0\,, \\ z_{h,max} &= 0.1\,m\,. \end{aligned}$$

4.1.3 Transfer Coefficients Over Water

Over the sea surface, the same procedure as in the previous section is used to compute the transfer coefficients C^d_m and C^d_h. The only exception is an approximation to the denominator of the stability functions f_m and f_h for unstable stratification, which is based on the fact that over water z_0 and z_h are usually very small when compared to the height h of the first model layer adjacent to the surface. Thus, for $Ri_b < 0$ the functions f_m and f_h are replaced by

$$
\begin{aligned}
f_m &= 1 + \frac{2\,b\,|Ri_B|}{1 + 3\,b\,c\,C^d_{m,n}\,(h/z_0)^{1/2}\,\sqrt{|Ri_B|}}\,, \\
f_h &= 1 + \frac{3\,b\,|Ri_B|}{1 + 3\,b\,c\,C^d_{h,n}\,(h/z_h))^{1/2}\,\sqrt{|Ri_B|}}\,.
\end{aligned}
\tag{4.18}
$$

In contrast to the land surface, however, the surface roughness over water is a function of surface conditions which vary with the wind speed. In LM, we use the modified Charnock-formula

$$
z_0 = \frac{\alpha_c}{g}\,\max(u_*^2, w_*^2) \tag{4.19}
$$

with $\alpha_c = 0.0123$ to calculate the surface roughness length for momentum over open water. For water surfaces covered with ice the constant value $z_0 = 0.001\,m$ is specified. w_* is the scaling velocity for free convection which is defined according to

$$
w_* = \left\{ \frac{g(h - z_0)}{\rho c_{pd} T_{sfc}} H^3_{sfc} \right\}^{1/3}
$$

in terms of the surface heat flux H^3_{sfc}. The maximum of u_*^2 and w_*^2 is chosen in (4.19) to avoid too small values of z_0 for stability ranges close to the limit of free convection.

Inserting the drag-law formulation (4.1) to the definition of the friction velocity (4.4) and the heat flux formulation (4.2) into the definition of the convective velocity scale yields

$$
\begin{aligned}
{u_*}^2 &= C^d_{m,n} |\mathbf{v}_h|^2\, f_m(Ri_B\,, h/z_0)\,, \\
{w_*}^2 &= \begin{cases} \left\{ C^d_{h,n} |\mathbf{v}_h|^3\, |Ri_B|\, f_h(Ri_B\,, h/z_0\,, h/z_h) \right\}^{2/3} & \text{if } Ri_B < 0\,, \\ 0 & \text{if } Ri_B \geq 0\,. \end{cases}
\end{aligned}
\tag{4.20}
$$

The direct use of (4.20) in the Charnock-formula (4.19) results in a complex relationship for the sea surface roughness length because u_* and w_* depend also on z_0. An iteration technique could be applied to solve this equation. Such an expensive method is avoided by shifting the iteration to the time integration: The z_0-value from the previous time step $t - \Delta t$ is used for the calculation of $u*$ and w_* with (4.20) at time level t; z_0 is then easily calculated from (4.19) and used in the next time step $t + \Delta t$ to evaluate the new values of u_* and w_*.

This procedure requires an estimate z_0^i of the roughness length at initial time. The estimate is taken from an empirical bulk-formula for the stresses in terms of the wind speed at screen level height $h_{10} = 10\,m$, and from free convective scaling using the limiting value (4.17):

$$
g z_0^i = \max \left\{ \frac{\alpha_c |\mathbf{v}_h|^2}{\left[(1/\beta_{10}) + (1/\kappa) \ln(h/h_{10}) \right]^2}\,,\; \frac{\left(\alpha_c |\mathbf{v}_h|^2 |Ri_B| \right)^{3/2}}{c (gh)^{1/2}} \right\} \tag{4.21}
$$

This maximum condition is evaluated for unstable stratification with $Ri_B < 0$. For a statically stable surface layer, z_0^i is calculated from the first term in (4.21). The constant parameter β_{10} is set to $\beta_{10} = 0.042$.

4.2 The New TKE-Based Surface Transfer Scheme

The new LM surface-layer scheme is intimately related to the TKE scheme described in Section 3.3. Here, the surface layer is defined to be the layer of air between the earth surface and the lowest model level. We subdivide the surface layer into a laminar-turbulent sublayer, the roughness layer, and a constant-flux or Prandtl layer above. The roughness layer extends from the non-planar irregular surface, where the turbulent distance $l = \lambda/\kappa$ (λ is the turbulent length scale and κ is the von Karman constant) is zero, up to a level $l = H$, such that l is proportional to the vertical height z within the Prandtl layer above. We choose H to be equal to the dynamical roughness length z_0. The lower boundary of the constant-flux layer (and of the atmospheric model) is defined to be a planar surface at a turbulent distance $l = H$ from the surface. This subdivision allows to discriminate between the values of the model variables at the rigid surfaces (predicted by the soil model) and values at the level $l = H$, which are 'seen' by the atmosphere.

For both layers, the fluxes are written in resistance form, where a roughness layer resistance is acting for scalar properties but not for momentum. Specific interpolation schemes are used to calculate the transport resistances of the layers. The new surface scheme does not make use of empirical Monin-Obukhov stability functions, rather it generates these functions by the use of the dimensionless coefficients of the Mellor-Yamada closure and the interpolation rules. As the Mellor-Yamada closure has been comprehensively tested in numerous applications, the estimates of its coefficients are fairly reliable. This tends to reduce the number of LM model parameters to be tuned. However, a number of additional model parameters and external parameters related to the roughness layer have been introduced. They describe the impact of various types of the underlying surface on the vertical profiles functions and the transport resistances of momentum, heat and moisture in more detail. These parameters have been tuned in a number of parallel runs.

Section 5

Grid-Scale Clouds and Precipitation

Clouds and precipitation are of crucial importance in the water and energy cycle of the atmosphere. A good representation of clouds, precipitation and the cloud/radiation interaction is thus essential for an accurate direct prediction of local weather elements.

The formation of clouds and the subsequent development of precipitation result from various microphysical processes which are highly interactive and quite dependent on the ambient thermodynamic conditions. Furthermore, the microphysical processes have a strong impact on the thermodynamics and the overall hydrological cycle via both direct and indirect feedback mechanisms.

5.1 General Aspects

In a cloudy atmosphere, water substance can take on a wide variety of forms that develop under the influence of three basic microphysical processes:

- Nucleation of particles
- Particle growth by diffusion
- Growth by interparticle collection and break-up

With respect to precipitation formation, these processes form a temporal sequence, where nucleation precedes diffusion growth, which precedes growth by collection. Additional microphysical processes that have to be taken into account are

- Fallout of particles due to gravity diffusion (sedimentation)
- Melting of ice particles
- Ice enhancement due to fragmentation and splintering

These individual processes may be studied separately in the laboratory or by theoretical and numerical models. However, one should realize that in the life cycle of a natural cloud several or all of the microphysical processes occur simultaneously. Thus, as the various forms of water and ice particles coexist and interact with the overall cloud ensemble, the result of the action of the microphysical processes is often synergistic, i.e. the result is more than a simple summation of the individual processes.

Most microphysical processes are quite dependent on the particle size and shape. That is, the size distribution of the particles may have a strong impact on the overall evolution of a cloud. Whereas liquid-phase particles can be assumed to be spherical drops, the theoretical formulation of ice-phase processes is complicated by the wide variety of shapes that ice crystals may have. Furthermore, the various basic crystal habits may change with temperature and humidity conditions. Generally, the understanding of ice-phase microphysics is by far less complete than warm rain microphysics.

Besides the microphysical interactions, the thermodynamic structure of the atmosphere has a dominating impact on the formation of clouds and precipitation. To initiate cloud particles via nucleation, the air must first become supersaturated due to adiabatic or diabatic cooling or due to mixing. Frequent thermodynamic forcings are by radiative cooling and by vertical motions related to widespread mesoscale ascent in frontal systems or related to buoyant small-scale thermals. Subsequent to cloud formation, these forcings will also drive the diffusion growth of particles, but at the same time the microphysical processes will start to interact with the cloud's dynamical structure by various feedback mechanisms.

A prominent direct feedback is the release of latent heat associated with condensation, deposition and riming, which alters the thermal stratification within the cloud and may intensify the vertical motions due to an increase in buoyancy. This will in turn intensify the vapour supply for diffusion growth. On the other hand, the loading of the air with growing particles exerts an increasing drag force on the air which has a reverse effect on buoyancy and may initiate cloud dissipation. Sedimentation redistributes the particles vertically and affects the dynamics by water loading and by cooling due to melting as well as evaporation and sublimation in the sub-cloud layer. Especially, cooling of air due to the melting of ice particles may result in the formation of an isothermal layer which cuts off the vapour supply from vertical turbulent moisture fluxes. Advective and turbulent transports of particles across the cloud edges will result in evaporation and sublimation, and the associated dynamical effects from cooling due to consumption of latent heat can contribute to the overall cloud-scale circulation. Additional indirect feedback mechanisms, which may be relevant for the cloud evolution, result from cloud-radiation and cloud-turbulence interactions.

Depending on the environmental conditions, there is a variety of different paths for precipitation formation, especially when the ice phase is involved. The main controlling parameters are the availability of condensation and ice nuclei in the air mass where the cloud forms and the stability of the thermal stratification. The latter determines whether the dynamical evolution will be in form of a stratiform or of a convective cloud. However, there is a continuum of cloud types between these two basic forms.

The primary interest in the numerical modelling of clouds and precipitation is the behaviour of the overall ensemble of cloud particles, where it is generally unnecessary to keep track of every individual particle. To retain the essentials of the microphysical processes, their interactions within the cloud ensemble and the associated feedback mechanisms on the thermodynamics, it is convenient to group the various types of hydrometeors into several broad

categories of water substance. A traditional grouping (Houze (1993)) is the following.

- *Water Vapour*
  is the gaseous phase of water substance in the atmosphere.
- *Cloud Water*
  is in the form of small suspended liquid-phase drops. Cloud droplets are smaller than about 50 μm in radius and thus have no appreciable terminal fall speed relative to the airflow.
- *Precipitation Water*
  is in the form of liquid-phase spherical drops which are large enough to have a non-negligible fall velocity. Precipitation water may be subdivided into *drizzle* (comprised of drops with 50 – 250 μm radius) and *rain* (comprised of drops larger than 250 μm in radius).
- *Cloud Ice*
  refers to small ice crystals which have little or no appreciable terminal fall speed. These particles may be in the form of pristine crystals that have been nucleated directly from the water or the vapour phase, or they may be very small ice particles that have been produced by ice enhancement processes.
- *Precipitation Ice*
  is composed of ice particles that are large enough to have a non-negligible terminal velocity. These particles may have various forms, e.g. large pristine crystals with different habits, larger fragments of ice particles, rimed particles, aggregates of crystals, graupel or hail. To simplify the description, these particles are often grouped into only a few categories of precipitation ice. Obviously, due to the variety of basic crystal forms and habit changes during the particle growth, such groupings are arbitrary. However, a commonly used scheme is to subdivide precipitation ice into
  - *snow*, composed of rimed aggregates of ice crystals with fall speeds of about 0.3 – 1.5 m/s,
  - *graupel*, referring to particles with spherical shape, higher density than snow and fall speeds of about 1 – 3 m/s, and
  - *hail* with very large particle terminal velocities (up to 50 m/s).

The various categories are interactive, i.e. the increase of water mass, due to a specific microphysical process, in one category is at the expense of water content in another category. Clearly, the change of total water mass resulting from the microphysical interactions must be zero.

The mathematical description of the overall evolution of a cloud, in which any combination of the water categories with corresponding microphysical processes may be present simultaneously in the context of the changing airflow, is based on budget equations for the water substances. These equations allow to predict numerically the water mass in each category, as it changes due to advection, turbulent diffusion, sedimentation and various microphysical sources and sinks throughout the evolving cloud. The resulting system of equations is also often referred to as a water-continuity model. Three basic strategies for water-continuity modelling may be used to represent cloud microphysics in a numerical meteorological model.

(a) Spectral water-continuity models

In this type of models, which are also termed detailed or explicit models, the hydrometeors are subdivided according to size within each category of water substance. The number of particles with different sizes in category x is predicted using budget equations for the number-density size-distribution function $f_x(m)$. $f_x(m)dm$ represents the number of particles of type x per unit volume of air in an infinitesimal size range from m to $m + dm$, where m is the particle mass. Clearly, any other quantity $y(m)$ being a unique function of m could be used as spectral size coordinate instead of m (e.g. radius, diameter or surface area). The transformation between the distribution functions is given by

$$f_x(m)dm \;=\; f_x(y)dy\,. \tag{5.1}$$

The total number density N^x of particles in category x is calculated from the integral over the spectral distribution,

$$N^x \;=\; \int_0^\infty f_x(m)dm \;=\; \int_0^\infty f_x(y)dy\,, \tag{5.2}$$

and the total mass fraction q^x results from the integration of the mass of the particles in each size interval:

$$q^x \;=\; \frac{1}{\rho}\int_0^\infty m f_x(m)dm \;=\; \frac{1}{\rho}\int_0^\infty m(y) f_x(y)dy\,. \tag{5.3}$$

Thus, N^x and q^x are related to the zero and first moment of the spectral distribution function $f_x(m)$. Since $f_x(m)$ is predicted, these quantities are diagnosed from the particle distribution.

The detailed spectral method is the most direct approach to represent cloud microphysics in a dynamical model because many microphysical principles can be applied directly to the calculation of the size distributions (e.g., the particle growth equations for diffusion and the kinetic equation for interparticle stochastic collection). However, the detailed method becomes very complex when the ice phase is included since various crystal types including their interactions and their habit changes have to be considered. The major disadvantage is computational. A large number of size categories (~ 100) for each type of hydrometeors is required to discretize accurately the corresponding spectral budget equation. With the present computer limitations, such a sophistication is impractical for application in threedimensional NWP-models.

(b) Bulk water-continuity models

A practical alternative to the spectral representation of cloud microphysics are bulk or parameterized water-continuity models. The basic idea of this method is to assume as few categories of water as possible and to predict directly the total mass fraction q^x in each category in order to minimize the number of equations and calculations. To accomplish this simplification, the shapes and the size distributions of particles must be assumed and the microphysical processes must be parameterized in terms of q^x.

Basically, bulk schemes rely on the assumption of a self-similar or limiting size distribution for the particles. That is, it is supposed that the evolution of a particle spectrum can be approximated by varying the free parameters of an assumed specific mathematical function for the spectrum. Generally, these parameters are related to the moments

of the size distribution function, which then have to be predicted by corresponding budget equations. Thus, in contrast to the detailed method where the moments are diagnosed from the predicted spectra, the shape of the spectrum is diagnosed from the predicted moments in bulk schemes.

In case of usual bulk water-continuity models the mass fractions q^x are the only dependent variables. Consequently, the functions for the spectral shapes must have only one free parameter. The non-precipitating water categories are usually supposed to be monodisperse whereas the precipitation particles are assumed to be exponentially distributed in size with respect to particle diameter D as spectral coordinate:

$$f_x(D) \;=\; N_0^x \exp(-\lambda_x D)\,. \tag{5.4}$$

For raindrops, (5.4) is called the Marshall-Palmer distribution, which has been obtained by fitting experimental data (Marshall and W.M. (1948)). Numerical studies (Valdez and Young (1985)) have reproduced this exponential nature of the raindrop size spectrum as a limiting distribution resulting from collection and breakup processes. In bulk schemes, the exponential spectral shape is usually also supposed for various ice particle categories.

Setting the intercept value N_0^x to a constant value, the slope parameter λ_x is determined from the predicted mass fraction q^x by inverting the integral (5.3):

$$q^x \;=\; \frac{N_0^x}{\rho} \int_0^\infty m(D) \exp(-\lambda_x D) dD\,. \tag{5.5}$$

The assumption of a self-similar size distribution in the form (5.4) allows to parameterize the microphysical source and sink terms in the budget equations for the mass fractions, taking the impact of the particle size distributions approximately into account.

(c) Multiple-moment water-continuity models

Obviously, the more moments of the particle spectra are predicted by budget equations, the more free parameters the assumed size distribution functions may have. This will allow for a more accurate description of the evolving spectral distribution of the hydrometeors than by traditional single-moment bulk schemes.

In double-moment schemes the number density N^x of particles in a water category x is usually chosen as dependent model variable besides the mass fraction q^x. Clearly, this increases drastically the computational costs compared to single-moment schemes because twice the number of prognostic variables and a much larger number of microphysical interactions have to be included. Nevertheless, this method is computationally much cheaper than detailed spectral modelling while at the same time individual microphysical processes can be represented very accurately, as e.g. the collision-coalescence mechanism (Lüpckes et al. (1989)). Double-moment schemes including the ice phase have been proposed by Ikawa et al. (1991), Levkov et al. (1992) and Ferrier (1994).

The method can be extended to include higher order moments. Clark and Hall (1983) use the mean radius of the particle distribution and Höller (1982) uses radar reflectivity as a third dependent model variable to parameterize cloud microphysics in a triple-moment scheme. At present, such schemes are computationally too expensive to be applied in operational models.

Bulk water-continuity schemes are extensively used in cloud and mesoscale models. The essential features of this method are outlined in the following subsections. LM offers options for a warm rain scheme, a one-category ice (snow) and a two-category ice (snow and cloud ice) scheme. A three-category ice bulk scheme including graupel to allow for an explicit simulation of deep convective clouds has been added recently. Also, for a later version of the model, it is intended to implement a double-moment scheme to represent grid scale clouds and precipitation more accurately.

5.2 Bulk Water-Continuity models in LM

As described above, the dependent variables in bulk water-continuity models are the total mass fractions q^x of various types x of hydrometeors. The interaction of microphysical processes and their feedback to the flow field is represented by budget equations for the q^x. The generic budget equation in advection form reads (cf. (3.65), Part I)

$$\frac{\partial q^{l,f}}{\partial t} + \mathbf{v} \cdot \nabla q^{l,f} - \frac{1}{\rho} \frac{\partial P_{l,f}}{\partial z} = S^{l,f} - \frac{1}{\rho} \nabla \cdot \mathbf{F}^{l,f} , \tag{5.6}$$

where the indices l and f indicate liquid and solid forms of water substance. $S^{l,f}$ represent the corresponing cloud microphysical sources and sinks per unit mass of moist air, $\mathbf{F}^{l,f}$ are the turbulent fluxes and $P_{l,f}$ denotes the corresponding precipitation or sedimentation fluxes. They are defined by

$$P_{l,f} = \rho q^{l,f} v_T^{l,f} \tag{5.7}$$

and depend on the mean fall velocities of the particles, i.e. their mean terminal velocities $v_T^{l,f}$. In general, $v_T^{l,f}$ is a nonlinar function of the mass fractions $q^{l,f}$.

Using the traditional grouping of hydrometeors into broad classes of hydrometeors as described in Section 5.1, we will distinguish between precipitating and non-precipitating particles. The non-precipitating water substance is made up of cloud water with mass fraction q^c, and of cloud ice with mass fraction q^i. As both particle categories have neglegible fall velocities, the sedimentation fluxes P_c and P_i are set to zero. With respect to the precipitating particle categories, we consider rain with mass fraction q^r and the two precipitation phases snow and graupel, with mass fractions q^s and q^g, respectively. Since for precipitating particles the sedimentation fluxes are much larger than the turbulent fluxes, we will neglect the latter contribution ($\nabla \cdot \mathbf{F}^{l,f}$) in (5.6). Thus, the general budget equation (5.6) can be split into two sets of equations, one for the non-precipitating and one for the precipitating water categories:

non-precipitating categories (cloud water and cloud ice)

$$\frac{\partial q^{c,i}}{\partial t} + \mathbf{v} \cdot \nabla q^{c,i} = S^{c,i} - \frac{1}{\rho} \nabla \cdot \mathbf{F}^{c,i} , \tag{5.8}$$

precipitating categories (rain, snow and graupel)

$$\frac{\partial q^x}{\partial t} + \mathbf{v} \cdot \nabla q^x - \frac{1}{\rho} \frac{\partial \rho q^x v_T^x}{\partial z} = S^x , \tag{5.9}$$

where x stands for r (rain), s (snow) and g (graupel).

At present, LM provides four bulk-water continuity schemes to parameterize precipitation formation, which differ by the number of hydrometeor categories considered.

- *A warm rain scheme with the dependent variables q_c and q_r.*
  As the ice phase is neglected, this scheme describes precipitation formation in warm clouds. It is intended to be used in idealized test simulations only. Section 5.4 describes details of the scheme.
- *A snow scheme with the dependent variables q_c, q_r and q_s.*
  This scheme describes precipitation formation in water and mixed phase clouds, where clouds are assumed to exist at water saturation. Details of the scheme are outlined in Section 5.5. This scheme was applied for operational NWP until September 2003.
- *A cloud-ice scheme with the dependent variables q_c, q_i, q_r and q_s.*
  As an extension to the snow scheme, this parameterization consideres cloud ice as an additional variable in the hydrological cycle and allows for the simulation of precipitation formation in water, mixed phase and ice clouds. This scheme is used for operational NWP since September 2003 and is described in detail in Section 5.6.
- *A graupel scheme with the dependent variables q_c, q_i, q_r, q_s and q_g.*
  As an extension to the cloud-ice scheme, this parameterization adds the graupel phase to the hydrological cycle. The scheme is intended to be used in very-high resolution simulations with explicit representation of deep moist convection only. Details are described in Section 5.7.

When precipitation formation is switched off, the LM simulates warm non-precipitating clouds by a reversible thermodynamic treatment of water vapour condensation and evaporation of cloud water. The method used is a simple saturation adjustment and is described in Section 5.3. The same method is used to calculate the condensation rate as part of the microphysical source terms $S^{l,f}$ occuring in all of the four LM precipitation schemes.

In the literature it has become common practice to classify bulk-water schemes according to the total number of water categories considered (classes, including water vapour) or by the number of ice hydrometeors considered. This classification for the LM precipitation schemes is summarized in Table 5.2, together with the name of the corresponding subroutines.

Table 5.1: Parameterization Schemes for Grid-Scale Precipitation in LM

Parameterization	Variables	Subroutine	Classes	Ice Categories
Warm Rain Scheme	q_v, q_c, q_r	`kessler(_pp)`	3	0
Snow Scheme	q_v, q_c, q_r, q_s	`hydor(_pp)`	4	1
Cloud-Ice Scheme	q_v, q_c, q_i, q_r, q_s	`hydci(_pp)`	5	2
Graupel Scheme	q_v, q_c, q_i, q_r, q_s, q_g	`hydci_pp_gr`	6	3

The first three schemes can be run in diagnostic or prognostic (_pp) mode, where these terms refer to the treatment of the budget equations for the precipitation phases. The grau-

pel scheme can be run prognostically only. In prognostic mode, the full budget equations (5.9) for the precipitating hydrometeors are solved, whereas in diagnostic mode an approximated quasi-stationary version is utilized. The prognostic treatment is recommended for high-resolution simulations with grid spacings below ∼10 km. For coarse-grid simulations, the approximate solution from the diagnostic treatment gives sufficient accuracy at low numerical costs. The difference between diagnostic and prognostic treatment of precipitation is oulined below.

5.2.1 Diagnostic Treatment of Precipitation

As a significant numerical-dynamical simplification to the budget equations (5.9) for the precipitating categories (rain, snow), equilibrium in vertical columns can be assumed in case of coarse-grid simulations: On the meso-α and meso-β scale the vertical velocity is very small compared to the terminal fall velocities of rain and snow particles. Consequently, these precipitation particles will fall through the atmosphere within a time that is smaller than the characteristic time scale for horizontal transports – i.e., the particles will reach the ground before entering the adjacent grid-point column. In this case, we can prescribe stationarity and horizontal homogeneity for q^r and q^s and can neglect the impact due to vertical advection. By this assumption the full prognostic budget equations (5.9) for rain and snow are reduced to diagnostic relations which describe an equilibrium between the vertical divergence of the precipitation fluxes and the sum of the source and sink terms of the various microphysical processes α:

$$-\frac{1}{\rho}\frac{\partial P_x}{\partial z} \;=\; \frac{g}{\sqrt{\gamma}}\frac{\rho_0}{\rho}\frac{\partial P_x}{\partial \zeta} \;=\; \sum_\alpha S_\alpha^x\,, \tag{5.10}$$

where the vertical derivative can also be formulated using the terrain-following coordinate ζ of LM. Since the precipitation fluxes $P_x = \rho q^x v_T^x$ are unique functions of the mass fractions q^x, the source terms S^x can be reformulated in therms of P_x. Thereby the precipitation fluxes P_x become the dependent (diagnostic) variables replacing the (prognostic) q^x. At each time step, the diagnostic budget equations (5.10) are integrated from the top of the model domain to the surface, resulting in corresponding precipitation fluxes at the ground. The interaction with water vapour and the (still prognostic) cloud phases q^c and q^i is calculated at each layer by the source terms S^x during this integration.

Clearly, this condition of vertical equilibrium for the precipitating water categories limits the scheme to applications on hydrostatic scales of motion. However, at these scales (using grid spacings of about 10 km or larger) the numerical solution obtained by the reduced, i.e. diagnostic budget equations for rain and snow, is nearly as accurate as a complete threedimensional treatment (Ghan and Easter (1992)), but saves an enormous amount of computation time and computer memory.

5.2.2 Numerical Solution for Diagnostic Schemes

In diagnostic mode, the various microphysical source and sink terms in the budget equations of the hydrological cycle are evaluated at the present time-level ($n-1$ in case of the Leapfrog scheme, or n in case of the two time-level scheme). These terms are then added to the other

tendencies (e.g. due to advection) in the equations (5.8) for cloud water and cloud ice, and correspondingly in the equations for water vapour and temperature. An exception is made for the cloud water condensation rate S_c, which is calculated at the end of a time step using the saturation adjustment technique (see Section 5.3). In case of the cloud ice scheme, the evaluation is at the end of a time step by Marchuk-splitting following the calculation of the condensation rate. This ensures positive definite solutions for cloud water and cloud ice.

In order to solve the equations for the precipitation fluxes (5.10) numerically, P_x (P_r for rain and P_s for snow) have to be integrated from the top of the model domain to the surface. The integration is performed by a simple forward scheme where P_x is defined at model half levels $k \pm 1/2$. The source terms S_α^x due to various microphysical processes α are calculated at main levels using the layer mean values of the thermodynamic quantities, i.e. $(q^c, q^i, q^v, T)_k$, and the precipitation fluxes entering the layer from above:

$$(S_\alpha^x)_k \;=\; S_\alpha^x \left\{ (q^c, q^r, q^v, T)_k \,,\, (P_x)_{k-1/2} \right\} . \tag{5.11}$$

The precipitation flux at the lower boundary of the layer then results from

$$(P_x)_{k+1/2} \;=\; (P_x)_{k-1/2} + \sum_\alpha (S_\alpha^x)_k \left(\frac{\rho}{\rho_0} \right)_k \frac{\sqrt{\gamma}_k}{g} \,. \tag{5.12}$$

Stepping (5.12) from the top of the model atmosphere ($k = 1$), with $(P_x)_{1/2} = 0$ as upper boundary condition, to the lowest layer ($k = N_\zeta$) yields the precipitation rates at the surface.

Because cloud microphysics involves small time scales, all cloud water being available at time level $n - 1$ can become depleted by a single microphysical process (e.g. riming) within one timestep, especially when Δt is relatively large. In order to allow all processes to act simultaneously, we use a quasi-implicit formulation to calculate the sink terms for cloud water (and cloud ice).

5.2.3 Prognostic Treatment of Precipitation

By increasing the model's spatial resolution, the assumption of column equilibrium for the precipitating constituents becomes more and more unrealistic. Assuming a characteristic value of 5 m/s for the terminal fall velocity for rain and of 1 m/s for snow and a vertical fall distance of typically 2500 m for frontal precipitation, the time scales for sedimentation of rain and snow are estimated as 500 s and 2500 s, respectively. At 15 m/s wind speed, the corresponding horizontal displacements are about 8 km for rain and 40 km for snow – an effect that should be taken into account for grid spacings of about 10 km or smaller.

Horizontal transport is particularly important for the generation of lee-side precipitation, which is not sufficiently recognized by using the diagnostic schemes. The diagnostic treatment tends to largely overestimate the precipitation amount on mountain tops and to underestimate the amount on the downstream lee-side. Using the prognostic version of the scheme results in a significant reduction of the peak values as well as the area-mean values of precipitation (Gaßmann (2002); Baldauf and Schulz (2004)) in mountaineous areas. We suggest two physical reasons to be responsible for this beneficial impact. Advection of the mixing ratios q^x results in a large horizontal displacement before precipitation reaches the

surface. Consequently, a larger spatial area is available for sub-cloud evaporation (particularly in the dry lee-side region) than in the diagnostic scheme. Another reason contributing to the reduction of precipitation amount is a weakening of the seeder-feeder mechanism: In contrast to the prognostic scheme, all snow crystals must fall through the same vertical column where they are generated aloft when using the diagnostic scheme. This certainly gives the maximum effect of precipitation enhancement due to the seeder-feeder process.

When going to the meso-γ scale, deep convection becomes resolved explicitly and all instationary effects of cloud development must be considered to simulate realistically the life-cycle of deep convective cells. Especially, the vertical advection of the precipitation phases must be taken into account since the air's vertical velocity is in the same range as the fall velocity of rain and snow.

In order to take these effects into account, the diagnostic equations for the precipitation fluxes P_x from the equation set (5.10) have to be replaced by full prognostic equations (5.9) for the mixing ratios q^x:

$$\frac{\partial q^x}{\partial t} + \mathbf{v} \cdot \nabla q^x - \frac{1}{\rho}\frac{\partial}{\partial z}(\rho q^x v_T^x) \;=\; S^x \,,$$

where x stands for r (rain), s (snow) or g (graupel). The transformation of the "diagnostic" parameterization schemes of LM into "prognostic" ones using (5.9) requires three steps:

- The microphysical processes S^x have to be reformulated in terms of q^x as dependent model variables. In the following sections we will describe only the prognostic version in detail and the conversion rates for the diagnostic version will be summarized at the end of each section.
- An accurate and positive definite advection scheme has to be formulated. Since the integration is from time-level $n-1$ to $n+1$ over a $2\Delta t$ interval in the standard Leapfrog integration, the transport scheme should be able to cope with Courant numbers up to 2 (also, in the new 2-timelevel RK3 integration scheme, Courant numbers up to 1.8 are aspired). In this respect, a semi-Lagrangian scheme for 3-d advection of precipitation phases has been developed (Baldauf and Schulz (2004)).
- A numerically efficient treatment of the sedimentation term is required. Usually, quite thin model layers are specified close to the ground, where (vertical) Courant numbers can become larger than one.

Some detail of the numerical treatment of prognostic precititation schemes are summarized below.

5.2.4 Numerical Solution for Prognostic Schemes

With the partitioning of water substance into water vapour (q^v), the non-precipitating categories cloud water (q^c) and cloud ice (q^i), and the precipitating categories (q^x), i.e. rain (q^r), snow (q^s) and graupel (q^g), the equations for the hydrological cycle in the atmosphere may be formally written as

$$\begin{aligned}
\frac{\partial T}{\partial t} &= A_T + \frac{L_V}{c_{pd}}\left(S^c + S^r\right) + \frac{L_S}{c_{pd}}\left(S^i + S^s + S^g\right), \\
\frac{\partial q^v}{\partial t} &= A_{q^v} + S^v, \\
\frac{\partial q^{c,i}}{\partial t} &= A_{q^{c,i}} + S^{c,i}, \\
\frac{\partial q^x}{\partial t} &= A_{q^x} + \frac{1}{\rho}\frac{\partial}{\partial z}(\rho q^x v_T^x) + S^x .
\end{aligned} \tag{5.13}$$

The A-terms represent 3-d advective transport and other processes (e.g. turbulent diffusion in the equations for T, q^v and $q^{c,i}$, (cf. (3.65), Part I, and (5.8)–(5.9)), the S-terms are the sum of various microphysical conversion rates in each water category.

The numerical treatment of the set (5.13) is by the Marchuk or process time splitting method. That is, first the transport terms A are integrated over a timestep, resulting in provisional values for the prognostic variables. These intermediate values are then taken as input for a second step, where the variables are updated due to the S-terms and due to sedimentation of the precipitating categories q^x. The numerical techniques used for the first "dynamical" time step are outlined in Part I of the documentation.

The numerical treatment of the second "microphysical" step in the splitting, i.e. microphysical source terms and sedimentation, turns out to be quite difficult. In case of precipitation falling through thin model layers near the surface, the Courant number may become larger than one. An explicit scheme with simple flux limiting would result in an unphysical increase of q^x in the lower layers, and an implicit scheme cannot be applied directly because the sedimentation velocity is a nonlinear function of the mixing ratio. Also, a semi-Lagrangian technique will be difficult to apply since the source terms have to be taken into account to allow for microphysical interactions during fallout. For a first testversion of the prognostic scheme, Gaßmann (2002) has developed an integration method based on symmetric Strang process-splitting combined with local time-splitting for the sedimentation process (i.e. smaller time-steps are applied only for those layers where the local Courant number exceeds the stability limit).

Since this scheme turned out to be too time comsuming, it was replaced by a quasi-implicit formulation with a predictor-corrector method to include the source-terms S in the sedimentation algorithm (Gaßmann (2003)), allowing for microphysical interactions during fallout. The recent version of the quasi-implicit scheme is described below.

The budget equation to solve for the precipitating categories in the second "microphysical" step of the splitting of (5.13) reads

$$\frac{\partial q^x}{\partial t} = \frac{1}{\rho}\frac{\partial}{\partial z}(\rho q^x v_T^x) + S^x . \tag{5.14}$$

Since the total density ρ of air does not change during this step, (5.14) can be rewritten in the form

$$\frac{\partial \rho q^x}{\partial t} = \frac{\partial}{\partial z}(\rho q^x v_T^x) + \rho S^x . \tag{5.15}$$

Let $\phi = \rho q^x$ denote the partial density of a precipitating hydrometeor category x, $P = \rho q^x v_T^x$ the corresponding precipitation flux, $v = v_T^x(\phi)$ the mean fall velocity of the quantity ϕ (see

Sections 5.4–5.7 for the formulation of $v_T^x(\phi)$), and $S = S^x(\phi)$ the microphysical source terms. Then an implicit mass-conserving Crank-Nicolson discretization for (5.15) reads

$$\phi_k^{\text{new}} \;=\; \phi_k^{\text{start}} + \frac{\Delta t}{2\Delta z_k}\left(P_{k-1/2}^{\text{new}} - P_{k+1/2k}^{\text{new}} + P_{k-1/2}^{\text{start}} + P_{k+1/2}^{\text{start}}\right) + (\rho S)_k \Delta t\,, \tag{5.16}$$

where the superscript "start" denotes the start values of the current time step Δt – i.e. the result of the first dynamical integration step within the Marchuk-splitting – and the superscript "new" denotes the final values at timelevel $n+1$. Using the Leapfrog time-integration scheme instead of the two-timelevel Runge-Kutta scheme, Δt has to be replaced by $2\Delta t$. The index k is the level index, counting from top to bottom. Choosing a simple upstream approximation for the fluxes at half-levels $k \pm 1/2$ and estimating the fall velocities with the values of ϕ from the corresponding main level above yields a one-sided difference formulation:

$$\phi_k^{\text{new}} \;=\; \phi_k^{\text{start}} + \frac{\Delta t}{2\Delta z_k}\left(\phi_{k-1}^{\text{new}} v_{k-1}^{\text{new}} - \phi_k^{\text{new}} v_k^{\text{new}} + \phi_{k-1}^{\text{start}} v_{k-1}^{\text{start}} - \phi_k^{\text{start}} v_k^{\text{start}}\right) + (\rho S)_k \Delta t\,. \tag{5.17}$$

Because we do not know the new value v_k^{new} at the vertical level k, we replace this unknown value in $F_k^{\text{new}} = \phi_k^{\text{new}} v_k^{\text{new}}$ by the value of v computed from an average of already known new ϕ values from the upper layer $(k-1)$ and from current layer k start values:

$$v_k^{\text{new}} = v\left(0.5\phi_{k-1}^{\text{new}} + 0.5\phi_k^{\text{start}}\right)\,. \tag{5.18}$$

With this assumption, we obtain:

$$\phi_k^{\text{new}} = y_k^{\text{im}}\left\{\phi_k^{\text{start}} + \frac{\Delta t}{2\Delta z_k}\left(\phi_{k-1}^{\text{start}} v_{k-1}^{\text{start}} + \phi_{k-1}^{\text{new}} v_{k-1}^{\text{new}} - \phi_k^{\text{start}} v_k^{\text{start}}\right) + (\rho S)_k \Delta t\right\}\,, \tag{5.19}$$

with the "implicit weight" $y_k^{\text{im}} = (1 + 0.5\Delta t v_k^{\text{new}}/\Delta z_k)^{-1}$. To avoid negative values of ϕ caused by the the explicit contributions in the sedimentation algorithm (5.19), a simple flux limiter is applied:

$$\phi_k^{\text{new}} = y_k^{\text{im}}\left\{\phi_k^{\text{start}} + \max\left[\frac{\Delta t}{2\Delta z}\left(\phi_{k-1}^{\text{start}} v_{k-1}^{\text{start}} + \phi_{k-1}^{\text{new}} v_{k-1}^{\text{new}} - \phi_k^{\text{start}} v_k^{\text{start}}\right), -\phi_k^{\text{start}}\right] + (\rho S)_k \Delta t\right\}. \tag{5.20}$$

At each gridpoint, the transport algorithm (5.20) can be solved explicitly from the top of the model domain to the bottom. In order to take microphysical processes during fallout into account, the source terms are included using a predictor-corrector method. In each layer k, the algorithm (5.20) is first solved without the source term S, resulting in provisional "predictor" values ϕ_k^* for the partial density of precipitating hydrometeors:

$$\phi_k^* = y_k^{\text{im}}\left\{\phi_k^{\text{start}} + \max\left[\frac{\Delta t}{2\Delta z}\left(\phi_{k-1}^{\text{start}} v_{k-1}^{\text{start}} + \phi_{k-1}^{\text{new}} v_{k-1}^{\text{new}} - \phi_k^{\text{start}} v_k^{\text{start}}\right), -\phi_k^{\text{start}}\right]\right\}. \tag{5.21}$$

These values are then used to calculate the microphysical conversion rates, i.e.

$$S_k \;=\; S_k(\phi_k^*, q_{\text{start}}^v, q_{\text{start}}^{c,i}, T_{\text{start}})\,, \tag{5.22}$$

where for the dependence on other variables the input values at timelevel "start" are evaluated. In a second "corrector" step, the variables ϕ_k are then updated according to (5.20), using S_k from (5.22). The same values of S are used to update the other variables (T, q^v and $q^{c,i}$) in (5.13) in this "microphysical" part of the Marchuk time split scheme, which is done by a simple forward stepping.

5.3 Cloud Condensation and Evaporation

The simplest type of cloud is a warm non-precipitating cloud. To describe it with a bulk-scheme, only two categories of water substance are required: water vapour with specific humidity q^v and cloud water with liquid water content q^c. The only microphysical process that has to be considered is condensation-evaporation. Denoting the corresponding source rate by S_c, where $S_c > 0$ represents condensation of water vapour and $S_c < 0$ represents evaporation of cloud water, the budget equations for the hydrological cycle in the atmosphere read

$$\begin{aligned} \frac{\partial T}{\partial t} &= A_T + \frac{L_V}{c_{pd}} S_c \,, \\ \frac{\partial q^v}{\partial t} &= A_{q^v} - S_c \,, \\ \frac{\partial q^c}{\partial t} &= A_{q^c} + S_c \,. \end{aligned} \tag{5.23}$$

In (5.23), the A_ψ-terms summarize the tendencies due to advection, diffusion and other processes that are not related to cloud microphysics (see Eqs. (3-147) – (3-14), Part I). Clearly, the total water content q^T and the enthalpy related temperature T_h, defined by

$$q^T = q^v + q^c \,, \qquad T_h = T + \frac{L_V}{c_{pd}} q^v \,, \tag{5.24}$$

are conserved with respect to phase transitions of water vapour and cloud water. Another cloud-conservative variable that is frequently used in bulk modelling is the liquid-water temperature $T_l = T - L_V q^c / c_{pd}$.

The parameterization of the condensation rate S_c is based on the assumption of saturation equilibrium with respect to water within clouds. This closure condition is in accordance with numerous measurements revealing that the in-cloud supersaturation is usually very small (in general less than about 1%). S_c may then be calculated using the saturation-adjustment technique: if a grid box becomes supersaturated during a time step, the temperature and the concentration of the water vapour and cloud water are isobarically adjusted to a saturated state, taking the latent heating into account. The resulting decrease (increase) in specific humidity defines the amount of cloud water which is condensed (evaporated) in the time step. In case of $q^c > 0$ and subsaturation, the cloud water is instantaneously evaporated until either $q^c = 0$ or water saturation is achieved. The nucleation process is encompassed by saturation adjustment, i.e. it is assumed that there is always a sufficient number of CCN present to initiate the condensed water phase whenever the air becomes supersaturated.

By using saturation equilibrium as a closure condition for S_c, condensation-evaporation is treated as a quasi-reversible process, where only two different thermodynamic states may

occur: Either the saturated cloud case with $q^v = q^v_{sw}(T,p)$ and $q^c > 0$, where $q^v_{sw}(T,p)$ is the specific humidity at saturation with respect to water, or the subsaturated no-cloud case with $q^v < q^v_{sw}(T,p)$ and $q^c = 0$. Consequently, the description of the thermodynamic state requires only two dependent variables, e.g. q^T and T_h, instead of T, q^v and q^c. Cloud conservative variables which filter the condensation rate from the set of model equations are sometimes used in numerical models to save computation time and core memory.

The numerical procedure to compute the condensation rate is as follows. First, the budget equations (5.23) are stepped for one time step yielding provisional values $\tilde{T}$, $\tilde{q}^v$ and $\tilde{q}^c$ at time level $n+1$. Then, the cloud-conservative variables q^T and T_h from (5.24) are calculated using these provisional values. In the next step the provisional values will be adjusted due to condensation and evaporation to yield the final values of T, q^v and q^c at time level $n+1$. As the conservative variables do not change during the adjustment, we have

$$\begin{aligned} T + \frac{L_V}{c_{pd}} q^v &= \tilde{T} + \frac{L_V}{c_{pd}} \tilde{q}^v = \tilde{T}_h \,, \\ q^v + q^c &= \tilde{q}^v + \tilde{q}^c = \tilde{q}^T \,. \end{aligned} \tag{5.25}$$

To distinguish the subsaturated and the saturated thermodynamic states, we first test for the no-cloud case by setting $q^c = 0$ and $q^v = \tilde{q}^T$ in (5.25). This results in a preliminary temperature T^* and a corresponding saturation specific humidity q^{v*}_{sw}:

$$T^* = \tilde{T} - \frac{L_V}{c_{pd}} \tilde{q}^c \,, \qquad q^{v*}_{sw} = q^v_{sw}(T^*, p) \,. \tag{5.26}$$

(1) The subsaturated or just saturated no-cloud case is realized if $\tilde{q}^T \leq q^{v*}_{sw}$. For this condition, the final values of the variables are simply given by

$$\begin{aligned} T &= T^* = \tilde{T} - L_V \tilde{q}^c / c_{pd} \,, \\ q^v &= \tilde{q}^T \,, \\ q^c &= 0 \,. \end{aligned} \tag{5.27}$$

(2) The saturated cloud case is realized if $\tilde{q}^T > q^{v*}_{sw}$. For this condition, (5.25) results in a transcendental equation for temperature:

$$T = \tilde{T}_h - \frac{L_V}{c_{pd}} q^v_{sw}(T,p) \,.) \tag{5.28}$$

The Newton iteration method is used to solve (5.28):

$$T^\nu = \frac{\tilde{T}_h - \frac{L_V}{c_{pd}} \left\{ q^v_{sw}(T^{\nu-1}, p) - T^{\nu-1} \left(\frac{\partial q^v_{sw}}{\partial T} \right)_{T^{\nu-1}} \right\}}{1 + \frac{L_V}{c_{pd}} \left(\frac{\partial q^v_{sw}}{\partial T} \right)_{T^{\nu-1}}} \,, \tag{5.29}$$

where $\nu = 1, \cdots, N$ denotes the iteration index. The temperature at time level n is used as an initial estimate for the iteration, i.e. $T^{\nu=0} = T^n$. Following the last iteration step, the saturation specific humidity is not calculated from T^N but extrapolated from

its value for T^{N-1} using a linearly truncated Taylor series expansion. This is done to satisfy thermal energy conservation for the approximate iterative solution. The final values of the variables at time level $n+1$ are given by

$$\begin{aligned} T &= T^N\,, \\ q^v &= q^v_{sw}(T^{N-1},p) \,+\, (T^N - T^{N-1}) \left(\frac{\partial q^v_{sw}}{\partial T}\right)_{T^{N-1}}\,, \\ q^c &= \tilde{q}^T \,-\, q^v\,. \end{aligned} \tag{5.30}$$

By default, the number of iterations is set to one. Only in regions with large vertical velocities, where larger deviations from the saturation equilibrium can occur within a time step, the number of iterations is increased to $N = 2$.

Following the adjustment step defined by (5.27) and (5.30), the source term S_c due to condensation and evaporation can be calculated for diagnostic purposes, e.g. for integral area mean budgets of water mass and latent energy, using the updated cloud water content:

$$S_c \,=\, \frac{q^c \,-\, \tilde{q}^c}{2\Delta t}\,. \tag{5.31}$$

To apply the saturation adjustment technique to parameterize the condensation-evaporation process, the specific humidity at water saturation has to be specified in terms of temperature and pressure. q^v_{sw} is calculated from

$$q^v_{sw}(T,p) \,=\, \frac{R_d}{R_v}\frac{p^v_{sw}(T)}{p \,-\, (1-R_d/R_v)p^v_{sw}(T)}\,, \tag{5.32}$$

where $p^v_{sw}(T)$ is the equilibrium vapour pressure over a plane surface of water. We apply Teten's empirical formula

$$p^v_{sw}(T) \,=\, p^v_0 \exp\left(a_w \frac{T - T_r)}{T - b_w}\right) \tag{5.33}$$

to calculate p^v_{sw} as function of temperature using the parameters $p^v_0 = 610.78$ Pa, $T_r = 273.16$ K, $a_w = 17.27$ and $b_w = 35.86$ K.

For later use in subsequent sections, the specific humidity q^v_{si} at ice saturation and the equilibrium vapour pressure $p^v_{si}(T)$ over a plane surface of ice are also defined using the equations

$$q^v_{si}(T,p) \;=\; \frac{R_d}{R_v}\frac{p^v_{si}(T)}{p \,-\, (1-R_d/R_v)p^v_{si}(T)}\,, \tag{5.34}$$

$$p^v_{si}(T) \;=\; p^v_0 \exp\left(a_i \frac{T - T_r)}{T - b_i}\right)\,, \tag{5.35}$$

where $a_i = 21.875$ and $b_i = 7.66$ K.

5.4 Warm Rain Scheme

In case of a warm precipitating cloud, rain is included as an additional category of water substance (usually, drizzle is ignored). The mass fraction q^l of liquid-phase water is thus split into cloud water with mass fraction q^c as nonprecipitating category and rain water with mass fraction q^r as precipitating category.

5.4.1 The Set of Conservation Equations

The equations for the warm-rain bulk water-continuity scheme read

$$\begin{aligned}
\frac{\partial T}{\partial t} &= A_T + \frac{L_V}{c_{pd}}\left(S_c - S_{ev}\right), \\
\frac{\partial q^v}{\partial t} &= A_{q^v} - S_c + S_{ev}, \\
\frac{\partial q^c}{\partial t} &= A_{q^c} + S_c - S_{au} - S_{ac}, \\
\frac{\partial q^r}{\partial t} &= A_{q^r} + \frac{1}{\rho}\frac{\partial}{\partial z}(\rho q^r v_T^r) - S_{ev} + S_{au} + S_{ac}.
\end{aligned} \tag{5.36}$$

As in the previous section, the A_ψ-terms represent the tendencies due to all processes which are not related to microphysics. The impact of turbulent diffusion on rain water is usually neglected.

In (5.36), S_c denotes the rate of cloud water condensation and evaporation. The saturation adjustment scheme described in Section 5.3 is used to calculate S_c. P_r is the precipitation flux of rainwater due gravitational sedimentation of raindrops and S_{ev} is the evaporation rate of rainwater in subcloud layers (in-cloud diffusion growth of raindrops is ignored, i.e. vapour is assumed not to condense directly onto raindrops). S_{au} denotes the increase of rainwater with time due to autoconversion, which is the rate at which raindrops are initially formed at the expense of cloud droplets growing to precipitation size by collection and/or vapour diffusion. S_{ac} is the accretion rate, which is the rate at which the rainwater mass fraction increases as a result of the collection of cloud droplets by falling rain drops. Except for S_c, all of these terms are defined to be positive quantities.

This three-category bulk water-continuity model has originally been proposed by Kessler (1969). By parameterization of the source terms and the precipitation flux P_r in terms of the dependent variables (i.e. T, p, q^v, q^c and q^r), the scheme allows to represent numerically the evolution of warm-cloud precipitation formation in space and time. Most of the bulk schemes used today, including various extensions to take the ice-phase into account, are directly based on the concepts introduced by Kessler. Thus, bulk water-continuity models are often referred to as Kessler-type schemes.

According to the Kessler-scheme, cloud water is first generated by condensation. Once sufficient cloud water has been produced, the collision-coalescence mechanism can result in the initial formation of raindrops (autoconversion). The rainwater mass fraction can then be further increased due to collection of cloud droplets by raindrops (accretion). Rainwater that has been produced has a sedimentation flux relative to the air. If this flux becomes larger than the upward flux of rainwater due to grid-scale vertical motion, rainwater may leave the cloud and evaporate below cloud-base. Depending on humidity conditions in the sub-cloud layer, the precipitation particles may evaporate completely or partially before reaching the surface.

5.4.2 Parameterization of the Conversion Terms

In order to close the warm-rain scheme (5.36) the microphysical source/sink terms S and the precipitation flux P_r of rain have to be formulated in terms of the dependent model variables

(q^c, q^r, T and p). We will only summarize the basic assumptions for these parameterizations since the warm-rain scheme is part of a one-category ice scheme which is described in more detail in Section 5.5.

To calculate the source terms for rainwater, a number of key assumptions are made for the raindrops. First, the precipitation particles are assumed to be exponentially distributed with respect to drop diameter D:

$$f_r(D) \;=\; N_0^r \exp(-\lambda_r D)\,, \tag{5.37}$$

where N_0^r is an empirically determined distribution parameter. A typical value of N_0^r is $N_0^r = 8 \times 10^6$ m^{-4}. Given the Marshall-Palmer distribution (5.37), the slope parameter λ_r can be calculated from the rainwater mixing ratio q^r by calculating the integral (5.5), i.e.

$$\rho\, q^r \;=\; N_0^r \int_0^\infty m(D) \exp(-\lambda_r D) dD \;=\; \pi \rho_w N_0^r\, \lambda_r^{-4}\,, \tag{5.38}$$

where ρ_w is the density of water and $m(D) = \pi \rho_w D^3/6$ is the mass of a raindrop with diameter D. Second, the terminal fall speed v_T^r of individual raindrops is assumed to be uniquely related to drop size. A frequently used empirical relation to approximate experimental data is

$$v_T^{rp}(D) = v_0^r D^{1/2}\,, \tag{5.39}$$

with $v_0^r = 130$ m$^{1/2}$s^{-1}. Given (5.39) and (5.37), the precipitation flux P_r of rain can then be calculated in terms of the rainwater mixing ratio by evaluating the spectral definition of the rainwater massflux

$$P_r \;=\; \int_0^\infty m(D) v_T^r(D) f_r(D) dD\,. \tag{5.40}$$

Using (5.7) as a definition for the mean fall velocity v_T^r of rainwater, we have from (5.40) and (5.38) the following relation to calculate the mean fall velocity in terms of the rainwater mass fraction (for use in the prognostic equation for q^r):

$$v_T^r \;=\; \frac{P_r}{\rho\, q^r} \;=\; \frac{v_0^r \Gamma(4.5)}{6} \lambda_r^{-1/2} \;=\; (\pi \rho_w N_0^r)^{-1/8} \frac{v_0^r \Gamma(4.5)}{6} (\rho q^r)^{1/8}\,. \tag{5.41}$$

The parameterization of the accretional growth rate of rain is based on the continuous model for drop growth by collection. If a drop of radius R, mass m and fall speed $v_T(R)$ falls through a polydisperse population of smaller cloud droplets with radii r and fall speeds $v_T(r)$, distributed in size according to a number density size distribution $f_c(r)$, then the particle mass of the large drop is assumed to increase continually at a rate given by the continuous collection equation

$$(\dot{m})_{ac} \;=\; \frac{4\pi \rho_w}{3} \int K(R,r) f_c(r) r^3 dr\,. \tag{5.42}$$

$K(R,r)$ is the collection kernel for hydrodynamic gravitational capture,

$$K(R,r) \;=\; E_c(R,r) \pi (R+r)^2 [v_T(R) - v_T(r)]\,, \tag{5.43}$$

where E_c is the collection efficiency describing the efficiency with which a drop intercepts and unites with the smaller drops it overtakes. E_c is largely determined by the relative airflow around the falling drop. Smaller particles may be carried out of the path of the collector drop ($E_c < 1$) or droplets not in the geometrical sweep-out volume may collide with the large drop due to turbulence or electric effects ($E_c > 0$).

With respect to the parameterization of accretional growth of rain, the continuous collection equation is used in an approximated form. In accordance with the definition of cloud water, the fall velocity of the small droplets in (5.43) is set to zero. Since raindrops are much larger than cloud droplets, the geometrical collision cross section $\pi(R+r)^2$ may be approximated by πR^2. Furthermore, we assume that the collection efficiency $E_c(R,r)$ can be replaced by a constant mean value $\overline{E}_r$, which is usually taken to be close to one. Thus, the collection equation (5.42) becomes

$$(\dot{m})_{ac} \;=\; \frac{\pi}{4} D^2 v_T^r(D) \overline{E}_r \rho q^c \,. \tag{5.44}$$

The accretion rate, i.e. the depletion of cloud water due to collection by all raindrops, is then given by integration of the individual growth rates (5.44) over the entire spectrum (5.37) of raindrops,

$$S_{ac} \;=\; \frac{\pi N_0^r \overline{E}_r}{4}\, q^c \int_0^\infty D^2 v_T^r(D)\, e^{-\lambda_r D} dD \,. \tag{5.45}$$

Performing the integration using the empirical relation (5.39) for the terminal velocities of raindrops yields the accretion rate S_{ac} in terms of the dependent model variable q^c and q^r:

$$S_{ac} \;=\; c_{ac} q^c (\rho q^r)^{7/8} \quad \text{with} \quad c_{ac} \;=\; \frac{15}{32}\sqrt{\pi}\frac{\overline{E}_r}{\rho_w} v_0^r (\pi \rho_w N_0^r)^{1/8} \,. \tag{5.46}$$

Using the constant value $\overline{E}_r = 0.8$ for the mean collecting efficiency, we have the numerical value $c_{ac} = 1.72$ for the rate coefficient.

In an analogous manner, the bulk rate of evaporation of rainwater mass from all raindrops can be derived from the integral

$$S_{ev} \;=\; \frac{N_0^r}{\rho} \int_0^\infty (\dot{m})_{ev}\, e^{-\lambda_r D} dD \,, \tag{5.47}$$

where $(\dot{m})_{ev}$ is the rate of evaporation by diffusion of water vapour away from a single raindrop of diameter D falling through subsaturated air. Details on the diffusional growth equation used in (5.47) and on various parameters to derive the final form of the rate equation for S_{ac} and S_{ev} can be found in the next section and are not repeated here. The functional form is

$$S_{ev} = \alpha_{ev} \left(1 + \beta_{ev} (\rho q^r)^{3/16}\right) (q_{sw}^v - q^v) \, (\rho q^r)^{1/2} \,,$$

where β_{ev} is set to a constant value of 9.1 and α_{ev} is approximated by the temperature dependent function (in corresponding SI-units)

$$\alpha_{ev} \;=\; 3.86 \cdot 10^{-3} - 9.41 \cdot 10^{-5} \, (T - T_0) \,. \tag{5.48}$$

A more empirical approach is necessary to describe the initial formation of rainwater mass due to autoconversion of cloud droplets. The autoconversion rate S_{au} is usually assumed to

be proportional to the amount of cloud water mass fraction above a threshold value q_0^c and inversely proportional to a time constant τ_r defining the speed of the conversion mechanism:

$$S_{au} \;=\; \tau_r^{-1} \max(q^c - q_0^c, 0)\,. \tag{5.49}$$

Thus, whenever the cloud water content exceeds the autoconversion threshold q_0^c, it is converted to form rainwater at an exponential rate. The constants q_0^c and τ_r may be adjusted to reflect the impact of the cloud condensation nuclei on precipitation formation in different air-masses. The formulation (5.49) was originally postulated by (Kessler 1969) and meanwhile a number of other autoconversion formulas have been developed by various authors. In the warm rain scheme used in LM, we apply (5.49) with the default values $q_0^c = 0$ and $\tau_r = 10^3\,\mathrm{s}$.

5.4.3 Diagnostic Version

In the diagnostic version of the snow scheme, the prognostic equation for the rain water mass fraction q^r (5.36) is replaced by the column-equilibrium relation (5.10) for the precipitation flux P_r:

$$\frac{g}{\sqrt{\gamma}}\frac{\rho_0}{\rho}\frac{\partial P_r}{\partial \zeta} \;=\; -S_{ev} + S_{au} + S_{ac}\,. \tag{5.50}$$

The discretization and integration of this diagnostic budget equation for P_r has been described in Section 5.2.2. The microphysical conversion rates S_{ev} and S_{ac} are formulated with P_r as the dependent model variable, using (5.62). The autoconversion rate is the same as in the prognostic version. The modified rates read

$$\begin{aligned} S_{ac} &= c_{ac} q^c P_r^{\frac{7}{9}}\,, \\ S_{ev} &= \alpha_{ev}\left(1 + \beta_{ev} P_r^{\frac{1}{6}}\right)(q_{sw}^v - q^v)\, P_r^{\frac{4}{9}}\,, \end{aligned}$$

where the coefficients are defined by (using B_r from (5.60)):

$$c_{ac} = \frac{3}{7}\frac{\overline{E}_r}{\rho_w} B_r^{\frac{2}{9}}\,, \qquad \alpha_{ev} = \frac{2\pi d_v}{1 + H_w} N_0^r B_r^{-\frac{4}{9}}\,, \qquad \beta_{ev} = 0.26\left(\frac{\rho v_0^r}{2\eta_a}\right)^{\frac{1}{2}} \Gamma(2.75) B_r^{-\frac{1}{6}}\,.$$

The rate coefficient for accrecion is set to $c_{ac} = 0.24$, β_{ev} is approximated by the constant value $\beta_{ev} = 8.05$ and the rate coefficient α_{ev} for evaporation is approximated by the following temperature-dependent function (all coefficients in corresponding SI units):

$$\alpha_{ev} \;=\; 2.76 \cdot 10^{-3} \exp\{0.055(T_0 - T)\}\,.$$

5.5 A One-Category Ice Scheme

The bulk water-continuity model described in this section is designed for applications on the meso-β and meso-α scale to take microphysical processes in stratiform mixed-phase cold clouds into account. The scheme has been adapted (with a slightly different numerical treatment) from the operational hydrostatic models EM and DM.

5.5.1 Basic Assumptions

For mixed-phase precipitating stratiform clouds, snow is included as an additional category of water substance besides water vapour, cloud water and rain. Snow is assumed to be in the form of rimed aggregates of ice-crystals that have become large enough to have an appreciable fall velocity. Thus, water vapour and cloud water (with mass fraction q^v and q^c, respectively) constitute the cloud phase and rain and snow (with mass fraction q^r and q^s, respectively) constitute the precipitation phase. Since snow is the only category of solid forms of water considered, the scheme may be referred to as one-category bulk ice-scheme.

Other ice species in the precipitation phase, as e.g. graupel and hail, are neglected. Such particles are usually related to precipitation formation in meso-γ scale convective cloud systems that are not resolved by mesoscale NWP models using a grid spacing of about 10 km. Within resolvable stratiform cloud types, graupel and hail are unlikely to be generated by the comparatively weak dynamical forcings.

Also, cloud ice in the form of small suspended crystals with negligible fall velocity is not considered explicitly. Cloud ice particles consist of pristine crystals formed by ice nucleation processes or of crystal fragments produced by some ice enhancement processes. Many observations show that most of the different nucleation modes and ice enhancement processes operate at or near water saturation. The initially generated crystals will thus grow very quickly by deposition in a water saturated environment due to the corresponding high ice supersaturation. This growth is at the expense of cloud droplets which will evaporate partly to maintain water saturation. The time constant for this initial growth of ice particles, the Bergeron-Findeisen process, is generally much smaller than the characteristic dynamic time scale of stratiform clouds.

We will thus assume that cloud ice is transformed instantaneously to snow particles. Consequently, the cloud ice category is skipped in the parameterization scheme and the initial formation of snow due to nucleation and subsequent depositional growth of cloud ice particles at the expense of cloud water has to be parameterized.

5.5.2 The Set of Conservation Equations

Using these basic assumptions, the equations for the one-category ice bulk scheme read

$$\begin{aligned}
\frac{\partial T}{\partial t} &= A_T + \frac{L_V}{c_{pd}}\,(S_c - S_{ev}) + \frac{L_S}{c_{pd}}\,S_{dep} \\
&\quad + \frac{L_F}{c_{pd}}\,(S_{nuc} + S_{rim} + S_{frz} - S_{melt})\,, \\
\frac{\partial q^v}{\partial t} &= A_{q^v} - S_c + S_{ev} - S_{dep}\,, \\
\frac{\partial q^c}{\partial t} &= A_{q^c} + S_c - S_{au} - S_{ac} - S_{nuc} - S_{rim} - S_{shed}\,, \\
\frac{\partial q^r}{\partial t} &= A_{q^r} + \frac{1}{\rho}\frac{\partial}{\partial z}(\rho q^r v_T^r) - S_{ev} + S_{au} + S_{ac} + S_{melt} - S_{frz} + S_{shed}\,, \\
\frac{\partial q^s}{\partial t} &= A_{q^s} + \frac{1}{\rho}\frac{\partial}{\partial z}(\rho q^s v_T^s) + S_{nuc} + S_{rim} - S_{melt} + S_{frz} + S_{dep}\,.
\end{aligned} \tag{5.51}$$

As in the previous sections, the A_ψ-terms represent the tendencies due to all processes which

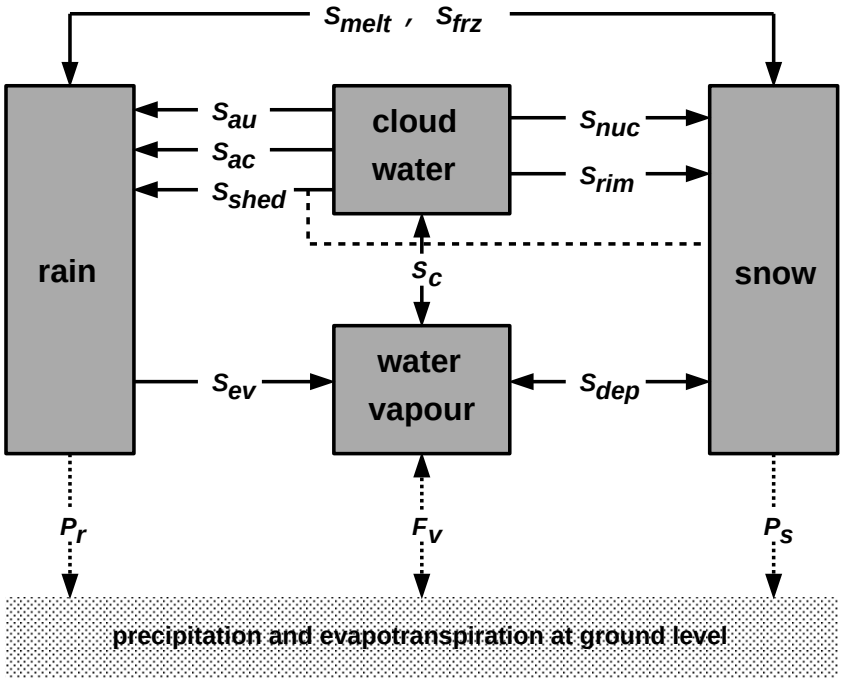

Figure 5.1: *Cloud microphysical processes considered in the one-category ice scheme*

are not related to microphysics. L_V and L_S are, respectively, the latent heat of vapourization and of sublimation and $L_F = L_S - L_V$ is the latent heat of fusion.

Besides the warm-rain microphysics discussed in Section 5.4, i.e. condensation and evaporation of cloud water, autoconversion, accretion and evaporation of rain water, additional conversion terms are considered by the scheme (5.51). These are related to microphysical processes in mixed-phase cold clouds: S_{nuc} is the rate of the initial formation of snow due to nucleation and subsequent diffusional growth of pristine ice crystals. S_{dep} denotes the rate of change of snow mass fraction resulting from diffusion growth of snow particles, where $S_{dep} > 0$ in case of deposition and $S_{dep} < 0$ in case of sublimation. S_{rim} is the riming rate, which is the rate at which the snow mass increases due to the collection of supercooled cloud droplets by falling snow particles. S_{melt} denotes the melting rate of snow to form rain and S_{frz} is the freezing rate of rain to form snow. S_{shed} is the rate at which water is shed by melting wet snow particles collecting cloud droplets to produce rain. Except for S_c and S_{dep}, all terms are defined to be positive quantities. Figure 5.1 shows the microphysical processes considered in this parameterization scheme.

To close the set (5.51) of equations for the hydrological cycle, the various conversion terms S describing microphysical processes must be formulated in terms of the dependent grid-scale variables. The parameterization of these terms is discussed in the next section, except for the cloud condensation rate S_c which is calculated as in Section 5.3. That is, clouds are assumed to exist always at water saturation, independent of how low the temperature will actually be.

5.5.3 Parameterization of the Conversion Terms

To parameterize the conversion terms, cloud water is treated as a bulk phase without spectral distribution, whereas size distribution functions are specified for the precipitation phases rain and snow. These functions have only one free parameter. A Marshall-Palmer distribution is assumed for rain and a Gunn-Marshall distribution is assumed for snow:

$$f_r(D) \;=\; N_0^r \exp(-\lambda_r D)\,, \qquad f_s(D) \;=\; N_0^s \exp(-\lambda_s D)\,. \tag{5.52}$$

$f_{r,s}(D)dD$ defines the number of raindrops and snow particles, respectively, per unit volume of air in the infinitesimal size interval $(D, D + dD)$, where the spectral size coordinate D is the diameter of a spherical water drop corresponding to particle mass m (i.e. the equivalent diameter). The intercept parameters N_0^r and N_0^s are assumed to be empirically determined constants. We use the values $N_0^r = 8 \times 10^6$ m^{-4} for rain and $N_0^s = 4 \times 10^5$ m^{-4} for snow.

The following relation holds between the mass m and the equivalent diameter D of raindrops and snow particles,

$$m \;=\; \frac{\pi \rho_w}{6}\, D^3\,, \tag{5.53}$$

where ρ_w is the bulk density of liquid water. Raindrops are assumed to be spherical drops with diameter D and the snow particles are interpreted as rimed aggregates of crystals in the form of thin circular plates with diameter D_s. The equation

$$m \;=\; a_m(T)\,(D_s)^2 \tag{5.54}$$

is used to specify their mass-size relation where $a_m(T)$ is a temperature dependent form factor given by

$$a_m(T) \;=\; \begin{cases} a_{mc} - a_{mv}\left[1 + \cos\left\{\dfrac{2\pi(T - T_{m1})}{(T_0 - T_1)}\right\}\right] & \text{if } T_0 > T > T_1, \\ a_{mc} & \text{else,} \end{cases} \tag{5.55}$$

where $T_0 = 273.15$ K, $T_1 = 253.15$ K, $T_{m1} = 0.5(T_0 + T_1)$, $a_{mc} = 0.08$ kg m^{-2} and $a_{mv} = 0.02$ kg m^{-2} are constant parameters. This factor approximates the dependence of both the aspect ratio and the density of a snow particle. According to (5.55), the snow aggregates will attain their largest extension D_s at -10°C.

Using (5.53) and (5.54), the equivalent diameter and the plate diameter of snow particles are related by

$$D_s \;=\; D^{\frac{3}{2}} \sqrt{\frac{\pi \rho_w}{6 a_m(T)}}\,. \tag{5.56}$$

For the terminal fall velocities of single raindrops and snow particles as functions of size we use the following empirical relations (derived from measurements):

$$v_T^{rp}(D) \;=\; v_0^r D^{1/2}\,, \qquad v_T^{sp}(D) \;=\; v_0^s D^{0.3}\,, \tag{5.57}$$

where $v_0^r = 130$ m$^{1/2}$s^{-1} and $v_0^s = 9.356$ m$^{0.7}$s^{-1}.

Given the size distribution functions (5.52), the mass fractions q^r and q^s, the precipitation fluxes P_r and P_s, and the mass-weighted spectral-mean fall velocities v_T^r and v_T^s of rain and snow (from (5.7)) are defined by the integrals

$$\begin{aligned} \rho\, q^{r,s} &= \int_0^\infty m(D) f_{r,s}(D) dD\,, \\ P_{r,s} &= \int_0^\infty m(D) v_T^{rp,sp}(D) f_{r,s}(D) dD\,, \\ v_T^{r,s} &= \frac{1}{\rho\, q^{r,s}} \int_0^\infty m(D) v_T^{rp,sp}(D) f_{r,s}(D) dD\,. \end{aligned} \tag{5.58}$$

The integration yields the following relations for the slope parameters and the mixing ratios

$$\begin{aligned} \rho\, q^r &= A_r\, \lambda_r^{-4}\,, \qquad A_r = \rho_w \pi N_0^r\,, \\ \rho\, q^s &= A_s\, \lambda_s^{-4}\,, \qquad A_s = \rho_w \pi N_0^s\,, \end{aligned} \tag{5.59}$$

for the slope parameters and the precipitation fluxes

$$\begin{aligned} P_r &= B_r\, \lambda_r^{-4.5}\,, \qquad B_r = \rho_w \pi N_0^r v_0^r\, \Gamma(4.5)/\Gamma(4)\,, \\ P_s &= B_s\, \lambda_s^{-4.3}\,, \qquad B_s = \rho_w \pi N_0^s v_0^s\, \Gamma(4.3)/\Gamma(4)\,, \end{aligned} \tag{5.60}$$

and for the slope paramters and the terminal fall velocities

$$v_T^r = A_r^{-1} B_r\, \lambda_r^{-1/2}\,, \qquad v_T^s = A_s^{-1} B_s\, \lambda_s^{-0.3}\,. \tag{5.61}$$

A and B are constant parameters that have been introduced for convenience and Γ is the Gamma-function. The free parameters λ_r and λ_s of the size distribution function can thus be determined as unique functions of the mass fractions or the precipitation fluxes which in turn are related by

$$\rho\, q^r = A_r B_r^{-\frac{8}{9}} P_r^{\frac{8}{9}}\,, \qquad \rho\, q^s = A_s B_s^{-\frac{4}{4.3}} P_s^{\frac{4}{4.3}}\,. \tag{5.62}$$

In the prognostic version of the scheme, we use the mass fractions q^r and q^s as the dependent model variables. (5.62) can be used to recalculate the microphysical conversion rates described below in terms of the precipitation fluxes P_r and P_s, which are the dependent variables in the diagnostic version of the scheme (see Section 5.5.4). Using (5.59) and (5.61), the terminal fall velocities are formulated directly in terms of q^r and q^s:

$$v_T^r = c_T^r (\rho\, q^r)^{\frac{1}{8}}\,, \qquad v_T^s = c_T^s (\rho\, q^s)^{\frac{0.3}{4}}\,. \tag{5.63}$$

The coefficients are defined by $c_T^r = A_r^{-\frac{9}{8}} B_r$ and $c_T^s = A_s^{-\frac{4.3}{4}} B_s$. With the parameters for the size distribution and the particle fall velocities, we have the numerical values $c_T^r = 12.63$ and $c_T^s = 2.87$ (in corresponding SI-units). The relations (5.63) are required for the numerical solution of the set (5.51) for the hydrolocical cycle using the sedimentation algorithm described in Section 5.2.4.

In order to parameterize the various source and sink terms S, mass growth rates $\dot{m}$ of the precipitation particles referring to a specific microphysical process are formulated first. The corresponding total rate of change is then given by integration over the entire spectral distribution:

$$S = \frac{1}{\rho} \int_0^\infty (\dot{m}) f(D) dD\,. \tag{5.64}$$

By analytic integration of (5.64), the conversion rate S can then be formulated in terms of the dependent model variables.

An exception to this strategy are the autoconversion and the nucleation processes which initiate the formation of precipitation. Empirical approaches are necessary to describe the initial formation of rain and snow from the cloud water phase. Here, we assume that a temperature dependent function $\varepsilon(T)$ determines which fraction of the cloud water content q^c above a threshold value q_0^c will be converted into rain (autoconversion) and into snow (nucleation). The corresponding production rates are assumed to be proportional to the cloud water content,

$$\begin{aligned} S_{au} &= \tau_r^{-1}\{1-\varepsilon(T)\}\max(0, q^c - q_0^c)\,, \\ S_{nuc} &= \tau_s^{-1}\varepsilon(T)\max(0, q^c - q_0^c)\,, \end{aligned} \tag{5.65}$$

where τ_r and τ_s are time constants defining the speed of the conversion processes. In the present version of the scheme, the time constants are set to $\tau_r = 10^4\,\mathrm{s}$ and $\tau_s = 10^3\,\mathrm{s}$, and a cloud water threshold is ignored ($q_0^c = 0$). The function $\varepsilon(T)$ follows the empirical relation

$$\varepsilon(T) = \begin{cases} 0 & \text{if } T \geq T_0\,, \\ 0.5\left[1 + \sin\left\{\dfrac{\pi(T_{m2} - T)}{(T_0 - T_2)}\right\}\right] & \text{if } T_2 < T < T_0\,, \\ 1 & \text{if } T \leq T_2\,, \end{cases} \tag{5.66}$$

where the constant parameters are $T_0 = 273.15\,\mathrm{K}$, $T_2 = 235.15\,\mathrm{K}$, $T_{m2} = 0.5(T_0 + T_2)$. Eq. (5.66) is based on the observed frequency distribution of water, ice and mixed-phase clouds as given by Matveev (1984). Using this function in (5.65), the production rate of rain at temperatures below 0°C is gradually suppressed with decreasing temperatures, while the nucleation rate of snow is enhanced. The autoconversion process disappears completely at temperatures below −38°C, where $\varepsilon(T) = 1$. At such low temperatures, all supercooled cloud water is made available for the nucleation process.

The parameterization of accretion and riming is based on the continuous model for particle growth by collection (see Section 5.4.2). According to this model, the mass growth rates of raindrops and snow crystals collecting cloud droplets are given by

$$\begin{aligned} (\dot{m})_{ac} &= \frac{\pi}{4} D^2 E_r(D)\, v_T^r(D)\, \rho q^c\,, \\ (\dot{m})_{rim} &= \frac{\pi}{4} D_s^2 E_s(D_s)\, v_T^s(D)\, \rho q^c\,, \end{aligned} \tag{5.67}$$

where E_r and E_s are the collection efficiencies of rain and snow particles and the geometric collision cross-section of snow crystals has been defined by the plate diameter D_s. In case of melting ice particles at temperatures above the freezing point T_0, it is assumed that the cloud water collected will no longer freeze but is shed from the crystal to form a larger drop. For this case, the riming growth rate in (5.67) is interpreted as a production rate for raindrops due to shedding. Assuming constant spectral average values for the collection efficiencies and integrating according to (5.64) yields the parameterized conversion rates due to accretion, riming and shedding. For accretion, analogous to the autoconversion rate in

Eq. (5.65), the additional temperature-dependent factor $\{1 - \varepsilon(T)\}$ according to (5.66) is applied. The conversion rates read:

$$\begin{aligned} S_{ac} &= \{1-\varepsilon(T)\} c_{ac} q^c (\rho q^r)^{7/8} \,, \\ S_{rim} &= \begin{cases} \dfrac{1}{a_m(T)} c_{rim}\, q^c (\rho q^s)^{\frac{4.3}{4}} & \text{if } T < T_0 \,, \\ 0 & \text{if } T \geq T_0 \,, \end{cases} \\ S_{shed} &= \begin{cases} 0 & \text{if } T < T_0 \,, \\ \dfrac{1}{a_m(T)} c_{rim}\, q^c (\rho q^s)^{\frac{4.3}{4}} & \text{if } T \geq T_0 \,. \end{cases} \end{aligned} \tag{5.68}$$

The rate coefficients c_{ac} and c_{rim} are defined by

$$c_{ac} = \frac{15}{32}\sqrt{\pi}\frac{\overline{E}_r}{\rho_w} v_0^r A_r{}^{1/8} \,, \qquad c_{rim} = \frac{\pi}{24}\overline{E}_s v_0^s \Gamma(4.3) A_s{}^{-\frac{0.3}{4}} \,. \tag{5.69}$$

The collection efficiencies for raindrops and snow particles collecting much smaller cloud droplets are usually close to unity. We use the constant mean values $\overline{E}_r = 0.8$ and $\overline{E}_s = 0.875$, resulting in the numerical values $c_{ac} = 1.72$ and $c_{rim} = 1.97$ for the rate coefficients.

With respect to evaporation of rain, deposition/sublimation and melting of snow, the parameterization is based on the following particle growth rates:

$$\begin{aligned} (\dot{m})_{ev} &= \frac{2\pi D d_v}{1 + H_w} F_v^r(D)\, \rho (q^v - q_{sw}^v) \,, \\ (\dot{m})_{dep} &= \frac{4\pi C(D) d_v}{1 + H_i} F_v^s(D)\, \rho (q^v - q_{si}^v) \,, \\ (\dot{m})_{melt} &= \frac{4\pi C(D) l_h}{L_F} F_v^s(D)\, (T_0 - T) \,, \quad T > T_0 \,. \end{aligned} \tag{5.70}$$

The first two rates in (5.70) are the well-known Howell equations for diffusion growth which take the impact of temperature differences between the particles and their environment by the Howell-factors H_w (for water) and H_i (for ice) into account. Additionally, convective vapour transport due to the fall velocity of the particles is considered by the ventilation factors F_v^r and F_v^s. Within clouds, the diffusional rate of change of raindrops vanishes because of the prescribed saturation equilibrium, i.e. raindrops may only evaporate below cloud base where $q^v < q_{sw}^v$. The mass growth rate of snow crystals, however, is always positive in cold clouds since $q^v = q_{sw}^v > q_{si}^v$ results in large supersaturations with respect to ice. The melting rate results from the assumption of thermal equilibrium for the melting particle, i.e. the release of latent heat is balanced by the heat transport between the particle and the surrounding air.

In (5.70), d_v is the molecular diffusion coefficient of water vapour, l_h the thermal conductivity of dry air and C the capacity of the snow crystals. C is assumed to be the capacity for thin circular disks of diameter D_s, i.e. $C = D_s/\pi$. The Howell and the ventilation factors are

defined by

$$H_w = \frac{d_v L_V^2}{l_h R_v T^2}\,\rho q_{sw}^v \quad , \quad H_i = \frac{d_v L_S^2}{l_h R_v T^2}\,\rho q_{si}^v \,,$$
$$F_v^r = 1 + 0.26\left(\frac{D v_T^r(D)\rho}{2\eta_a}\right)^{1/2} \quad , \quad F_v^s = 1 + 0.26\left(\frac{D_s v_T^s(D)\rho}{2\eta_a}\right)^{1/2} \tag{5.71}$$

where η_a is the dynamic viscosity of dry air. The conversion rates due to diffusion and melting result from the integration of the particle growth rates over the spectral distribution according to (5.64). Since S_{ev} and S_{melt} have been defined to be positive quantities, the individual mass growth rates are multiplied by minus one prior to integration. Finally, the equations for the parameterized rates are obtained as

$$\begin{aligned} S_{ev} &= \alpha_{ev}\left(1 + \beta_{ev}(\rho q^r)^{3/16}\right)(q_{sw}^v - q^v)\,(\rho q^r)^{1/2}\,, \\ S_{dep} &= \alpha_{dep}\,a_m^{-1/2}\left(1 + \beta_{dep}\,a_m^{-1/4}(\rho q^s)^{\frac{0.9}{4.0}}\right)(q^v - q_{si}^v)\,(\rho q^s)^{5/8}\,, \\ S_{melt} &= \alpha_{melt}\,a_{mc}^{-1/2}\left(1 + \beta_{melt}\,a_{mc}^{1/4}(\rho q^s)^{\frac{0.9}{4.0}}\right)(T - T_0)\,(\rho q^s)^{5/8}\,. \end{aligned} \tag{5.72}$$

The factors α and β depend in a complex way on the distribution parameters but also on temperature and air density. Formally, they are given by

$$\begin{aligned} \alpha_{ev} &= \frac{2\pi d_v}{1 + H_w} N_0^r (A_r)^{-1/2}\,, \\ \beta_{ev} &= 0.26\left(\frac{\rho v_0^r}{2\eta_a}\right)^{1/2}\Gamma(2.75)(A_r)^{-3/16}\,, \\ \alpha_{dep} &= \frac{4 d_v}{1 + H_i}\left(\frac{\pi\rho_w}{6}\right)^{1/2} N_0^s \Gamma(2.5) {A_s}^{-5/8}\,, \\ \beta_{dep} &= 0.26\left(\frac{\rho v_0^s}{2\eta_a}\right)^{1/2}\left(\frac{\pi\rho_w}{6}\right)^{1/4}\frac{\Gamma(3.4)}{\Gamma(2.5)} {A_s}^{-\frac{0.9}{4.0}}\,, \\ \alpha_{melt} &= \frac{4 l_h}{\rho L_F}\left(\frac{\pi\rho_w}{6}\right)^{1/2} N_0^s \Gamma(2.5) {A_s}^{-5/8}\,, \\ \beta_{melt} &= \beta_{dep}\,. \end{aligned} \tag{5.73}$$

The coefficients α_{ev} and α_{dep} in (5.73) are approximated by the following temperature-dependent functions (in corresponding SI units):

$$\alpha_{ev} = 3.86 \cdot 10^{-3} - 9.41 \cdot 10^{-5}\,(T - T_0) \tag{5.74}$$
$$\alpha_{dep} = 1.09 \cdot 10^{-3} - 3.34 \cdot 10^{-5}\,(T - T_0) \tag{5.75}$$

The other coefficients from (5.73) are approximated by the following constant values (in corresponding SI units): $\beta_{ev} = 9.1$, $\alpha_{melt} = 7.2 \cdot 10^{-6}$, $\beta_{melt} = \beta_{dep} = 13.0$.

Freezing of supercooled raindrops may occur due to heterogeneous nucleation. Two mechanisms are taken into account: (1) immersion freezing resulting from various drop impurities which become active as ice nuclei, and (2) contact freezing nucleation due to collection of ice nuclei by falling drops. The source term S_{frz} for the mixing ratio of snow in the budget equations (5.51) is thus made up of two terms,

$$S_{frz} = S_{frz}^{if} + S_{frz}^{cf}\,, \tag{5.76}$$

where S^{if}_{frz} denotes the contribution from immersion freezing and S^{cf}_{frz} is the contribution from contact nucleation.

The parameterization of S^{if}_{frz} is based on Bigg's equation (Bigg (1953)) for the decrease of the number N_u of unfrozen drops with volume V_d due to immersion nucleation per time interval dt,

$$\frac{dN_u}{dt}_{if} = -N_u V_d J(T_s)\,, \tag{5.77}$$

where $T_s = T_0 - T$ is the supercooling and J is the nucleation rate of frozen drops (i.e. snow particles) given by

$$J(T_s) = B_{if}\left(e^{a_{if}T_s} - 1\right) \tag{5.78}$$

and the parameters $a_{if} = 0.66\ \mathrm{K}^{-1}$, $B_{if} = 100.0\ \mathrm{m}^{-3}\mathrm{s}^{-1}$ have been determined by laboratory experiments. Applying (5.77) to a spectral distribution $f_r(D)$ of raindrops and integrating mass-weighted over the spectrum results in the following expression for the source rate of snow mixing ratio due to immersion freezing of raindrops:

$$\begin{aligned} S^{if}_{frz} &= -\frac{1}{\rho}\left(\frac{\pi\rho_w}{6}\right)\int_0^\infty D^3(\partial f_r(D)/\partial t)_{if}\,dD \\ &= \frac{\rho_w}{\rho}\left(\frac{\pi}{6}\right)^2 J(T_s)\int_0^\infty D^6 f_r(D)\,dD\,. \end{aligned} \tag{5.79}$$

Using the Marshall-Palmer size distribution (5.52) for $f_r(D)$, we finally obtain the parameterized rate equation as

$$S^{if}_{frz} = \frac{\rho_w}{\rho} 20\pi^2 N_0^r J(T_s)\lambda_r^{-7}\,,$$

or, by applying (5.59) to formulate S^{if}_{frz} in terms of the mass fraction of rain as the dependent model variable,

$$S^{if}_{frz} = \alpha_{if}\left(e^{a_{if}(T_0-T)} - 1\right)(\rho q^r)^{7/4}\,. \tag{5.80}$$

The parameter $\alpha_{if} = (\rho_w/\rho)20\pi^2 B_{if} N_0^r (A_r)^{-7/4}$ is approximated by the constant value $\alpha_{if} = 9.95 \cdot 10^{-5}$ in corresponding SI-units.

The activation of ice nuclei as contact freezing nuclei requires that they are collected by the liquid phase. In case of supercooled raindrops it is being assumed that the collection is due to gravitational sedimentation and that freezing occurs instantaneously at the moment of contact. Denoting the number of nuclei active as contact nuclei at drop temperature T by N_{cf}, the decrease in the size-distribution function $f_r(D)$ of raindrops may be formulated as

$$\left(\frac{\partial f_r(D)}{\partial t}\right)_{cf} = -f_r(D)\frac{\pi}{4}D^2 E_{cf} v_T^r(D) N_{cf}\,, \tag{5.81}$$

where E_{cf} is the mean collection efficiency of raindrops collecting ice nuclei. The correspond-

ing source rate S^{cf}_{frz} of the snow mass fraction then results as the mass-weighted integral

$$\begin{aligned} S^{cf}_{frz} &= -\frac{1}{\rho}\left(\frac{\pi\rho_w}{6}\right)\int_0^\infty D^3(\partial f_r(D)/\partial t)_{cf}dD \\ &= \frac{\rho_w}{\rho}\left(\frac{\pi^2}{24}\right)N_{cf}\int_0^\infty D^5 v_T^r(D)f_r(D)dD\,. \end{aligned} \tag{5.82}$$

By integration of Eq. (5.82) using the Marshall-Palmer size distribution for $f_r(D)$ and the relation (5.57) for the fall velocity of raindrops, we finally obtain the parameterized rate equation as

$$S^{cf}_{frz} = \alpha_{cf}E_{cf}N_{cf}(\rho q^r)^{13/8}\,. \tag{5.83}$$

The parameter $\alpha_{cf} = (\rho_w/\rho)(\pi^2/24)N_0^r v_0^r \Gamma(6.5)B_r^{-13/9}$ is approximated by the constant value $\alpha_{cf} = 1.55\cdot 10^{-3}$ in corresponding SI-units, where the collection efficiency has been set to $E_{cf} = 5.0\cdot 10^{-3}$.

In order to apply Eq. (5.83), the number density of contact nuclei active at a given temperature and height must be specified. According to Young (1974) the activity spectrum is formulated as

$$N_{cf} = \begin{cases} N_{cf,0}(270.16 - T)^{1.3} & \text{if } T < 270.16 \text{ K}, \\ 0.0 & \text{if } T \geq 270.16 \text{ K} \end{cases} \tag{5.84}$$

with a contact nuclei threshold temperature of -3°C. The concentration of natural contact nuclei active at -4°C is estimated to be $N_{cf,0} = 2.0\cdot 10^5$ m^{-3} at sea level. As contact nuclei are predominately produced near the surface, $N_{cf,0}$ will in general decrease with height. In lieu of observational data, the concentration of contact nuclei active at -4°C is assumed to decrease linearly from its surface value to a background concentration of $N_{cf,0} = 10^4$ m^{-3} in 500 hPa.

5.5.4 Diagnostic Version

In the diagnostic version of the snow scheme, the prognostic equations for q^r and q^s in (5.51) are replaced by the column-equilibrium relations (5.10) for the corresponding precipitation fluxes P_r and P_s:

$$\frac{g}{\sqrt{\gamma}}\frac{\rho_0}{\rho}\frac{\partial P_r}{\partial \zeta} = S^r\,, \qquad \frac{g}{\sqrt{\gamma}}\frac{\rho_0}{\rho}\frac{\partial P_s}{\partial \zeta} = S^s\,.$$

The discretization and integration of these diagnostic budget equations for P_r and P_s has been described in Section 5.2.2. The microphysical conversion rates S are formulated with P_r and P_s as the dependent model variables, using (5.62). They read:

$$
\begin{aligned}
S_{ac} &= \{1-\varepsilon(T)\}c_{ac}q^c P_r^{\frac{7}{9}} \\
S_{rim} &= \begin{cases} \dfrac{1}{a_m(T)}c_{rim}\,q^c P_s & \text{if } T < T_0 \\ 0 & \text{if } T \geq T_0 \end{cases} \\
S_{shed} &= \begin{cases} 0 & \text{if } T < T_0 \\ \dfrac{1}{a_m(T)}c_{rim}\,q^c P_s & \text{if } T \geq T_0 \end{cases} \\
S_{ev} &= \alpha_{ev}\left(1+\beta_{ev}P_r^{\frac{1}{6}}\right)(q_{sw}^v - q^v)\,P_r^{\frac{4}{9}} \\
S_{dep} &= \alpha_{dep}\,a_m^{-\frac{1}{2}}\left(1+\beta_{dep}\,a_m^{-\frac{1}{4}}P_s^{\frac{0.9}{4.3}}\right)(q^v - q_{si}^v)\,P_s^{\frac{5}{8.6}} \\
S_{melt} &= \alpha_{melt}\,a_{mc}^{-\frac{1}{2}}\left(1+\beta_{melt}\,a_{mc}^{-\frac{1}{4}}P_s^{\frac{0.9}{4.3}}\right)(T-T_0)\,P_s^{\frac{5}{8.6}} \\
S_{frz}^{if} &= \alpha_{if}\left(e^{a_{if}(T_0-T)}-1\right)P_r^{14/9} \\
S_{frz}^{cf} &= \alpha_{cf}E_{cf}N_{cf}P_r^{13/9}
\end{aligned}
$$

The autoconversion and nucleation rate are the same as in the prognostic version. The coefficients in the modified source terms above are defined by (using B_r and B_s from (5.60)):

$$
\begin{aligned}
c_{ac} &= \frac{3}{7}\frac{\overline{E}_r}{\rho_w}B_r^{\frac{2}{9}} \\
c_{rim} &= \frac{\pi}{4}\overline{E}_s \\
\alpha_{ev} &= \frac{2\pi d_v}{1+H_w}N_0^r B_r^{-\frac{4}{9}} \\
\alpha_{dep} &= \frac{4d_v}{1+H_i}\left(\frac{\pi\rho_w}{6}\right)^{\frac{1}{2}}N_0^s\Gamma(2.5)\,B_s^{-\frac{5}{8.6}} \\
\alpha_{melt} &= \frac{4l_h}{\rho L_F}\left(\frac{\pi\rho_w}{6}\right)^{\frac{1}{2}}N_0^s\Gamma(2.5)\,B_s^{-\frac{5}{8.6}} \\
\beta_{ev} &= 0.26\left(\frac{\rho v_0^r}{2\eta_a}\right)^{\frac{1}{2}}\Gamma(2.75)B_r^{-\frac{1}{6}} \\
\beta_{dep} &= 0.26\left(\frac{\rho v_0^s}{2\eta_a}\right)^{\frac{1}{2}}\left(\frac{\pi\rho_w}{6}\right)^{\frac{1}{4}}\frac{\Gamma(3.4)}{\Gamma(2.5)}B_s^{-\frac{0.9}{8.6}} \\
\beta_{melt} &= \beta_{dep} \\
\alpha_{if} &= (\rho_w/\rho)20\pi^2 B_{if}N_0^r B_r^{-14/9} \\
\alpha_{cf} &= (\rho_w/\rho)(\pi^2/24)N_0^r v_0^r\Gamma(6.5)B_r^{-13/9}
\end{aligned}
$$

The coefficients α_{ev} and α_{dep} are approximated by the following temperature-dependent functions (in corresponding SI units):

$$\alpha_{ev} = 2.76\cdot 10^{-3}\exp\{0.055(T_0-T)\}\,, \tag{5.85}$$

$$\alpha_{dep} = 1.13\cdot 10^{-3}\exp\{0.073(T_0-T)\}\,. \tag{5.86}$$

The other coefficients are approximated by the following constant values (in corresponding SI units): $c_{ac} = 0.24$, $c_{rim} = 0.69$, $\beta_{ev} = 5.98$, $\alpha_{melt} = 3.90 \cdot 10^{-6}$, $\beta_{melt} = \beta_{dep} = 10.50$, $\alpha_{if} = 1.92 \cdot 10^{-6}$ and $\alpha_{cf} = 3.97 \cdot 10^{-5}$.

5.6 A Two-Category Ice Scheme

The bulk water-continuity model described in this section is designed for applications on the meso-β and meso-α scale to take microphysical processes in stratiform mixed-phase and ice clouds into account. Compared to the one-category ice scheme, cloud ice is included as an additional solid form of water substance besides snow. The parameterization scheme will be referred to as cloud ice scheme.

5.6.1 Basic Assumptions

For mixed- and ice-phase stratiform clouds, cloud ice and snow are included as solid forms of water substance besides the categories water vapour, cloud water and rain. Snow is assumed to be in the form of rimed aggregates of ice-crystals that have become large enough to have an appreciable fall velocity. Cloud ice is assumed to be in the form of small hexagonal plates that are suspended in the air and have no appreciable fall velocity. Thus, cloud water and rain water (with mass fraction q^c and q^r, respectively) constitute the liquid phase and cloud ice and snow (with mass fraction q^i and q^s, respectively) constitute the solid phase.

Similar to the EM/DM scheme described in Section 5.5, other ice species in the precipitation phase, as e.g. graupel and hail, are neglected. Also, equilibrium in vertical columns is assumed for the precipitation phases rain and snow. These conditions limit the cloud ice scheme to applications on hydrostatic scales of motion.

Most parameterization schemes for mixed phase clouds rely on an extended saturation adjustment technique proposed by Lord et al. (1984) to calculate simultaneously condensation of cloud water as well as depositional growth of cloud ice at temperatures below the freezing point. This method supposes that both cloud droplets and cloud ice particles are in thermodynamic equilibrium with respect to a hypothetical saturation vapour pressure which is defined as a weighted mean of the equilibrium pressure of water and over ice in the temperature range $-40°\mathrm{C} < T < 0°\mathrm{C}$. In this temperature range, the method will always result in mixed phase clouds with an almost linear partitioning of the condensate in q^i and q^c, independent of the dynamic conditions. Also, as the rapid growth of ice crystals in water saturated mixed-phase clouds cannot be described adequately by this scheme, the Findeisen-Bergeron process has to be parameterized completely.

To avoid such an artificial assumption, we formulate the depositional growth of cloud ice as a non-equilibrium process and require, at all temperatures, saturation with respect to water for cloud water to exist. Ice crystals which are nucleated in a water saturated environment will then grow very quickly by deposition at the expense of cloud droplets. Depending on local dynamic conditions, the cloud water will either evaporate completely or will be resupplied by condensation. For strong dynamical forcings it is expected that water saturation will be maintained, resulting in a mixed phase cloud. In case of a comparatively weak forcing, the cloud will be readily transformed to an ice cloud existing at or near ice saturation (i.e. at subsaturation with respect to water). The latter type of clouds cannot be simulated with the

EM/DM scheme from Section 5.5.

An explicit treatment of the depositional growth of cloud ice requires assumptions on the shape, size and number density of crystals. We assume a monodisperse size distribution for cloud ice with mean crystal mass

$$m_i \;=\; \rho q^i N_i^{-1}\,, \tag{5.87}$$

where N_i is the number of cloud ice particles per unit volume of air. Since only the mass fraction q^i is predicted in a single moment scheme, either m_i or N_i must be specified in terms of the dependent model variables. We chose to prescribe the number density of crystals as a function of temperature because the mean crystal mass will change rapidly due to deposition and sublimation. N_i, however, is also highly variable in space and time, depending on the availability of ice nuclei and their modes of action as well as collection and ice multiplication processes.

An estimate of N_i could be based on the classical Fletcher-formula (Fletcher (1962)) for the number N_{in}^a of ice nuclei which become activated at temperature T below the freezing point T_0:

$$N_{in}^a \;=\; N_0^a \exp\{\,0.6\,(T_0 - T)\}\,, \qquad N_0^a \;=\; 0.01\,\mathrm{m}^{-3}\,. \tag{5.88}$$

Eq. (5.88) represents an average of many measurements made at various locations using expansion chambers. Generally, these measurements did not distinguish between the nucleation mechanisms (condensation, immersion, contact and deposition nucleation) and did not indicate the effect of varying the humidity. The concentration of ice crystals measured in natural cold clouds is very often found to be much higher than can be accounted for by the typical concentration (5.88) of ice nuclei, especially at relatively low supercooling ($T > -20°\mathrm{C}$). This is referred to as ice enhancement. The processes by which the concentrations of ice particles become so highly enhanced are not certain. Some hypotheses are fragmentation of crystals, ice splinter production in riming, contact nucleation and condensation nucleation.

To take the impact of ice enhancement implicitly into account, the number density of cloud ice crystals as a function of temperature is parameterized by

$$N_i(T) \;=\; N_0^i \exp\{\,0.2\,(T_0 - T)\}\,, \qquad N_0^i \;=\; 1.0 \cdot 10^2\,\mathrm{m}^{-3}\,. \tag{5.89}$$

This approximation is based on aircraft measurements of the concentration of pristine crystals in stratiform clouds using data of Hobbs and Rangno (1985) and (Meyers et al. 1992). For a given temperature, the experimental data may scatter by about two orders of magnitude. Nevertheless, we assume that (5.89) represents a meaningful average value for the cloud ice crystal concentration in cold stratiform clouds. Clearly, a more physically based approach must involve a double-moment representation of cloud ice including a budget equation for the concentration of ice nuclei. This, however, is beyond the scope of our single-moment cloud ice scheme.

Pristine cloud ice crystals are assumed to be in the form of thin hexagonal plates with diameter D_i and thickness h_i, where the maximum linear dimension D_i is smaller than about 200 μm. Thus, the particles will be in the constant aspect ratio growth regime. Assuming an aspect ratio of $h/D_i = 0.2$ and an ice density of $5 \cdot 10^{-2}\,\mathrm{kg\,m}^{-3}$ yields the following mass-size relation for cloud ice particles,

$$m_i \;=\; a_m^i\, D_i^3\,, \tag{5.90}$$

where $a_m^i = 130\,\mathrm{kg\,m}^{-3}$. A temperature dependency of the form factor a_m^i is neglected.

Snow is assumed to be in the form of densely rimed aggregates of dendrites with a maximum linear dimension D_s, the diameter of snow particles. These particles are in the limiting (or linear) growth regime. Based on data of Locatelli and Hobbs (1974), their mass-size relation is approximated by

$$m_s \;=\; a_m^s \, D_s^2 \,. \tag{5.91}$$

In contrast to the one-category ice scheme, the form factor a_m^s is assumed to be independent of temperature for simplicity and is set to $a_m^s = 0.038\,\mathrm{kg\,m^{-2}}$.

Exponential size distribution functions for the precipitation categories rain and snow are prescribed,

$$f_r(D) \;=\; N_0^r \exp(-\lambda_r D)\,, \qquad f_s(D_s) \;=\; N_0^s \exp(-\lambda_s D_s)\,. \tag{5.92}$$

where D is the equivalent diameter of raindrops. The size distribution functions (5.92) are similar to those for the one-category ice scheme in Eq. (5.52), except that the diameter of snow particles is used as spectral coordinate. An exponential nature of ice particle spectra with respect to maximum linear dimension is supported by various in-situ measurements using optical probes. The intercept parameters N_0^r and N_0^s are assumed to be empirically determined constants. We use the typical values $N_0^r = 8 \times 10^6$ m^{-4} for rain and $N_0^s = 8 \times 10^5$ m^{-4} for snow.

For the terminal fall velocities of single raindrops and snow particles as functions of size the following empirical relations (derived from measurements) are applied:

$$v_T^{rp}(D) \;=\; v_0^r D^{0.5}\,, \qquad v_T^{sp}(D_s) \;=\; v_0^s D_s^{0.25}\,, \tag{5.93}$$

where $v_0^r = 130$ m$^{1/2}$s^{-1} and $v_0^s = 4.9$ m$^{0.75}$s^{-1}. As in the EM/DM-scheme, a correction term depending on air density (to take changes in the areodynamical drag forces into account) is neglected.

5.6.2 The Set of Conservation Equations

Using these basic assumptions, the conservation equations of the two-category ice scheme for water vapour, cloud water, cloud ice, rain and snow read

$$\begin{aligned}
\frac{\partial T}{\partial t} &= A_T \;+\; \frac{L_V}{c_{pd}}\,(S^c + S^r) \;+\; \frac{L_S}{c_{pd}}\,(S^i + S^s)\,, \\
\frac{\partial q^v}{\partial t} &= A_{q^v} \;+\; S^v\,, \\
\frac{\partial q^c}{\partial t} &= A_{q^c} \;+\; S^c\,, \\
\frac{\partial q^i}{\partial t} &= A_{q^i} \;+\; S^i\,, \\
\frac{\partial q^r}{\partial t} &= A_{q^r} \;+\; \frac{1}{\rho}\frac{\partial}{\partial z}(\rho q^r v_T^r) \;+\; S^r\,, \\
\frac{\partial q^s}{\partial t} &= A_{q^s} \;+\; \frac{1}{\rho}\frac{\partial}{\partial z}(\rho q^s v_T^s) \;+\; S^s\,.
\end{aligned} \tag{5.94}$$

As in the previous sections, the A_ψ-terms represent the tendencies due to all processes which are not related to microphysics. For q^i, this includes threedimensional advection, turbulent diffusion and computational mixing, for the precipitating categories rain and snow only 3-d

advective transport. L_V and L_S are, respectively, the latent heat of vapourization and of sublimation.

The terms S^x describe the sources and sinks for a water category x ($x = i$ denotes cloud ice) due to various microphysical transfers between the hydrometeor species, and their sum is zero. The following microphysical processes are taken into account:

$$\begin{aligned} S^v &= -S_c + S_{ev} - S^i_{dep} - S^s_{dep} - S_{nuc} \\ S^c &= S_c - S^c_{au} - S_{ac} - S^c_{frz} + S^i_{melt} - S_{rim} - S_{shed} \\ S^i &= S_{nuc} + S^c_{frz} + S^i_{dep} - S^i_{melt} - S^i_{au} - S_{aud} - S_{agg} - S^i_{cri} \\ S^r &= S^c_{au} + S_{ac} - S_{ev} + S_{shed} - S^r_{cri} - S^r_{frz} + S^s_{melt} \\ S^s &= S^i_{au} + S_{aud} + S_{agg} + S_{rim} + S^s_{dep} + S^i_{cri} + S^r_{cri} + S^r_{frz} - S^s_{melt} \end{aligned} \tag{5.95}$$

The symbols S_α denote specific transfer rates which are explained in the table below. Figure 5.2 sketches the microphysical processes considered in this two category ice scheme of LM.

S_c	condensation and evaporation of cloud water
S^c_{au}	autoconversion of cloud water to form rain
S_{ac}	accretion of cloud water by raindrops
S_{ev}	evaporation of rain water
S_{nuc}	heterogeneous nucleation of cloud ice
S^c_{frz}	nucleation of cloud ice due to homogeneous freezing of cloud water
S^i_{dep}	deposition growth and sublimation of cloud ice
S^i_{melt}	melting of cloud ice to form cloud water
S^i_{au}	autoconversion of cloud ice to form snow due to aggregation
S_{aud}	autoconversion of cloud ice to form snow due to deposition
S_{agg}	collection of cloud ice by snow (aggregation)
S_{rim}	collection of cloud water by snow (riming)
S_{shed}	collection of cloud water by wet snow to form rain (shedding)
S^i_{cri}	collection of cloud ice by rain to form snow
S^r_{cri}	freezing of rain due to collection of cloud ice to form snow
S^r_{frz}	freezing of rain due heterogeneous nucleation to form snow
S^s_{dep}	deposition growth and sublimation of snow
S^s_{melt}	melting of snow to form rain water

5.6.3 Parameterization of the Conversion Terms

The parameterization of the transfer rates proceeds in a similar way as has been outlined in Section 5.5.3 for the one-category ice scheme. That is, the rate equations are obtained by integration of individual particle growth rates over the spectral distribution whenever possible.

Given the size distribution functions (5.92) and the fall velocities (5.93), we have – according to (5.58) – the following relations for the slope parameters λ and the mixing ratios

$$\begin{aligned} \rho\, q^r &= A_r\, \lambda_r^{-4}\,, \qquad A_r = \rho_w \pi N_0^r\,, \\ \rho\, q^s &= A_s\, \lambda_s^{-3}\,, \qquad A_s = 2 a_m^s N_0^s\,, \end{aligned} \tag{5.96}$$

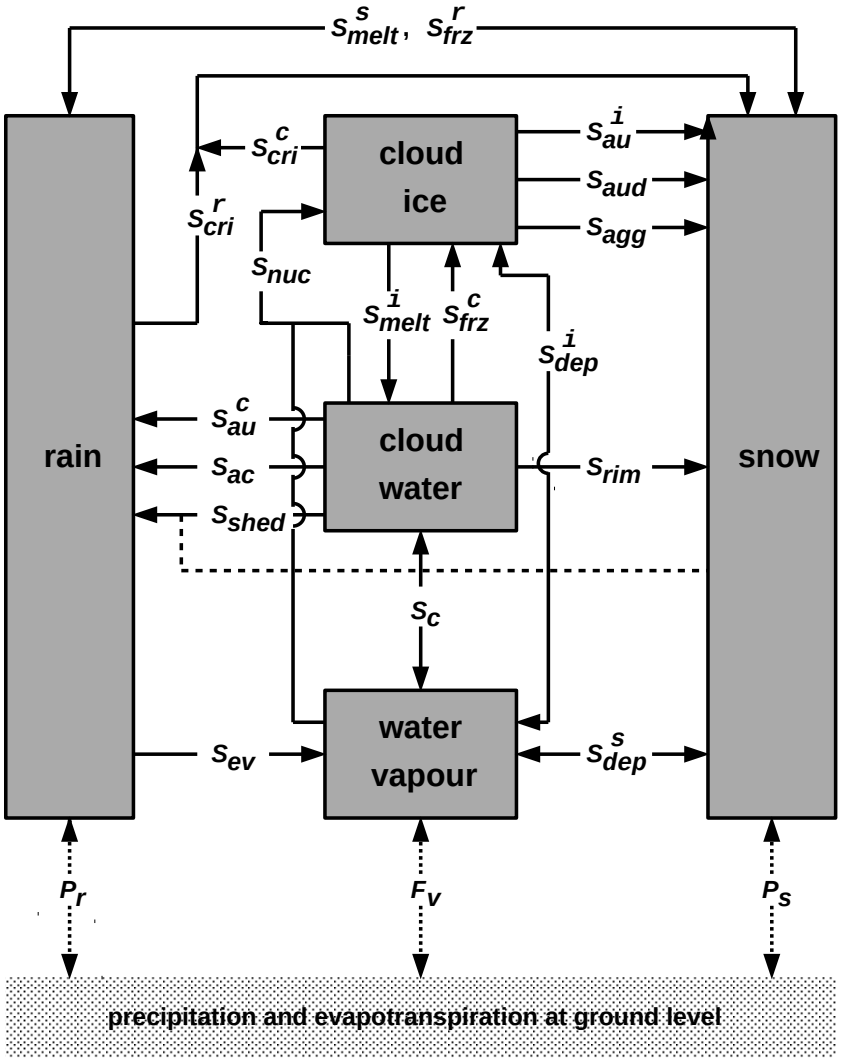

Figure 5.2: *Cloud microphysical processes considered in the two-category ice scheme*

for the slope parameters and the precipitation fluxes of rain and snow:

$$\begin{aligned} P_r &= B_r\,\lambda_r^{-4.5}\,, \qquad B_r = \rho_w \pi N_0^r v_0^r\,\Gamma(4.5)/\Gamma(4)\,, \\ P_s &= B_s\,\lambda_s^{-3.25}\,, \qquad B_s = N_0^s v_0^s a_m^s\,\Gamma(3.25)\,, \end{aligned} \tag{5.97}$$

and for the slope paramters and the terminal fall velocities

$$v_T^r = A_r^{-1} B_r\,\lambda_r^{-1/2}\,, \qquad v_T^s = A_s^{-1} B_s\,\lambda_s^{-1/4}\,. \tag{5.98}$$

A_r, B_r, A_s and B_s are constant parameters that have been introduced for convenience and Γ is the Gamma-function. The free parameters λ_r and λ_s of the size distribution function can thus be determined as unique functions of the mass fractions or the precipitation fluxes which in turn are related by

$$\rho\, q^r = A_r B_r^{-\frac{8}{9}} P_r^{\frac{8}{9}}\,, \qquad \rho\, q^s = A_s B_s^{-\frac{12}{13}} P_s^{\frac{12}{13}}\,. \tag{5.99}$$

In the prognostic version of the scheme, we use the mass fractions q^r and q^s as the dependent model variables. (5.99) can be used to recalculate the microphysical conversion rates

described below in terms of the precipitation fluxes P_r and P_s, which are the dependent variables in the diagnostic version of the scheme (see Section 5.6.4). Using (5.96) and (5.98), the terminal fall velocities are formulated directly in terms of q^r and q^s:

$$v_T^r \;=\; c_T^r(\rho\, q^r)^{\frac{1}{8}}\,, \qquad v_T^s \;=\; c_T^s(\rho\, q^s)^{\frac{1}{12}}\,. \tag{5.100}$$

The coefficients are defined by $c_T^r = A_r^{-\frac{9}{8}} B_r$ and $c_T^s = A_s^{-\frac{13}{12}} B_s$. With the parameters for the size distribution and the particle fall velocities from (5.92) and (5.93), we have the numerical values $c_T^r = 12.63$ and $c_T^s = 2.49$ (in corresponding SI-units). The relations (5.100) are required in the numerical solution of the set (5.94) for the hydrolocical cycle in prognostic mode using the sedimentation algorithm described in Section 5.2.4.

The transfer rate S_c of cloud water condensation and evaporation is obtained by saturation adjustment. Cloud ice being formed by nucleation in a supercooled water saturated environment will thus grow quickly by deposition due to the corresponding high ice supersaturation. The formulation of ice nucleation and depositional growth of cloud ice as well as the other transfer rates is described below.

(a) Nucleation and depositional growth of cloud ice

Recent field experiments show that ice nucleation is not likely to occur in regions of the atmosphere which are subsaturated with respect to water. In the present version of the scheme we thus require water saturation for the onset of cloud ice formation above a temperature threshold of $T_d = 248.15\,\mathrm{K}$. For temperatures below that threshold, deposition nucleation may occur for ice supersaturation.

To formulate heterogeneous nucleation, we simply assume that the number of ice forming nuclei activated within a time step Δt is given by Eq. (5.89). In this way, the various nucleation mechanisms are not distinguished. We will also neglect nucleation whenever ice is already present since this has been found to be of minor importance. Assuming that a small initial crystal m_i^0 is formed within a nucleation time step, the rate of cloud ice formation due to heterogeneous nucleation reads

$$S_{nuc} \;=\; \begin{cases} \dfrac{1}{\rho}\dfrac{m_i^0}{\Delta t}\, N_i(T) & \text{if } T < T_d\,,\; q^i = 0 \text{ and } q^v \geq q_{si}^v\,, \\ \dfrac{1}{\rho}\dfrac{m_i^0}{\Delta t}\, N_i(T) & \text{if } T_d \leq T \leq T_{nuc}\,,\; q^i = 0 \text{ and } q^v \geq q_{sw}^v\,, \\ 0 & \text{else}\,. \end{cases} \tag{5.101}$$

T_{nuc} is a nucleation threshold temperature which is set to 267.15 K. We use $m_i^0 = 10^{-12}$ kg for the initial mass of the cloud ice crystals.

Cloud ice may also be nucleated by homogeneous freezing of supercooled cloud droplets. It is simply assumed that all cloud water freezes instantaneously whenever the temperature falls below a threshold temperature T_{hn} which is set to 236.15 K. The rate of homogeneous nucleation of cloud ice due to freezing of droplets is then

$$S_{frz}^c \;=\; \begin{cases} q^c/\Delta t & \text{if } T < T_{hn} \text{ and } q^c > 0\,, \\ 0 & \text{else}\;. \end{cases} \tag{5.102}$$

Once being formed, the pristine crystals will grow by vapour deposition. The formulation of this non-equilibrium process is based on the growth equation

$$(\dot{m}_i)_{dep} \;=\; 4\, D_i\, G_i\, d_v\, \rho\, (q^v - q_{si}^v) \tag{5.103}$$

of the mass m_i of a cloud ice crystal with diameter D_i. d_v is the molecular diffusion coefficient for water vapour, q^v_{si} is the saturation specific humidity over ice and $G_i = 1/(1+H_i)$ where H_i is the Howell factor defined in (5.71). Using the mass-size relation (5.90) the total deposition rate of all crystals, $S^i_{dep} = N_i \dot{m}_i/\rho$, may then be written as

$$S^i_{dep} \;=\; c^i_{dep} N_i \, m_i^{1/3} \, (q^v - q^v_{si}) \qquad \text{if } q^v > q^v_{si} \tag{5.104}$$

with $c^i_{dep} = 4 G_i d_v a_m^{-1/3}$. The Howell factor varies relatively slowly with temperature and pressure. To simplify the scheme, we use a representative value and set the rate coefficient c^i_{dep} to a constant value of $c^i_{dep} = 1.3 \cdot 10^{-5}$ (in corresponding SI-units). The number density N_i of cloud ice crystals is prescribed by Eq. (5.89) as function of temperature and the crystal mass m_i is diagnosed from q^i and N_i. For temperatures close to the melting point the crystal sizes can become very large due to the small number density. To avoid this, we limit the crystal mass by a maximum value m_i^{max}, i.e.

$$m_i \;=\; \min(\rho q^i / N_i \, , m_i^{max}) \, , \tag{5.105}$$

where m_i^{max} is set to 10^{-9} kg. This value corresponds to a maximum crystal diameter of $D_i^{max} \simeq 200\,\mu$m.

For cloud ice sublimation at ice subsaturation, we do not apply (5.104), but

$$S^i_{dep} = \max\{-q^i/\Delta t \, , \, (q^v - q^v_{si})/\Delta t\} \qquad \text{if } q^v < q^v_{si} \, . \tag{5.106}$$

(b) Autoconversion processes

The rate of autoconversion from cloud water to rain due to cloud droplet collection (S^c_{au}) and of autoconversion of cloud ice to snow due to cloud ice crystal aggregation (S^i_{au}) is parameterized by the simple relations

$$\begin{aligned} S^c_{au} &= \max\{c^c_{au} \, (q^c - q^c_0) \, , \, 0 \} \, , \\ S^i_{au} &= \max\{c^i_{au} \, (q^i - q^i_0) \, , \, 0 \} \, . \end{aligned} \tag{5.107}$$

Currently we do not use any autoconversion threshold values ($q^c_0 = q^i_0 = 0$). The rate coefficients are set to $c^c_{au} = 4 \cdot 10^{-4}\,\mathrm{s}^{-1}$ for cloud water and $c^i_{au} = 10^{-3}\,\mathrm{s}^{-1}$ for cloud ice.

Besides autoconversion due to cloud ice aggregation, snow may also be formed initially due to fast depositional growth of small crystals. The parameterization of this process is based on the time-scale τ_s for cloud ice particles with mass m_i to grow to snow crystal size with an initial mass m^0_s. Integration of the mass growth equation (5.103) in the form $dm_i = \alpha m^{1/3} dt$ yields the time-scale

$$\tau_s = \frac{3}{2\alpha} \left\{ (m^0_s)^{2/3} - (m_i)^{2/3} \right\} \, .$$

The rate of autoconversion S^d_{au} due to depositional growth of cloud ice is then assumed to be given by $S^d_{au} = q^i/\tau_s$ and we end up with

$$S^d_{au} \;=\; \frac{S^i_{dep}}{1.5 \left\{ (m^0_s/m_i)^{2/3} - 1 \right\}} \, . \tag{5.108}$$

The initial mass m^0_s of snow crystals is set to $m^0_s = 3.0 \cdot 10^{-9}$ kg which corresponds to a particle diameter of $D^0_s \simeq 300\,\mu$m. For $m_i = m_i^{max}$, about 65% of the cloud ice deposition rate is available for snow formation due to depositional growth.

(c) Collection mechanisms

The further mass increase of the precipitating water categories rain and snow due to collection of cloud water and cloud ice is formulated by using the continuous model for particle growth. Accretion, riming and shedding are based on the mass growth equations (5.67) and a corresponding equation is used for aggregation, i.e. the collection of cloud ice by snow particles. Performing the integration over the particle spectra according to (5.64) yields the following parameterized rate equations:

$$S_{ac} = c_{ac} q^c (\rho q^r)^{7/8} , \tag{5.109}$$

$$S_{rim} = \begin{cases} c_{rim}\, q^c (\rho q^s)^{\frac{13}{12}} & \text{if } T < T_0 , \\ 0 & \text{if } T \geq T_0 , \end{cases} \tag{5.110}$$

$$S_{shed} = \begin{cases} 0 & \text{if } T < T_0 , \\ c_{rim}\, q^c (\rho q^s)^{\frac{13}{12}} & \text{if } T \geq T_0 . \end{cases} \tag{5.111}$$

$$S_{agg} = c_{agg}\, q^i (\rho q^s)^{\frac{13}{12}} \tag{5.112}$$

In these relations, the rate coefficients are defined by

$$\begin{aligned} c_{ac} &= \frac{15}{32}\sqrt{\pi}\frac{\overline{E}_r}{\rho_w} v_0^r {A_r}^{1/8} , \\ c_{rim} &= \frac{\pi}{4}\,\bar{E}_{cs} N_0^s v_0^s \Gamma(3.25) {A_s}^{-\frac{13}{12}} , \\ c_{agg} &= \frac{\pi}{4}\,\bar{E}_{is} N_0^s v_0^s \Gamma(3.25) {A_s}^{-\frac{13}{12}} . \end{aligned} \tag{5.113}$$

The mean collection efficiency for raindrops collecting cloud droplets is set to $\bar{E}_{cr} = 0.8$, for snow crystals collecting cloud droplets to $\bar{E}_{cs} = 0.9$ and for snow crystals collecting cloud ice particles to $\bar{E}_{is} = 0.5$. By inserting the other parameters from Section 5.6.1 we obtain the values $c_{ac} = 1.72$, $c_{rim} = 46.4$ and $c_{agg} = 25.8$ for the rate coefficients in corresponding SI-units.

Supercooled raindrops may also collide with cloud ice crystals. This will result in an instantaneous freezing of the drops which then are interpreted as snow particles. Two transfer rates have to be considered in this case: first the decrease in cloud ice mass due to the collision/coalescence interaction with raindrops ($-S^i_{cri}$) and second the decrease in rainwater due to freezing as a result from the collection of ice crystals ($-S^r_{cri}$). The sum of both transfer rates, $S^i_{cri} + S^r_{cri}$, forms the corresponding source term for snow.

The parameterization of these transfer rates is based on the collection integrals

$$\begin{aligned} S^i_{cri} &= -\left(\frac{\partial q^i}{\partial t}\right)_{cri} = \frac{\pi}{4}\,\bar{E}_{ir} q^i \int_0^\infty D^2 v_T^r(D) f_r(D) dD , \\ S^r_{cri} &= -\left(\frac{\partial q^r}{\partial t}\right)_{cri} = \frac{\pi N_i}{4\rho}\,\bar{E}_{ir} \frac{\pi \rho_w}{6} \int_0^\infty D^5 v_T^r(D) f_r(D) dD , \end{aligned}$$

where we have assumed that the diameter of cloud ice crystals is much smaller than the diameter of raindrops (which is not necessarily the case). $\bar{E}_{ir}$ denotes the collection efficiency of raindrops collecting small ice particles. Evaluating these integrals yields the transfer rates in the form

$$S^i_{cri} = c^i_{cri}\, q^i\, (\rho q^r)^{7/8} , \tag{5.114}$$

$$S^r_{cri} = c^r_{cri}\, (m_i)^{-1} q^i\, (\rho q^r)^{13/8} . \tag{5.115}$$

The rate coefficients c^i_{cri} and c^r_{cri} are given by

$$c^i_{cri} \;=\; \frac{15}{32}\sqrt{\pi}\frac{\bar{E}_{ir}}{\rho_w}v_0^r {A_r}^{1/8}\,, \qquad c^r_{cri} \;=\; \frac{\pi}{24}\bar{E}_{ir}v_0^r\Gamma(6.5){A_r}^{-5/8}\,. \tag{5.116}$$

We set the mean collection efficiency to $\bar{E}_{ir} = 0.8$ and obtain the numerical values $c^i_{cri} = 1.72$ and $c^r_{cri} = 1.24 \cdot 10^{-3}$ for the rate coefficients in corresponding SI-units.

(d) Diffusional growth of rain and snow

The parameterization of the transfer rates for rain and snow due to vapour diffusion, i.e evaporation of rain and deposition/sublimation of snow, is based on the mass growth equations (5.70) from Section 5.5 and uses also the formulation (5.71) for the ventilation factors. The only difference is that we integrate over the size distribution (5.92) for snow, which is formulated with respect to the linear dimension of the crystals, and that we approximate the temperature dependent Howell factors by characteristic constant values. The parametric transfer rates are obtained as

$$S_{ev} \;=\; \alpha_{ev}\left(1+\beta_{ev}(\rho q^r)^{3/16}\right)(q^v_{sw}-q^v)\,(\rho q^r)^{1/2}\,, \tag{5.117}$$

$$S^s_{dep} \;=\; c^s_{dep}\left(1+b^s_{dep}(\rho q^s)^{5/24}\right)(q^v-q^v_{si})\,(\rho q^s)^{2/3}\,, \tag{5.118}$$

The coefficients for evaporation of rain read

$$\alpha_{ev} \;=\; \frac{2\pi d_v}{1+H_w}N_0^r(A_r)^{-1/2}\,, \quad \beta_{ev} \;=\; 0.26\left(\frac{\rho v_0^r}{2\eta_a}\right)^{1/2}\Gamma(2.75)(A_r)^{-3/16}\,, \tag{5.119}$$

and the corresponding coefficients for deposition/sublimation of snow are:

$$c^s_{dep} \;=, \frac{4d_v}{1+H_i}N_0^s {A_s}^{-2/3}\,, \quad b^s_{dep} \;=\; 0.26\left(\frac{\rho v_0^s}{2\eta_a}\right)^{1/2}\Gamma(21/8)A_s^{-5/24}\,, \tag{5.120}$$

where we use the numerical values $\alpha_{ev} = 3.1{\cdot}10^{-3}$, $\beta_{ev} = 9.0$, $c^s_{dep} = 3.2{\cdot}10^{-2}$ and $b^s_{dep} = 14.7$ (in corresponding SI-units) for the rate coefficients.

(e) Melting and freezing

Cloud ice particles are assumed to melt instantaneously when the ambient temperature rises above 0°C. All cloud ice present will be completely transformed to cloud water within a time step Δt and the conversion rate is simply

$$S^i_{melt} \;=\; \begin{cases} q^i/\Delta t & \text{if } T > T_0 \text{ and } q^i > 0\,, \\ 0 & \text{else}\,. \end{cases} \tag{5.121}$$

The parameterization of the melting rate of snow is based on the stationary heat budget of a snow particle. It is assumed that the release of latent heat from melting as well as from condensation/evaporation is balanced by the heat flux between the particle and the ambient air. The change in mass of a melting particle is then given by (if $T > T_0$)

$$(-\dot{m})_{melt} \;=\; \frac{4D_sF^s_v(D_s)}{L_F}\left\{\, l_h(T-T_0) + L_V d_v\rho(q^v - q^v_{sw}(T_0))\,\right\}\,. \tag{5.122}$$

By interpreting the water mass formed by melting as the source term for rain and integrating Eq. (5.122) over the size distribution of snow particles, we obtain the transfer rate due to melting as

$$S^s_{melt} \;=\; c^s_{melt}\left(1 + b^s_{melt}(\rho q^s)^{5/24}\right)\left\{\,(T - T_0) + a^s_{melt}(q^v - q^v_{sw}(T_0))\,\right\}\,(\rho q^s)^{2/3}\,. \qquad (5.123)$$

The rate coefficients are given by

$$c^s_{melt} \;=\; \frac{4 l_h}{\rho L_F} N_0^s {A_s}^{-2/3}\,, \quad b^s_{melt} \;=\; b^s_{dep}\,, \quad a^s_{melt} \;=\; \frac{\rho L_V d_v}{l_h}\,, \qquad (5.124)$$

and are set to the constant numerical values $c^s_{melt} = 1.48 \cdot 10^{-4}$, $b^s_{melt} = 14.37$ and $a^s_{melt} = 2.31 \cdot 10^3$ (in corresponding SI units).

Besides freezing due to collection of cloud ice crystals, supercooled raindrops may also freeze due to immersion and contact nucleation. The parameterization is based on the rate equations derived in the one-category ice scheme, i.e.

$$S^r_{frz} \;=\; S^{if}_{frz} \;+\; S^{cf}_{frz}\,, \qquad (5.125)$$

where S^{if}_{frz} denotes the contribution from immersion freezing and S^{cf}_{frz} is the contribution from contact nucleation. These transfer rates are formulated by Eqs. (5.80) and (5.83) but for computational efficiency we combine these two contributions in a single rate equation according to

$$S^r_{frz} \;=\; c^r_{frz}(\max(T^r_{frz} - T,\, 0))^{3/2}(\rho q^r)^{27/16}\,, \qquad (5.126)$$

which gives a reasonable approximation to Eq. (5.125) over relevant temperature ranges. The rate coefficient is set to $c^r_{frz} = 1.68$ (in corresponding SI-units) and a threshold temperature $T^r_{frz} = 271.15$ K for heterogeneous freezing of raindrops is used.

Because cloud microphysics involves small time scales, all cloud water or all cloud ice being available at a given timelevel can become depleted by a single microphysical process (e.g. riming) within one timestep, especially when Δt is relatively large. In order to allow all processes to act simultaneously, we use a quasi-implicit formulation to calculate the sink terms for both cloud water and cloud ice.

5.6.4 Diagnostic Version

In the diagnostic version of the cloud-ice scheme, the prognostic equations for q^r and q^s in (5.94) are replaced by the column-equilibrium relations (5.10) for the corresponding precipitation fluxes P_r and P_s:

$$\frac{g}{\sqrt{\gamma}}\frac{\rho_0}{\rho}\frac{\partial P_r}{\partial \zeta} \;=\; S^r\,, \qquad \frac{g}{\sqrt{\gamma}}\frac{\rho_0}{\rho}\frac{\partial P_s}{\partial \zeta} \;=\; S^s\,.$$

The discretization and integration of these diagnostic budget equations for P_r and P_s has been described in Section 5.2.2. The budget equation for cloud ice is integrated by the two time-level Lin and Rood scheme (cf. Part I, Section 4.1) In order to combine this scheme where the integration is from time level n to $n+1$, with the Leapfrog scheme where the integration steps are from $n-1$ to $n+1$, the microphysical source and sink terms described above have to be evaluated at time level $n+1$, i.e. after a dynamical time step.

For the diagnostic version, the microphysical conversion rates S are formulated with P_r and P_s as the dependent model variables. They read:

$$
\begin{aligned}
S_{ac} &= c_{ac}\, q^c\, P_r^{\frac{7}{9}} \\
S_{rim} &= \begin{cases} c_{rim}\, q^c\, P_s & \text{if } T < T_0\,, \\ 0 & \text{if } T \geq T_0\,, \end{cases} \\
S_{shed} &= \begin{cases} 0 & \text{if } T < T_0\,, \\ c_{rim}\, q^c\, P_s & \text{if } T \geq T_0\,, \end{cases} \\
S_{agg} &= c_{agg}\, q^i\, P_s \\
S^i_{cri} &= c^i_{cri}\, q^i\, P_r^{7/9} \\
S^r_{cri} &= c^r_{cri}\, (m_i)^{-1} q^i\, P_r^{13/9} \\
S_{ev} &= \alpha_{ev} \left(1 + b_{ev} P_r^{1/6}\right) (q^v_{sw} - q^v)\, P_r^{4/9} \\
S^s_{dep} &= c^s_{dep} \left(1 + b^s_{dep} P_s^{5/26}\right) (q^v - q^v_{si})\, P_s^{8/13} \\
S^s_{melt} &= c^s_{melt} \left(1 + b^s_{melt} P_s^{5/26}\right) \{\, (T - T_0) + a^s_{melt} (q^v - q^v_{sw}(T_0))\,\}\; P_s^{8/13} \\
S^r_{frz} &= c^r_{frz} (\max(T^r_{frz} - T,\, 0))^{3/2} P_r^{3/2}
\end{aligned}
$$

All other conversion rate are the same as in the prognostic version. The coefficients in the modified source terms above are defined by (using B_r and B_s from (5.99)):

$$
\begin{aligned}
c_{ac} &= \frac{3}{7} \frac{\bar{E}_{cr}}{\rho_w}\, B_r^{2/9} \\
c_{rim} &= \frac{\pi}{4 a^s_m}\, \bar{E}_{cs} \\
c_{agg} &= \frac{\pi}{4 a^s_m}\, \bar{E}_{is} \\
c^i_{cri} &= \frac{3}{7} \frac{\bar{E}_{ir}}{\rho_w}\, B_r^{2/9} \\
c^r_{cri} &= \frac{\pi}{4} \bar{E}_{ir} (5.5 \cdot 4.5)\, B_r^{-4/9} \\
\alpha_{ev} &= \frac{2\pi d_v}{1 + H_w} N^r_0 B_r^{-\frac{4}{9}} \\
\beta_{ev} &= 0.26 \left(\frac{\rho v^r_0}{2\eta_a}\right)^{\frac{1}{2}} \Gamma(2.75) B_r^{-\frac{1}{6}} \\
c^s_{dep} &= \frac{4 d_v}{1 + H_i} N^s_0 B_s{}^{-8/13} && (5.127) \\
b^s_{dep} &= 0.26 \left(\frac{\rho v^s_0}{2\eta_a}\right)^{1/2} \Gamma(21/8) B_s^{-5/26} && (5.128) \\
c^s_{melt} &= \frac{4 l_h}{\rho L_F} N^s_0 B_s{}^{-8/13} && (5.129) \\
b^s_{melt} &= b^s_{dep} && (5.130) \\
a^s_{melt} &= \frac{\rho L_V d_v}{l_h} && (5.131)
\end{aligned}
$$

In contrast to the the one category ice scheme, temperature dependencies in the coefficients are neglected at present. The coefficients are approximated by the following constant values

(in corresponding SI units): $c_{ac} = 0.24$, $c_{rim} = 18.6$, $c_{agg} = 10.3$, $c^i_{cri} = 0.24$, $c^r_{cri} = 3.2 \cdot 10^{-5}$, $\alpha_{ev} = 1.0 \cdot 10^{-3}$, $\beta_{ev} = 5.9$, $c^s_{dep} = 1.8 \cdot 10^{-2}$, $b^s_{dep} = 12.3$, $c^s_{melt} = 8.43 \cdot 10^{-5}$, $b^s_{melt} = 12.05$, $a^s_{melt} = 2.31 \cdot 10^3$ and $c^r_{frz} = 3.75 \cdot 10^{-2}$.

5.7 A Three Category Ice Scheme

to be completed

Section 6

Parameterization of Moist Convection

6.1 General Aspects

Cumulus convection has a major impact on the vertical structure of the temperature and moisture fields of the atmosphere. However, convective processes operate on horizontal scales which are much smaller than those resolved by large-scale and mesoscale NWP-models. Thus, the only way to represent the overall effect of moist convection in these type of models is by means of parameterization.

Some basic effects of moist convection have to be considered by cumulus parameterization schemes. These are diabatic heating due to the release of latent heat resulting from cloud condensation and from the formation and evaporation of precipitation and the vertical transports of heat, moisture and momentum in cumulus updrafts and downdrafts as well as in the regions with compensating downward motions, which in turn interact with the cumulus clouds by lateral exchange processes (entrainment and detrainment). All these processes tend to stabilize the original thermally unstable stratification. Mesoscale circulations within systems of organized convection, e.g. squall-lines and convective cloud clusters, can also be important for the large-scale heat and moisture budgets. Most parameterization schemes, however, neglect the impact of mesoscale circulations because they are presently not well understood.

Various methods are presently applied for cumulus parameterization in mesoscale NWP models such as Kuo-type, mass flux and adjustment approaches. For each of these basic methods numerous parameterization schemes have been proposed in the literature. This shows both the complexity of the processes to be considered and the uncertainty as to whether moist convection can be correctly represented by means of parameterization.

For applications of LM to the meso-β scale, the mass flux scheme of Tiedtke (1989) has been implemented. We plan to add additional options for other schemes (e.g. Kain and Fritsch (1993)) in the near future.

6.2 The Tiedtke Mass-Flux Scheme

The cumulus parameterization scheme according to Tiedtke (1989) uses a mass-flux approach to represent moist convection in numerical models. The feedback of subgrid-scale vertical fluxes of mass, heat, moisture and momentum in up- and downdrafts is calculated by using a simple bulk cloud model. The basic concept of the scheme is outlined in this section. A more detailed description of the physics and the numerics can be found in Tiedtke (1989) and ECMWF (1991).

6.2.1 Formulation of the Convective Forcing

The prognostic equations for the grid-scale variables are obtained by averaging the microturbulent equations for heat, moisture and momentum over the spatial scales which correspond to the model grid spacing. Neglecting nonhydrostatic effects on the mesoscale as well as changes in the mean vertical velocity, the thermodynamic forcing due to moist convection can be formulated by the following tendencies, which have been denoted by M_ψ^{MC} in the model equations (cf. Part I, (3-143) - (3-150)).

$$\begin{aligned}
c_{pd} M_T^{MC} = \left(\frac{\partial s}{\partial t}\right)_{MC} &= -\frac{1}{\rho}\frac{\partial}{\partial z}\left\{M_u(s_u - s) + M_d(s_d - s)\right\} \\
&\quad + L(c_u - e_d - e_l - e_p) \\
M_{q^v}^{MC} = \left(\frac{\partial q^v}{\partial t}\right)_{MC} &= -\frac{1}{\rho}\frac{\partial}{\partial z}\left\{M_u(q_u^v - q^v) + M_d(q_d^v - q^v)\right\} \\
&\quad - (c_u - e_d - e_l - e_p) \\
M_\alpha^{MC} = \left(\frac{\partial \alpha}{\partial t}\right)_{MC} &= -\frac{1}{\rho}\frac{\partial}{\partial z}\left\{M_u(\alpha_u - \alpha) + M_d(\alpha_d - \alpha)\right\}
\end{aligned} \tag{6.1}$$

In (6.1), $s = c_{pd}T + gz$ is the dry static energy, α denotes the horizontal wind components (u or v) and the subscripts u and d indicate variables within the updrafts and the downdrafts, respectively. The horizontal area for averaging has been assumed to be large enough to contain an ensemble of cumulus clouds. However, the convective-scale eddy transports of dry static energy, moisture and momentum from cumulus updrafts, downdrafts and the cumulus-induced subsidence in the environmental air are not described in terms of contributions from the individual ensemble components, but are represented by their average values using a one-dimensional bulk cloud model after Yanai et al. (1973). This approximates the net effects of an ensemble of clouds as resulting from a representative single cloud.

Additionally, it is assumed that the area fraction of updrafts and downdrafts is very small such that the values of the variables in the environment can be approximated by the area mean values. The following symbols are used in (6.1):

M_u	updraft mass flux, defined by $M_u = \rho a_u(w_u - w)$
a_u	area fraction of the updraft
w_u	vertical velocity in the updraft
M_d	downdraft mass flux, defined by $M_d = \rho a_d(w_d - w)$
a_d	area fraction of the downdraft

w_d	vertical velocity in the downdraft
s_u, s_d	dry static energy within the up- and downdraft, resp.
q_u, q_d	specific humidity within the up- and downdraft, resp.
α_u, α_d	horizontal wind components in the up- and downdraft, resp.
c_u	condensation in the updraft (area mean)
e_d	evaporation of precipitation in the downdraft (area mean)
e_l	evaporation of cloud water in the environment (area mean)
e_p	evaporation of precipitation below cloud base (area mean)
L	latent heat with $L = L_V$ (heat of evaporation) for $T \geq 0°$C and $L = L_S$ (heat of sublimation) for $T < 0°$ C

Column equilibrium is supposed for rain water formed in convective clouds. The budget equation for the area mean value of the flux of convective precipitation (denoted by P) then reads

$$\frac{\partial P}{\partial z} = -\rho\,(g_p - e_d - e_p)\,, \tag{6.2}$$

where g_p denotes the conversion rate of cloud water to form rain. The precipitation rate at the surface results from vertical integration of Eq. (6.2).

6.2.2 The Cloud Model

A simple one-dimensional cloud model is used to compute the convective tendencies in Eq. (6.1). The updraft of the cloud ensemble is assumed to be in steady state. The budget equations for mass, heat, moisture and momentum for the ascending air are

$$\begin{aligned}
\frac{\partial M_u}{\partial z} &= E_u - D_u \\
\frac{\partial}{\partial z}(M_u s_u) &= E_u s - D_u s_u + L\rho c_u \\
\frac{\partial}{\partial z}(M_u q_u^v) &= E_u q^v - D_u q_u^v - \rho c_u \\
\frac{\partial}{\partial z}(M_u q_u^c) &= -D_u q_u^c + \rho(c_u - g_p) \\
\frac{\partial}{\partial z}(M_u \alpha_u) &= E_u \alpha - D_u \alpha_u\,,
\end{aligned} \tag{6.3}$$

where q_u^c is the cloud water content in the updrafts. A similar system of equations is applied to calculate the variables within the downdraft of the cloud ensemble. The downdraft region is assumed to be at saturation (being maintained at saturation by evaporation of rainwater) and to contain no cloud water:

$$\begin{aligned}
\frac{\partial M_d}{\partial z} &= E_d - D_d \\
\frac{\partial}{\partial z}(M_d s_d) &= E_d s - D_d s_d - L\rho e_d \\
\frac{\partial}{\partial z}(M_d q_d^v) &= E_d q^v - D_d q_d^v + \rho e_d \\
\frac{\partial}{\partial z}(M_d \alpha_d) &= E_d \alpha - D_d \alpha_d\,.
\end{aligned} \tag{6.4}$$

The vertical integration of (6.3) from cloud base to cloud top and of (6.4) from the top of the downdrafts to the surface yields the values of the variables within the updraft and the downdraft, respectively, which can then be used to calculate the convective tendencies. To perform the integration, we have to specify

- the mass flux M_u and the values of the variables s_u, q_u^v, q_u^c and α_u at the cloud base as lower boundary conditions,
- the mass flux M_d and the values of the variables s_d, q_d^v and α_d at the top of the downdrafts as upper boundary condition,
- the entrainment rates E_u and E_d and the detrainment rates D_u and D_d of the up- and downdrafts, respectively, as functions of the available grid-scale model parameters and
- a parameterization of the microphysical processes.

All assumptions made in this context can be generally regarded as closure conditions. However, only those assumptions which connect the intensity of cumulus convection directly to the grid-scale forcing are usually referred to as closure conditions. These conditions are related to the first three points above and are discussed in the Section 6.2.3. The parameterization of microphysical processes is specific to the cloud model (and thus a parameterization within a parameterization) and briefly summarized below.

(a) Condensation/deposition within the updraft
The calculation of the condensation rate of water vapour in the ascending updraft air is based on saturation adjustment. Whenever supersaturation occurs, the specific humidity q_u^v is set back to the saturation value and the difference is interpreted as the condensed cloud water. The release of latent heat is taken into account by this procedure (see Section 5.3). At temperatures below the freezing point, saturation over ice is assumed to diagnose the deposition rate.

(b) Evaporation of precipitation within the downdraft
The computation of e_d is also based on the saturation adjustment technique. Downdrafts are assumed to be at saturation which is maintained by evaporation of rainwater. The associated evaporative cooling is taken into account in the heat equation.

(c) Formation of precipitation within the updraft
A simple parameterization is used to estimate the conversion of cloud droplets to raindrops. The rate of formation of convective precipitation is set to

$$g_p \;=\; K_p(z)\, q_u^c\,, \tag{6.5}$$

depending linearly on the updraft cloud water content and a height dependent conversion function K_p. The growth of rainwater due to collection (i.e. the accretion process) is not taken into account explicitly. The conversion function is chosen to be of the form

$$K_p(z) \;=\; \begin{cases} 0 & \text{if } z \le z_b + \Delta z_c, \\ \beta_p & \text{if } z > z_b + \Delta z_c. \end{cases} \tag{6.6}$$

This functional form suppresses the formation of precipitation in a region Δz_c above cloud base at height z_b. In LM the parameters in (6.6) are set to $\beta_p = 2.0 \cdot 10^{-3}$ s^{-1}, $\Delta z_c = 1500$ m over water and $\Delta z_c = 3000$ m over land.

(d) Evaporation of cloud water in the environment
Cloud water which has been detrained into the subsaturated environment is assumed to evaporate immediately. Thus, e_l is set to

$$e_l \;=\; \frac{1}{\rho}\, D_u\, q_u^c\,. \tag{6.7}$$

(e) Evaporation of precipitation below cloud base
The evaporation rate of precipitation is calculated according to Kessler (1969) with slightly modified coefficients. As the evaporation rate depends nonlinearly on the precipitation flux, we have to take into account that convective precipitation covers only a area fraction C_p of a grid cell. Thus, the area mean of the evaporation rate is formulated as

$$e_p \;=\; C_p \alpha_1 \,(q_{sw}^v - q^v)\, \sqrt{\frac{(p/ps)^{1/2}}{\alpha_2}\frac{P}{C_p}}\,, \tag{6.8}$$

where q_{sw}^v is the saturation specific humidity. The constants α_1 and α_2 are set to $\alpha_1 = 5.0{\cdot}10^{-4}$ and $\alpha_2 = 0.011$. The correction factor $(p/ps)^{1/2}$ considers approximately the impact of air density on the fall velocity of the particles. In the original version of the scheme the area fraction C_p of a grid cell covered with convective precipitation was set to a constant value of 0.05. For LM, we let C_p depend on the mesh size Δs by using the heuristic relation

$$C_p \;=\; \min(1.0, \sqrt{\Delta s_0/\Delta s})\,. \tag{6.9}$$

Δs_0 is a limiting horizontal scale which is set to 4 km.

6.2.3 Closure Assumptions

The Tiedtke mass-flux scheme discriminates three types of convection,

- *penetrative convection,*
- *shallow convection and*
- *midlevel convection,*

which are treated by different closure hypotheses. Only one type of convection may be present at a grid point at a time. Thus, layered convection (i.e. midlevel convection above a layer of shallow convection) can not be described by the scheme.

Both shallow and penetrative convection have their roots in the atmospheric boundary layer. They differ, however, in vertical extend, which is predefined by the vertical extend of the unstable thermal stratification where convection is formed. Penetrative convection often occurs in regions with large-scale convergence in the lower troposphere, while shallow convective clouds can also be formed in case of slightly divergent flow. The latter are often driven by evaporation from the ground or water surface.

Midlevel convection, on the other hand, has its roots not in the boundary layer but originates at levels within the free atmosphere. Convective cells of this type often occur in rainbands

at warm fronts or in the warm sector of extratropical cyclones. They are probably formed by dynamically forced lifting of low-level air until it becomes saturated at the level of free convection. Often a low-level temperature inversion exists which inhibits convection to be initiated freely from the surface layer.

Depending on the presence of a specific type of convection, the following closure hypotheses are applied.

(a) Updraft mass flux at cloud base

In case of shallow or penetrative convection, an equilibrium type of closure is applied by imposing a moisture balance for the subcloud layer such that the vertically integrated specific humidity is maintained in the presence of grid-scale, turbulent and convective transports (Kuo-type closure). Using the source term $M_{q^v}^{MC}$ from (6.1) in the budget equation for the specific humidity q_v, this balance may be formulated by

$$\{M_u(q_u^v - q^v) + M_d(q_d^v - q^v)\}_{z_b} \;=\; -\int_{z_s}^{z_b} \left(\rho \mathbf{v}\cdot\nabla q^v + \frac{\partial F^{q^v}}{\partial z}\right) dz\,, \tag{6.10}$$

where z_s is terrain height, z_b is the height of the cloud base and F^{q^v} is the vertical turbulent flux of specific humidity. Convection will only occur when the right hand side of Eq. (6.10) is positive, i.e. when moisture convergence tends to increase the subcloud moisture content.

In case of penetrative convection it is supposed that the advective forcing is the major contribution to the moisture convergence. The closure condition (6.10) is well justified over the tropical oceans where the boundary layer moisture content usually changed little with time during convective activity, but little is known on how well it holds for other areas. The quasi- steady moisture balance condition is also applied for shallow convection. The difference is that the moisture supply to cumulus clouds is now largely through vertical turbulent transports driven by surface evaporation whereas the contribution of grid-scale advective transports are either small or even negative.

In case of midlevel convection the updraft mass flux at cloud base is simply set equal to the grid-scale vertical mass transport,

$$(M_u)_{z_b} \;=\; (\rho w)_{z_b}\,. \tag{6.11}$$

This implies that the amount of moisture which is vertically advected through cloud base is made fully available for the formation of convective cells.

(b) Downdraft mass flux at the level of free sinking

Precipitation from deep convective cells is usually associated with downdrafts initiated due to water loading and evaporative cooling during the life cycle of the clouds. In the parameterization scheme downdrafts are considered to originate from cloud air influenced by the mixing with environmental air at the level of free sinking (LFS). The LFS is assumed to be the highest model level where a mixture of equal parts of cloud air and saturated environmental air at wet-bulb temperature becomes negative buoyant with respect to the environment. This procedure defines also the boundary values for s_d, q_d^v and α_d at the top of the downdrafts. The downdraft mass flux at z_{LFS}, the height of the level of free sinking, is assumed to be directly proportional to the updraft mass flux at cloud base. That is,

$$(M_d)_{z_{LFS}} \;=\; \gamma_d\,(M_u)_{z_b}\,. \tag{6.12}$$

The coefficient γ_d is a disposable parameter which determines the intensity of the downdrafts. In the present model version γ_d is set to a constant value of 0.3.

(c) Specification of entrainment and detrainment

Lateral transports across cloud boundaries is represented by entrainment and detrainment. For the updraft, entrainment is assumed to occur via turbulent exchange of mass (turbulent entrainment E_u^T) and through organized inflow associated with large-scale convergence (dynamic entrainment E_u^D). Detrainment form the updraft is supposed to be made up of contributions from turbulent mixing (turbulent Detrainment D_u^T) and from organized outflow at cloud top (dynamic detrainment D_u^D). For the downdraft, only turbulent entrainment and detrainment (E_d^T, D_d^T) is considered:

$$\begin{aligned} E_u &= E_u^T + E_u^D\,, \\ D_u &= D_u^T + D_u^D\,, \\ E_d &= E_d^T\,, \\ D_d &= D_d^T\,. \end{aligned} \tag{6.13}$$

The lateral turbulent mixing terms are parameterized according to

$$\begin{aligned} E_u^T &= \epsilon_u M_u\,, \\ D_u^T &= \delta_u M_u\,, \\ E_d^T &= \epsilon_d |M_d|\,, \\ D_d^T &= \delta_d |M_d|\,, \end{aligned} \tag{6.14}$$

where $\epsilon_u = \delta_u$ and $\epsilon_d = \delta_d$ is assumed for the entrainment/detrainment parameters to ensure that there is no vertical change of the updraft mass flux due to turbulent mixing processes. By default, the fractional entrainment rate is set to $\epsilon_u = 1.0 \cdot 10^{-4} m^{-1}$ for penetrative and midlevel convection. For shallow convection, ϵ_u is set to $\epsilon_u = 3.0 \cdot 10^{-4} m^{-1}$. In case of deep convective clouds, however, turbulent entrainment is only considered at lower cloud levels. For the upper levels ϵ_u is set to zero, assuming that entrainment is very small.

Dynamic entrainment is parameterized on the assumption that organized lateral flow into the cloud is directly proportional to the local grid-scale moisture convergence, i.e.

$$E_u^D = -\frac{\rho}{q^v} \mathbf{v} \cdot \nabla q^v\,. \tag{6.15}$$

Organized entrainment is considered only in the lower part of the convective cloud where large-scale convergence is encountered, i.e. below the level of maximum vertical velocity. For shallow convection, dynamic entrainment is neglected.

Dynamic detrainment usually occurs in the upper regions of cumulus clouds, where the rising air loses its buoyancy relative to the environment resulting in a deceleration of the updraft vertical velocity and a corresponding organized lateral outflow. The parameterization scheme approximates roughly the effect of overshooting cumuli by assuming that only a fraction $(1 - b_u)$ of the updraft mass flux is made available for lateral outflow in the layer k_T that contains the zero-buoyancy level. The remaining fraction b_u is allowed to penetrate into the stable layer above $(k_T - 1)$ and to detrain there:

$$D_u^D = \begin{cases} (1 - b_u)(M_u)_{k+1/2}/\Delta z_k & \text{if } k = k_T, \\ b_u (M_u)_{k+1/2} & \text{if } k = k_T - 1, \\ 0.0 & \text{else.} \end{cases} \tag{6.16}$$

This formulation for dynamic detrainment is applied for all types of convective clouds. b_u is a disposable parameter which is set to 0.33. Because (6.16) is formulated in the computational space (and originally for the relatively coarse vertical resolution of the ECMWF global model), care must be taken when the vertical resolution is increased.

(d) Temperature and humidity parameters at cloud base
In order to integrate the updraft equations (6.3) using the above closure assumptions, the variables T, q^v, q^c and α at cloud base must be specified as lower boundary conditions.

For this, it is first checked whether free convection (shallow or penetrative) can occur at a grid point. At the first model level above the surface ($k = N_\zeta$) an air parcel is defined with the grid-scale values of temperature (plus a small excess value), specific humidity and horizontal momentum. Lifting the parcel adiabatically allows to compute its condensation level at $k = k_B$. This level defines the cloud base, i.e. the level of free convection, if the parcel becomes buoyant with respect to the environment. The parcels values of T, q_v, q_c and α at cloud base $k = N_B$ are then used as boundary conditions to integrate the updraft equations.

When the parcel is non-buoyant at the lifting condensation level, the grid point is checked for the occurrence of mid-level convection. Starting from the model level $k = N_\zeta - 1$, an air parcel with environmental properties is defined and lifted adiabatically for one layer. If the parcel becomes buoyant, this layer is considered to be the cloud base ($k = k_B$) of mid-level convection. Again, the values of the lifted air parcel are used as initial values to integrate vertically the updraft equations. When the parcel is stable at the new level, the next model layer ($k = N_{\zeta-2}$) is checked for convection and so on.

As a further condition for midlevel convection to occur, at $k = k_B$ the grid-scale vertical velocity is required to be positive and the relative humidity must be larger than 90%.

6.2.4 Discretization and Numerical Solution

The flux divergence terms in the tendencies (6.1) for the grid-scale variables and in the cloud equations (6.3) and (6.4) are evaluated at full model levels according to

$$-\frac{1}{\rho}\frac{\partial(M\psi)}{\partial z} = \frac{l}{\rho_k}\frac{M_{k+1/2}\psi_{k+1/2} - M_{k-1/2}\psi_{k-1/2}}{z_{k+1/2} - z_{k-1/2}}, \tag{6.17}$$

where M represents the updraft or the downdraft mass flux and ψ stands for the gridscale variables, the updraft or the downdraft variables. The cloud variables ψ_u and ψ_d are defined at model half levels and (6.17) is used as a simple forward scheme to integrate the updraft and the downdraft equations.

In order to calculate the net upward and downward transports from (6.1), the half-level values of dry static energy and of specific humidity must be specified. Tiedtke (1989) has shown that the definition of grid-scale variables at half levels pose a problem. When half-level values are defined by linear interpolation of full-level values, very noisy profiles may evolve in time, particularly with regard to humidity. Much smoother profiles have been obtained when the half-level values are derived by downward extrapolation from the next full level

above along a saturated descent through that level:

$$\begin{aligned} T_{k+1/2} &= T_k + \left(\frac{\partial T}{\partial z}\right)_{h_k^s} (z_{k+1/2} - z_k) , \\ q^v_{k+1/2} &= q^v_k + \left(\frac{\partial T}{\partial z}\right)_{h_k^s} (z_{k+1/2} - z_k) . \end{aligned} \tag{6.18}$$

Here, $h^s = s + L_V q^v_{sw}$ is the saturation moist static energy. The choice of a moist adiabat for extrapolating is dictated by the conservation properties of moist static energy h. In case of convection in the absence of downdrafts, h is only changed the flux divergence

$$\left(\frac{\partial h}{\partial t}\right)_{MC} = -\frac{1}{\rho}\frac{\partial}{\partial z}\left\{M_u(h_u - h)\right\} . \tag{6.19}$$

As the lines of the saturation moist static energy h^s through point $(z_{k-1/2}, T_{k-1/2})$ and the updraft moist static energy h_u are almost parallel, apart from entrainment/detrainment effects, the difference $h_u - h$ is little affected by vertical discretization.

6.3 The Kain-Fritsch Scheme

to be completed

Section 7

Subgrid-Scale Cloudiness

to be completed

Section 8

Parameterization of Radiative Processes

8.1 General Aspects

Radiative processes control the overall energy balance of the earth-atmosphere system and are the initial cause of diurnal and seasonal variations in the state of the atmosphere and at the earth's surface. The divergence of solar and thermal radiative fluxes in the atmosphere, which interact strongly with the simulated cloud field and its inherent properties, contributes considerably to the diabatic forcing in the prognostic model equations. At the earth's surface radiative fluxes constitute the major forcing for the thermodynamic state of the soil and the interaction with the atmosphere via turbulent fluxes of heat and moisture.

To capture the impact of radiative processes in a NWP model the general complexity of the radiative transfer problem needs to be considered in a simplified, parameterized approach. The radiative transfer equation (RTE) in its original form describes the interaction between directional radiances and the optically active constituents within the earth's atmosphere and at the surface. If the RTE were solved for radiances, fluxes, which are required by the NWP model, could be obtained from the radiances via integration over solid angle. This approach would not be feasible within the computational constraints of NWP and for this reason, based on simplifying assumptions with regard to the directional distribution of radiances the RTE is reformulated in terms of upward and downward fluxes leading to the so-called two-stream methods (see below).

Another simplification that the parameterization of radiative transfer shares with that of other diabatic processes is the assumption of a horizontally homogeneous plane-parallel atmospheric structure within each model grid box. This fundamental assumption allows the reduction of the 3D-problem to the much simpler 1D-case of independent vertical columns, allowing a column-by-column solution to the parameterization problem in grid space. For the solution of the RTE this assumption is relaxed partially by allowing partial cloudiness within each model layer, i. e. the distinction between optical properties of a cloud free part and an adjacent cloudy part. Radiative fluxes may then be computed separately for the cloud free and cloudy regions. It is generally assumed that cloud free and cloudy fluxes interact only between adjacent layers but not within a given model layer. However, one should bear in mind, that radiative transfer in reality is a 3-dimensional process and that the validity of the

1D-approach becomes more than questionable for models with high horizontal resolution.

Due to the non-linear nature of the RTE its solution is strictly valid only for monochromatic radiation, i. e. for infinitesimally small spectral intervals. This implies that in order to minimize computational errors the RTE should be solved for a huge number of small intervals covering the energetically relevant part of the solar and thermal radiative spectrum and the final fluxes would be obtained from a subsequent integration over wavelength. The computational burden of such a brute force approach would be enormous and therefore unacceptable with regard to computational constraints of numerical weather prediction. For this reason the problem is further simplified through the application of rather wide spectral intervals for which the RTE is solved. Even though this so-called wide-band approach is generally used by all NWP applications of radiative transfer schemes one should bear in mind that it creates a potential source of non-negligible errors in the calculation of fluxes and heating rates.

Despite the above mentioned severe simplifications radiative transfer schemes are still computationally expensive parts of the NWP system. In order to keep the computational costs within acceptable limits, the full computation of fluxes including the interaction with optically active constituents in the atmosphere is performed at a reduced temporal frequency compared to the normal model time step. In between full radiative time steps fluxes and heating rates are kept constant or are only adjusted for temporal variations in the solar zenith angle.

The radiative transfer scheme employed in the LM is described in detail in Ritter and Geleyn (1992) (in the following abbreviated as RG92). Beyond the features described in RG92 the current version of the scheme considers optical properties of ice clouds, which are based on data provided by Rockel et al. (1991).

8.2 The RG92 Radiative Transfer Scheme: Spectral Intervals and Optically Active Constituents

The radiative transfer scheme of RG92 is based on the so-called δ-two-stream solution of the radiative transfer equation for plane-parallel horizontally homogeneous atmospheres. The RTE is solved for 3 spectral intervals in the solar part and 5 spectral intervals in the thermal part of the spectrum (cf. Table 8.1).

Table 8.1: Spectral intervals employed by the RG92 radiative transfer scheme

interval no.	solar/thermal	wavelength limits
1	s	1.53-4.64
2	s	0.70-1.53
3	s	0.25-0.70
4	t	20.0-104.5
5	t	12.5-20.0
6	t	8.33-9.01 & 10.31-12.5
7	t	9.01-10.31
8	t	4.64-8.33

The division in solar and thermal spectral intervals allows a computationally more efficient solution of the RTE depending on the need to consider either solar radiation at the top of the atmosphere or thermal emission by optical constituents as sources of radiative fluxes.

Within each model layer the effect of the following optical constituents on the transfer of radiation through that layer is considered:

- cloud water droplets
- cloud ice crystals
- water vapour
- ozone
- carbon dioxide and other minor trace gases
- aerosols

In the solar part of the spectrum Rayleigh scattering by air molecules is considered in addition to the above mentioned constituents. Depending on the characteristics of each constituent and the spectral wave length the interaction with radiative fluxes takes place in the form of scattering, absorption and emission. Scattering and absorption are considered both at solar and thermal wavelengths but emission is only relevant in the thermal part of the spectrum.

8.3 Basic Equations

The reader is referred to RG92 for a detailed description of the employed equations and the underlying assumptions. Here, we will only provide information directly related to the code of the radiation scheme as used by the LM.

For the δ-two-stream solution of the RTE three components of the radiative fluxes, namely the diffuse upward and downward fluxes and the parallel, direct solar flux are considered. Based on the assumption that the atmosphere can be subdivided in layers of constant optical properties as discussed by Geleyn and Hollingsworth (1979), flux components directed outward of any given layer can be written as linear combinations of the corresponding flux components entering the layer. With the introduction of black body differential flux components, i. e. the difference between the black body radiation ΠB and the diffuse flux components F_1 (upward) and F_2 (downward): $\widetilde{F}_{1,j} = \Pi B_j - F_{1,j}$ and $\widetilde{F}_{2,j} = \Pi B_j - F_{2,j}$ we may write a linear equation system for each layer j:

$$\begin{pmatrix} S_{j+1} \\ \widetilde{F}_{2,j+1} \\ \widetilde{F}_{1,j} \end{pmatrix} = \begin{pmatrix} \overline{a}_1 & 0 & 0 \\ \overline{a}_2 & \overline{a}_4 & \overline{a}_5 \\ \overline{a}_3 & \overline{a}_5 & \overline{a}_4 \end{pmatrix} \begin{pmatrix} Q_j \\ \widetilde{F}_{2,j} \\ \widetilde{F}_{1,j+1} \end{pmatrix} \tag{8.1}$$

with

S_{j+1}: parallel solar radiative flux at bottom of layer j and

$$Q_j = \begin{cases} S_j & \text{solar} \\ \Pi(B_{j+1} - B_j) & \text{thermal} \end{cases}$$

The layer transmittance, reflectance and emittance coefficients $\overline{a}_i$ are functions of the optical properties of each layer and described in RG92 and the black body radiation is computed based on the corresponding temperature at the layer boundaries. The solution of the equation system requires approriate boundary conditions. In the solar case, the incoming parallel solar radiation for a given zenith angle μ_0 at the top of the atmosphere forms the upper boundary condition for the direct component and the diffuse downward flux component is zero. In the thermal case, the upper boundary condition consists of the vanishing diffuse downward component only. At the lower boundary the reflectivity of the surface, specified as albedo for parallel and diffuse downward radiation ($A_S(\mu_0)$ and A_s^d) provides the appropriate condition in the solar case, i. e.:

$$\widetilde{F}_{1,N+1} = -F_{1,N+1} = -A_S(\mu_0)\, S_{N+1} - A_S^d\, F_{2,N+1}$$

Here we assume a directional dependance of the surface albedo for parallel radiation, but no directional information is retained after the reflection of the solar beam at the surface.

The lower boundary condition for the thermal case results from the thermal surface albedo $(1 - E_s)$ and emissivity E_s applied to the downward diffuse flux component and the surface black body radiation $\Pi\, B_s$, i. e.:

$\widetilde{F}_{1,N+1} = (1 - E_s)\, \widetilde{F}_{2,N+1}$ respectively

$$F_{1,N+1} = (1 - E_s)\, F_{2,N+1} + E_s\, \Pi\, B_s$$

Once the linear equation system with corresponding coefficients and boundary conditions is established for a given spectral interval, the system is solved by a dedicated Gauss elimination-backsubstitution method, which exploits the sparsity of the coefficient matrix for computational efficiency.

8.4 Partial Cloudiness

Clouds which form the most important optical constituent in the atmosphere may cover part or all of any given model layer depending on the current atmospheric state. Apart from the specification of their optical properties, which take into account cloud phase, i. e. liquid water or ice, the solution of the RTE in the presence of clouds requires information about geometrical properties of the cloud fraction. In the RG92 scheme it is assumed that clouds in adjacent model layers overlap completely, whereas random overlap occurs if clouds in different layers are seperated by at least one cloud-free layer between them. This is in agreement with observations, as a strong spatial correlation exists in the vertical direction for contigous cloud systems like a deep convective cloud, whereas little correlation is found in situations of seperated cloud decks at different altitudes. The overlap assumptions can be expressed in geometry factors as described in Geleyn and Hollingsworth (1979). Based on these geometry factors (8.1) can be rewritten for both cloudy and cloud-free flux components with optical properties associated to the corresponding matrix coefficients accordingly.

8.5 Spectral Integration

The distinction between solar and thermal intervals simplifies the right hand side of the linear system, but the number of spectral intervals is by far too small to account for non-linear effects due to the extreme variation of optical properties of gases as function of wave length. As the absorption/emission properties of gases may change by several orders of magnitude within a certain spectral interval, gross errors would occur, if the RTE was solved for gaseous optical properties that were simply averaged over the corresponding spectral domain. In order to alleviate the non-linearity problem the transmission function $\overline{\tau}\,(u_{gas})$ for each spectral interval and gaseous absorber is approximated by a series of exponentials as function of the amount of the considered gas u_{gas}, i. e.:

$$\overline{\tau}(u_{gas}) \;\cong\; \sum_{i}^{I} \; w_i \, e^{-k_i \, u_{gas}}$$

This so-called exponential sum fitting technique generates for each gas and spectral interval pseudo-absorption coefficients k_i and associated weigthing coefficients w_i. Solving the RTE for each permutation of gaseous absorption coefficients and associated weights in conjunction with the non-gaseous optical properties of each layer provides flux results, which are then weighted and accumulated to obtain the overall result for each interval. Finally the fluxes obtained for the individual spectral intervals are accumulated to obtain the total radiative flux and the corresponding heating rates are derived from the vertical flux divergence within each model layer. The advantage of this approach compared to a direct solution at high spectral resolution and subsequent spectral integration results from the fact that the number of pseudo-absorption coefficients required for an adequate approximation of the transmission functions is rather small compared to the number of spectral intervals that would be needed for the direct method. For further details the reader is refered to RG92.

8.6 Input to the Radiation Parameterization Scheme

The computation of radiative fluxes is performed at half-levels of the NWP model. For the source term in the RTE this requires the specification of layer boundary temperatures which are obtained from the prognostic layer mean temperatures via interpolation. Optical properties are required as layer mean properties and are computed from relevant prognostic and/or diagnostic model variables like specific humidity, cloud water and ice content and cloud fraction. Some layer properties, like ozone, carbon dioxide and aerosols are specified as climatological estimates. In particular the spatially variable aerosol distribution is derived from a climatology provided by Tanre et al. (1984). The actual layer mean values of optically relevant substances are converted to radiative properties like optical depth, single scattering albedo and backscattered fraction through the use of empiral relations described in RG92.

Section 9

Parameterization of Sub-Grid Scale Orographic (SSO) Effects

9.1 Introduction

When the domain of the operational 7-km COSMO model at DWD was expanded in order to cover almost all Europe (COSMO-EU domain, see Schulz 2006), it turned out that the surface pressure in the model forecasts becomes systematically biased. In particular, in wintertime high pressure systems tend to develop a positive pressure bias, by 1-2 hPa after 48 h, low pressure systems a negative bias ("highs too high, lows too low"). At the same time the wind speed tends to be overestimated by up to 1 m/s throughout the entire troposphere. The wind direction near the surface shows a positive bias of some degrees.

The combination of these deficiencies leads to the hypothesis that in the model there is too little surface drag, causing an underestimation of the cross-isobar flow in the planetary boundary layer. Consequently, the solution would be to increase the surface drag in the model. This may be accomplished, for instance, by introducing an envelope orography (Wallace et al. 1983, Tibaldi 1986), but this has unfavourable effects e. g. for the simulated precipitation, or by including sub-grid scale orographic (SSO) effects, which were neglected in the COSMO model before. The SSO scheme by Lott and Miller (1997) was selected for this. Its implementation in the operational COSMO-EU model at DWD is described by Schulz (2008). It is also included e. g. in the global models at ECMWF or DWD and works here well.

9.2 The Sub-Grid Scale Orography Scheme

The SSO scheme by Lott and Miller (1997) deals explicitly with a low-level flow which is blocked when the sub-grid scale orography is sufficiently high. For this blocked flow separation occurs at the mountain flanks, resulting in a form drag. The upper part of the low-level flow is lead over the orography, while generating gravity waves.

In order to describe the low-level flow behaviour in the SSO scheme a non-dimensional height

H_{n} of the sub-grid scale mountain is introduced:

$$H_{\mathrm{n}} = \frac{N\,H}{|U|} \tag{9.1}$$

where H is the maximum height of the mountain, U the wind speed and N the Brunt-Väisälä frequency of the incident flow. The latter is computed by

$$N = \sqrt{\frac{g}{\theta}\frac{\partial\theta}{\partial z}} \tag{9.2}$$

where θ is the potential temperature, g the acceleration of gravity and z the height coordinate.

A small H_{n} will mean that there is an unblocked regime, all the flow goes over the mountain and gravity waves are forced by the vertical motion of the fluid. A large H_{n} will mean that there is a blocked regime, the vertical motion of the fluid is limited and part of the low-level flow goes around the mountain. The SSO scheme requires four external parameters, which are the standard deviation, the anisotropy, the slope and the geographical orientation of the sub-grid scale orography. They are computed following Baines and Palmer (1990) from the same raw data set of orographic height which is also used for computing the mean orographic height in the model. This is currently the GLOBE data set (GLOBE-Task-Team 1999) which has a resolution of approximately 1 km.

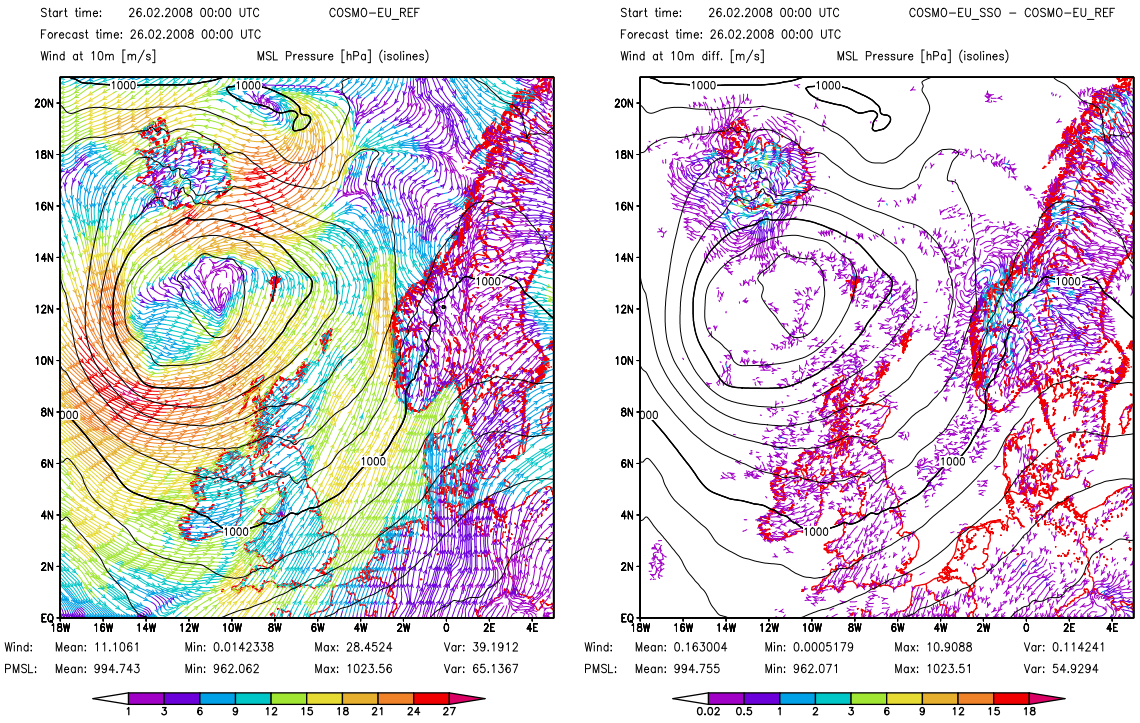

Figure 9.1: Left: 10-m wind (m/s) and mean sea level pressure (hPa) (isolines) simulated by the reference COSMO-EU without SSO scheme, 26 Feb. 2008, 00 UTC + 00h. Right: Difference of 10-m wind (m/s) between COSMO-EU with and without SSO scheme (SSO - REF), same date. The difference flow is usually pointing in opposite direction than the flow itself (over land), indicating that the flow is slowing down due to the SSO scheme.

The two components of the SSO scheme, i. e. the blocking and the gravity wave drag, can both be individually adjusted, or even be switched off, by a tuning parameter. Generally,

these two SSO parameters need to be adjusted depending on the mesh size of the model. For this study, the same two parameter values were chosen in COSMO-EU (mesh size 7 km) as in the DWD global model GME (mesh size 40 km). This setting yields already good and satisfying results.

9.3 Effect of the SSO Scheme on the COSMO Model

In order to demonstrate the effect of the SSO scheme on COSMO-EU two continuous numerical parallel experiments, running analogously to the operational analyses and forecasts, were carried out: A reference experiment of COSMO-EU without SSO scheme (called REF), and an experiment of COSMO-EU with SSO scheme (called SSO).

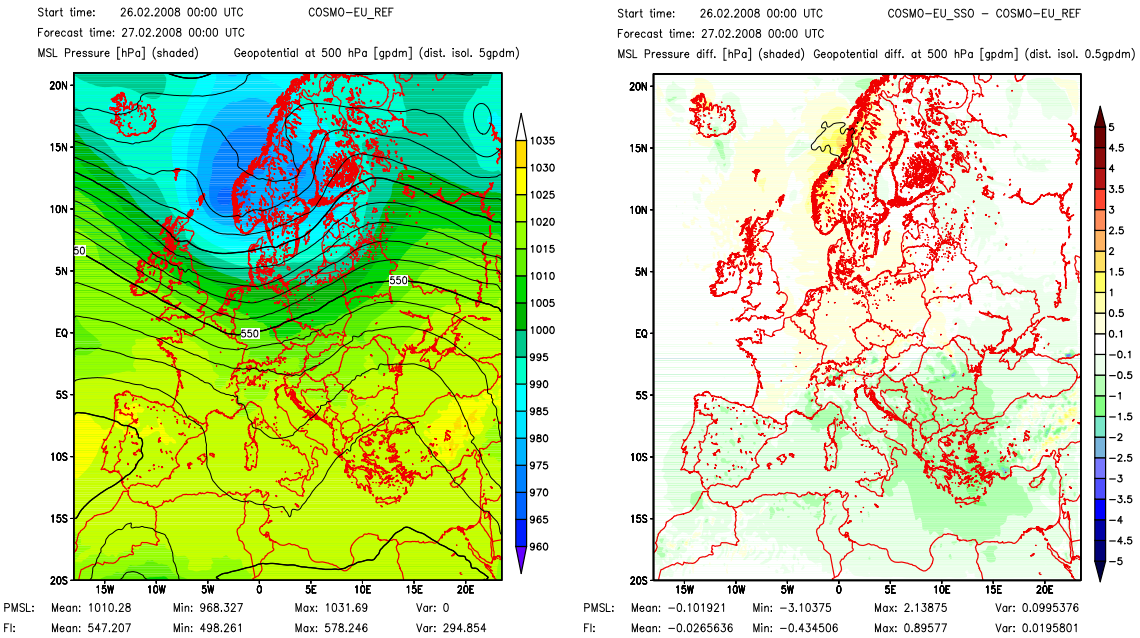

Figure 9.2: Left: Mean sea level pressure (hPa) and geopotential at 500 hPa (gpdm) (isolines) simulated by the reference COSMO-EU without SSO scheme, 26 Feb. 2008, 00 UTC + 24h. Right: Difference of mean sea level pressure (hPa) between COSMO-EU with and without SSO scheme (SSO - REF), same date.

Figure 9.1 shows the mean sea level pressure for the REF experiment in the Northwestern part of the model domain on 26 Feb. 2008, 00 UTC, at the beginning of the forecast, depicting a low pressure system over the Atlantic ocean, which was travelling eastward across Scandinavia during the next few days. The streamlines of the 10-m wind encircle the pressure system, with highest wind speeds southwest of the core, where the pressure gradient is high, and generally lower wind speeds over land. Differences in the 10-m wind between the two experiments (SSO - REF) are mainly found over land. The difference flow is usually pointing in opposite direction than the flow itself, well seen for instance over the British Isles, indicating that the flow is slowing down due to the SSO scheme.

Figure 9.2 shows the mean sea level pressure for the REF experiment in the full model domain on 26 Feb. 2008, 00 UTC + 24h. The low pressure system is clearly visible in the North, in the Southern half of the domain, the mediterranean area, there stretches a region

of prevailing high pressure. The geopotential at 500 hPa is overlaid as isolines showing the wave over Northern Europe. After 24h the low pressure system has already moved further eastward. Pressure differences between the two experiments started to develop in a sort of dipole structure, the low pressure system in the North is filling up more efficiently in the SSO experiment compared to the REF experiment, the high pressure region in the South is weakening. This development continues during the further course of the forecasts while the low pressure system is moving eastward.

This case study shows that the SSO scheme, particularly by increasing the form drag, enhances the cross-isobar flow in the planetary boundary layer, which as a consequence helps filling up low pressure systems and weakening high pressure systems.

Section 10

The Soil and Vegetation Model TERRA

The coupling between the atmosphere and the underlying surface is modeled by a stability and roughness-length dependent surface flux formulation. These surface fluxes constitute the lower boundary conditions for the atmospheric part of the model. Their calculation requires the knowledge of the temperature and the specific humidity at the ground. The task of the soil model is to predict these quantities by the simultaneous solution of a separate set of equations which describes various thermal and hydrological processes within the soil. If vegetation is considered explicitly, additional exchange processes between plants, ground and air have to be taken into account.

In LM, the soil model TERRA from the operational hydrostatic model EM and DM has been implemented. In contrast to EM/DM now the impact of plants on evaporation from the ground is taken into account by a Penman-Monteith type formulation.

10.1 Introduction

For land surfaces, the soil model TERRA provides the surface temperature and the specific humidity at the ground. The ground temperature is calculated by the equation of heat conduction which is solved in an optimized two-layer model using the extended force-restore method (Jacobsen and Heise (1982)). The soil water content is predicted for two, three or more layers by the Richards equation. Evaporation from bare land surfaces as well as transpiration by plants are derived as functions of the water content, and - only for transpiration - of radiation and ambient temperature.

Most parameters of the soil model (heat capacity, water storage capacity, etc.) strongly depend on soil texture. Five different types are distinguished: sand, sandy loam, loam, loamy clay and clay. Three special soil types are considered additionally: ice, rock and peat. Hydrological processes in the ground are not considered for ice and rock. Potential evaporation, however, is assumed to occur over ice, where the soil water content remains unchanged.

For practical purposes, the soil model is split into two parts: In the first part evapotranspiration is computed (TERRA1). The second part (TERRA2) deals with heat and water transfer in the soil and with the prediction of soil temperature and soil water content. The

soil model is described for short in the following. For detailed information on the parameterization and calculation of the various source and sink terms in the prognostic equations for soil moisture and temperature, please refer to the comprehensive description of TERRA in the *Documentation of the EM/DM system* by Majewski and Schrodin (1995).

10.2 Hydrological section

The hydrological part of TERRA predicts the water contents of various stores of water at the surface and in the soil. These are the interception store (which contains all surface water including dew on plants), the snow store (containing snow but also frozen surface water and rime) and two or more layers of soil. To calculate the mass budget of water in these stores, a number of exchange and transport processes have to be considered.

The coupling of the soil and the atmosphere is by precipitation and by the formation of dew and rime as a source of water as well as by evaporation and transpiration as a sink of water. As an additional sink the loss of soil water by runoff is taken into account. Exchange and transport of water between the stores is assumed to occur via infiltration, percolation and capillary movement as well as by melting and freezing of water in the snow and in the interception store, respectively.

The governing equations for the mass budget of the various water stores may then be formulated as

$$\rho_w \frac{\partial W_i}{\partial t} = P_r + E_i - R_i - I_i \,, \tag{10.1}$$

$$\rho_w \frac{\partial W_s}{\partial t} = P_s + E_s - R_s - I_s \,, \tag{10.2}$$

$$\rho_w \Delta z_1 \frac{\partial \eta_1}{\partial t} = E_b + T_1 - R_1 + F_{1,2} + I_s + I_i \,, \tag{10.3}$$

$$\rho_w \Delta z_k \frac{\partial \eta_k}{\partial t} = T_k - R_k + F_{k,k+1} - F_{k-1,k} \,, \tag{10.4}$$

where the suffixes i and s denote the interception and the snow store, respectively. The suffix 1 stands for the first hydrologically active soil layer below the surface and the suffix k for additional soil layers below the first layer, i.e $k = 2, \ldots, N_{hl}$. A climatological soil moisture layer $N_{hl} + 1$ below the lowest active layer is also specified to provide the lower boundary conditions. For this climatological layer, either the soil moisture content or the water flux between layers N_{hl} and $N_{hl} + 1$ can be prescribed with fixed values. Figure 10.1 shows a sketch of the hydrological processes considered by the soil model.

The total number N_{hl} of active soil layers may be arbitrarily specified, but for the application in LM N_{hl} is restricted to 2 or 3. For the present version of the model the default number of hydrological soil layer is $N_{hl} = 2$ and the water flux between the lowest active soil layer and the adjacent climatological layer is set to zero. The various symbols and terms in Eqs. (10.1)-(10.4) have the following meaning:

W_i, W_s	water content of interception and snow store, resp.
η_1, η_k	water content of soil layers
Δz_1, Δz_k	thickness of soil layers
P_r, P_s	precipitation rate of rain and snow, resp.

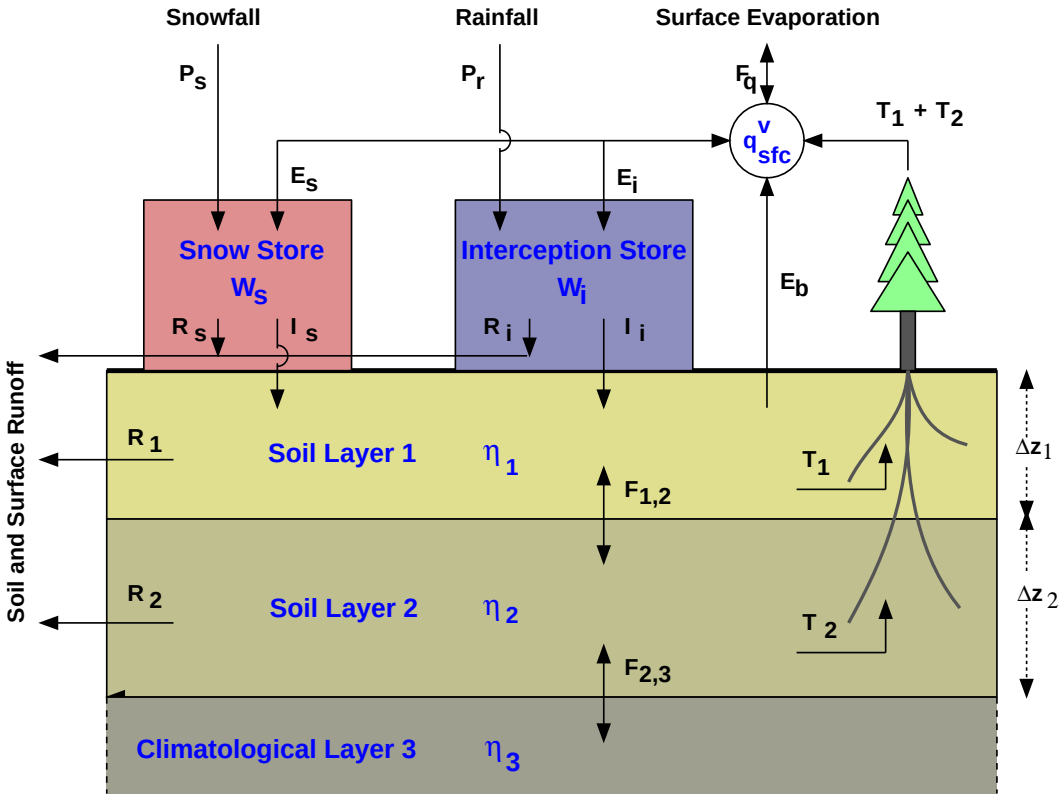

Figure 10.1: *Hydrological processes considered by the soil model TERRA*

R_i, R_s	runoff from interception and snow store, resp.
R_1, R_k	runoff from soil layers
I_i, I_s	infiltration from interception and snow store, resp.
E_i, E_s	evaporation from interception and snow store, resp.
E_b	evaporation from bare soil surface
T_1, T_k	transpiration by plants
$F_{k,k+1}$	flux between soil layers k and $k+1$
ρ_w	density of water

Vertical water fluxes are defined to be positive when they are directed towards the earth's surface, i.e upwards in the soil and downwards in the atmosphere. A basic assumption of the soil model is that the interception store can only contain water if the snow store is empty and vice versa. That is, snow and interception water may not be present simultaneously and the corresponding water contents will be uniquely related to the surface temperature T_b ($W_i = 0$ for $T_b < T_0$ and $W_s = 0$ for $T_b > T_0$ where T_0 is the freezing point).

The parameterization of the surface fluxes in the atmospheric part of the model is by drag-law formulations (see Section 6.3) and the parametric relation for the surface flux of water vapour reads (Eq. (4.3))

$$(F^3_{q^v})_{sfc} \;=\; -\,\rho\, C^d_q\, |\mathbf{v}_h|\, (q^v - q^v_{sfc})\,, \tag{10.5}$$

where q^v is the specific humidity at the lowest grid level above the ground and q^v_{sfc} is the ground level specific humidity ($(F^3_{q^v})_{sfc}$ is abbreviated with F_q in Fig. 10.1). To apply this

lower flux boundary condition, q^v_{sfc} must be specified. We assume that all surface fluxes of moisture predicted by the soil model sum up to a total moisture flux given by Eq. (4.3). Taking the sign convention into account, we have

$$E_b + \sum_{k=1}^{k=N_{hl}} T_k + E_i + E_s = -(F^3_{q^v})_{sfc}\,. \tag{10.6}$$

From (10.5) and (10.6), the ground level specific humidity can be calculated according to

$$q^v_{sfc} = q^v - \frac{1}{\rho\, C^d_q}\left(E_b + \sum_{k=1}^{k=N_{hl}} T_k + E_i + E_s\right)\,. \tag{10.7}$$

A detailed description on the parameterization of the various source and sink terms on the right hand sides of Eqs. (10.1) - (10.4) as well as the numerical method of solution is given in the *Documentation of the EM/DM system*. In the following, evaporation from bare soil and plant transpiration is described as the parameterization of these processes was changed compared to the EM/DM system.

10.2.1 Bare soil evaporation

The rate of evaporation from bare soil, E_b, is computed using the assumption $E_b = Min(E_p; F_m)$, where E_p is potential evaporation and F_m the maximum moisture flux through the surface that the soil can sustain (Dickinson (1984)). The potential evaporation is given by (compare equation (10.5)):

$$E_p = -\rho\, C^d_q\, |\mathbf{v}_h|\, [q^v - q_{sat}(T_{sfc})]\,. \tag{10.8}$$

According to Dickinson (1984) the following parameterization formulae for the determination of F_m results from tuning based on computations with a high resolution soil model (providing a number of cumbersome expressions and constants):

$$F_m = C_k D \frac{s_1}{(z_0 z_1)^{1/2}}\,, \tag{10.9}$$

where s_0 is the average soil water content in the total active layer divided by the volume of voids in the soil (pore volume,η_{pv}), z_0 is the corresponding depth of the total active layer and z_1 the depth of the surface soil layer.

$$C_k = 1 + 1550\frac{D_{min}}{D_{max}} \cdot \frac{B - 3.7 + 5/B}{B + 5}\,, \tag{10.10}$$

$$D_{min} = 2.5 \cdot 10^{-10} m^2/s\,, \tag{10.11}$$

$$D_{max} = B\Phi_0 K_0/\rho_{wm}\,, \tag{10.12}$$

with the soil water suction (negative potential) at saturation $\Phi_0 = 0.2m$ and the fraction of saturated soil filled by water $\rho_{wm} = 0.8$. The parameters B and K_0 depend on the soil type.

$$D = 1.02 D_{max} s_1^{B+2} (s_0/s_1)^{B_f}\,, \tag{10.13}$$

$$B_f = 5.5 - 0.8B[1 + 0.1(B-4) log_{10}\frac{K_0}{K_R}]\,, \tag{10.14}$$

with $K_R = 10^{-5} m/s$. s_1 is the water content of the surface soil layer divided by η_{pv}.

10.2.2 Plant transpiration

The computation of plant transpiration T_p basically follows Dickinson (1984). In the version adopted here we assume the moisture flux between the plant foliage and the air inside the canopy to equal the flux between the air inside and the air above the canopy. We additionally assume the foliage temperature to be equal to the surface temperature. Then the transpiration can easily be computed by taking into account both the resistance for water vapour transport from the foliage to the canopy air (foliage resistance r_f) and the resistance for water vapour transport from the canopy air to the air above the canopy (atmospheric resistance r_a):

$$T_p = \rho_a \left[q_a - q_{sat}(T_{sfc})\right] (r_a + r_f)^{-1} . \tag{10.15}$$

Here r_a is given by $r_a^{-1} = C_q^d |\mathbf{v}_h| = C_A$, and r_f^{-1} is parameterized by $r_f^{-1} = r' C_F = C_V$, with $C_F = \sigma_{LAI} r_{la}^{-1}$, $r_{la}^{-1} = C' u_*^{1/2}$, and $r' = r_{la}(r_{la} + r_s)^{-1}$. σ_{LAI} is the leaf area index and the resistance r' describes the reduction of transpiration by the stomatal resistance r_s. The functional form of this resistance is adopted from Dickinson (1984):

$$r_s^{-1} = r_{max}^{-1} + (r_{min}^{-1} - r_{max}^{-1}) \left[F_{rad} F_{wat} F_{tem} F_{hum}\right] . \tag{10.16}$$

The functions F describe the influence on the stomatal resistance of radiation (F_{rad}), soil water content (F_{wat}), ambient temperature (F_{tem}), and ambient specific humidity (F_{hum}), respectively. These functions take the value 1 if optimum conditions are present, and they are 0 for unfavorable conditions. The F-functions take the following forms:

$$F_{rad} = Min(1; \frac{PAR}{PAR_{crit}}) , \tag{10.17}$$

where PAR is the photosynthetically active radiation and PAR_{crit} a tuning parameter.

$$F_{wat} = Max(0; Min(1; \frac{\eta_{root} - \eta_{PWP}}{\eta_{TLP} - \eta_{PWP}})) , \tag{10.18}$$

here η_{root} is the water content of the soil averaged over the root depth rd:

$$\eta_{root} = \frac{1}{rd} \int_{z=0}^{z=rd} \eta(z) dz , \tag{10.19}$$

η_{PWP} is the permanent wilting point, η_{TLP} is the turgor loss point.

$$F_{tem} = Max(0; Min(1; 4\frac{(T - T_o)(T_{end} - T)}{(T_{end} - T_o)^2})) , \tag{10.20}$$

where T is the soil surface temperature, $T_o = 273.15K$, and T_{end} is a tuning parameter.

$$F_{hum} = 1 - \min(1; \max(0; 4(\frac{\Delta q}{q_{sat}} - FR_{sat}))) . \tag{10.21}$$

We use $r_{min} = 90 s/m$, $r_{max} = 1000 s/m$, $PAR_{crit} = 100 W/m^2$, $T_{end} = 313.15K$, and $FR_{sat} = 0.75$. The parameters η_{pv}, and η_{PWP} depend on the soil texture. Other parameters required are the leaf area index, the fraction of the ground covered by plants, and the root depth rd.

If we replace the resistances r_a and r_f by the corresponding transfer coefficients C_A and C_V we arrive at the following formula for the total transpiration rate:

$$T_p = E_p \, C_V \, (C_A + C_V)^{-1} \, . \tag{10.22}$$

Once the total transpiration rate T_p has been computed, the extraction of water is distributed to the soil layers k according to

$$T_k = T_p \frac{\Delta z_{root,k}}{rd} \frac{\eta_k}{\eta_{root}} \, , \tag{10.23}$$

where $\Delta z_{root,k}$ is the depth of layer k which is filled by roots.

10.3 Thermal section

The thermal part of the soil model TERRA uses a two-layer model to predict the temperatures at the layer interfaces. These are the temperature of the soil surface (T_b), the temperature of the snow surface (T_s) and the temperature at the interface between the first and the second soil layer (T_m). As a lower boundary condition for the temperature T_c at the interface between the second layer and a lower climatological layer of deep soil, $T_c = const$ is assumed. Between the layer interfaces, a linear temperature profile is prescribed. Thus, the mean temperature of the snow store is given by $0.5(T_s + T_b)$, the mean temperature of the first layer by $0.5(T_b + T_m)$ and the mean temperature of the second soil layer by $0.5(T_b + T_c)$.

In order to predict the layer mean temperatures by budget equations, various heat fluxes between the soil and the atmosphere and between the soil layers have to be taken into account. Additionally, the heat fluxes resulting from melting of falling snow, from freezing of rain, from freezing of water in the interception store and from melting of ice in the snow store must be considered. The following prognostic equations are used for the layer mean temperatures:

$$\frac{c_s \, \Delta z_s}{2} \frac{\partial}{\partial t}(T_s + T_b) = r_s R_{net} + H_s + L_S E_s - G_{sb} + G_f \, , \tag{10.24}$$

$$\frac{c \, \Delta z_{th,1}}{2} \frac{\partial}{\partial t}(T_b + T_m) = (1 - r_s) R_{net} + H_b + L_V E_i + V_{tr} + V_b + G_{mb} + G_{sb} \, , \tag{10.25}$$

$$\frac{c \, \Delta z_{th,2}}{2} \frac{\partial}{\partial t}(T_m + T_c) = G_{cm} - G_{mb} \, . \tag{10.26}$$

Because of the lower boundary condition, $\partial T_c / \partial t = 0$ in Eq. (10.26). The various symbols and terms in Eqs. (10.24) - (10.26) have the following meaning:

c_s, c	volumetric heat capacity of snow and soil, resp.
Δz_s	thickness of snow layer
$\Delta z_{th,1}, \Delta z_{th,2}$	thickness of upper and lower soil layer, resp.
r_s	fraction of land covered by snow
R_{net}	surface budget of radiation fluxes
H_s	sensible heat flux over snow
H_b	sensible heat flux over bare soil

L_V, L_S, L_F	latent heat of vapourization, sublimation and fusion
G_{sb}	heat flux between snow store and soil
G_f	heat flux due to melting and freezing
G_{mb}	heat flux between upper and lower soil layer
G_{cm}	heat flux between lower soil layer and deep soil
V_{tr}	latent heat flux due to transpiration
V_b	latent heat flux due to evaporation from bare soil

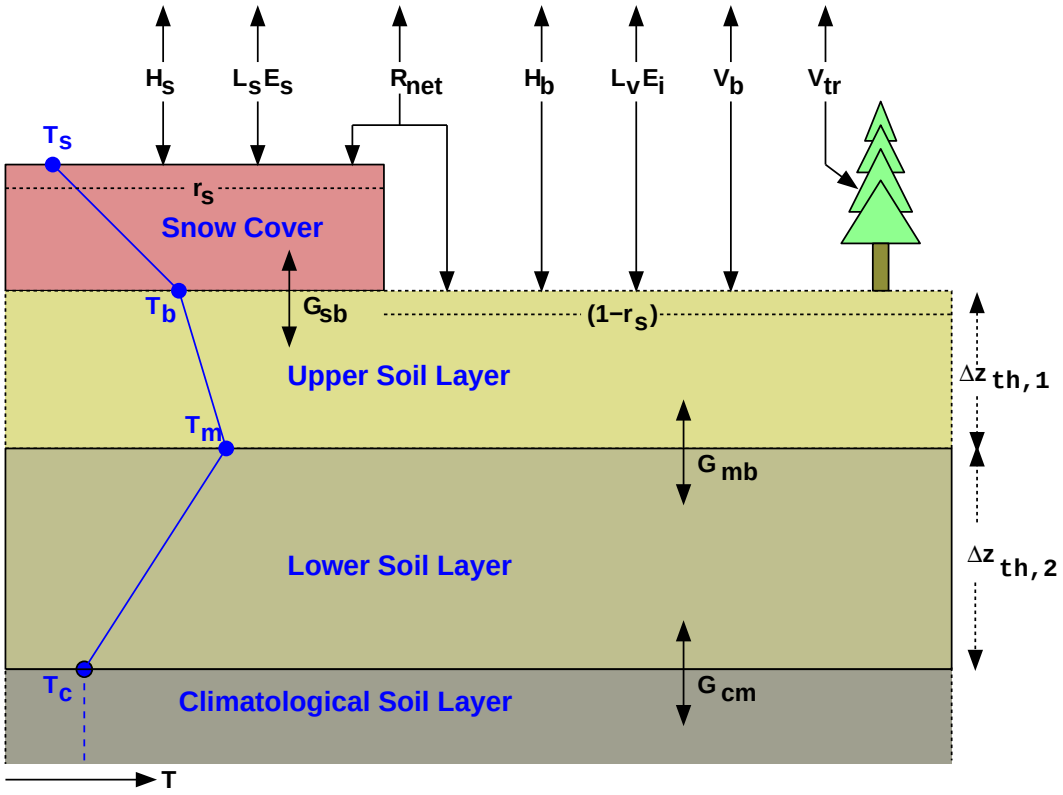

Figure 10.2: *Thermal processes considered by the soil model TERRA*

Figure 10.2 shows a sketch of the processes considered in the thermal part of the soil model. The calculation of the soil layer thicknesses $\Delta z_{th,1}$ and $\Delta z_{th,2}$ and of the soil heat fluxes G_{mb} and G_{cm} is based on the *Extended Force Restore* (EFR) method. The EFR-technique is an optimized two-layer model to solve the equation of heat conduction. It is assumed that the driving atmospheric processes (the sum of radiation, sensible and latent heat fluxes at the earth surface) can be described by a harmonic function of time. For two arbitrary tuning time periods τ_1 and τ_2, the EFR-method exactly solves the equation of heat conduction for the temperatures at the surface and at depth $\Delta z_{th,1}$.

This method prescribes the layer depths and the heat fluxes as a function of soil parameters (the thermal conductivity λ and the volumetric heat capacity c), the time periods and the vertical temperature differences. The layer depths are given by

$$\Delta z_{th,1} = D_1(1+x)^{-1}\,, \tag{10.27}$$

$$\Delta z_{th,2} = \Delta z_{th,1}(\alpha_s \beta_m^{-1} - 1)\,, \tag{10.28}$$

where D_1 is the penetration depth of a temperature wave for the frequency $\omega_1 = 2\pi/\tau_1$. The

parameter x is given by the ratio of the two periods τ_1 and τ_2 via $x^2 = \tau_1/\tau_2$. D_1, α_s and β_m are defined by

$$\begin{aligned} D_1 &= \sqrt{2\lambda/c\,\omega_1}\,, \\ \alpha_s &= \omega_1(1+x+x^2)\,, \\ \beta_m &= \omega_1 x\sqrt{x+x^2}\exp\{-x/(1+x)\}\,. \end{aligned}$$

Basically, both the thermal conductivity λ and the volumetric heat capacity c of the soil depend on soil moisture but time independent values of λ and c are required by the EFR-method. Thus, an average water content $\overline{\eta}$ is prescribed for their calculation:

$$\overline{\eta} = 0.5(\eta_{fc} + \eta_{wilt}) \tag{10.29}$$

$\overline{\eta}$ is held fixed and depends only on soil type via the field capacity η_{fc} and the permanent wilting point η_{wilt}. Using (10.29), the following parametric relations are applied to calculate λ and c:

$$\lambda = \lambda_0 + \{0.25 + 0.3\Delta\lambda(1+0.75\Delta\lambda)^{-1}\}\,\Delta\lambda\, f_\lambda\,, \tag{10.30}$$

$$c = c_0 + \rho_w c_w \overline{\eta}\,, \tag{10.31}$$

where c_0, λ_0 and $\Delta\lambda$ are parameters depending on soil type and c_w is the specific heat capacity of water. The factor f_λ in Eq. (10.30) has the functional form

$$f_\lambda = \min\left\{\frac{4\overline{\eta}}{\eta_{pv}}\,,\, 1 + \left(\frac{4\overline{\eta}}{\eta_{pv}} - 1\right)\frac{1+0.35\Delta\lambda}{1+1.95\Delta\lambda}\right\} \tag{10.32}$$

and depends on the pore volume η_{pv} of the soil.

The default values for the time periods are set to $\tau_1 = 24$ h and $\tau_2 = 5\tau_1$. This yields the following form for the soil heat fluxes G_{cm} and G_{mb}:

$$G_{cm} = -\sqrt{\lambda\, c/\tau_1}\,\{0.68(T_m - T_c)\}\,, \tag{10.33}$$

$$G_{mb} = -\sqrt{\lambda\, c/\tau_1}\,\{1.28(T_c - T_m) + 1.58(T_b - T_c)\}\,. \tag{10.34}$$

Given the heat fluxes from Eqs. (10.33) and (10.34), the set of prognostic equations for T_s, T_b and T_c is solved by using an implicit numerical scheme. For details on this scheme and on the parameterization of the other source and sink terms in Eqs. (10.24) - (10.26), please refer to the *Documentation of the EM/DM system.*

Section 11

The Multi-Layer Soil and Vegetation Model TERRA_ML

11.1 Introduction

The coupling between the atmosphere and the underlying surface is modeled by a stability and roughness-length dependent surface flux formulation. These surface fluxes constitute the lower boundary conditions for the atmospheric part of the model. Their calculation requires the knowledge of the temperature and the specific humidity at the ground. The task of the soil model is to predict these quantities by the simultaneous solution of a separate set of equations which describes various thermal and hydrological processes within the soil.

In this chapter the multi-layer version of the soil model (TERRA_ML) is described. The main differences of this version in comparison to the older version (TERRA) are:

- The EFR-method (Jacobsen and Heise (1982)) for the temperature prediction is replaced by a direct solution of the heat conduction equation.
- The effect of freezing/thawing of soil water/ice is included.
- The process of snow melting is changed.
- A time dependent snow albedo is introduced.

The multi-layer concept avoids the dependence of layer thicknesses on the soil type. Additionally, it avoids the use of different layer structures for the thermal and the hydrological section of the model.

Most parameters of the soil model (heat capacity, water storage capacity, etc.) strongly depend on soil texture. Five different types are distinguished: sand, sandy loam, loam, loamy clay and clay. Three special soil types are considered additionally: ice, rock and peat. Hydrological processes in the ground are not considered for ice and rock. Potential evaporation, however, is assumed to occur over ice, where the soil water content remains unchanged.

The soil model consists of two parts. In the first part the computation of bare soil evaporation and plant transpiration is performed. In the second part the equation of heat conduction and the Richards equation are solved. Also, melting of snow is computed here. In a former version of TERRA_ML, the convection subroutine was called after finishing the first part, using the

evaporation rate computed by the soil model. And the second part of the soil model used the grid-scale and convective precipitation rates as input to the hydrological computations. In view of the short timestep of LM, the two parts have now been combined into a single subroutine, which is called before the convection scheme.

The process of freezing/thawing of soil water/ice is accomplished by a diagnostic change of water/ice content and of temperature using energy and water budget considerations. This avoids an iterative solution of the thermodynamic and hydraulic equations which are coupled by the freezing/thawing process. The small timestep of LM justifies this simple method.

11.2 Layer Structure and Sign Convention of the Multi-Layer Soil Model

In principle the layer structure of the multi-layer soil model (Fig. 11.1) can be chosen arbitrarily. But interactions with the provision of initial data for temperature and for soil water content have to be taken into account.

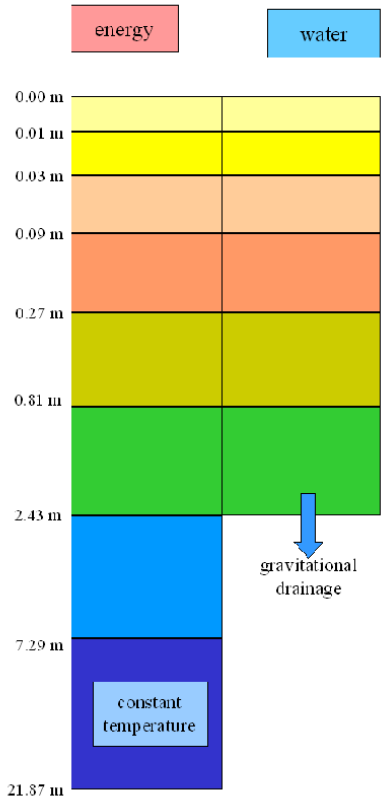

Figure 11.1: Layer structure of the soil model

At present for the solution of the heat conduction equation the following depths of half levels (layer boundaries) are used: $z_{h,k} = 0.01 \cdot 3^{(k-1)}$ (m) with $k = 1, 2, \ldots, ke_{soil,th} + 1$, where $ke_{soil,th} = 7$ is the number of active soil layers. This gives a total active depth of 7.29 m to the soil. The depths of the main levels (layer centres) are given by $z_{m,k} = 0.5 \cdot (z_{h,k} + z_{h,k-1})$ with $k = 1, 2, \ldots, ke_{soil,th} + 1$, where $z_{h,0} = 0$. The 8^{th} layer is the so-called climate layer, where the annual mean near surface air temperature is prescribed as a boundary value. The thicknesses of the layers are defined by $\Delta z_k = z_{h,k} - z_{h,k-1}$.

For the solution of the Richards equation in the hydrological section the same layers as in the thermal section are used, but we restrict the number of active layers to $ke_{soil,hy} = 6$. Instead of a climate layer with prescribed water content a flux boundary condition is used: At the lower boundary of the 6^{th} layer at a depth of 2.43 m only the downward gravitational transport is considered. Capillary transports are neglected here.

In this documentation the vertical fluxes are defined to be positive when they are directed towards the soil surface, i. e. upwards in the soil and downwards in the atmosphere. This is in accordance with the model's program code.

11.3 Hydrological Processes

The hydrological section of the soil model predicts the liquid water contents of various reservoirs of water at the surface and in the soil. These are the interception reservoir (which contains all surface water including dew on plants and on the soil), the snow reservoir (containing snow but also frozen surface water and rime) and the specified number of soil layers. In order to calculate the mass budgets of water in these reservoirs, a number of exchange and transport processes have to be considered, as shown in Fig. 11.2.

The coupling of the soil and the atmosphere is by precipitation and by the formation of dew and rime as a source of water as well as by evaporation and transpiration as a sink of water. As an additional sink the loss of soil water by runoff is taken into account. Exchange and transport of water between the reservoirs is assumed to occur via infiltration, percolation and capillary movement as well as by melting of snow and by freezing of water in the interception reservoir.

The governing equations for the mass budgets of the various water reservoirs may be formulated as

$$\rho_w \frac{\partial W_i}{\partial t} = \alpha \cdot P_r + E_i - I_{perc} - R_{inter}, \tag{11.1}$$

$$\rho_w \frac{\partial W_{snow}}{\partial t} = P_{snow} + E_{snow} - I_{snow} - R_{snow}, \tag{11.2}$$

$$\rho_w \frac{\partial W_{l,k}}{\partial t} = \delta_{1,k}[E_b + I_{snow} + I_{perc} + (1-\alpha)P_r - R_{infil}] + F_{k,k+1} - (1-\delta_{1,k})F_{k-1,k} + Tr_k - R_k + S_k, \tag{11.3}$$

$$\rho_w \frac{\partial W_{ice,k}}{\partial t} = -S_k, \tag{11.4}$$

where ρ_w is the density of water. The suffixes i and *snow* denote the interception and the snow reservoir, respectively. $\delta_{1,k}$ is the Kronecker symbol being 1 for $k = 1$ and 0 for $k \neq 1$. The suffix 1 stands for the first layer ($k = 1$) below the surface. The other symbols and terms in (11.1) to (11.4) have the following meanings:

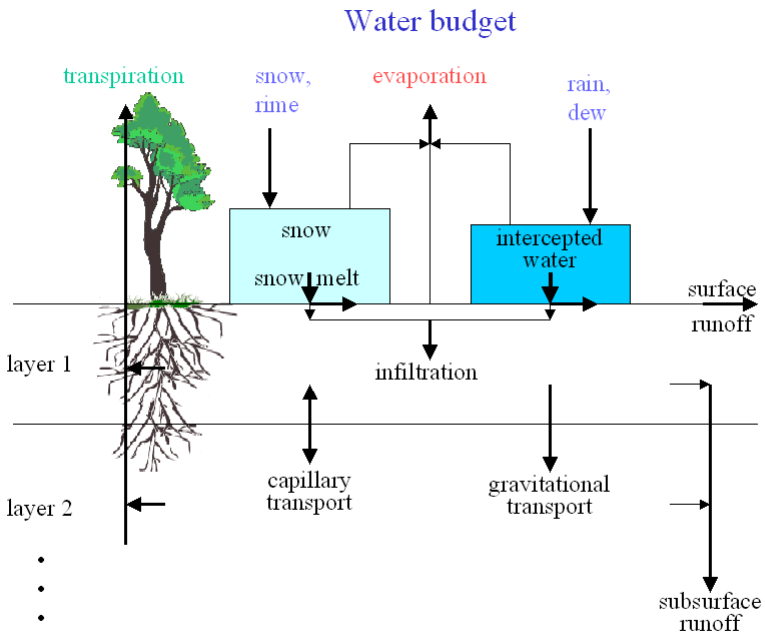

Figure 11.2: Hydrologic processes considered in the soil model

W_i, W_{snow}	water content of interception and snow reservoir, resp. [m H_2O]
$W_{l,k}$	liquid water content of soil layers [m H_2O]
$W_{ice,k}$	ice content of soil layers [m H_2O]
E_i, E_{snow}	evaporation from interception and snow reservoir, resp. [kg/(m^2 s)]
E_b	evaporation from bare soil [kg/(m^2 s)]
Tr_k	water extraction by roots [kg/(m^2 s)]
P_r, P_{snow}	precipitation rate of rain and snow, resp. [kg/(m^2 s)]
α	factor for distributing rain between interception reservoir and infiltration [-]
I_{perc}, I_{snow}	infiltration contributions from percolation and from melting snow, resp. [kg/(m^2 s)]
$R_{inter}, R_{snow}, R_{infil}$	runoff from interception and snow reservoir and from limited infiltration rate, resp. [kg/(m^2 s)]
R_k	runoff from soil layers [kg/(m^2 s)]
$F_{k,k+1}$	gravitational and capillary flux of water between layers $k+1$ and k [kg/(m^2 s)]
S_k	source term of liquid water by thawing soil ice

Out of all terms on the right hand sides of (11.1) to (11.4) only the two precipitation components P_r and P_{snow} are given by the atmospheric part of the model. All other terms have to be determined in the context of the soil model. At the end of the present section, all terms with the exception of runoff and infiltration from the snow store, and the source terms of liquid water by melting of soil ice (R_{snow}, I_{snow}, S_k) will be known. These last three terms will be determined in the context of the treatment of snow (Section 11.4.3) and soil ice (Section 11.5).

In addition to the water content values given in m H_2O, at some places the fractional water content $w_{l,k} = W_{l,k}/\Delta z_k$ will be used. These values are denoted by lowercase letters. Moreover, the total water content is given by the sum of the liquid part (index l) and the frozen part (index ice), where $W_k = W_{l,k} + W_{ice,k}$ and analogous for the fractional water content. The process of freezing/thawing in the soil will be described in Section 11.5.

As a basic assumption of the soil model the interception reservoir can only contain water if the snow reservoir is empty and vice versa. That is, snow and interception water may not be present simultaneously and the corresponding water contents will be uniquely related to the surface temperature T_{sfc} ($W_i = 0$ for $T_{sfc} < T_0$ and $W_{snow} = 0$ for $T_{sfc} > T_0$, where T_0 is the freezing point).

The parameterization of the surface fluxes in the atmospheric part of the model is based on drag-law formulations and the parametric relation for the surface flux of water vapour reads (see Section 4, Eq. 4.3)

$$(F^3_{q^v})_{sfc} = \rho C^d_q |\mathbf{v}_h|(q^v - q^v_{sfc}), \tag{11.5}$$

where q^v is the specific humidity at the lowest grid level above the ground and q^v_{sfc} is the ground level specific humidity. To apply this lower flux boundary condition, q^v_{sfc} must be specified. We assume that all surface fluxes of moisture parameterized by the soil model sum up to a total moisture flux given by (11.5). Taking the sign convention into account, we have

$$E_b + \sum_{k=1}^{ke_{soil,hy}} Tr_k + E_i + E_{snow} = -(F^3_{q^v})_{sfc}. \tag{11.6}$$

From (11.5) and (11.6), a fictitious ground level specific humidity can be calculated according to

$$q^v_{sfc} = q^v + \frac{1}{\rho C^d_q}(F^3_{q^v})_{sfc}. \tag{11.7}$$

11.3.1 Evapotranspiration

In this section the parameterization of evaporation E_i from the interception reservoir W_i, evaporation E_{snow} from the snow reservoir W_{snow} and the bare soil evaporation E_b from the uppermost soil layer W_1, as well as the plant transpiration Tr_k are described. The starting point for all components of total evapotranspiration is the potential evaporation E_{pot} which follows from the drag-law formula (11.5):

$$E_{pot}(T_{sfc}) = \rho C^d_q |\mathbf{v}_h|(q^v - Q^v(T_{sfc})), \tag{11.8}$$

where T_{sfc} is the temperature of the respective surface (interception or snow reservoir or uppermost soil model layer) and Q^v denotes the saturation specific humidity.

(a) Evaporation from the Interception and the Snow Reservoir, Formation of Dew and Rime

The parameterization of evaporation from the interception and the snow reservoir, respectively, takes into account a partial coverage of the soil surface by interception water or by snow. The fractional areas are computed by

$$f_i = Max\left[0.01\ ;\ 1.0 - e^{Max(-5.0;-W_i/\delta_i)}\right] \tag{11.9}$$

with $\delta_i = 0.0010$ m for interception water and by

$$f_{snow} = Max\,[0.01\ ;\ Min(1.0\ ;\ W_{snow}/\delta_s)] \tag{11.10}$$

with $\delta_s = 0.015$ m for snow.

If $W_i > 0$ and if $E_{pot}(T_{sfc}) < 0$ indicates upward directed potential evaporation at soil surface temperature T_{sfc} then interception water is evaporated limited by the total content of the interception reservoir W_i:

$$E_i = Max\left[-\frac{\rho_w}{\Delta t}W_i\ ;\ f_i E_{pot}(T_{sfc})\right]. \tag{11.11}$$

Similarly, if $W_{snow} > 0$ and if $E_{pot}(T_{snow,sfc}) < 0$ the evaporation rate of snow is

$$E_{snow} = Max\left[-\frac{\rho_w}{\Delta t}W_{snow}\ ;\ f_{snow}E_{pot}(T_{snow,sfc})\right]. \tag{11.12}$$

Formation of dew is simulated if $E_{pot}(T_{sfc}) > 0$ and $T_{sfc} > T_0$. In this case

$$E_i = E_{pot}(T_{sfc}). \tag{11.13}$$

The formation of rime is simulated if $E_{pot}(T_{snow,sfc}) > 0$ and $T_{snow,sfc} < T_0$. Here

$$E_{snow} = E_{pot}(T_{snow,sfc}). \tag{11.14}$$

(If $W_{snow} \equiv 0$, $T_{snow,sfc} \equiv T_{sfc}$.)

(b) Bare Soil Evaporation

Evaporation from bare soil is not considered for soil type rock. For soil type ice, potential evaporation according to (11.8) is used for E_b, but no change of water content of the soil is accounted for. For all other soil types the following method is used: If $E_{pot}(T_{sfc}) < 0$, the evaporation rate of bare soil E_b is parameterized using the assumption

$$E_b = (1 - f_i) \cdot (1 - f_{snow}) \cdot (1 - f_{plnt}) \cdot Min[-E_{pot}(T_{sfc})\ ;\ F_m] \tag{11.15}$$

where F_m is the maximum moisture flux through the surface that the soil can sustain (Dickinson (1984)), f_{plnt} is the fractional area covered by plants (given as an external parameter field), and the potential evaporation is given by (11.8). The pameterization formulae for the determination of F_m result from tuning a two layer soil model with the results of a high resolution soil model (resulting in a number of cumbersome expressions and constants). The tuning is based on average values of soil water content s_u normalised by the volume of voids (w_{PV}) for an uppermost layer z_u of 0.1 m thickness and for the soil water content s_t for a total active layer z_t of 1 m thickness:

$$s_{u,t} = \frac{\sum_{k=1}^{n_{u,t}} W_k}{w_{PV} \sum_{k=1}^{n_{u,t}} \Delta z_k}, \tag{11.16}$$

In our version we approximate Dickinson's layers by using $n_u = 3$ and $n_t = 5$, corresponding to thicknesses of $z_u = 0.09$ m and $z_t = 0.81$ m, respectively. The water flux F_m is given by

$$F_m = \rho_w C_k D \frac{s_t}{(z_u z_t)^{1/2}} \quad , \tag{11.17}$$

where C_k is calculated by

$$C_k = 1 + 1550\frac{D_{min}}{D_{max}} \cdot \frac{B - 3.7 + 5/B}{B + 5} \tag{11.18}$$

with

$$D_{min} = 2.5 \cdot 10^{-10} m^2/s \tag{11.19}$$

$$D_{max} = B\Phi_0 K_0/\rho_{wm} \quad , \tag{11.20}$$

where the soil water suction (negative potential) at saturation $\Phi_0 = 0.2$m and the fraction of saturated soil filled by water $\rho_{wm} = 0.8$. The parameters B and K_0 depend on the soil type (see Table 11.1). D is

$$D = 1.02 D_{max} s_u^{B+2} (s_t/s_u)^{B_f}. \tag{11.21}$$

B_f is given by

$$B_f = 5.5 - 0.8B \left[1 + 0.1(B-4) log_{10}\frac{K_0}{K_R}\right] \quad , \tag{11.22}$$

with $K_R = 10^{-5} m/s$.

(c) Plant Transpiration

Plant transpiration is not considered for soil types ice and rock. For the other soil types the following method is used: If $E_{pot}(T_{sfc}) < 0$, transpiration by plants is parameterized, basically following Dickinson (1984). In the version adopted here we assume the moisture flux between the plant foliage and the air inside the canopy to be equal to the flux between the air inside and the air above the canopy. We additionally assume the foliage temperature to be equal to the surface temperature. Then the total transpiration Tr can easily be computed by taking into account both the resistance for water vapour transport from the foliage to the canopy air (foliage resistance r_f) and the resistance for water vapour transport from the canopy air to the air above the canopy (atmospheric resistance r_a):

$$Tr = f_{plnt} \cdot (1 - f_i) \cdot (1 - f_{snow}) \cdot E_{pot}(T_{sfc}) r_a (r_a + r_f)^{-1} \tag{11.23}$$

r_a is given by $r_a^{-1} = C_q^d |v_h| = C_A$ and r_f^{-1} is parameterized by $r_f^{-1} = r' C_F = C_V$, with $C_F = f_{LAI} r_{la}^{-1}$, $r_{la}^{-1} = C' u_*^{1/2}$, and $r' = r_{la}(r_{la} + r_s)^{-1}$. f_{LAI} is the leaf area index and the resistance r' describes the reduction of transpiration by the stomatal resistance r_s. The functional form of this resistance is adopted from Dickinson (1984):

$$r_s^{-1} = r_{max}^{-1} + (r_{min}^{-1} - r_{max}^{-1}) \left[F_{rad} F_{wat} F_{tem} F_{hum}\right] \tag{11.24}$$

At present we use $r_{min} = 150$ s/m, $r_{max} = 4000$ s/m. The functions F describe the influence on the stomatal resistance of radiation F_{rad}, soil water content F_{wat}, ambient temperature F_{tem}, and ambient specific humidity F_{hum}, respectively. These functions take the value 1 if optimum conditions are present, and they are 0 for unfavourable conditions. The F-functions take the following forms:

$$F_{rad} = Min\left(1\,;\, \frac{Rad_{PAR}}{Rad_{PAR,crit}}\right) \quad , \tag{11.25}$$

where Rad_{PAR} is the photosynthetically active radiation and $Rad_{PAR,crit} = 100$ W/m^2 is a tuning parameter.

$$F_{wat} = Max\left[0\,;\, Min\left(1\,;\, \frac{w_{l,root} - w_{PWP}}{w_{TLP} - w_{PWP}}\right)\right] \quad , \tag{11.26}$$

here $w_{l,root}$ is the liquid water content fraction of the soil averaged over the root depth z_{root}

$$w_{l,root} = \frac{1}{z_{root}} \int_{z=0}^{z=z_{root}} w_l(z)dz \quad , \tag{11.27}$$

w_{PWP} is the permanent wilting point of plants (see Table 11.1), and w_{TLP} is the turgor loss point of plants, which is parameterized after (Denmead and Shaw 1962)

$$w_{TLP} = w_{PWP} + (w_{FC} - w_{PWP}) \cdot (0.81 + 0.121 arctg(E_{pot}(T_{sfc}) - E_{pot,norm})) \quad , \tag{11.28}$$

where w_{FC} is the water content at field capacity (Table 11.1) and $E_{pot,norm} = 4.75$ mm/d.

$$F_{tem} = Max \left[0 \; ; \; Min \left(1 \; ; \; 4 \frac{(T_{2m} - T_0)(T_{end} - T_{2m})}{(T_{end} - T_0)^2} \right) \right] \quad , \tag{11.29}$$

where T_{2m} is the temperature in 2 m above the soil surface and $T_{end} = 313.15$ K is a tuning parameter. At present $F_{hum} = 1$ is used.

If we replace the resistances r_a and r_f by the corresponding transfer coefficients C_A and C_V we arrive at the following formula for the total transpiration rate Tr:

$$Tr = f_{plnt} \cdot (1 - f_i) \cdot (1 - f_{snow}) E_{pot}(T_{sfc}) C_V (C_A + C_V)^{-1}. \tag{11.30}$$

Once the total transpitation rate Tr has been computed, the extraction of water is distributed to the soil layers k according to

$$Tr_k = Tr \frac{\Delta z_{root,k}}{z_{root}} \frac{w_{l,k}}{w_{l,root}} \quad , \tag{11.31}$$

where $\Delta z_{root,k}$ is the part of layer k, which is filled by roots.

11.3.2 Interception Reservoir, Infiltration of Rain and Runoff from Interception Reservoir

When it rains, the interception reservoir is used to collect a small amount of water. This water can be evaporated at the potential rate. The maximum capacity of this reservoir is estimated depending on the fractional area of plants by

$$W_{i,max} = W_{i,0}(1.0 + 5.0 \cdot f_{plnt}) \quad , \tag{11.32}$$

with $W_{i,0} = 5 \cdot 10^{-4}$ m. If $W_i > 0$, part of the intercepted water will percolate to the uppermost soil layer according to

$$I_{perc} = \begin{cases} 0 & : \quad T_{sfc} \leq T_0 \\ W_i' \frac{\rho_w}{\tau_{perc}} & : \quad T_{sfc} > T_0 \end{cases} \quad , \tag{11.33}$$

where W_i' is a provisional new value of the interception reservoir content taking into account evaporation:

$$W_i' = W_i + E_i \frac{2\Delta t}{\rho_w} \tag{11.34}$$

The time constant τ_{perc} has to be chosen such that $\tau_{perc} \geq 2\Delta t$. Actually we use $\tau_{perc} = 1000$ s.

If $P_r > 0$ and $T_{sfc} > T_0$, the interception reservoir content increases by the fraction αP_r, while the remainder

$$I_{rain} = (1 - \alpha)P_r \tag{11.35}$$

is available for infiltration. The parameter α depends on the ratio between the actual interception reservoir content W_i and its maximum content $W_{i,max}$. We parameterize α by

$$\alpha = Max\left[\left(1.0 - \frac{W_i'}{W_{i,max}}\right)^{1/2} \; ; \; \frac{(W_{i,max} - W_i')\rho_w/(2\Delta t) + I_{perc}}{P_r}\right] \tag{11.36}$$

The first term of the maximum function is based on the concept developed by Crawford and Linsley (1966), whereas the second term avoids a reduction of the interception reservoir content as long as $P_r > 0$. Aditionally α is restricted to a value ≤ 1.

Remark: To avoid numerical noise, presently a strongly reduced maximum water content of the interception reservoir $W_{i,0} = 1 \cdot 10^{-6}$ m is used. Therefore, the fraction αP_r of the total precipitation cannot be intercepted but is (nearly) completely used as runoff. To avoid this unrealistic water loss for the upper soil layer the limitation of the interception reservoir actually has to be combined with $\alpha = 0$.

The maximum infiltration rate is given by a simplified Holtan-equation (e. g. Hillel (1980)):

$$I'_{max} = \begin{cases} 0 & : \quad T_{sfc} \leq T_0 \\ f_r \; S_{oro}[Max(0.5 \; ; \; f_{plnt})I_{k1}(w_{PV} - w_1)/w_{PV} + I_{k2}] & : \quad T_{sfc} > T_0 \end{cases} \tag{11.37}$$

f_r considers the reduction of I_{max} if soil ice exists in the uppermost soil layer:

$$f_r = 1 - \frac{w_{ice,1}}{w_{PV}} \tag{11.38}$$

Additionally I'_{max} is limited by the available pore volume of the uppermost soil layer:

$$I_{max} = Min(I'_{max} \; ; \; \frac{w_{PV} - w_1}{2\Delta t} \; \Delta z_1 \; \rho_w) \tag{11.39}$$

At present the influence of the subgrid-scale orographic variations is neglected ($S_{oro} = 1$). It is $I_{k1} = 0.002$ kg/(m^2 s) and the infiltration parameter I_{k2} depends on soil type (see Table 11.1). If $I_{perc} + (1 - \alpha)P_r$ exceeds I_{max}, a contribution to surface runoff is given by

$$R_{infil} = \begin{cases} I_{perc} + (1 - \alpha)P_r - I_{max} & : \quad I_{perc} + (1 - \alpha)P_r > I_{max} \\ 0 & : \quad \text{otherwise} \end{cases} \tag{11.40}$$

Now a provisional new value W_i' of the interception reservoir content is computed by

$$W_i' = W_i + (\alpha P_r + E_i - I_{perc})\frac{2\Delta t}{\rho_w} \quad . \tag{11.41}$$

If $W_i' > W_{i,max}$, a second contribution to runoff is determined by

$$R_{i,m} = Max[0.0 \; ; \; W_i' - W_{i,max})]\frac{\rho_w}{2\Delta t} \tag{11.42}$$

If, on the other hand, $W_i' < \epsilon = 1.0 \cdot 10^{-6}$ m, this water is no longer considered as interception reservoir. But in order to keep the mass budget correct, it is considered as runoff:

$$R_{i,\epsilon} = \begin{cases} W_i' \; \rho_w/2\Delta t & : \quad W_i' < \epsilon \\ 0 & : \quad \text{otherwise} \end{cases} \tag{11.43}$$

Now the runoff from the interception reservoir is given by

$$R_{inter} = R_{i,m} + R_{i,\epsilon}, \tag{11.44}$$

and the total runoff from all these processes is

$$R_i = R_{infil} + R_{inter} \quad . \tag{11.45}$$

Special cases

1. If $P_r > 0$ in cases where snow is present ($W_{snow} > 0$), we use $\alpha = 0$, as there is no storage of liquid water in the snow. This leads to all rain going into runoff, as in this case also $T_{sfc} \leq T_0$.
2. If $P_r > 0$, $W_{snow} = 0$ and $T_{sfc} < T_0$ (the case of freezing rain), we treat P_r as snowfall, i. e., first we set $P_s = P_r$ and then $P_r = 0$.
3. If $P_s > 0$ and $T_{sfc} > T_0$ we treat P_s as rain, i. e., first we set $P_r = P_s$ and then $P_s = 0$.

The last two special cases have to be considered in the upper boundary condition for the solution of the heat conduction equation for the case of snowfree soil.

11.3.3 Vertical Soil Water Transport and Runoff from Soil Layers

Vertical soil water transport and runoff from soil layers are not considered for soil types ice and rock. For the other soil types, the water budget of the soil layers depends on the boundary values at the upper and the lower boundary of the soil model, on the water extraction by evapotranspiration, on gravitational and capillary transports and on the runoff formation.

(a) Vertical Soil Water Transport

In this subsection we deal with the vertical water transport between the soil layers. Neglecting the effects of evapotranspiration and runoff formation, the one-dimensional equation for the liquid water budget reads

$$\frac{\partial w_l}{\partial t} = \frac{1}{\rho_w}\frac{\partial F}{\partial z} \quad , \tag{11.46}$$

where w_l is the liquid water fraction defined by the liquid water content W_l (m H_2O) in the layer of thickness Δz:

$$w_l = \frac{W_l}{\Delta z} \tag{11.47}$$

Vertical water transports are due to gravity and capillary forces, and they are expressed by the general Richards equation (e. g. Hillel (1980)) for the soil water flux F:

$$F = -\rho_w \left[- D_w(w_l)\frac{\partial w_l}{\partial z} + K_w(w_l) \right] \tag{11.48}$$

Hydraulic diffusivity $D_w(w_l)$ and hydraulic conductivity $K_w(w_l)$ depend on the water content. According to Rijtema (1969) they are expressed by

$$D_w(w_l) = D_0 \ \ exp \ \left[D_1(w_{PV} - \bar{w}_l)/(w_{PV} - w_{ADP}) \right] \tag{11.49}$$

and

$$K_w(w_l) = K_0 \ \ exp \ \left[K_1(w_{PV} - \bar{w}_l)/(w_{PV} - w_{ADP})\right] \tag{11.50}$$

Here $\bar{w}_l$ is the weighted mean of the liquid water content on half levels. The determination of this weighted mean is of critical importance to the magnitude of the fluxes, as there are large changes of hydraulic diffusivity and of hydraulic conductivity with water content. At present we use a mean weighted by the respective layer thicknesses. The four constants D_0, D_1, K_0, K_1 depend on soil type (see Table 11.1).

At the lower boundary (at $z_{h,ke_{soil,hy}}$), we use $D_w = 0$, which means that only the downward gravitational transport is considered. At the upper boundary, the infiltration $I_s + I_i$ replaces the flux (11.48).

Table 11.1: Hydraulic and thermal parameters of the different soil types

soil type	**1 ice**	**2 rock**	**3 sand**	**4 sandy loam**	**5 loam**	**6 loamy clay**	**7 clay**	**8 peat**
volume of voids w_{PV} [1]	-	-	0.364	0.445	0.455	0.475	0.507	0.863
field capacity w_{FC} [1]	-	-	0.196	0.260	0.340	0.370	0.463	0.763
permanent wilting point w_{PWP} [1]	-	-	0.042	0.100	0.110	0.185	0.257	0.265
air dryness point w_{ADP} [1]	-	-	0.012	0.030	0.035	0.060	0.065	0.098
minimum infiltration rate I_{K2} [kg/(m^2 s)]	-	-	0.0035	0.0023	0.0010	0.0006	0.0001	0.0002
hydraulic diffusivity parameter D_0 [10^{-9} m^2/s]	-	-	18400	3460	3570	1180	442	106
hydraulic diffusivity parameter D_1 [1]	-	-	-8.45	-9.47	-7.44	-7.76	-6.74	-5.97
hydraulic conductivity parameter K_0 [10^{-9} m/s]	-	-	47900	9430	5310	764	17	58
hydraulic conductivity parameter K_1 [1]	-	-	-19.27	-20.86	-19.66	-18.52	-16.32	-16.48
heat capacity $\rho_0 c_0$ [10^6 J/(m^3 K)]	1.92	2.10	1.28	1.35	1.42	1.50	1.63	0.58
heat conductivity								
λ_0 [W/(K m)]	2.26	2.41	0.30	0.28	0.25	0.21	0.18	0.06
$\Delta\lambda$ [W/(K m)]	0.0	0.0	2.40	2.40	1.58	1.55	1.50	0.50
exponent B [1]	1.0	1.0	3.5	4.8	6.1	8.6	10.0	9.0

This treatment of the liquid water transport presumes that no ice exists in any of the soil layers (for the treatment of freezing and thawing processes in the soil layers see Section 11.5). If ice is present, a large liquid water gradient can occur between neighbouring layers, but the water transport can be significantly reduced if a large part of one of the layers is mostly filled by ice. This behaviour is considered by defining a scaled fraction of the liquid water content w_l':

$$w_l' = \frac{w_l}{1 - w_{ice}} \tag{11.51}$$

This scaled liquid water content replaces the water content w_l in (11.48), (11.49) and (11.50). But the scaling only accounts for changes in the gradient of liquid water due to the presence of ice. Therefore, additionally we restrict the flux to the non-frozen parts of the layers by multiplying the hydraulic coefficients by the reduction factor

$$r_{k+1/2} = 1 - \frac{Max(w_{ice,k}, w_{ice,k+1})}{w_{PV}} \tag{11.52}$$

Complete overlapping of the frozen parts of the two layers involved is assumed.

Because of the very thin uppermost soil layer, a semi-implicit solution of (11.46) has to be used to predict the water content from timestep n to timestep $n+1$. As usual, the implicit formulation is simplified by only using the water content of timestep n for the determination of the hydraulic diffusivity $D_w(w_l)$ and hydraulic conductivity $K_w(w_l)$. Then the discretization of (11.46) in time using (11.48) and (11.51) leads to

$$w_l^{'n+1} = w_l^{'n} + \Delta t \left\{ \beta \frac{\partial}{\partial z} \left[D_w^n(w_l^{'}) \frac{\partial w_l^{'n+1}}{\partial z} \right] + (1-\beta) \frac{\partial}{\partial z} \left[D_w^n(w_l^{'}) \frac{\partial w_l^{'n}}{\partial z} \right] - \frac{\partial K_w^n(w_l^{'})}{\partial z} \right\} \tag{11.53}$$

The parameter β governs the degree of implicitness. The vertical discretization of (11.53) results in a three-diagonal linear system of the form

$$A_k w_{k-1}^{'n+1} + B_k w_k^{'n+1} + C_k w_{k+1}^{'n+1} = D_k \quad , \tag{11.54}$$

which can easily be solved by standard methods.

(b) Runoff from Soil Layers

Runoff from any soil layer k occurs if the total water content w_k of the layer exceeds field capacity w_{FC} and if the divergence of the fluxes (11.48) in this layer is negative. In this case

$$R_k = -\frac{w_k - w_{FC}}{w_{PV} - w_{FC}} \left(\frac{\partial F}{\partial z} \right)_k \Delta z_k \tag{11.55}$$

This treatment has to be modified in the case of presence of ice in the respective layers. But this remains to be done.

11.4 Thermal Processes

This section deals with the thermal processes in the soil and in the snow pack (if $W_{snow} > 0$) and predicts the mean temperatures of the active soil layers and of an existing snow layer (Fig. 11.3). As the temperature of the water content of the interception reservoir is assumed to be equal to the soil surface temperature, no separate heat budget equation is necessary for this reservoir.

The basic equation for the temperature prediction is the heat conduction equation

$$\frac{\partial T_{so}}{\partial t} = \frac{1}{(\rho c)} \frac{\partial}{\partial z} \left(\lambda \frac{\partial T_{so}}{\partial z} \right) \quad , \tag{11.56}$$

where T_{so} is soil temperature, ρc is heat capacity, and λ is heat conductivity. The lower boundary condition for the solution of (11.56) is provided by a climatological temperature prescribed in layer $ke_{soil,th}+1$. This temperature is constant in time. At the upper boundary the coupling between soil (or snow) and atmosphere is by radiation and by sensible and latent heat fluxes. A heat flux is parameterized between snow and soil if $W_{snow} > 0$, providing the upper boundary condition for the soil and the lower boundary condition for the snow.

In addition, the effects of melting of falling snow, freezing of rain, freezing of water in the interception reservoir, melting of snow in the snow reservoir, freezing/thawing of water/ice in the soil layers have to be considered. All these effects will be dealt with in the following sections.

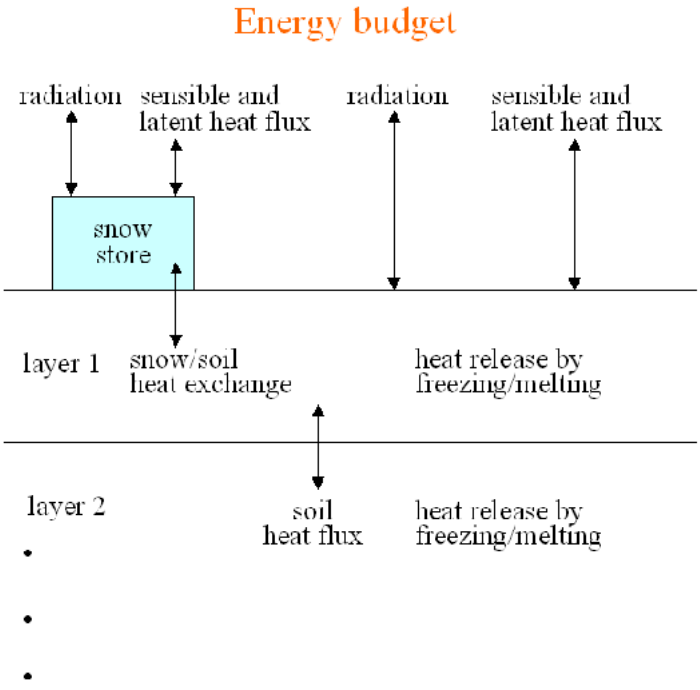

Figure 11.3: Energetic processes considered in the soil model

11.4.1 Temperature Prediction for Snowfree Soil

In this section we deal with the simplest case of solving the heat conduction equation. A snowfree soil is assumed, and all the effects connected with freezing/thawing of water/ice are neglected. These effects will be introduced step by step in later sections.

(a) Determination of Parameters

The volumetric heat capacity ρc is determined taking into account the respective values for a dry soil ($\rho_0 c_0$ Table 11.1), for water ($\rho_w c_w = 4.18{\cdot}10^6$ J/(m^3 K)) and for ice ($\rho_w c_{ice} = 2.10{\cdot}10^6$ J/(m^3 K)):

$$\rho c = \rho_0 c_0 + \rho_w c_w w_l + \rho_w c_{ice} w_{ice} \tag{11.57}$$

In contrast to the heat capacity the determination of the heat conductivity at present takes into account only the liquid water content of the soil:

$$\lambda = \lambda_0 + \left(0.25 + \frac{0.3\Delta\lambda}{1+0.75\Delta\lambda}\right) \Delta\lambda Min\left\{\left[\frac{4w_m}{w_{PV}}\right]; \left[1+\left(\frac{4w_m}{w_{PV}}-1\right)\frac{1+0.35\Delta\lambda}{1+1.95\Delta\lambda}\right]\right\} \quad (11.58)$$

This formula approximates some data given by Benoit (1976) and by van Wijk and de Vries (1966). The respective values for λ_0 and $\Delta\lambda$ are given in Table 11.1. At present an average soil water content w_m, which is kept constant, is assumed in this parameterization:

$$w_m = 0.5(w_{FC} + w_{PWP}) \quad (11.59)$$

Besides this simplification, additionally the modification of the soil heat conductivity in the case of presence of soil ice is not considered.

(b) Upper Boundary Condition

At the upper boundary of the soil the heat flux $\lambda\partial T/\partial z$ is replaced by the atmospheric forcing G_{sfc}, i. e., the sum of the radiation budget and the sensible and the latent heat flux. This results in the following form of (11.56)

$$\left(\frac{\partial T_{so}}{\partial t}\right)_{k=1} = \frac{1}{\rho c \Delta z_1}\left[\lambda\frac{(T_{so})_{k=2}-(T_{so})_{k=1}}{z_{m,2}-z_{m,1}} + G_{sfc}\right] \quad . \quad (11.60)$$

The forcing at the soil surface G_{sfc} is given by

$$G_{sfc} = c_p\hat{H}^3_{sfc} + L(F^3_{q^v})_{sfc} + Q_{rad,net} + G_P + G_{snow,melt} \quad , \quad (11.61)$$

where the sensible heat flux is known from the surface layer parameterization (see Section 4, Eq. 4.2)

$$\hat{H}^3_{sfc} = \rho C^d_h |\mathbf{v}_h|(\theta\pi_{sfc} - T_{sfc}) \quad . \quad (11.62)$$

The latent heat flux is determined using the evapotranspiration computed in the hydrological section of the soil model by (11.5) and (11.7). $Q_{rad,net}$ is the net radiation budget at the soil surface as given by the radiation parameterization. G_P accounts for the effects of freezing rain and melting snowfall, respectively. The water budget part of these processes was treated already in Section 11.3.2. The thermal consequences are accounted for by the following determination of G_P:

1. If the soil surface temperature is below the freezing point ($T_{sfc} < T_0$) and $P_r > 0$, we have $G_P = L_f \cdot P_r$.
2. If the soil surface temperature is above the freezing point and $P_{snow} > 0$, we have $G_P = -L_f \cdot P_{snow}$.

The term $G_{snow,melt}$ (see Section 11.4.3) accounts for the possible influence on the soil temperature by snow melt processes.

(c) Transfer Coefficient Limitation

As long as the energetic inertia of the model layers in atmosphere or soil is large compared to the magnitude of the changes in state by forcing fluxes, a new balanced state can be achieved within a limited number of forecast time steps. Because of the thin soil layers close to the surface an abrupt change of the surface fluxes can cause overshooting reactions which could lead to numerical instability.

An overshooting reaction in temperature for the uppermost soil layers can be alleviated by introducing a situation dependent upper limit to the turbulent fluxes exchanged between atmosphere and soil. The constraint fluxes must ensure that the temporal change of temperature in the topmost soil layer (which has the smallest inertia of all soil layers) does not exceed a prescribed temperature limit $\Delta T_{so,max}$. Equation (11.60) then reads in time-discretisized form

$$|G_{sfc} - G(1)| \leq \rho c \Delta z_1 \frac{\Delta T_{so,max}}{\Delta t} \tag{11.63}$$

In the following a modification of this equation caused by the presence of snow is disregarded. Then (11.61) can be written as

$$G_{sfc} = c_p \hat{H}^3_{sfc} + L(F^3_{q^v})_{sfc} + Q_{rad,net} \quad . \tag{11.64}$$

Introducing (11.64) in (11.63) we have

$$|c_p \hat{H}^3_{sfc} + L(F^3_{q^v})_{sfc} + Q_{rad,net} - G(1)| \leq \rho c \Delta z_1 \frac{\Delta T_{so,max}}{\Delta t} \quad , \tag{11.65}$$

(11.65) poses an upper limit on the total heat flux divergence for the uppermost layer. Substituting (11.5) and (11.62) in (11.65) and using additionally $C^d_q = C^d_h = C^d$ we obtain

$$|C^d|\mathbf{v}_h|\rho(c\Delta T_{as} + L\Delta q_{as}) + Q_{rad,net} - G(1)| \leq \rho c \Delta z_1 \frac{\Delta T_{so,max}}{\Delta t} \quad , \tag{11.66}$$

where $\Delta T_{as} = (\theta \pi_{sfc} - T_{sfc})$ and $\Delta q_{as} = (q^v - q^v_{sfc})$ and θ and q^v are, respectively, the potential temperature and the specific humidity at the lowest grid level above the earth's surface.

In order to isolate the transfer coefficient C^d in (11.66) a distinction between heating and cooling situations for the topmost layer has to be introduced.

Heating of the soil: The sum of all contributions on the left hand side of (11.66) is positive even before taking the absolute value. In this case (11.66) can be rewritten as

$$C^d|\mathbf{v}_h|\rho(c\Delta T_{as} + L\Delta q_{as}) \leq \rho c \Delta z_1 \frac{\Delta T_{so,max}}{\Delta t} - Q_{rad,net} + G(1) \quad , \tag{11.67}$$

If turbulent fluxes would provide a positive contribution to the energy budget of the soil and thereby enhance the overall heating in situations when atmosphere and soil are not in balance (e. g. after the data assimilation step) a limitation of the transfer coefficient can alleviate the problem. In this situation, we may solve (11.66) for C^d to obtain the following constraint for the transfer coefficient:

$$C^d \leq \frac{\rho c \frac{\Delta T_{so,max}}{\Delta t} \Delta z_1 - Q_{rad,net} + G(1)}{|\mathbf{v}_h|\rho(c\Delta T_{as} + L\Delta q_{as})} \tag{11.68}$$

Cooling of the soil: Let us now consider a cooling of the soil, i. e. the sum of all contributions on the left hand side of (11.66) is negative before taking the absolute value. In this case we may rewrite (11.66) as

$$C^d|\mathbf{v}_h|\rho(c\Delta T_{as} + L\Delta q_{as}) + Q_{rad,net} - G(1) \geq -\rho c\Delta z_1 \frac{\Delta T_{so,max}}{\Delta t} \quad , \tag{11.69}$$

and subsequently

$$C^d|\mathbf{v}_h|\rho(c\Delta T_{as} + L\Delta q_{as}) \geq -Q_{rad,net} + G(1) - \rho c\Delta z_1 \frac{\Delta T_{so,max}}{\Delta t} \quad . \tag{11.70}$$

If the total unconstrained flux divergence leads to a cooling in conjunction with an energy gain by turbulent surface fluxes, the turbulent fluxes are already contributing to a reduction of the soil cooling and should not be constrained.

However, in the case when energy transfer by turbulent fluxes is directed from the soil to the atmosphere a reduction of the turbulent transfer coefficients may provide the required modification of the soil temperature tendency. Solving (11.70) for C^d, we obtain the following constraint for the transfer coefficient:

$$C^d \leq \frac{-\rho c\frac{\Delta T_{so,max}}{\Delta t}\Delta z_1 - Q_{rad,net} + G(1)}{|\mathbf{v}_h|\rho(c\Delta T_{as} + L\Delta q_{as})} \tag{11.71}$$

The threshold value for the temperature increment in the uppermost soil layer will be set to 2.5 K, a fairly large value bearing in mind that the typical model timestep is less than a minute.

(d) Lower Boundary Condition

As stated already in the introduction to the section on the thermal section, the lower boundary condition is provided by prescribing a climatological temperature in layer $ke_{soil,th} + 1$, which is constant in time. An annual mean field of the near surface air temperature, which is provided on a global 0.5° x 0.5° grid is interpolated to the LM grid. This method is justified by the very small annual cycle of the temperature at the upper boundary of the layer $ke_{soil,th} + 1$, which is of the order of 5 to 10% of the amplitude at the earth's surface, if $ke_{soil,th} = 7$ as in the present version.

(e) Implicit Solution of the Heat Conduction Equation for the Soil Layers

As in the case of the equation for the soil water transport, the heat conduction equation has to be solved implicitely because of the very thin upper layer. Therefore, the discretization in time of (11.56) is given by

$$T_{so}^{n+1} = T_{so}^n + \frac{\Delta t}{\rho c}\left\{\beta\frac{\partial}{\partial z}\left[\lambda\frac{\partial T_{so}^{n+1}}{\partial z}\right] + (1-\beta)\frac{\partial}{\partial z}\left[\lambda\frac{\partial T_{so}^{n}}{\partial z}\right]\right\} \quad , \tag{11.72}$$

where the parameter β governs the degree of implicitness. The vertical discretization of (11.72) results in a three-diagonal linear system, which can be solved by standard methods. This procedure also provides a solution for the soil surface temperature T_{sfc} at $z = 0$. But

sometimes spurious oscillations in this temperature occur after abrupt changes of the surface energy budget (11.61). Therefore, we replace the soil surface temperature by $(T_{so})_{k=1}$, the mean temperature of the first soil layer.

11.4.2 Temperature Prediction for Snow and for Snow-Covered Soil

In the case of a (partially) snow-covered soil, the vertical mean of the snow temperature T_{snow} has to be predicted. The snow surface temperature $T_{snow,sfc}$ is then diagnosed from the soil surface temperature T_{sfc} and the mean snow temperature by linear extrapolation $T_{snow,sfc} = 2T_{snow} - T_{sfc}$. The prognostic equation for the mean temperature of the snow deck is given by

$$\frac{\partial T_{snow}}{\partial t} = \frac{1}{(\rho c \Delta z)_{snow}} \left(G_{snow,sfc} - G_{snow} + G_{melt}\right) \quad , \tag{11.73}$$

where $G_{snow,sfc}$ is the atmospheric forcing at the snow surface, G_{snow} is the heat flux from the snow to the soil, and G_{melt} stands for all melting processes connected to the snow deck.

(a) Time-Dependent Snow Albedo

An ageing function $0 \leq S_{age} \leq 1$ for snow albedo is considered. The snow albedo is calculated by

$$\alpha_s = \alpha_{s,max} S_{age} + \alpha_{s,min}(1 - S_{age}) \tag{11.74}$$

with $\alpha_{s,max} = 0.7$ and $\alpha_{s,min} = 0.4$. The value of S_{age} is 1 for 'fresh' snow and approaches 0 for old snow. The variation of S_{age} with time consists of a constant ageing and a regeneration by falling snow:

$$\Delta S_{age} = S_{age} \left[\frac{P_{snow}}{P_{norm}} - \frac{\Delta t}{\tau_\alpha}\right] \tag{11.75}$$

P_{snow} is the snowfall rate, $P_{norm} = 5$ mm/24h. The ageing-function is communicated between the snow analysis and the forecast model. If no snow exists, $S_{age} = 1$ is prescribed.

(b) Prognostic Density of Snow

$(\rho c \Delta z)_{snow}$ is the heat capacity of the snow with a prognostic snow density ρ_{snow}. Two processes are considered: An ageing (increasing compactness) of snow dependent on the snow temperature, and a decrease of density due to falling snow dependent on the ambient air temperature. The prognostic value of snow density ρ_{snow}^{n+1} is given by

$$\rho_{snow}^{n+1} = \left\{\rho_{snow,age} W_{snow}^n + \rho_{snow,fresh} P_{snow} \frac{\Delta t}{\rho_w}\right\} / z_{norm} \quad . \tag{11.76}$$

W_{snow}^n is the snow water equivalent at the beginning of the time step Δt. The ageing is accounted for by

$$\rho_{snow,age} = \rho_{snow,max} + (\rho_{snow}^n - \rho_{snow,max}) \exp^{\frac{-C_{age}\Delta t}{\tau_\rho}} \tag{11.77}$$

where

$$C_{age} = 0.2 + (0.4 - 0.2)\frac{(T_{snow} - T_{min})}{T_0 - T_{min}} \quad , \tag{11.78}$$

with a time-constant $\tau_\rho = 1$d, freezing point T_0 and $T_{min} = 258.15$. ρ_{snow}^n is the snow density at the beginning of the time step.

The density of fresh falling snow is determined by

$$\rho_{snow,fresh} = \rho_{s,f,min} + (\rho_{s,f,max} - \rho_{s,f,min}) \frac{T_{low} - T_{min}}{T_0 - T_{min}} \tag{11.79}$$

where $\rho_{s,f,min} = 50$ kg/m^3, $\rho_{s,f,max} = 150$ kg/m^3, and T_{low} is the temperature of the lowest atmospheric model level. Finally

$$z_{norm} = W_{snow}^n + P_{snow} \frac{\Delta t}{\rho_w} \tag{11.80}$$

The whole range of snow densities is restricted to $\rho_{snow,min} = 50$ kg/m^3 and $\rho_{snow,max} = 400$ kg/m^3.

(c) Snow Depth

The depth of the snow deck is given by

$$\Delta z_s = \frac{\rho_w}{\rho_{snow}} \frac{W_{snow}}{f_{snow}} \tag{11.81}$$

The fractional area f_{snow} covered by snow is given by (11.10). A minimum value of $\Delta z_{snow,min} = 0.01$ m is prescribed. Extreme snow depths which can be found in some regions of the model cannot be properly accounted for by this concept. Therefore, for thermal processes in snow a maximum snow depth of 1.5 m is prescribed.

(d) Boundary Conditions for Snow and Soil Surfaces, Heatflux through the Snow Deck

At the snow surface, the boundary condition is the same as at the soil surface (11.61). Only the evapotranspiration has to be replaced by the snow surface evaporation, which is given either by (11.12) in the form

$$E_{snow} = Max \left[-\frac{\rho_w}{\Delta t} W_{snow} \; ; \; E_{pot}(T_{snow,sfc}) \right], \tag{11.82}$$

or by (11.14). The evaporation has to be multiplied by the latent heat of sublimation. This gives the latent heat flux in W/m^2. Therefore, when using (11.12) in the upper boundary condition for (11.73), the fractional area covered by the snow deck has to be omitted.

The heat flux through the snow deck is parameterized by

$$G_{snow} = \lambda_{snow} \frac{T_{snow,sfc} - T_{sfc}}{\Delta z_{snow}} \tag{11.83}$$

The thermal conductivity λ_{snow} is parameterized depending on the time dependent snow density ρ_{snow}:

$$\lambda_{snow} = \lambda_{ice} \left\{ \frac{\rho_{snow}}{\rho_w} \right\}^{1.88} \tag{11.84}$$

where $\lambda_{ice} = 2.22$ W/(mK) is the heat conductivity of ice.

The upper boundary condition (11.61) at the soil surface has to be changed to

$$G_{sfc} = (1 - f_{snow}) \cdot \left(c_p \hat{H}^3_{sfc} + L(F^3_{q^v})_{sfc} + Q_{rad,net} \right) + f_{snow} \cdot G_{snow} \tag{11.85}$$

in order to account for the influence of the snow deck.

(e) Implicit Solution of the Heat Conduction Equation for the Snow Deck

Because of the possibly very thin (0.01 m) snow deck an implicit solution for the temperature prediction of the snow deck is necessary. The general forecast equation for the mean temperature of the snow deck is

$$\frac{\partial T_{snow}}{\partial t} = F(T) \quad , \tag{11.86}$$

where the function $F(T_{snow})$ stands for the forcing terms $G_{sfc,snow}$ and G_{snow} in (11.73). The implicit solution is accomplished by averaging the function F over the old and the new time step

$$T^{n+1}_{snow} = T^{n-1}_{snow} + 2\Delta t \left[(1 - \beta) F(T^{n-1}_{snow}) + \beta F(T^{n+1}_{snow}) \right]. \tag{11.87}$$

Approximating

$$F(T^{n+1}_{snow}) \approx F(T^{n-1}_{snow}) + \left(\frac{\partial F}{\partial T_{snow}} \right)^{n-1} (T^{n+1}_{snow} - T^{n-1}_{snow}) \tag{11.88}$$

we get

$$T^{n+1}_{snow} = T^{n-1}_{snow} + \frac{2\Delta t F(T^{n-1}_{snow})}{1 - 2\Delta t \beta (\partial F / \partial T_{snow})^{n-1}} \tag{11.89}$$

If T'_{snow} is the preliminary temperature at time n+1 as given by the explicit forecast, then

$$T^{n+1}_{snow} = T^{n-1}_{snow} + \frac{T'_{snow} - T^{n-1}_{snow}}{1 - 2\Delta t \beta (\partial F / \partial T_{snow})^{n-1}}. \tag{11.90}$$

An estimation of the different contributions to the forcing terms being part of the function F shows the sensible and latent heat fluxes as well as the heatflux through the snow deck to provide the largest contributions. Differentiation with respect to time of the relations for the turbulent fluxes and for the heat flux through the snow deck leads to the following form

$$\frac{\partial F}{\partial T_{snow}} = - \frac{g \rho C_h (c_p + L_s dQ_{sat}/dT) + \lambda_{snow} / \Delta z_{snow}}{(\rho c \Delta z)_{snow}} \quad , \tag{11.91}$$

where dQ_{sat}/dT is the slope of the saturation curve. Operationally $\beta = 1.0$ is used.

11.4.3 Melting of Snow

If a snow deck is present, the temperature prediction step in soil and snow provides preliminary values only. If the snow surface temperature or the soil surface temperature exceed the freezing point, they are reduced to freezing point and melting of snow is considered.

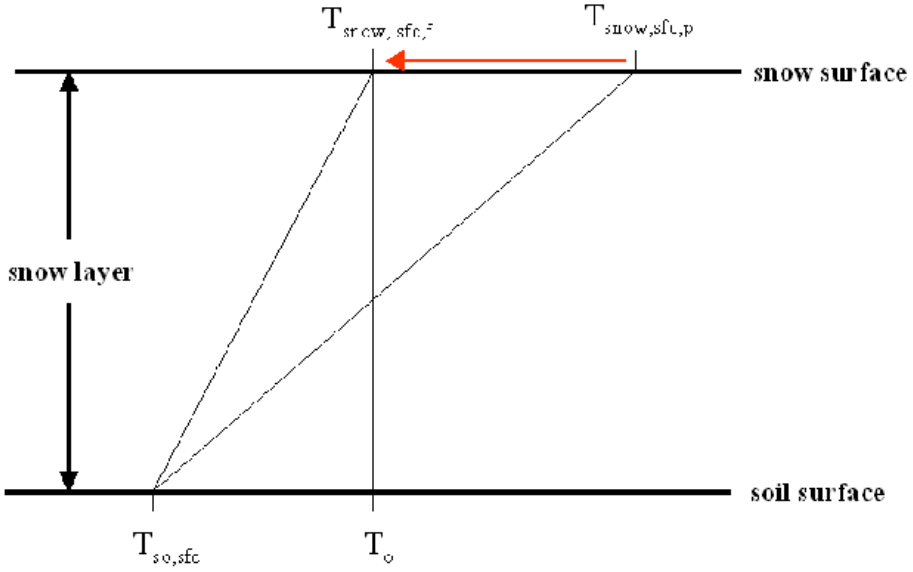

Figure 11.4: Preliminary and final snow temperature profile per time step, Case 1

Case 1:
The preliminary snow surface temperature $T^{n+1}_{snow,sfc,p}$ exceeds the freezing point, whereas the soil surface temperature T^{n+1}_{sfc} is below the freezing point.

Case 1 is graphically shown in Fig. 11.4. Starting at the preliminary snow surface temperature, the temperature is reduced to the final temperature $T_{snow,sfc,f} = T_0$. The soil surface temperature T_{sfc} is held constant. Energy considerations provide the amount of melted snow: The thermal energy of the snow deck before melting is given by $E_1 = \rho_w c_{ice} W_{snow}(T_{snow,sfc,p} + T_{sfc})/2$. The melting reduces the snow water content to $W_{snow} - \Delta W_1$, this requires the energy $E_m = \rho_w L_f \Delta W_1$. The melted snow carries the amount of energy $E_w = \rho_w c_{ice} \Delta W_1 T_0$, and after melting the energy of the snow is $E_2 = \rho_w c_{ice}(W_{snow} - \Delta W_1)(T_0 + T_{sfc})/2$. Energy conservation requires $E_1 = E_2 + E_m + E_w$. This relation can be solved to provide the change of the water content of the snow deck:

$$\Delta W_1 = W_{snow} \cdot \frac{T_{snow,sfc,p} - T_0}{T_0 - T_{sfc} + 2L_f/c_{ice}} \tag{11.92}$$

Because of the large value $2L_f/c_w \approx 160$ K no provision has to be made for a complete melting of the snow deck in this step. Actually, T_0 is replaced by a somewhat lower temperature $T_0 - \epsilon$ with $\epsilon = 10^{-6}$ K in order to avoid temperatures of exactly the freezing point. The mean snow temperature is changed by the amount $\Delta T_{snow,1} = 0.5(T_{snow,sfc,p} - T_0)$.

Case 2:
If the preliminary soil surface temperature $T^{n+1}_{sfc,p}$ exceeds the freezing point, the preliminary snow surface temperature $T_{snow,sfc,p}$ can be either $> T_0$ or $< T_0$ (only the second case is shown in Fig. 11.5).

First a heat transfer from the soil to the snow deck is performed. The mean temperature of the uppermost soil layer ($T_{sfc,p} \equiv T_{k=1}$) is reduced to T_0. This makes available the energy $(\rho c \Delta z)_{k=1}(T_{sfc,p} - T_0)$ for increasing the mean snow temperature from the value $T_{snow,p} = 0.5(T_{sfc} + T_{snow,sfc,p})$ to $T_{snow,p2} = 0.5(T_0 + T_{snow,sfc,p2}) = T_{snow,p} + \Delta T_{snow,2}$,

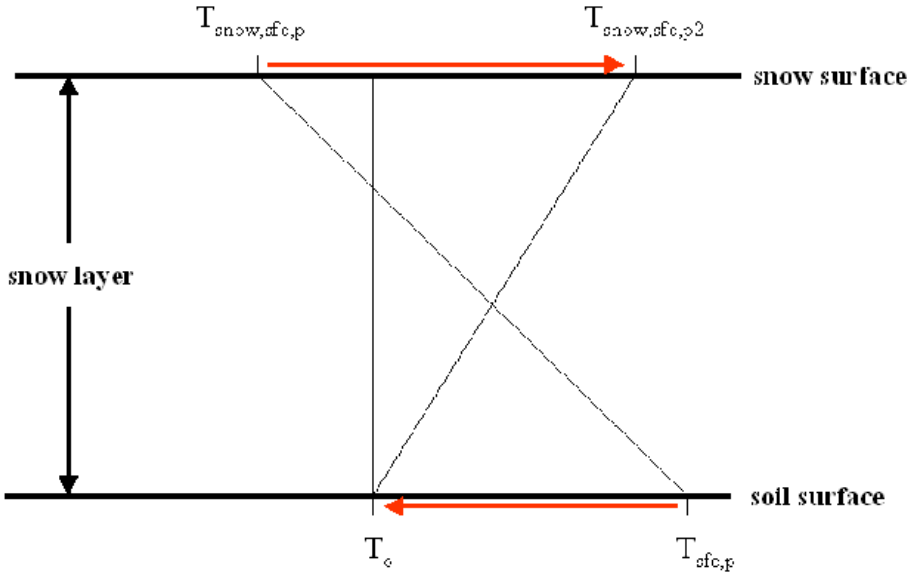

Figure 11.5: Preliminary and possible final snow temperature profile per time step, Case 2

where

$$\Delta T_{snow,2} = \frac{(\rho c \Delta z)_{k=1}}{(\rho c \Delta z)_{snow}} (T_{sfc,p} - T_0). \tag{11.93}$$

Accordingly, the new snow surface temperature is

$$T_{snow,sfc,p2} = 2[T_{snow,p} + \Delta T_{snow,2}] - T_0, \tag{11.94}$$

If this redistribution results in $T_{snow,sfc,p2} > T_0$, a melting step follows. The energy required for melting the total snow deck is $E_{mt} = L_f \rho_w W_{snow}$. The energy available from a reduction of the mean snow temperature to the freezing point is $E_{av} = 0.5(\rho c \Delta z)_{snow}$ $(T_{snow,sfc,p2} - T_0)$. This provides a further contribution to the change of the mean snow temperature $\Delta T_{snow,3} = 0.5(T_{snow,sfc,p2} - T_0)$. The fraction $m_{fr} = Min\{1; E_{av}/E_{mt}\}$ of the snow deck will be melted, and $\Delta W_2 = m_{fr} \cdot W_{snow}$. If $E_{av} > E_{mt}$, the remaining energy goes into warming the uppermost soil layer by the amount $\Delta T_{soil} = (E_{av} - E_{mt})/(\rho c \Delta z)_{k=1}$.

Infiltration and runoff

In the situation of a frozen soil surface as in Case 1 (and generally for soil types 1 and 2) infiltration of water is not possible. The total amount ΔW_1 of melted snow is considered as runoff. In the situation of Case 2 a splitting of the amount ΔW_2 of melted snow into infiltration and runoff is governed by the parameter

$$R_{fr} = Max \left\{ 0.0 \; ; \; Min\{1.0 \; ; \; \frac{w_{k=1} - w_{FC}}{w_{PV} - w_{FC}}\} \right\} \tag{11.95}$$

This yields

$$I_{snow} = \rho_w (1 - R_{fr}) \Delta W_2 / 2\Delta t \tag{11.96}$$

$$R_{snow} = \rho_w (\Delta W_1 + R_{fr} \Delta W_2) / 2\Delta t \tag{11.97}$$

Influence on the prediction of soil and snow temperatures

The heatflux G_{melt} describing the thermal effects on the tendency of the mean snow temperature of the melting snow is given by

$$G_{melt} = (\rho c \Delta z)_{snow}(\Delta T_{snow,1} + \Delta T_{snow,2} + \Delta T_{snow,3})/2\Delta t. \tag{11.98}$$

The influence on the temperature of the uppermost soil layer is given by

$$G_{snow,melt} = (\rho c \Delta z)_{k=1} \Delta T_{soil}/2\Delta t. \tag{11.99}$$

11.5 Freezing/Thawing Processes in the Soil

The exact treatment of freezing/thawing processes of water/ice in the soil requires an iterative solution of the heat conduction and the Richards equations in the soil, as they are coupled through these processes. But because of the very short timestep of LM, a simpler diagnostic approach seems to be sufficient.

Freezing/thawing processes in the soil layers are considered after finishing steps a) solution of the heat conduction equation and b) melting of snow. If by these processes the predicted preliminary temperature $T_{so,p}$ falls below (exceeds) a prescribed threshold temperature T_*, freezing (thawing) is considered.

The simplest approach would be to use the freezing point as a threshold temperature. But tests showed a much too strong influence on the near surface temperatures of the freezing/thawing process. It is well known from soil physics that a considerable amount of unfrozen water can remain in a soil even at temperatures well below the freezing point. Warrach (2000) uses a relation for the maximum of the unfrozen volumetric water content $w_{l,max}$ in the soil based on a suggestion by Flerchinger and Saxton (1989). The unfrozen (i. e. liquid) water content depends on the temperature and on the hydrologic characteristics of the soil:

$$w_{l,max} = w_{PV} \left[\frac{L_f (T_{so} - T_0)}{T_{so} g \Psi_s} \right]^{-1/b}. \tag{11.100}$$

Here g is the gravitational acceleration, Ψ_s is the air entry potential at saturation, and b is the pore-size distribution index ((Brooks and Corey 1966)). After Cosby et al. (1984) the air entry potential Ψ_s and the pore-size distribution index b are determined by the soil type,

$$\Psi_s = \Psi_0 \cdot 10^{1.88 - 1.3 f_s} \tag{11.101}$$

$$b = 2.91 + 15.9 f_c \quad , \tag{11.102}$$

where Ψ_0 is -0.01 m, and f_s and f_c are the fractions of sand and of clay in the soil, respectively. Table 11.2 shows for the different soil types the fractions f_s and f_c (the remaining part of the soil fractions is assumed to be silt), the air entry potential Ψ_s calculated by (11.101) and the pore-size distribution index b calculated by (11.102). There are non values available for peat. Tentatively we use the same values as for sand.

Equation (11.100) can be transformed to calculate the equilibrium temperature T_* as function of the water content w_l at the beginning of the current time step:

$$T_* = T_0 \left[1 - \frac{g \Psi_s}{L_f} \left(\frac{w_{PV}}{w_l} \right)^b \right]^{-1}. \tag{11.103}$$

Table 11.2: Soil-type dependent parameters for the determination of the soil ice/water content. See text for details.

	f_s	f_c	Ψ_s(m)	b
sand	0.90	0.05	- 0.0513	3.705
sandy loam	0.65	0.10	- 0.1084	4.50
loam	0.40	0.20	- 0.2291	6.09
loamy clay	0.35	0.35	- 0.2661	8.47
clay	0.15	0.70	- 0.4842	14.04

This equilibrium temperature is used as a threshold temperature for the initiation of freezing/thawing processes in the soil.

The energy difference, which is proportional to the temperature difference $T_{so,p}$ - T_*, is used to melt ice or to freeze liquid water, that is

$$\Delta E = (\rho c)\Delta z(T_{so,p} - T_*) \quad . \tag{11.104}$$

This energy amount is used to determine the change of the water/ice content by

$$\Delta W_{l,max} = -\Delta W_{ice,max} = \frac{\Delta E}{L_f \rho_w} \tag{11.105}$$

This computed maximum value for the change of the water and ice contents, respectively, has to be restricted by the available amounts:

$$\Delta w_{ice} = -Min\{-\Delta w_{ice,max}; Min\,[-(w - w_{l,max} - w_{ice})]\} \text{ if } \Delta w_{ice,max} < 0 \tag{11.106}$$

$$\Delta w_{ice} = Min\{\ \Delta w_{ice,max}; Max[\ (w - w_{l,max} - w_{ice})]\} \text{ if } \Delta w_{ice,max} > 0 \tag{11.107}$$

These equations can be used to calculate the source term S_k in (11.3).

$$S_k = -\rho_w \frac{\Delta W_{ice,k}}{\Delta t} \quad . \tag{11.108}$$

The final temperature T_{so} can be calculated through the relation

$$T_{so} = T_* + (\Delta w_{ice} - \Delta w_{ice,max}) \frac{(L_f \rho_w)}{(\rho c \Delta z)} \quad . \tag{11.109}$$

Section 12

Fresh-Water Lake Parameterization Scheme FLake

In this section, a brief description of the lake model (parameterisation scheme) is presented. A detailed description of the model, that is termed FLake, is given in Mironov (2008), where an overview of previous studies, an extensive discussion of various parameterisation assumptions and of the model disposable constants and parameters, and references to relevant publications can be found (see also the FLake web page http://lakemodel.net).

FLake is a bulk model capable of predicting the vertical temperature structure and mixing conditions in lakes of various depth on the time scales from a few hours to many years. The model is based on a two-layer parametric representation of the evolving temperature profile and on the integral budgets of energy for the layers in question. The structure of the stratified layer between the upper mixed layer and the basin bottom, the lake thermocline, is described using the concept of self-similarity (assumed shape) of the temperature-depth curve (Kitaigorodskii and Miropolsky (1970)). The same concept is used to describe the temperature structure of the thermally active upper layer of bottom sediments and of the ice and snow cover. Using the integral approach, the problem of solving partial differential equations (in depth and time) for the temperature and turbulence characteristics is reduced to solving a number of ordinary differential equations for the time-dependent quantities that specify the evolving temperature profile. These are the mixed-layer temperature and the mixed-layer depth, the temperature at the water-bottom sediment interface, the mean temperature of the water column, the shape factor with respect to the temperature profile in the thermocline, the temperature at the upper surface of lake ice, and the ice thickness. Optionally, the bottom sediment module can be switched on to account for the interaction between the lake water and the bottom sediment. Then, two additional quantities are predicted, viz., the depth of the upper layer of bottom sediments penetrated by thermal wave and the temperature at that depth. Provision is made to explicitly account for the layer of snow above the lake ice. Then, prognostic equations are carried for the temperature at the snow upper surface and for the snow thickness. FLake has been favourably tested against observational data through single-column numerical experiments. Further information about FLake, including an on-line version of the model (Kirillin et al. (2011)), can be found at http://lakemodel.net.

In what follows, a short summary of FLake is presented, more specifically, of its simplified configuration currently used within COSMO (Mironov et al. (2010)). The bottom-sediment module is switched off and the heat flux through the water-bottom sediment interface is set

to zero. Snow over lake ice is not considered explicitly; the effect of snow is accounted for implicitly through the temperature dependence of the surface albedo with respect to solar radiation.

The following quadratic equation of state of the fresh water is utilised:

$$\rho_w = \rho_r \left[1 - \frac{1}{2} a_T \left(\theta - \theta_r\right)^2\right], \tag{12.1}$$

where ρ_w is the water density, $\rho_r = 999.98 \approx 1.0 \cdot 10^3$ kg·m^{-3} is the maximum density of the fresh water at the temperature $\theta_r = 277.13$ K, and $a_T = 1.6509 \cdot 10^{-5}$ K^{-2} is an empirical coefficient. According to Eq. (12.1), the thermal expansion coefficient α_T and the buoyancy parameter β depend on the water temperature,

$$\beta(\theta) = g\alpha_T(\theta) = g a_T(\theta - \theta_r), \tag{12.2}$$

where $g = 9.81$ m·s^{-2} is the acceleration due to gravity.

The following two-layer parametric representation of the evolving temperature profile is adopted (Kitaigorodskii and Miropolsky 1970):

$$\theta = \begin{cases} \theta_s & \text{at} \quad 0 \le z \le h \\ \theta_s - (\theta_s - \theta_b)\Phi_\theta(\zeta) & \text{at} \quad h \le z \le D. \end{cases} \tag{12.3}$$

Here, $\theta_s(t)$ is the temperature of the upper mixed layer of depth $h(t)$, $\theta_b(t)$ is the bottom temperature, i.e. the temperature at the water-bottom sediment interface $z = D$, and $\Phi_\theta \equiv (\theta_s - \theta) / (\theta_s - \theta_b)$ is a dimensionless "universal" function of dimensionless depth $\zeta \equiv (z - h) / (D - h)$ that satisfies the boundary conditions $\Phi_\theta(0) = 0$ and $\Phi_\theta(1) = 1$. With rare exceptions, the arguments of variables dependent on time t and vertical co-ordinate z (positive downward) are not indicated in what follows.

According to Eq. (12.3), h, D, θ_s, θ_b, and the mean temperature of the water column,

$$\overline{\theta} \equiv D^{-1} \int_0^D \theta dz, \tag{12.4}$$

are related through

$$\overline{\theta} = \theta_s - C_\theta(1 - h/D)(\theta_s - \theta_b), \tag{12.5}$$

where C_θ is the shape factor with respect to the temperature profile in the thermocline,

$$C_\theta = \int_0^1 \Phi_\theta(\zeta) d\zeta. \tag{12.6}$$

It should be emphasised at once that the exact form of the shape function is not required within the framework of the integral approach used to develop FLake. It is not Φ_θ but the shape factor C_θ that enters the model equations.

The equation for the mean temperature of the water column (i.e. the equation of the total heat budget obtained by integrating one-dimensional heat transfer equation over z from 0 to D) reads

$$D\frac{d\overline{\theta}}{dt} = \frac{1}{\rho_w c_w} \left[Q_s + I_s - Q_b - I(D)\right], \tag{12.7}$$

where $c_w = 4.2 \cdot 10^3 \mathrm{J \cdot kg^{-1} \cdot K^{-1}}$ is the specific heat of water, Q_s and I_s are the values of the vertical turbulent heat flux Q and of the heat flux due to solar radiation I, respectively, at the lake surface, and Q_b is the heat flux through the lake bottom. The radiation heat flux I_s that penetrates into the water is the surface value of the incident solar radiation flux from the atmosphere multiplied by $1 - \alpha_w$, where α_w is the albedo of the water surface with respect to solar radiation. The surface flux Q_s is a sum of the sensible and latent heat fluxes and the net heat flux due to long-wave radiation at the air-water interface.

The equation of heat budget of the mixed layer reads

$$h\frac{d\theta_s}{dt} = \frac{1}{\rho_w c_w}\left[Q_s + I_s - Q_h - I(h)\right], \tag{12.8}$$

where Q_h is the heat flux at the bottom of the mixed layer.

In the case of the mixed-layer stationary state or retreat, $dh/dt \leq 0$, the bottom temperature is assumed to remain constant,

$$\frac{d\theta_b}{dt} = 0. \tag{12.9}$$

In the case of the mixed-layer deepening, $dh/dt > 0$, the following equation is used:

$$\frac{1}{2}(D-h)^2\frac{d\theta_s}{dt} - \frac{d}{dt}\left[C_{\theta\theta}(D-h)^2(\theta_s - \theta_b)\right] =$$

$$\frac{1}{\rho_w c_w}\left[C_Q(D-h)(Q_h - Q_b) + (D-h)I(h) - \int_h^D I(z)dz\right], \tag{12.10}$$

where

$$C_{\theta\theta} = \int_0^1 d\zeta \int_0^\zeta \Phi_\theta(\zeta')d\zeta' \tag{12.11}$$

is a dimensionless parameter, and

$$C_Q = 2C_{\theta\theta}/C_\theta \tag{12.12}$$

is the shape factor with respect to the heat flux.

If $h = D$, then both θ_s and θ_b are equal to the mean temperature of the water column that is computed from Eq. (12.7). Recall that the bottom heat flux Q_b is set to zero in the present model configuration.

During convective mixed-layer deepening, h is determined from the following entrainment equation:

$$-\frac{Q_h}{Q_*} + \frac{C_{c2}}{w_*}\frac{dh}{dt} = C_{c1}. \tag{12.13}$$

Here, Q_* and w_* are generalised convective scales of heat flux and of velocity, respectively, that account for the volumetric character of the solar radiation heating,

$$Q_* = Q_s + I_s + I(h) - 2h^{-1}\int_0^h I(z)dz, \qquad w_* = \left[-h\beta(\theta_s)Q_*/(\rho_w c_w)\right]^{1/3}, \tag{12.14}$$

and $C_{c1} = 0.17$ and $C_{c2} = 1.0$ are dimensionless constants.

The depth of a stably or neutrally stratified wind-mixed layer is determined from the following relaxation-type rate equation:

$$\frac{dh}{dt} = \frac{h_e - h}{t_{rh}}. \tag{12.15}$$

Here, t_{rh} is the relaxation time scale estimated as

$$t_{rh} = \frac{h_e}{C_{rh} u_*}, \tag{12.16}$$

where $u_* = |\tau_s/\rho_w|^{1/2}$ is the surface friction velocity, τ_s being the surface stress, and $C_{rh} = 0.03$ is a dimensionless constant. The equilibrium mixed-layer depth h_e is computed from

$$\left(\frac{f h_e}{C_n u_*}\right)^2 + \frac{h_e}{C_s L} + \frac{N h_e}{C_i u_*} = 1, \tag{12.17}$$

where $f = 2\Omega \sin\phi$ is the Coriolis parameter, $\Omega = 7.29 \cdot 10^{-5}$ s^{-1} is the angular velocity of the Earth's rotation, ϕ is the geographical latitude, $L = u_*^3/[\beta(\theta_s) Q_* / \rho_w c_w]$ is the Obukhov length, N is the buoyancy frequency below the mixed layer, and $C_{sn} = 0.5$, $C_{ss} = 10$, and $C_{si} = 20$ are dimensionless constants. A generalised formulation of the Obukhov length that accounts for the vertically distributed character of the solar radiation heating is used. A mean-square buoyancy frequency in the thermocline,

$$\overline{N} = \left[(D-h)^{-1} \int_h^D N^2 dz\right]^{1/2}, \tag{12.18}$$

is used as an estimate of N in Eq. (12.17).

The equilibrium mixed-layer depth is limited from below by the depth of a convectively mixed layer whose deepening driven by the surface cooling ($Qs < 0$) is arrested by the volumetric radiation heating ($I > 0$). The equilibrium depth h_c of such layer is computed from

$$Q_*(h_c) = Q_s + I_s + I(h_c) - 2h_c^{-1} \int_0^{h_c} I(z) dz = 0, \tag{12.19}$$

where a finite solution $h_c < \infty$ exists if $-Qs/Is < 1$. If Eq. (12.17) predicts a very shallow stably-stratified equilibrium mixed layer to which the mixed layer (whose current depth h exceeds h_e) should relax, then it is required that $h_e \geq h_c$. This limitation is imposed if the mixed-layer temperature θ_s exceeds the temperature θ_r of maximum density of fresh water and $Q_*(h) > 0$ [a negative $Q_*(h)$ indicates that the mixed layer is convective, so that Eq. (12.13) should be used to compute h].

The approach used to describe the temperature structure of the lake ice is conceptually similar to the approach used to describe the temperature structure of the lake thermocline. The following parametric representation of the evolving temperature profile within the ice is adopted [cf. Eq. (12.3)]:

$$\theta = \theta_f - (\theta_f - \theta_i)\Phi_i(\zeta_i), \tag{12.20}$$

where z is the vertical co-ordinate (positive downward) with the origin at the ice-water interface, $h_i(t)$ is the ice thickness, θ_f=273.15 K is the fresh-water freezing point, and $\theta_i(t)$

is the temperature at the ice upper surface. Dimensionless "universal" function $\Phi_i \equiv [\theta_f - \theta(z,t)]/[(\theta_f - \theta_i(t)]$ of dimensionless depth $\zeta_i \equiv -z/h_i(t)$ satisfies the boundary conditions $\Phi_i(0) = 0$, and $\Phi_i(1) = 1$.

The equation of the heat budget of the ice layer reads

$$\frac{d}{dt}\{\rho_i c_i h_i \left[\theta_f - C_i(\theta_f - \theta_i)\right]\} - \rho_i c_i \theta_i \frac{dh_i}{dt} =$$

$$Q_s + I_s - I(0) + \kappa_i \frac{\theta_f - \theta_i}{h_i}\Phi_i'(0). \tag{12.21}$$

where $\rho_i = 9.1 \cdot 10^2$ kg·m^{-3}, $c_i = 2.1 \cdot 10^3$ J·kg^{-1}·K^{-1} and $\kappa_i = 2.29$ J·m^{-1}·s^{-1}·K^{-1} are the density, the specific heat and the heat conductivity of ice, respectively, Q_s and I_s are the values of Q and I, respectively, at the ice upper surface $z = -h_i(t)$, and $\Phi_i'(0) = d\Phi_i/d\zeta_i$ at $\zeta_i = 0$. The radiation heat flux I_s that penetrates into the ice interior is the surface value of the incident solar radiation flux from the atmosphere multiplied by $1 - \alpha_i$, where α_i is the ice surface albedo with respect to solar radiation. The dimensionless parameters C_i is the shape factor with respect to the temperature profile within the ice,

$$C_i = \int_0^1 \Phi_i(\zeta_i) d\zeta_i. \tag{12.22}$$

Equation (12.21) serves to determine θ_i when this temperature is below the freezing point θ_f, i.e. when no melting at the ice upper surface takes place. During the ice melting from above, θ_i remains equal to θ_f.

During the ice growth or ice melting from below (these occur as $\theta_i < \theta_f$), the ice thickness is computed from the following equation:

$$L_f \frac{d\rho_i h_i}{dt} = Q_w + \kappa_i \frac{\theta_f - \theta_i}{h_i}\Phi_i'(0), \tag{12.23}$$

where $L_f = 3.3 \cdot 10^5 \cdot$ J·kgi^{-1} is the latent heat of fusion, and Q_w is the heat flux in the near-surface water layer just beneath the ice. If the right-hand side of Eq. (12.23) is negative (this may occur due to a negative Q_w), ice ablation takes place.

During the ice melting from above, the following equation is used:

$$L_f \frac{d\rho_i h_i}{dt} = -(Q_s + I_s) + Q_w + I(0), \tag{12.24}$$

that holds as the atmosphere heats the ice upper surface and θ_i is equal to θ_f.

The evolution of the temperature profile beneath the ice is described as follows. The temperature at the ice-water interface is fixed at the freezing point, $\theta_i = \theta_f$. The mean temperature of the water column is computed from Eq. (12.7), where Q_s and I_s are replaced with Q_w and $I(0)$, respectively. If the bottom temperature is less than the temperature of maximum density, $\theta_b < \theta_r$, the mixed-layer depth and the shape factor with respect to the temperature profile in the thermocline are kept unchanged, $dh/dt = 0$ and $dC_\theta/dt = 0$, and the bottom temperature is computed from Eq. (12.5). If the entire water column appears to be mixed at the moment of freezing, i.e. $h = D$ and $\theta_s = \theta_b$, the mixed-layer depth is reset to zero, $h = 0$, and the shape factor is reset to its minimum value, $C_\theta = C_\theta^{min}$. As the bottom temperature reaches the temperature of maximum density, its further increase is prevented and θ_b is kept

constant equal to θ_r. If $h > 0$, the shape factor C_θ is kept unchanged, and the mixed-layer depth is computed from Eq. (12.5). As the mixed-layer depth approaches zero, Eq. (12.5) is used to compute the shape factor C_θ that in this regime increases towards its maximum value, $C_\theta = C_\theta^{max}$ (estimates of C_θ^{min} and C_θ^{max} are given below). If $h = 0$, the heat flux from water to ice is estimated from

$$Q_w = -\kappa_w \frac{\theta_b - \theta_s}{D} \max\left[1, \Phi'_\theta(0)\right], \tag{12.25}$$

where $\kappa_w = 5.46 \cdot 10^{-1}$ J·m^{-1}·s^{-1}·K^{-1} is the molecular heat conductivity of water, and $\Phi'_\theta(0) = d\Phi_\theta/d\zeta$ at $\zeta = 0$. If $h > 0$, $Q_w = 0$.

The shape factor with respect to the temperature profile in the thermocline is computed from

$$\frac{dC_\theta}{dt} = \mathrm{sign}(dh/dt)\frac{C_\theta^{max} - C_\theta^{min}}{t_{rc}}, \qquad C_\theta^{min} \le C_\theta \le C_\theta^{max}, \tag{12.26}$$

where sign is the sign function [sign$(x) = -1$ if $x \le 0$ and sign$(x) = 1$ if $x > 0$]; $C_\theta^{min} = 0.5$ and $C_\theta^{max} = 0.8$ are minimum and maximum values of the shape factor, respectively. The shape factor C_θ evolves towards its maximum value during the mixed-layer deepening, and towards its minimum value during the mixed-layer stationary state or retreat. The adjustment occurs on a relaxation time scale t_{rc} estimated as

$$t_{rc} = \frac{(D-h)^2\overline{N}}{C_{rc}u_T^2}, \qquad u_T = \max(w_*, u_*), \tag{12.27}$$

where $C_{rc} = 0.003$ is a dimensionless constant, and the mean-square buoyancy frequency in the thermocline is given by Eq. (12.18). Notice that Eqs. (12.26) and (12.27) are used during the period of open water. During the period of ice cover, a different procedure is used as outlined above.

The dimensionless parameter $C_{\theta\theta}$ defined through Eq. (12.11) is given by

$$C_{\theta\theta} = \frac{11}{18}C_\theta - \frac{7}{45}, \tag{12.28}$$

and the quantity $\Phi'_\theta(0)$ that enters Eq. (12.25) is given by

$$\Phi'_\theta(0) = \frac{40}{3}C_\theta - \frac{20}{3}. \tag{12.29}$$

The shape factor with respect to the temperature profile within the ice is computed from

$$C_i = \frac{1}{2} - \frac{1}{12}(1 + \Phi_{*i})\frac{h_i}{h_i^{max}}. \tag{12.30}$$

where $h_i^{max} = 3$ m and $\Phi_{*i} = 2$. The quantity $\Phi'_i(0)$ that enters Eqs. (12.21) and (12.23) is given by

$$\Phi'_i(0) = 1 - \frac{h_i}{h_i^{max}}. \tag{12.31}$$

The exponential approximation of the decay law for the flux of solar radiation is used,

$$I(t,z) = I_s(t)\sum_{k=1}^{n} a_k \exp[-\gamma_k(z + h_i)], \tag{12.32}$$

where I_s is the surface value of the incident solar radiation flux multiplied by $1-\alpha$, α being the albedo of the water surface or of the ice surface with respect to solar radiation, n is the number of wavelength bands, a_k are fractions of the total radiation flux for different wavelength bands, and γ_k are attenuation coefficients for different bands. The attenuation coefficients are piece-wise constant functions of z, i.e. they have different values for water and ice but remain constant within these media. At present, the simplest one-band approximation is used with $\gamma = 3$ m^{-1} for water and $\gamma = 10^7$ m^{-1} for ice. With these values, the vertically distributed heating is basically confined to the uppermost metre of the water column of ice-free lakes (95% of solar radiation is absorbed there), and no solar radiation penetrates into the interior of ice-covered lakes so that the solar heating is confined to the ice surface.

The following parameterisation of the ice surface albedo with respect to solar radiation is adopted:

$$\alpha_i = \alpha_i^{max} - \left(\alpha_i^{max} - \alpha_i^{min}\right) \exp\left[-C_\alpha \left(\theta_f - \theta_i\right)/\theta_f\right], \tag{12.33}$$

where $\alpha_i^{max} = 0.6$ and $\alpha_i^{min} = 0.1$ are maximum and minimum values of the ice albedo, respectively, $C_\alpha = 95.6$ is a fitting coefficient. Equation (12.33) is meant to implicitly account, in an approximate manner, for the presence of snow over lake ice and for the seasonal changes of α_i. During the melting season, the ice surface temperature is close to the fresh-water freezing point. The presence of wet snow, puddles, melt-water ponds and leads on the surface of melting ice results in a decrease of the area-averaged surface albedo. The water surface albedo with respect to solar radiation, α_w, is taken to be constant equal to 0.07.

The two time level Euler scheme is used for time advance of FLake prognostic variables. Numerous comment lines are put into the source code to give details of the scheme implementation. In order to be used within COSMO, FLake requires a number of two-dimensional external-parameter fields. These are, first of all, the fields of lake fraction (area fraction of a given numerical-model grid box covered by the lake water) and of lake depth. The generation of lake-fraction and lake-depth external parameter fields is discussed in section 14. Other external parameters of FLake are set to their default values constant in space and time. Those parameters are handled internally within COSMO and are not part of COSMO IO. Although provision is made to explicitly account for the snow layer above the ice (see Mironov 2008, for details), the use of snow module of FLake in NWP and climate modelling is not recommended until it is comprehensively tested. Thermal interaction between the water column and the bottom sediments is an issue for shallow lakes only. Experience suggests that for lakes deeper than about 5 m the heat flux through the bottom can safely be neglected. If the interaction between the water column and the bottom sediments should be accounted for, empirical information is required to estimate the depth of the thermally active layer of bottom sediments and the climatological temperature at that depth. Such information is rarely available. For NWP, a recommended choice at present is to switch off the bottom-sediment module of FLake.

Section 13

Parameterization of Sea Ice

13.1 Introduction

The presence of sea ice on the ocean's surface has a significant impact on the air-sea interactions. Compared to an open water surface the sea ice completely changes the surface characteristics in terms of albedo and roughness, and therefore substantially changes the surface radiative balance and the turbulent exchange of momentum, heat and moisture between air and sea.

In order to deal with these processes the COSMO model includes a sea ice scheme (Mironov and Ritter 2004). Its implementation in the operational COSMO-EU model at DWD is described by Schulz (2011). The COSMO-EU model domain covers almost all Europe using a mesh size of 7 km, in particular it includes the entire Baltic Sea and parts of the White Sea and Barents Sea (Schulz 2006). Therefore, it is relevant to use an appropriate sea ice scheme in this model.

13.2 The Sea Ice Scheme

The sea ice scheme by Mironov and Ritter (2004) accounts for thermodynamic processes, while no rheology is considered. It basically computes the energy balance at the ice's surface, using one layer of sea ice. From this the evolution of the ice surface temperature T_{ice} and the ice thickness H_{ice} are deduced. These two prognostic variables allow for a thermodynamically coupled treatment of sea ice in the COSMO model as lower boundary condition for the atmosphere. In particular, the scheme allows for very low surface temperatures which can be significantly lower than the water temperature below the ice.

The sea ice surface temperature T_{ice} is computed by the surface energy balance equation:

$$\frac{\Delta T_{\mathrm{ice}}}{\Delta t} = \frac{1}{c\, H_{\mathrm{ice}}} \left[\frac{Q_{\mathrm{A}} + Q_{\mathrm{I}}}{\rho_{\mathrm{ice}}\, C_{\mathrm{ice}}} \right] \tag{13.1}$$

where Q_{A} is the sum of all atmospheric energy fluxes at the ice's surface (solar and thermal radiation plus sensible and latent heat flux), Q_{I} is the vertical conductive heat flux through the ice layer of thickness H_{ice}, $\rho_{\mathrm{ice}} = 910$ kg m^{-3} is the ice density, $C_{\mathrm{ice}} = 2100$ J kg^{-1} K^{-1} the ice heat capacity, $c = 0.5$ a shape factor and t the time.

The internal heat flux Q_I through the ice layer is computed by

$$Q_\mathrm{I} = -\lambda_\mathrm{ice} \frac{T_\mathrm{ice} - T_\mathrm{bot}}{H_\mathrm{ice}} \tag{13.2}$$

where $\lambda_\mathrm{ice} = 2.3$ W m^{-1} K^{-1} is the ice heat conductivity and T_bot the temperature at the bottom of the ice layer. It is set constant to $T_\mathrm{bot} = -1.7°\mathrm{C}$ which is assumed to be the freezing temperature of salty sea water.

In the case of $T_\mathrm{ice} = 0°\mathrm{C}$ and $Q_\mathrm{A} \geq 0$ W m^{-2} all available energy at the ice's surface is used for melting, leading to a reduction of the sea ice thickness H_ice according to

$$\frac{\Delta H_\mathrm{ice}}{\Delta t} = -\frac{Q_\mathrm{A}}{\rho_\mathrm{ice}\, L_\mathrm{f}} \tag{13.3}$$

where $L_\mathrm{f} = 0.334 \cdot 10^6$ J kg^{-1} is the latent heat of freezing. In this case the heat flux Q_I is neglected.

In all other cases the evolution of H_ice is governed by the following equation:

$$\frac{\Delta H_\mathrm{ice}}{\Delta t} = \frac{Q_\mathrm{I}}{\rho_\mathrm{ice}\, L_\mathrm{f}} \tag{13.4}$$

This means that the internal ice heat flux Q_I is balanced by the amount of energy involved in the phase transitions between liquid and frozen water at the bottom of the sea ice layer, i. e. the interface between ice and water. If for instance $T_\mathrm{ice} < -1.7°\mathrm{C}$, this will lead to an ice heat flux Q_I which is directed upward from the water into the ice layer. The source of this heat flux is assumed to be the latent heat of freezing of an equivalent amount of water, which while freezing will lead to a growing sea ice thickness H_ice.

13.3 The Sea Ice Distribution

The horizontal distribution of the sea ice cover in the model domain is governed by the data assimilation scheme. This means that the sea ice scheme can not create new sea ice points, it can not start freezing the water by itself.

For instance, in the model chain at DWD first the remote sensing based sea ice mask from NCEP (National Centers for Environmental Prediction, USA) is provided by the sea surface temperature (SST) analysis to the global model GME. This GME sea ice mask is then again interpolated by the SST analysis to the COSMO-EU grid. During this last interpolation an additional high-resolution sea ice mask is used to improve the ice distribution on the COSMO grid in particular in the Baltic Sea. This high-resolution sea ice mask is issued by BSH (Bundesamt für Seeschifffahrt und Hydrographie, Germany) and is updated every few days.

Section 14

External Parameters

14.1 Introduction

External parameters are mainly used to describe the status of the earth's surface (orography, land-sea-mask, etc.). In general, two different types of parameters have to be distinguished here:

a) the *primary data*, which are directly available from data sets offered by specialized institutions (e.g. orography or dominant land use of a grid element), and

b) the *secondary data*, which have to be derived from the primary data in order to serve the needs of the model (e.g. plant cover has to be derived from the dominant land use).

Some of the external parameter fields are generally constant (e.g. orography). Other fields are treated as constant during a forecast run, but they depend on the time of the year (plant characteristics). For these latter parameters the actual values are determined by interpolation in time between maximum and minimum values. This interpolation is done in connection with the provision of initial and boundary conditions. The maximum and minimum values of the respective characteristic parameters are provided as constant fields.

This section describes the input data sets and the methods to derive the fields required by LM. Most of the primary data needed can be downloaded from the Internet, some special data sets have to be purchased.

14.2 Primary data

The primary data are orography, dominant land use, dominant soil type, and annual mean near surface temperature. Whereas orography can directly be used as a lower boundary condition for LM, dominant land use and dominant soil type have to be transformed to the data required by LM.

14.2.1 Orography

The **GTOPO30** data set of the height of land surfaces used for LM is provided by the U.S. Geological Service (see: `http://edcdaac.usgs.gov/gtopo30/gtopo30.asp`). The Digital Elevation Model (DEM) has a truly global coverage of 30 arc seconds resolution in a geographic projection. This makes a total of 21600 × 43200 data points. Ocean points are assigned a value of -9999. The accuracy of the heights strongly depends on the source of the different regional DEM's used for this global compilation. Characteristic rmse-values range from 18 m (for areas where digital terrain elevation data are available, that is roughly 50% of the global land area) to 304 m (for the area of Peru, 0.1% of the global land area). Over Greenland the data are known to be affected by a rather large bias. The data set is available free of charge, it can be downloaded from the Internet.

A data set similar to GTOPO30 is **GLOBE**, a DEM provided by the National Geophysical Data Center (see: `http://www.ngdc.noaa.gov/mgg/topo/globe.html`). This is also a truly global 30 arc seconds data set. Because in Central Europe the differences between GTOPO30 and GLOBE are small and unsystematic, the change to use GLOBE was not made in LM, although in the global model GME GLOBE is used because of the Greenland-problem.

The transformation of either of the data sets to the LM-grid is done by a simple averaging of the available DEM-values in the respective LM grid-cell to describe the mean height of the grid-cell. At the same time the subgrid-scale variance of orography is computed, which is required for the determination of the roughness length.

For the external parameters of the new operational applications LME and LMK at DWD the GLOBE data set is used. Fig. 14.1 as an example shows the orography used for LMK with a resolution of 0.025° (about 2.8 km) for the highest part of the Alps. For LMK the resolution of the data set is three times higher than the model resolution. Therefore orographic details are clearly represented in the model resolution.

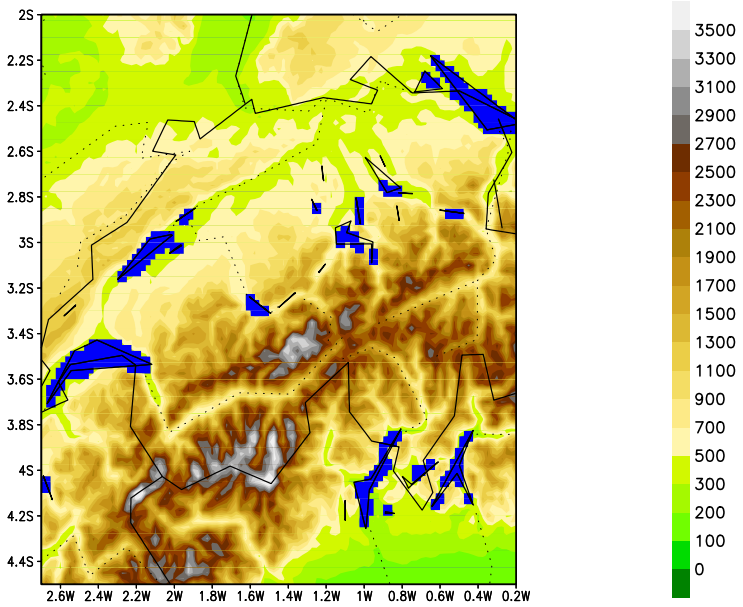

Figure 14.1: LMK-orography for part of the Alps

14.2.2 Dominant land cover

For land cover two data sets are used:

a) The **Global Land Cover Characteristics** (GLCC) data set is provided by the U.S. Geological Service (see: `http://edcdaac.usgs.gov/glcc/glcc.asp`). The data set covers most of the global land surfaces, the main exception is Antarctica. The resolution is 1 km on the Interrupted Goode Homolosine projection. The determination of land cover types is based on 1 year (April 1992 to March 1993) 1 km AVHRR-data. 24 different land cover types are interpreted from the AVHRR-data. The accuracy of the automatic interpretation was tested by classifying manually randomly chosen areas on the basis of AVHRR-data against Landsat- and Spot-data. This revealed an accuracy estimate of roughly 65% correct pixels. The data set is available free of charge, it can be downloaded from the Internet or copied by anonymous ftp.

b) The **CORINE** data set of land cover is based on a European Union initiative. It is available for (most of) the former 15 nations of the European Union in 250 m resolution on a Lambert azimuthal equal area projection. As the resolution of this data set is higher and as the quality seems to be very good, CORINE replaces the GLCC data set where it is available.

The **Global Landcover 2000 Database** (European Commission, Joint Research Centre; GLC2000, see: `http://www-gvm.jrc.it/glc2000`) is used in a re-evaluation of plant parameters. The data set with a resolution of 1 km covers the whole globe with the exception of Antarctica in a geographical latitude/longitude projection. The data set is based on the evaluation of NDVI-measurements of the SPOT4-satellite for the period 01 January to 31 December, 2000. Presently this data set is used for the determination of plant parameters for the GME and for the new operational applications at DWD, LME and LMK.

14.2.3 Dominant soil type

The dominant soil type data set is taken from the **Digital Soil Map of the World** (DSMW) CD-ROM (see: `http://www.fao.org/ag/agl/agll/dsmw.HTM`), which is based on the FAO/UNESCO Soil Map of the World (FAO-Unesco (1974)). The data set has a resolution of 5 arc minutes in a geographic projection. In order to get the data set, the CD-ROM has to be purchased from FAO (token fee). From the description of the Soil Map of the World it is worth to notice that

a) there is a great variety of soil classifications in the different nations of the world, from which a common definition had to be compiled, and that

b) there are large areas in the world were no systematic classification of soils was performed yet. In the latter areas, only occasional or reconnaissance field observations are available. Here soil types and their boundaries were deduced from land forms, geology, vegetation and climate information and partly from *general information*. This seriously restricts the accuracy of the data.

The main characteristic information used is the soil texture of the upper 30 cm of the soil. Three classes are distinguished, reflecting the relative proportions of clay (grain fraction less

Table 14.1: Correspondence between numbers, accompanying soil characteristics and short names

No.	**soil characteristic**	**name**
1	Glacier/Ice	'ice'
2	Lithosols	'rock'
3	Coarse textured	'sand'
4	Coarse to medium textured	'sandy loam'
5	Medium textured	'loam'
6	Medium to fine textured	'loamy clay'
7	Fine textured	'clay'
8	Histosols	'peat'

than 2 μm), silt (2 to 50 μm) and sand (50 to 2000 μm). The classes are: Coarse textured (less than 18% clay and more than 65% sand), medium textured (less than 35% clay and less than 65% sand), fine textured (more than 35% clay). These texture classes are assigned the soil types sand, loam and clay, respectively. In addition to the texture, the FAO Soil Map of the World distinguishes between 106 soil units. From these soil units only six generic terms are used for special evaluation. These are the codes for 'Inland water', 'Glacier/Ice', 'Lithosols', 'Salt', 'Histosols', and 'Dunes'. The code 'Inland water' in combination with 'sea' is used to define a land-sea-mask, 'Glacier/Ice' defines a separate soil type ice, 'Lithosols' define the soil type rock, and 'Histosols' the soil type peat. 'Salt' and 'Dunes', which do not provide a texture code, are associated with a coarse texture. Table 14.1 provides the soil types used. The search-algorithm is based on the frequency of occurrence of the different soil types in the respective grid element. But in view of the comparably coarse 5'-resolution of the FAO-data, normally there is only one soil type in one grid-element. Irrespective of this restriction similar fractions of coarse and medium textured or medium and fine textured soils are classified by intermediate types (sandy loam and loamy clay, respectively).

As an example, for the same region as in Fig. 14.1, in Fig. 14.2 the classified soil type is shown for the LMK-grid. In this case the resolution of the data set is more than three times coarser than the model resolution ($\sim$ 2.8 km). Therefore, the figure mainly depicts the resolution of the data set instead of the model resolution. It should be noted that - although a rather large number of model grid points are assigned the type 'ice' in the Alps - there are no model grid points which are assigned the type 'rock'.

14.2.4 Deep soil temperature

At the lower boundary of the active soil layers a temperature field has to be prescribed for the multi-layer soil model. Here the annual mean near surface temperature is used. The data set is provided by the University of East Anglia in 0.5° resolution for the whole globe except Antarctica (see: `http://www.cru.uea.ac.uk/cru/data/hrg.htm`; New et al. (1999)). In the program providing the initial and boundary data for LM, the data set is interpolated from the respective GME-field, a height-correction of $-0.7°C/100m$ is applied to reduce temperatures from the GME-orography to the LM-orography.

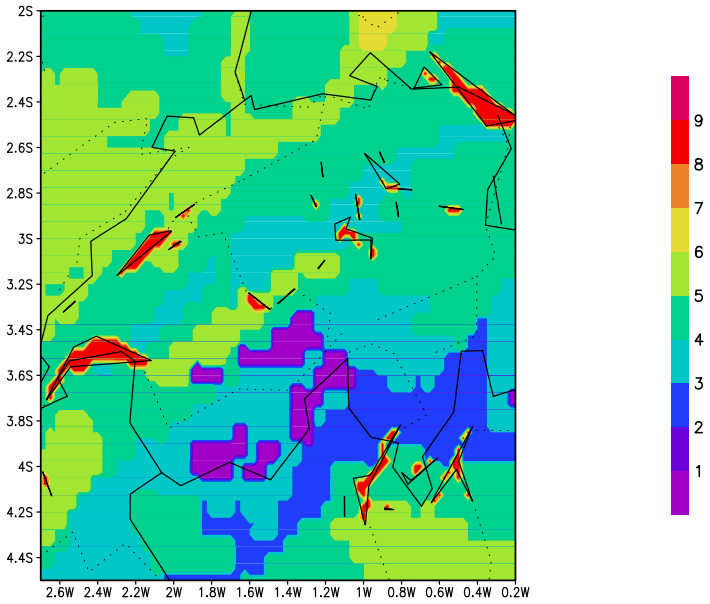

Figure 14.2: LMK soil types for part of the Alps

14.3 Secondary data

Secondary data have to be derived from the primary data to serve the needs of the model. In most cases association tables are used to relate the variables required by the model to the primary data.

14.3.1 Land fraction

The land fraction - or the land-sea-mask - is determined in two steps.

1) Three sets of primary data provide information, whether the respective pixel is land or water (orography, dominant soiltype, dominant land cover). This information is evaluated by counting the land pixels of the respective LM grid-element as a fraction of all pixels of this element. The GTOPO30 data set distinguishes between land points and the open sea. For the open sea a code -9999 is given, whereas for inland water the height of the lake surface above sea level is provided. Therefore, the evaluation of GTOPO30 only provides the coastlines of the open sea. The dominant soil type provides different codes for the open sea and inland water, a complete land fraction data set can be determined, but this data set suffers from the low resolution of the primary data. The land cover data set gives a complete differentiation between land, open sea and inland water, respectively.

2) After the evaluation of all three primary data sets three distributions of land fraction are available. Priority is given to the land fraction derived from the land cover data. But conflicts may occur if an LM grid-element is classified as land (land fraction ≥ 0.5), but no soil type is available. Such points have to be re-evaluated manually.

14.3.2 Roughness length

Roughness length over land in LM depends on two contributions, namely, the subgrid-scale variance of orography and the land-use. The subgrid-scale variance of orography σ^2 is computed in connection with the mean orography of the grid element. Then the roughness length contribution is parameterized according to $z_{0,var} = a_0\sigma^2 \arctan(\Delta x/b_0)$ with $a_0 = 10^{-5}m$ and $b_0 = 2.5m$, Δx is the average grid length. The roughness length $z_{0,i}$ of the different land cover classes is given in Tables 14.3, 14.4 and 14.5 at the end of this chapter. All i values in the respective LM grid-element of area F are logarithmically averaged, weighted by their respective areas F_i according to

$$z_{0,lu} = h \cdot \exp\left(-\frac{F}{\sum_{i=1}^{I} F_i/\left(\ln h - \ln z_{0,i}\right)}\right) \tag{14.1}$$

Here $h = 30m$ is an average height of the Prandtl-layer. The two contributions are added to obtain the total value of the roughness length $z_0 = z_{0,var} + z_{0,lu}$.

Over sea points the roughness length is not an external parameter but rather a variable computed on the basis of the Charnock-formula $z_{0,water} = \alpha_0 u_*^2/g$ with $\alpha_o = 0.0123$. Over ice-covered sea points the roughness length is assigned a constant value of $0.001m$.

14.3.3 Plant characteristics

The characteristic parameters of plants have to be determined from the dominant land cover. The parameters required by the soil model in LM are

i) the fractional area covered by plants,

ii) the leaf area index, and

iii) the root depth.

Apparently all these parameters depend on the time of the year. But normally only typical data for certain land cover classes are given, and for some classes there are no data available. Additional problems arise because different primary data sets are used. The basic table of characteristic plant parameters for a total of 59 land cover classes was compiled at the University of Osnabrück (Lieth and Esser, personal communication; see also Heise et al. (1988)). This table is used to define the characteristic values for the land cover classes of the primary data. In order to broadly simulate an annual course of the data, maximum plc_{max}, lai_{max} and minimum values plc_{min}, lai_{min} for plant cover plc and leaf area index lai are used and a simple analytical annual course depending on latitude and height is prescribed to interpolate between maximum and minimum values. This has to be done depending on the actual initial Julian Day J_d of the forecast. Therefore this determination is performed in the program which provides the initial and boundary data for LM. The following procedure is applied there:

a) Using the maps in WMO (1970) the starting Julian Day (V_s) of the vegetation period and the length (in days) of the vegetation period V_l were estimated. The criterion was a monthly mean near surface temperature exceeding $5 - 10°$C. These estimates were approximated by the following two formulae:

$$V_s = \max\left(1.0, 3(|\varphi| - 20°)\right) \text{and}$$

$$V_l = \min\left(365, 345 - 4.5(|\varphi| - 20°)\right).$$

b) A height-reduction factor $f_h(\Phi_s) = \exp(-5 \cdot 10^{-9} \cdot \Phi_s^2)$ with the geopotential height of the earth's surface Φ_s reduces the vegetation effect with increasing surface height.

If p denotes either plant cover or leaf area index, the interpolation in time is performed by

$$p(\varphi, J_d, \Phi_s) = p_{min} + (p_{max} - p_{min}) \cdot f_v \cdot f_h(\Phi_s), \tag{14.2}$$

where

$$f_v = \max\left(0.0, \min\left(1.0, C \cdot \sin(\pi \cdot \max\left(0.0, \left(J_d - V_s\right)/V_l\right))\right)\right). \tag{14.3}$$

The constant $C = 1.12$ defines the length of the period for which $f_v = 1$. For the root depth r_{depth} only very sparse and inconsistent data are available. This parameter does not only depend on the plant species but also on the structure of the soil. Because of these ambiguities the roots are treated more or less as a tuning parameter for plant transpiration. The time dependent values for LM are computed by

$$z_{root} = \min\left(r_{depth}, z_{r,min} + \left(z_{r,max} - z_{r,min}\right) f_v^2\right), \tag{14.4}$$

where $z_{r,min} = 0.12m$ and $z_{r,max} = 0.70m$.

As there is evidence that some of the values in Tables 14.3 and 14.4 are not realistic, especially the leaf area index seems to be too large for a number of species, a re-evaluation has taken place. This re-evaluation, based on the GLC2000 data set, considers plant parameters given in the EU-project ELDAS and a correspondence table between the GLC2000 plant types and the IGBP plant classification. The associations are given in Table 14.5.

14.3.4 Wooded areas

Although wooded areas are accounted for in the determination of secondary data (see the association tables), a special treatment of two different effects might be advisable for wooded areas. One effect is the influence on snow albedo of forests. For a given value of snow water equivalent the snow albedo for wooded areas is much lower than for areas covered by low vegetation only. The second aspect is the transpiration rate of wooded areas. As shown by different field campaigns, irrespective of the dense vegetation cover, the high leaf area index values and sometimes large rooting depths, for similar values of soil water content forests show lower transpiration rates compared to other vegetation types. This can be accounted for by increasing the minimum stomata resistance of forests. To provide for the inclusion of these effects, two additional fields were recently added to the set of external parameter fields. These additional fields are the fractions of the grid element covered by deciduous forest and by evergreen forest, respectively.

14.3.5 Thermal and hydraulic parameters of the soil

In LM all thermal and hydraulic parameters of the soil are uniquely related to a set of 8 different soil types. Therefore, only soil types have to be available on the LM-grid. The relevant parameters are taken from the association table available in the model code. The corresponding table is listed in Section 11.3.3, Tab. 11.1. These parameters are compiled from a lot of different literature sources and older model versions, partly the sources are no longer available. A consistent re-determination of these parameters seems to be advisable.

14.4 Final remarks

Presently the operational applications and the applications under development use different data sets for the external parameters. Additionally, different association tables are used to deduce plant parameters required by the model as external parameters, the secondary parameters, from the primary parameters (data sets). Therefore Table 14.2 summarises these data sets. Note that the parameter files provided for LME and LMK also have a different rotated pole than the ones provided for the other LM applications.

The program-system which is used at DWD for processing the primary data is available for COSMO members. A detailed documentation of the usage of the program-system is also available. But it is important to note that the change of external parameters requires a careful procedure. All changes which alter the evapotranspiration (plant cover, leaf area index, root depth and soil type) interfere in the water (and thermal) budget of the soil. Especially with the multi-layer soil model the active depth of the soil has a large storage capacity. As a consequence, the time required to adjust to new evapotranspiration is very long (some months). A good time for change is late winter, when plants are not active and the soil is normally filled by water. It is advised against changing external parameters in summer. For the same reason the interpolation of soil temperature and soil water content from LM applications using different models for the soil processes can lead to unwanted spinup problems in the LM soil model.

Table 14.2: Summary of the data sets used in different model versions (August 2005)

Ext. parameter file	**Model / Application**	**GTOPO30**	**GLOBE**	**GLCC**	**CORINE**	**GLC2000**
`invar.i128a`	GME		X			X
`invar.i192a`	GME		X			X
`lm_d1_28000_241x193.g1`		X		X	X	
`lm_d1_21000_321x257.g1`		X		X	X	
`lm_d1_14000_481x385.g1`	LM_IMGW, LM_HNMS	X		X	X	
`lm_d1_07000_961x769.g1`	LM_DWD, aLMo, LAMI	X		X	X	
`lm_d2_07000_381x379.g1`		X		X	X	
`lm_d3_02800_561x921.g1`		X		X	X	
`lm_d5_07000_965x773.g1`	LME (DWD)		X			X
`lm_d0_02800_1605x1605.g1`	LMK (DWD)		X			X

Table 14.3: Characteristic parameters for plants: GLCC-data set

No.	**Land use class**	$\mathbf{z_0}$ [m]	**root depth** [m]	**plant cover** Max	**plant cover** Min	**leaf area index** Max	**leaf area index** Min
1	urban and built up land	1.00	0.60	0.10	0.05	4.70	0.10
2	dryland cropland and pasture	0.10	1.00	0.90	0.45	5.00	0.20
3	irrigated cropl. and pasture	0.10	0.60	1.00	0.50	5.60	0.20
4	mixed dryland/irrigated	0.10	0.80	0.90	0.45	5.30	0.20
5	cropland/grassland mosaic	0.07	1.00	0.90	0.45	5.90	0.35
6	cropland/woodland mosaic	0.25	1.00	0.90	0.45	6.10	1.20
7	grassland	0.03	0.60	1.00	1.00	4.50	0.50
8	shrubland	0.20	1.00	0.40	0.10	4.00	0.10
9	mixed shrubland/grassland	0.15	1.00	0.60	0.10	4.00	0.10
10	savannah	0.15	2.00	0.80	0.20	3.00	1.00
11	deciduous broadleaf forest	1.00	1.00	1.00	0.00	6.00	0.00
12	deciduous needleleaf forest	1.00	0.60	1.00	0.00	6.00	0.00
13	evergreen broadleaf forest	1.00	1.00	1.00	1.00	9.00	9.00
14	evergreen needleleaf forest	1.00	0.60	1.00	1.00	8.00	8.00
15	mixed forest	1.00	0.80	1.00	0.50	7.00	2.25
16	water bodies	0.0002	0.00	0.00	0.00	0.00	0.00
17	herbaceous wetland	0.05	0.40	0.80	0.40	3.00	1.00
18	wooded wetland	0.20	0.40	0.90	0.10	4.00	1.00
19	barren or sparsely vegetated	0.05	0.30	0.05	0.02	1.00	0.50
20	herbaceous tundra	0.05	0.10	0.30	0.00	2.10	0.00
21	wooded tundra	0.20	0.10	0.40	0.20	3.20	0.50
22	mixed tundra	0.10	0.10	0.35	0.10	2.60	0.25
23	bare ground tundra	0.03	0.00	0.00	0.00	0.00	0.00
24	snow or ice	0.01	0.00	0.00	0.00	0.00	0.00

Table 14.4: Characteristic parameters for plants: CORINE data set

No.	Land use class	z_0 [m]	root depth [m]	plant cover		leaf area index	
				Max	Min	Max	Min
1	continuous urban fabric	1.00	0.60	0.05	0.05	4.70	0.10
2	discontinuous urban fabric	1.00	0.60	0.20	0.05	4.70	0.10
3	industrial/commercial units	1.00	0.60	0.05	0.05	4.70	0.10
4	road and rail networks	0.10	0.10	0.05	0.05	4.70	0.10
5	port areas	1.00	0.10	0.05	0.05	4.70	0.10
6	airports	0.10	0.10	0.30	0.10	4.50	0.50
7	mineral extraction sites	0.10	0.10	0.05	0.05	1.00	0.50
8	dump sites	0.10	0.10	0.05	0.05	1.00	0.50
9	construction sites	1.00	0.60	0.10	0.05	1.00	0.50
10	green urban areas	0.25	1.00	1.00	0.80	5.80	1.40
11	sport and leisure facilities	0.03	0.60	1.00	0.80	5.80	1.40
12	non-irrigated arable land	0.10	1.00	0.90	0.45	5.00	0.20
13	permanently irrigated land	0.10	0.60	1.00	0.50	5.60	0.20
14	rice fileds	0.10	0.60	1.00	0.00	4.50	0.00
15	vineyards	0.30	0.60	0.90	0.30	4.00	0.10
16	fruit trees and berry plant.	0.80	0.60	1.00	0.00	6.00	0.00
17	olive groves	1.00	0.60	1.00	0.50	5.00	3.00
18	pastures	0.10	0.60	1.00	0.50	4.50	0.50
19	annual crops	0.50	0.80	1.00	0.50	5.00	0.20
20	complex cultivation patterns	0.15	1.00	0.90	0.20	5.30	0.20
21	agriculture (principally)	0.15	1.00	0.90	0.30	5.30	0.20
22	agro-forestry areas	0.25	1.00	0.90	0.45	6.10	1.20
23	broadleaf forest	1.00	1.00	1.00	0.00	6.00	0.00
24	coniferous forest	1.00	0.60	1.00	1.00	8.00	8.00
25	mixed forest	1.00	0.80	1.00	0.50	7.00	4.00
26	natural grassland	0.03	0.60	1.00	1.00	4.50	0.50
27	moors and heathlands	0.05	0.40	0.80	0.40	3.00	1.00
28	sclerophyllus vegetation	0.50	0.60	0.80	0.65	4.30	3.00
29	transitional woodland-shrub	0.60	0.90	0.70	0.40	5.50	1.10
30	beaches, dunes, sand	0.02	0.30	0.10	0.05	1.00	0.50
31	bare rocks	0.10	0.00	0.00	0.00	0.00	0.00
32	sparsely vegetated areas	0.05	0.30	0.05	0.02	1.00	0.50
33	burnt areas	0.05	0.30	0.05	0.02	0.50	0.50
34	glaciers and perpetual snow	0.01	0.00	0.00	0.00	0.00	0.00
35	inland marshes	0.03	0.60	1.00	1.00	4.50	0.50
36	peat bogs	0.05	0.40	0.80	0.40	3.00	1.00
37	salt marshes	0.03	0.60	0.80	0.80	3.00	1.00
38	salines	0.02	0.00	0.00	0.00	0.00	0.00
39	intertidal flats	0.01	0.00	0.00	0.00	0.00	0.00
40	water courses	0.0002	0.00	0.00	0.00	0.00	0.00
41	water bodies	0.0002	0.00	0.00	0.00	0.00	0.00
42	coastal lagoones	0.0002	0.00	0.00	0.00	0.00	0.00
43	estuaries	0.0002	0.00	0.00	0.00	0.00	0.00
44	sea and ocean	0.0002	0.00	0.00	0.00	0.00	0.00

Table 14.5: Characteristic parameters for plants: GLC2000 data set

No.	**Land use class**	$\mathbf{z_0}$ [m]	**root depth** [m]	**plant cover** Max	**plant cover** Min	**leaf area index** Max	**leaf area index** Min
1	evergreen broadleaf forest	1.00	1.00	0.80	0.80	2.40	1.40
2	deciduous broad closed	1.00	1.00	0.90	0.75	3.40	1.00
3	deciduous broadleaf open	0.15	2.00	0.80	0.70	2.00	1.00
4	evergreen needleleaf forest	1.00	0.60	0.80	0.80	3.80	1.30
5	deciduous needleleaf forest	1.00	0.60	0.90	0.75	3.80	1.00
6	mixed leaf trees	1.00	0.80	0.90	0.75	3.40	1.10
7	fresh water flooded trees	1.00	1.00	0.80	0.80	2.40	1.40
8	saline water flooded trees	1.00	1.00	0.80	0.80	2.40	1.40
9	mosaic tree/natural veget.	0.20	1.00	0.80	0.70	1.50	0.60
10	burnt tree cover	0.05	0.30	0.50	0.50	0.60	0.40
11	evergreen shrubs closed/open	0.20	1.00	0.80	0.70	1.50	0.60
12	deciduous shrubs closed/open	0.15	2.00	0.80	0.70	2.00	1.00
13	herbaceous veget.closed/open	0.03	0.60	0.90	0.75	3.10	1.00
14	sparse herbaceous or grass	0.05	0.30	0.50	0.50	0.60	0.40
15	flooded shrubs or herbaceous	0.05	0.40	0.80	0.70	2.00	1.00
16	cultivated and managed	0.07	1.00	0.90	0.50	3.30	0.70
17	mosaic crop/tree/net veget.	0.25	1.00	0.80	0.65	2.10	1.00
18	mosaic crop/shrub/grass	0.07	1.00	0.90	0.50	3.30	0.70
19	bare areas	0.05	0.30	0.50	0.20	0.60	0.40
20	water	0.0002	0.00	0.00	0.00	0.00	0.00
21	snow and icea	0.01	0.00	0.00	0.00	0.00	0.00
22	artificial surface	1.00	0.60	0.20	0.10	1.00	0.10
23	undefined	-	-	-	-	-	-

References

Baines, P. and T. Palmer, 1990. Rationale for a new physically based parametrization of sub-grid scale orographic effects. *European Centre for Medium-Range Weather Forecasts*. Tech. Memo. 169, Reading. 11 pp. (Available at: http://www.ecmwf.int).

Baldauf, M. and J.-P. Schulz, 2004. Prognostic Precipitation in the Lokal Modell (LM) of DWD. COSMO Newsletter No. 4, Deutscher Wetterdienst. 177-180.

Benoit, R., 1976. A comprehensive parameterisation of the atmospheric boundary layer for general circulation models. Technical Report PB-264540, US Department of Commerce.

Bigg, E., 1953. The formulation of atmospheric ice crystals by the freezing of droplets. *J. Roy. Met. Soc.*, 79, 510–519.

Blackadar, A. K., 1962. The vertical distribution of wind and turbulent exchange in a neutral atmosphere. *J. Geophys. Res.*, 67, 3095–3102.

Brooks, R. H. and A. T. Corey, 1966. Properties of porous media affecting fluid flow. *Journal of the Irrigation and Drainage Division, ASCE*, 72, 61–88.

Businger, J. A., J. C. Wyngaard, Y. Izumi, and E. F. Bradley, 1971. Flux profile relationships in the atmospheric surface layer. *J. Atmos. Sci.*, 28, 181–189.

Clark, T. L. and W. D. Hall, 1983. A cloud physical parameterization method using movable basis functions: stochastic coalesence parcel calculations. *J. Atmos. Sci.*, 40, 1709–1728.

Cosby, B. J., G. M. Hornberger, R. B. Clapp, and T. R. Gin, 1984. A statistical exploration of the relationships of soil moisture characteristics to the physical properties of soils. *Water Resour. Res.*, 20, 682–690.

Crawford, N. H. and R. K. Linsley, 1966. Digital simulation in hydrology, Stanford Watershed Model IV. Technical Report Techn. Report No. 39, Stanford University.

Denmead, O. T. and R. H. Shaw, 1962. Availability of soilwater to plants as affected by soil moisture content and meteorological conditions. *Agron. Journ.*, 54, 385–390.

Dickinson, R. E., 1984. Modeling evapotranspiration for three-dimensional global climate models: Climate Processes and Climate Sensitivity. *Geophysical Monograph 29, Maurice Ewing Volume 5*, 5, 58–72.

Doms, G. and J. Förstner, 2004. Development of a kilometer-scale NWP-System: LMK. COSMO Newsletter No. 4, Deutscher Wetterdienst. 159-167.

Doms, G. and U. Schättler, 2002, November. *A Description of the Nonhydrostatic Regional Model LM. Part I: Dynamics and Numerics*. Postfach 100465, 63007 Offenbach, Germany: Deutscher Wetterdienst, Offenbach.

Dunst, M., 1980. Ergebnisse von Modellrechnungen zur Ausbreitung von Stoffbeimengungen in der planetarischen Grenzschicht. *Z. f. Meteorol.*, 30, 47–59.

Dyer, A., 1974. A review of flux-profile relations. *Bound. Layer Meteor.*, 1, 363–372.

ECMWF, 1991. *Research Manual 3, ECMWF forecast model, Physical parameterization, 3rd Edition.* Shinfield Park, Reading, Berkshire RG2 9AX, England: ECMWF Research Department.

FAO-Unesco, 1974. *Soil map of the world.* Unesco-Paris, 10 volumes plus 19 maps, scale 1:5000000, and CD-ROM.

Ferrier, B., 1994. A double-moment multiple-phase four-class bulk ice scheme. Part I: Description. *J. Atmos. Sci.*, 51, 249–280.

Flerchinger, G. and K. Saxton, 1989. Simultaneous heat and water model of freezing snow-residue-soil system. I. Theory and development. *Transactions of the ASEA*, 32, 2, 565–571.

Fletcher, N., 1962. *The Physics of Rainclouds.* Cambridge University Press.

Förstner, J. and G. Doms, 2004. Runge-Kutta time integration and high-order spatial discretization of advection - a new dynamical core for the LMK. COSMO Newsletter No. 4, Deutscher Wetterdienst. 168-176.

Gaßmann, A., 2002. 3D-transport of precipitation. COSMO Newsletter No. 2, Deutscher Wetterdienst. 113-117.

Gaßmann, A., 2003. Case Studies with the 2-Timelevel Scheme and Prognostic Precipitation. COSMO Newsletter No. 3, Deutscher Wetterdienst. 173-176.

Geleyn, J.-F. and A. Hollingsworth, 1979. An economical analytical method for the computation of the interaction between scattering and line absorption of radiation. *Contr. Atmos. Phys.*, 52, 1–16.

Ghan, S. and R. Easter, 1992. Computationally efficient approximations to stratiform cloud microphysics parameterization. *Mon. Wea. Rev.*, 120, 1572–1582.

GLOBE-Task-Team, 1999. The Global Land One-kilometer Base Elevation (GLOBE) Digital Elevation Model, version 1.0. Technical report, National Oceanic and Atmospheric Administration, National Geophysical Data Center, 325 Broadway, Boulder, Colorado 80305, USA. (Digital data base available at: http://www.ngdc.noaa.gov/mgg/topo/globe.html).

Heise, E., W. Jacobs, M. Ketterer, and V. Renner, 1988. Klimasimulation mit atmosphärischen Modellen im Zeitskalenbereich von Monaten. Technical Report Abschlußbericht Projekt BMFT-KF 2012 8, Deutscher Wetterdienst, Abteilung Forschung.

Herzog, H.-J., U. Schubert, G. Vogel, A. Fiedler, and R. Kirchner, 2002. LLM - the high-resolving nonhydrostatic simulation model in the DWD-project LITFASS. Part I: Modelling technique and simulation method. COSMO Technical Report No. 4, Deutscher Wetterdienst.

Herzog, H.-J., G. Vogel, and U. Schubert, 2002. LLM - a nonhydrostatic model applied to high-resolving simulations of turbulent fluxes over heteogeneous terrain. *Theor. Appl. Climatol.*, 73, 67–86.

Hillel, D., 1980. *Applications of Soil Physics.* Academic Press, New York.

Hinze, J. O., 1975. *Turbulence* (2nd ed.). New York: McGraw-Hill Book Company.

Hobbs, P. and A. Rangno, 1985. Ice particle concentrations in clouds. *J. Atmos. Sci.*, 42, 2523–2549.

Höller, H., 1982. Detaillierte und parametrisierte Modellierung der Wolken-Mikrophysik in einem stationären Wolkenmodell. Mitteilungen, Heft 36, Institut für Geophysik und Meteorologie der Universität zu Köln.

Houze, R.A., J., 1993. *Cloud Dynamics*, Volume 53 of *International Geophysics Series*. Academic Press, Inc.

Ikawa, M., H. Mizuno, T. Matsuo, M. Murakami, Y. Yamada, and K. Saito, 1991. Numerical modelling of the convective snow clod over the Sea of Japan. - precipitation mechanism and sensitivity to the ice nucleation mechanism. *J. Meteor. Soc. Jap.*, 69, 641–667.

Jacobsen, I. and E. Heise, 1982. A new economic method for the computation of the surface temperature in numerical models. *Contr. Atmos. Phys.*, 55, 128–141.

Kain, J. and J. Fritsch, 1993. Convective parameterization for mesoscale models: The Kain Fritsch scheme. In *The Representation of Cumulus Convection in Numerical Models, Meteor. Monogr., Vol. 24, No. 46*, pp. 165–170. American Meteorological Society, Boston.

Kessler, E., 1969. *On the Distribution and Continuity of water substance in the atmospheric circulations*, Volume 32 of *Meteorological Monographs Vol. 10*. American Meteorological Society, Boston.

Kirillin, G., J. Hochschild, D. Mironov, A. Terzhevik, S. Golosov, and G. Nützmann, 2011. FLake-Global: Online lake model with worldwide coverage. *Environ. Modell. Softw.*, 26, 683–684.

Kitaigorodskii, S. and Y. Miropolsky, 1970. On the theory of the open ocean active layer. *Izvestiya Atmosph. Ocean Physics*, 6, 178–188.

Levkov, L., B. Rockel, H. Kapitza, and E. Raschke, 1992. 3d Mesoscale Numerical Studies of Cirrus and stratus clouds by their time and space evolution. *Contr. Atmos. Phys.*, 65, 35–57.

Lin, S. J. and R. Rood, 1996. Multidimensional flux-form semi-lagrangian transport schemes. *Mon. Wea. Rev.*, 124, 2046–2070.

Locatelli, J. and P. Hobbs, 1974. Fall speeds and masses of solid precipitation particles. *J. Geophys. Res.*, 79, 1914–1932.

Lord, S., H. Willoughby, and J. Piotrowicz, 1984. Role of parameterized ice-phase microphysics in an axisymmetric nonhydrostatic tropical cyclone model. *J. Atmos. Sci.*, 41, 2836–2848.

Lott, F. and M. Miller, 1997. A new subgrid-scale orographic drag parametrization: Its formulation and testing. *Q. J. R. Meteor. Soc.*, 123, 101–127.

Louis, J.-F., 1979. A parametric model of vertical eddy fluxes in the atmosphere. *Bound. Layer Meteor.*, 17, 187–202.

Lüpckes, C., K.-D. Beheng, and G. Doms, 1989. A parametrization scheme for simulating collision/coalesence of water drops. *Contr. Phys. Atmos.*, 62, 289–306.

Majewski, D. and R. Schrodin, 1995. *Dokumentation des EM/DM-Systems*. Deutscher Wetterdienst.

Marshall, J. and P. W.M., 1948. The distribution of raindrops with size. *J. Meteor.*, 5, 154–166.

Matveev, L., 1984. *Cloud Dynamics*. D. Reidel Publ. Comp., Dortrecht.

Mellor, G. and T. Yamada, 1974. A hierarchy of turbulence closure models for planetary boundary layers. *J. Atm. Sc.*, 31, 1791–1806.

Mellor, G. and T. Yamada, 1982. Development of a turbulence closure model for geophysical fluid problems. *Rev. Geophys. and Space Phys.*, 20, 851–875.

Meyers, M., P. DeMott, and W. Cotton, 1992. New primary ice-nucleation parameterization in an explicit cloud model. *J. Appl. Meteor.*, 31, 708–721.

Mironov, D., 2008. Parameterization of lakes in numerical weather prediction. Description of a lake model. COSMO Technical Report No. 11. 41 pp. (Available at: http://www.cosmo-model.org).

Mironov, D., E. Heise, E. Kourzeneva, B. Ritter, N. Schneider, and A. Terzhevik, 2010. Implementation of the lake parameterisation scheme FLake into the numerical weather prediction model COSMO. *Boreal Env. Res.*, 15, 218–230.

Mironov, D. and B. Ritter, 2004. Testing the new ice model for the global NWP system GME of the German Weather Service; In: J. Cote (Ed.), *Research Activities in Atmospheric and Oceanic Modelling*. Rep. 34, WMO/TD 1220, WMO, Geneve. 4.21-4.22.

Müller, E., 1981. Turbulent flux parameterization in a regional-scale model. In *ECMWF Workshop on planetary boundary layer parameterization*, pp. 193–220. 25-27 November, 1981.

New, M., M. Hulme, and P. Jones, 1999. Representing twentieth-century space-time climate variability Part I: Development of a 1961-90 mean monthly terrestrial climatology. *J. Climate*, 12, 829–856.

Rijtema, P., 1969. Soil moisture forecasting. Technical Report Nota 513, Instituut voor Cultuurtechniek en Waterhuishouding, Wageningen.

Ritter, B. and J.-F. Geleyn, 1992. A comprehensive radiation scheme for numerical weather prediction models with potential applications in climate simulations. *Mon. Wea. Rev.*, 120, 303–325.

Rockel, B., E. Raschke, and B. Weyres, 1991. A parameterization of broad band radiative transfer properties of water, ice, and mixed clouds. *Beitr. Phys. Atmos.*, 64, 1–12.

Schulz, J.-P., 2006. The new Lokal-Modell LME of the German Weather Service. *COSMO Newsletter*, 6, 210–212. (Available at: http://www.cosmo-model.org).

Schulz, J.-P., 2008. Introducing sub-grid scale orographic effects in the COSMO model. *COSMO Newsletter*, 9, 29–36. (Available at: http://www.cosmo-model.org).

Schulz, J.-P., 2011. Introducing a sea ice scheme in the COSMO model. *COSMO Newsletter*, 11, 32–40. (Available at: http://www.cosmo-model.org).

Segami, A., K. Kurihara, H. Nakamura, M. Ueno, and I. Takano, 1989. Description of the Japan spectral model. Technical Report 25, Japan Meteorological Agency, Tokyo.

Sommeria, G. and J. W. Deardorff, 1977. Subgrid-scale condensation in models of non-precipitating clouds. *J. Atmos. Sci.*, 34, 344–355.

Stevens, D. et al., 2000. Small-scale processes and entrainment in a stratocumulus marine boundary. *J. Atm. Sc.*, 57, 567–581.

Stull, R., 1988. *An Introduction to Boundary Layer Meteorology*. Kluwer Academic Publishers, Dordrecht/Boston/London.

Tanre, D., J.-F. Geleyn, and J. Slingo, 1984. First results of the introduction of an advanced aerosol-radiation interaction in the ECMWF low resolution global model. In *Proc. of the Meetings of Experts on Aerosols and their Climatic Effects, Williamsburg, VA*, pp. 133–177. WMO and IAMAP.

Tibaldi, S., 1986. Envelope orography and maintenance of quasi-stationary waves in the ECMWF model. *Adv. Geophys.*, 29, 339–374.

Tiedtke, M., 1989. A comprehensive mass flux scheme for cumulus parameterization in large-scale models. *Mon. Wea. Rev.*, 117, 1779–1799.

Valdez, M. and K. Young, 1985. Number fluxes in equilibrium raindrop populations: A Markov chain analysis. *J. Atmos. Sci.*, 42, 1024–1032.

van Wijk, W. R. and D. A. de Vries, 1966. *The atmosphere and the soil*. Amsterdam.

Wallace, J., S. Tibaldi, and A. Simmons, 1983. Reduction of systematic forecast errors in the ECMWF model through the introduction of an envelope orography. *Q. J. R. Meteor. Soc.*, 109, 683–717.

Warrach, K., 2000. *Gefrorener Boden und Schneebedeckung unter besonderer Berücksichtigung des hydrologischen Verhaltens der Landoberfläche*. Ph. D. thesis, GKSS.

WMO, 1970. *Climatic Atlas of Europe*. WMO-UNESCO.

Yanai, M., S. Esbensen, and J. Chu, 1973. Determination of bulk properties of tropical cloud clusters from large-scale heat and moisture budgets. *J. Atmos. Sci.*, 30, 611–627.

Young, K., 1974. A numerical simulation of wintertime, orographic precipitation. Part I: Description of model microphysics and numerical techniques. *J. Atmos. Sci.*, 31, 1735–1748.